Enhancing Advanced NMR Applications through Parahydrogen-based Hyperpolarization Techniques

Zur Erlangung des akademischen Grades eines

DOKTORS DER INGENIEURWISSENSCHAFTEN (Dr.-Ing.)

von der KIT-Fakultät für Maschinenbau des
Karlsruher Instituts für Technologie (KIT)
angenommene

DISSERTATION

von

M.Sc. Jing Yang

Tag der mündlichen Prüfung:	September 23, 2025
Hauptreferent:	Prof. Dr. Jan Gerrit Korvink
Korreferent:	Prof. Dr. Jan-Bernd Hövener

Karlsruher Institut für Technologie
Institut für Mikrostrukturtechnik
Hermann-von-Helmholtz Platz 1
76344 Eggenstein-Leopoldshafen

Selbstständigkeitserklärung

Ich versichere wahrheitsgemäß, die Arbeit selbstständig verfasst, alle benutzten Hilfsmittel vollständig und genau angegeben und alles kenntlich gemacht zu haben, was aus Arbeiten anderer unverändert oder mit Abänderungen entnommen wurde sowie die Satzung des KIT zur Sicherung guter wissenschaftlicher Praxis in der jeweils gültigen Fassung beachtet zu haben.

Eggenstein-Leopoldshafen, September 23, 2025 Jing Yang

Abstract

Nuclear Magnetic Resonance (NMR) spectroscopy is a powerful analytical technique, yet its inherently low sensitivity limits its effectiveness in detecting low-concentration analytes. Parahydrogen (*para*-H_2)-based hyperpolarization methods, including ParaHydrogen Induced Polarization (PHIP) and Signal Amplification by Reversible Exchange (SABRE), offer rapid and cost-effective signal enhancement by several orders of magnitude. However, challenges such as substrate specificity, limited reproducibility, and the lack of high-throughput integration continue to hinder their widespread adoption.

To address these limitations from an engineering perspective, this work begins by systematically evaluating three practical PHIP and SABRE implementations: manual shake-and-drop, bubbling, and continuous-flow gas–liquid reactors based on polarization efficiency, reproducibility, and ease of operation. The results identify continuous-flow reactors as the optimal approach for efficient and consistent hyperpolarization, offering precise regulation of gas–liquid mixing under controlled pressure, flow rate, and temperature. In contrast, while the bubbling method provides a simple and broadly compatible solution, its reproducibility can be significantly improved through automation, making it more suitable for standardized and accessible hyperpolarization workflows.

Building on these insights, two complementary hyperpolarization platforms are developed. The first leverages continuous-flow gas–liquid reactors, particularly tube-in-tube configurations, to enable stable polarization under sustained *para*-H_2 supply. This system supports advanced strategies such as parallelized SABRE hyperpolarization with NMR coil arrays for high-throughput detection, and steady-state Radiation Amplification by Stimulated Emission of Radiation (RASER) emission across different detection regimes for precision J-coupling measurements and nonlinear spin dynamics studies.

In parallel, a fully automated workstation is established to address the reproducibility and usability challenges of bubbling-based setups. By standardizing gas–liquid mixing, automating polarization field control, and implementing programmable magnetic field cycling, the platform improves experimental consistency and reduces the barrier to broader adoption. It also facilitates quantitative optimization of polarization parameters and supports routine PHIP and SABRE experiments using benchtop NMR systems.

Together, these platforms demonstrate how targeted engineering solutions can address key implementation challenges in PHIP and SABRE workflows, unlocking broader applications of *para*-H_2-based hyperpolarization and paving the way for wider adoption and commercialization in high-throughput, high-precision NMR.

Zusammenfassung

Die Kernspinresonanzspektroskopie (NMR) ist eine leistungsfähige analytische Methode, deren inhärent geringe Empfindlichkeit jedoch ihre Wirksamkeit bei der Detektion von niedrig konzentrierten Analyten einschränkt. Parawasserstoff (*para*-H_2)-basierte Hyperpolarisationsmethoden, einschließlich der Parawasserstoff-induzierten Polarisation (PHIP) und der Signalverstärkung durch reversiblen Austausch (SABRE), ermöglichen eine schnelle und kostengünstige Signalverstärkung um mehrere Größenordnungen. Dennoch erschweren Herausforderungen wie Substratspezifität, begrenzte Reproduzierbarkeit und mangelnde Integration in Hochdurchsatz-Workflows ihre breite Anwendung.

Zur Überwindung dieser Einschränkungen wird in dieser Arbeit ein ingenieurwissenschaftlicher Ansatz verfolgt. Zunächst werden drei praktische Implementierungsstrategien für PHIP und SABRE: manuelles Schütteln („shake-and-drop“), Begasung („bubbling“, d.h. das Lösen von *para*-H_2 in der Flüssigkeit) und kontinuierlich betriebene Gas-Flüssig-Reaktoren, systematisch im Hinblick auf Polarisierungseffizienz, Reproduzierbarkeit und Bedienkomfort untersucht. Die Ergebnisse identifizieren kontinuierliche Durchflussreaktoren als die optimale Methode für eine effiziente und reproduzierbare Hyperpolarisation, da sie eine präzise Steuerung der Gas-Flüssig-Mischung unter kontrollierten Bedingungen hinsichtlich Druck, Durchflussrate und Temperatur ermöglichen. Dies verbessert die Polarisierungseffizienz, die Reproduzierbarkeit und die Benutzerfreundlichkeit des Verfahrens.

Im Gegensatz dazu bietet die Begasung eine einfache und breit kompatible Methode, deren Reproduzierbarkeit jedoch durch Automatisierung deutlich verbessert werden kann – ein entscheidender Schritt hin zu standardisierten und zugänglichen Hyperpolarisationsprozessen.

Auf Grundlage dieser Erkenntnisse werden zwei komplementäre Hyperpolarisationsplattformen entwickelt. Die erste basiert auf kontinuierlichen Gas-Flüssig-Reaktoren, insbesondere solchen mit „tube-in-tube“-Konfiguration, und erlaubt eine stabile Polarisation bei kontinuierlicher Versorgung mit *para*-H_2. Diese Plattform unterstützt fortgeschrittene Konzepte wie die parallele SABRE-Hyperpolarisation mittels NMR-Spulensystemen zur Hochdurchsatz-Detektion sowie den stationären RASER-Effekt (Radiowellenverstärkung durch stimulierte Emission von Strahlung) in verschiedenen Detektionsregimen zur präzisen Bestimmung von J-Kopplungskonstanten und zur Untersuchung nichtlinearer Spindynamiken.

Parallel dazu wird eine vollständig automatisierte Arbeitsstation entwickelt, um die Herausforderungen hinsichtlich Reproduzierbarkeit und Benutzerfreundlichkeit der Begasungsmethode zu adressieren. Durch die Standardisierung der Gas-Flüssig-Vermischung, die Automatisierung der Polarisationsfeldsteuerung und die Implementierung eines programmierbaren

Magnetfeld-Zyklus verbessert die Plattform die experimentelle Reproduzierbarkeit und senkt die Hürde für eine breitere Anwendung. Darüber hinaus ermöglicht es die quantitative Optimierung der Polarisierungsparameter und unterstützt routinemäßige PHIP- und SABRE-Experimente mit Tisch-NMR-Systemen.

Zusammen zeigen diese Plattformen, wie gezielte ingenieurtechnische Lösungen zentrale Herausforderungen bei der Umsetzung von PHIP- und SABRE-Prozessen überwinden können. Damit wird das Anwendungsspektrum der *para*-H_2-basierten Hyperpolarisation erweitert und ein Fundament für deren breitere Nutzung und zukünftige Kommerzialisierung in hochpräzisen und hochdurchsatzfähigen NMR-Anwendungen geschaffen.

Nomenclature

Abbreviations

Abbreviation	Definition
NMR	Nuclear Magnetic Resonance
MRI	Magnetic Resonance Imaging
LAC	Level Anti-Crossing
FID	Free Induction Decay
FFT	Fast Fourier Transform
PHIP	ParaHydrogen Induced Polarization
SABRE	Signal Amplification By Reversible Exchange
SABRE-SHEATH	Signal Amplification By Reversible Exchange in SHield Enables Alignment Transfer to Heteronuclei
RASER	Radio-frequency Amplification by Stimulated Emission of Radiation
HSQC	Heteronuclear Single Quantum Coherence
INEPT	Insensitive Nuclei Enhanced by Polarization Transfer
DNP	Dynamic Nuclear Polarization
SEOP	Spin-Exchange Optical Pumping
para-H_2	Parahydrogen
ortho-H_2	Orthohydrogen
T_1 Relaxation	Longitudinal relaxation time
T_2 Relaxation	Transverse relaxation time
T_2^* Relaxation	Effective transverse relaxation time
RF	Radio Frequency
SNR	Signal-to-Noise Ratio
PASADENA	Parahydrogen And Synthesis Allow Dramatically Enhanced Nuclear Alignment
ALTADENA	Adiabatic Longitudinal Transport After Dissociation Engenders Nuclear Alignment
ppm	Part per million
NCs	NMR cells
MASER	Microwave Amplification by Stimulated Emission of Radiation
LASER	Light Amplification by Stimulated Emission of Radiation
µT	Micro-Tesla
mT	Milli-Tesla

CIDNP	Chemically Induced Dynamic Nuclear Polarization
PTF	Polarization Transfer Field
PWM	Pulse Width Modulation
GUI	Graphical User Interface
HP	Hyperpolarized
RSD	Relative Standard Deviation

Symbols

Symbol	Definition	Unit
$\boldsymbol{S}$	Spin angular momentum	$\mathrm{J \cdot s}$
$\boldsymbol{\mu}$	Magnetic moment	$\mathrm{J \cdot T^{-1}}$
γ	Gyromagnetic ratio	$\mathrm{rad \cdot s^{-1} \cdot T^{-1}}$
$\boldsymbol{B_0}$	External magnetic field	T
$\boldsymbol{\tau}$	Torque	J
ω_0 (or ν_0)	Larmor frequency	$\mathrm{s^{-1}}$ (or Hz)
E	Energy	J
T	Temperature	K
δ	Chemical shift	ppm
M	Magnetization	$\mathrm{J \cdot T^{-1} \cdot m^{-3}}$
$\hat{\mathcal{H}}$	Hamiltonian operator related to NMR experiment	J
$\hat{\boldsymbol{I}}$	Operator for spin angular momentum	$\mathrm{J \cdot s}$
J	J-coupling	Hz
Θ	Momentum of inertia	$\mathrm{kg \cdot m^2}$
τ_{rd}	Radiation damping time	s
V_s	Sensitive volume of the NMR detection coil	$\mathrm{m^3}$
Δp	Pressure differential	psi
Γ_μ	Pumping rate of the RASER-active mode μ	$\mathrm{s^{-1}}$
${g_m}^2$	Magnetic coupling constant	$\mathrm{s^{-2}}$
κ_m	Radiation damping rate of the LC circuit	$\mathrm{s^{-1}}$
γ_m	Effective transverse relaxation rate	$\mathrm{s^{-1}}$
ϕ_μ	Phase factor of the RASER-active mode μ	rad

Dimensionless Numbers

Abbreviation	Definition
m_I	Magnetic spin quantum number
n	Populations of the spins
σ	Shielding constant
P	Polarization
J_{rot}	Rotational quantum number

η	Filling factor of the NMR detection coil
Q	Quality factor of the NMR detection coil
d_0	Population inversion
d_{th}	Threshold of RASER emission
A_μ	Amplitude of the transverse spin component
ϵ	Signal enhancement

Constants

Symbol	**Definition**	**Value**
k_B	Boltzmann constant	$1.381 \times 10^{-23}\ \mathrm{J \cdot K^{-1}}$
h	Planck constant	$6.626 \times 10^{-34}\ \mathrm{J \cdot s}$
$\hbar$	Reduced Planck constant	$1.054 \times 10^{-34}\ \mathrm{J \cdot s}$
μ_0	Magnetic permeability of vacuum	$1.257 \times 10^{-6}\ \mathrm{N \cdot A^{-2}}$
N_A	Avogadro's number	$6.022 \times 10^{23}\ \mathrm{mol^{-1}}$

Contents

Introduction

1.1 Motivation

Nuclear Magnetic Resonance (NMR) spectroscopy is a widely used analytical technique in chemistry, biology, and medicine, providing crucial insights into molecular structures and interactions. However, its inherently low sensitivity leads to long scan times, high detection thresholds for low-concentration analytes, reduced temporal resolution for dynamic studies, and the reliance on expensive hardware such as high-field magnets [1, 2] and cryogenically cooled probes [3, 4]. Although sensitivity-enhancing strategies like advanced instrumentation [5, 6], micro-NMR detector [7, 8], and optimized pulse sequences [9, 10, 11] have led to incremental improvements, they ultimately remain bound by the limits of thermal polarization.

In contrast, hyperpolarization techniques offer a transformative solution by boosting nuclear polarization by several orders of magnitude, enabling dramatic gains in NMR signal strength. Among available hyperpolarization methods, Parahydrogen-Induced Polarization (PHIP) and Signal Amplification by Reversible Exchange (SABRE) stand out for their simplicity, rapid polarization, and low-cost implementation. [12, 13, 14, 15, 16] Operating at room temperature with readily available *para*-H_2, they require minimal hardware compared to techniques like Dynamic Nuclear Polarization (DNP) [17, 18, 19] and Spin Exchange Optical Pumping (SEOP) [20, 21], which rely on sophisticated instrumentation.

Despite these advantages, traditional PHIP and SABRE methodologies have historically been constrained by the limited range of polarizable molecules. [15] Recent advancements including PHIP-SAH (Side Arm Hydrogenation) [22, 23], SABRE-Relay [24, 25], and SABRE-SHEATH (in SHield Enables Alignment Transfer to Heteronuclei) [26, 27] have significantly broadened the scope of hyperpolarizable substrates, enabling the polarization of biologically relevant molecules, metabolic tracers, and heteronuclei such as ^{13}C, ^{15}N, and ^{19}F.

While these chemical developments position PHIP and SABRE as promising alternatives to DNP, their broader adoption remains constrained. From an engineering standpoint, the core limitation arises not only from the poor reproducibility of widely used experimental methods—such as shaking and bubbling—but also from their inadequate coordination with the overall hyperpolarization workflow, including gas–liquid mixing, polarization field tuning,

and field cycling, along with insufficient integration with various protocols and modular hardware for process control.

Efficient gas–liquid mixing is a fundamental prerequisite for PHIP and SABRE, as both rely on dissolving gaseous *para*-H_2 into a liquid-phase solution containing the substrate and catalyst. A high efficiency gas-liquid mixing provides a sufficient source of spin order for hyperpolarization.

In practice, the gas-liquid mixing process in PHIP and SABRE is most commonly achieved using either manual shaking (shake-and-drop) or bubbling methods. While manual shaking provides simple operation without the need for specialized hardware, it suffers from poor reproducibility due to operator-dependent variability. Bubbling offers better consistency but typically requires interrupting gas flow during signal acquisition, which breaks polarization continuity. Alternatively, continuous bubbling can be maintained during acquisition, but at the cost of spectral resolution due to field inhomogeneities introduced by gas bubbles. Continuous-flow gas–liquid reactors, by contrast, offer a robust and scalable alternative. These systems allow independent and controllable flow of gas and liquid phases, maximize interfacial area, and support continuous para-H_2 supply during detection. With adjustable flow parameters such as pressure, rate, and temperature via modular control components, they provide high experimental flexibility and enable stable, real-time hyperpolarization.

The second challenges involves polarization field control, particularly for SABRE, whose polarization efficiency is highly sensitive to magnetic field strength. While PHIP operates effectively across a broad range, SABRE achieves optimal spin order transfer only at specific low-field conditions—typically milli-Tesla (mT) for ^{1}H and micro-Tesla (µT) for heteronuclei—where level anti-crossings (LACs) facilitate efficient transfer. In this step, manual shaking typically occurs in uncontrolled stray fields and is mostly limited to ^{1}H SABRE. In contrast, bubbling setups and gas–liquid reactors are compatible with well-defined field environments and can be integrated with external electromagnetic coils or shielding systems—enabling SABRE hyperpolarization of a broader range of nuclei including ^{13}C and ^{15}N.

The third challenge relates to magnetic field cycling—the transfer of hyperpolarized samples from the low-field polarization site to a high-field NMR spectrometer. This step is especially critical for applications like metabolic profiling, where spectral resolution is essential. Manual transfer, typical in shaking and bubbling setups, introduces variation in timing and field trajectory, reducing reproducibility. In contrast, continuous-flow reactors enable automated, well-timed transfer along set fixed paths, ensuring consistent polarization retention and high reproducibility.

Therefore, by enabling high-efficiency gas–liquid mixing, compatibility with various polarization fields, and synchronized sample delivery in both timing and magnetic field transitions, continuous-flow gas–liquid reactors offer an integrated platform with exceptional control and reproducibility across all key stages of the hyperpolarization process. While the flow rate must be balanced to maintain sufficient gas–liquid contact, the overall scalability, controlla-

bility, and long-term polarization stability of this approach provide a robust foundation for advanced experimental strategies.

One such direction is the integration of hyperpolarization with parallel NMR coil arrays, which enables the simultaneous detection of multiple hyperpolarized samples at low concentrations—paving the way for high-throughput applications such as drug screening and metabolic profiling. Another compelling example is radio-frequency amplification by stimulated emission of radiation (RASER), which emerges when the generated polarization exceeds the RASER threshold. Unlike conventional NMR signals that decay due to relaxation, a hyperpolarized RASER system can emit sustained coherent radiation as long as a continuous supply of fresh *para*-H_2 is maintained. This leads to an effectively infinite effective transverse relaxation time ($T_2{}^*$), resulting in ultra-narrow Free Induction Decay (FID) linewidths that enable high-precision measurements of key NMR parameters such as J-couplings—critical for molecular structure elucidation and quantum sensing.

Motivated not only by the need to overcome implementation challenges, but also by the opportunity to enable such advanced applications, the first major focus of this work is the development of continuous-flow hyperpolarization platforms based on gas–liquid contactors, along with their deployment in parallel SABRE hyperpolarization for high-throughput NMR detection and continuous RASER for precise J-coupling determination.

While continuous-flow platforms offer superior control and scalability, they may not always be practical for routine measurements or sample-limited applications, where only small amounts are available for hyperpolarization. In such cases, bubbling-based approaches remain widely adopted due to their operational simplicity, rapid setup, and compatibility with a wide range of PHIP and SABRE protocols. When integrated with automated platforms, the bubbling method can overcome its inherent reproducibility limitations by standardizing gas–liquid mixing, precisely controlling polarization transfer conditions, programming sample delivery, and automated detection within a unified workflow. Furthermore, it enables systematic optimization of polarization parameters (e.g., transfer field strength, temperature) and supports quantitative measurements of polarization buildup time and longitudinal relaxation time (T_1) at defined field strengths.

Motivated by the need to improve reproducibility, lower operational barriers, and support high-throughput workflows, the second major focus of this work is the development of a fully automated hyperpolarization workstation based on bubbling—designed to enable robust, user-friendly, and field-compatible PHIP and SABRE implementations. By minimizing manual intervention and consolidating key experimental steps, this platform provides a practical solution for routine use, laying the groundwork for broader adoption and future commercialization of *para*-H_2-based hyperpolarization technologies.

1.2 Objective

Based on these motivations, this PhD work aims to advance the engineering implementation of *para*-H_2-based hyperpolarization by addressing critical experimental bottlenecks and enabling new application scenarios. The research is structured around two complementary development pathways: (1) a continuous-flow hyperpolarization platform using gas–liquid contactors, designed to support scalable and sustained polarization for advanced applications such as parallel NMR detection and RASER; and (2) a fully automated bubbling-based workstation, tailored for reproducible, user-friendly, and modular operation in routine PHIP and SABRE experiments.

To realize these goals, the main research objectives are outlined as follows:

- **Enhancing the efficiency of hyperpolarization via optimized gas-liquid contact**
  The development of a high-efficiency gas–liquid reactor is essential for achieving robust and reproducible *para*-H_2-based hyperpolarization in continuous-flow systems. By enhancing gas–liquid mass transfer, such reactors improve polarization yield and temporal stability, which are critical for reliable PHIP and SABRE operation. Moreover, their compatibility with miniaturized and modular designs makes them well suited for integration into microfluidic platforms and compact NMR systems.
- **Accelerating NMR detection through parallelized hyperpolarization strategies**
  The inherently low thermal polarization in conventional NMR requires multiple scans to achieve a sufficient signal-to-noise ratio (SNR). This work introduces a novel methodology that combines SABRE hyperpolarization—implemented in tube-in-tube gas–liquid reactors—with parallel NMR coil arrays, significantly reducing acquisition time. By enabling simultaneous detection from multiple samples, this approach achieves a theoretical acceleration factor of $2 \times \epsilon_{SNR}^2$, thereby improving the efficiency of high-throughput NMR spectroscopy.
- **Achieving steady-state RASER**
  The high polarization levels achievable via PHIP and SABRE not only enhance the sensitivity of NMR detection but also enable the onset of RASER emission. Establishing a steady-state RASER over extended timescales facilitates high-precision measurement of J-coupling parameters and enables the investigation of nonlinear phenomena in spin systems. By tuning the polarization level through precise reactor control, this work explores how different degrees of population inversion give rise to distinct RASER regimes, offering new insights into nonlinear spin dynamics.
- **Developing a fully automated hyperpolarization workstation**
  To ensure reproducibility and facilitate practical implementation, this work establishes a fully automated SABRE hyperpolarization platform. The system integrates programmable magnetic field cycling, automated *para*-H_2 bubbling, synchronized NMR acquisition, and a user-friendly graphical interface. This automation enhances exper-

imental reliability and enables routine use of SABRE hyperpolarization, making the technique more accessible to a broader range of researchers, including those working with benchtop NMR systems.

Achieving these objectives is not only essential for addressing current technical limitations in PHIP and SABRE, but also for unlocking their full potential in practical applications. Together, these efforts bridge the gap between the theoretical promise of *para*-H_2-based hyperpolarization and its real-world implementation, paving the way for high-throughput NMR applications and future commercialization.

1.3 Scope of the thesis

This thesis focuses on the engineering-driven development of continuous-flow platforms based on gas–liquid reactors to expand the application scope of PHIP and SABRE, as well as the automated implementation of these hyperpolarization techniques. To guide the reader through the progression of this work, the content of each chapter is briefly outlined below:

Chapter 1 introduces the motivation and research objectives, setting the context for the subsequent exploration of advanced *para*-H_2-based hyperpolarization strategies.

Chapter 2 delves into the fundamental concepts of NMR spectroscopy. It introduces the quantum mechanical principles of nuclear spin and the relaxation mechanisms underlying NMR signal formation. Particular attention is given to the quantum description of J-coupling in a two-spin system, which serves as a theoretical basis for understanding its role in SABRE hyperpolarization discussed in later chapters.

Chapter 3 introduces the theoretical background and implementation strategies of *para*-H_2-based hyperpolarization, with a focus on PHIP and SABRE. It begins by discussing the limitations of thermal equilibrium polarization in conventional NMR and introduces hyperpolarization as a solution to improve sensitivity. A comparison of DNP, SEOP, and PHIP techniques highlights the simplicity and rapid polarization capability of PHIP, motivating its selection in this thesis. The physical properties of parahydrogen and its laboratory enrichment are then presented, followed by detailed explanations of PHIP and SABRE mechanisms, including catalytic cycles and the role of level anti-crossings (LACs). Moreover, this chapter presents a comparative review of three experimental methods—shake-and-drop, bubbling, and membrane-based gas–liquid reactors—highlighting the advantages of membrane reactors as microfluidic platforms for achieving continuous and efficient hyperpolarization.

Chapter 4 presents detailed introduction to several designed continuous-flow gas–liquid reactors with configuration of membrane (flat and tubular membranes) or without membrane, outlining their construction processes and validating their underlying concepts through experimental implementation.

Chapters 5 through 7 present key results that collectively address the three main goals of this PhD project. Chapter 5 details the integration of SABRE with parallel NMR coils to

facilitate parallel SABRE for high-throughput NMR measurements. Chapter 6 investigates different regimes observed in steady-state RASER signals generated via continuous PHIP in a tube-in-tube gas–liquid reactor, and corroborates the experimental observations through numerical simulations based on a nonlinear spin dynamics model. Chapter 7 presents the development of a fully automated platform for routine SABRE hyperpolarization of both ^{1}H and heteronuclei, demonstrating its reliability and flexibility in various experimental settings.

Chapter 8 summarizes the key contributions of the research, discusses the potential applications of *para*-H_2-based hyperpolarization in high-throughput NMR analysis of low-concentration samples and background-free SABRE-MRI, and suggests directions for future research.

1.4 Main results

The results presented in this thesis are summarized in four publications:

Integrating micro process chemistry into an NMR spectrometer (Published) [JY01]
Journal: Chemie Ingenieur Technik 2024 - Wiley
Authorship: Co-author
Content: This article explores the integration of micro process chemistry into an NMR spectrometer. It discusses the advantages of miniaturization in NMR applications, such as improved sensitivity, reduced reaction time, and better spatial efficiency. Specific applications include gas-liquid contactors for hyperpolarization, chemical processes in microreactors, and metabolic monitoring in small-scale bioreactors. The article also covers material selection and manufacturing methods for these applications, highlighting the potential of miniaturized NMR technology across different fields.
Contributions: Conceptualization, data curation, investigation, visualization, writing.

Accelerating NMR via parallel SABRE in a continuous-flow system (In preparation) [JY04]
Journal: Review of Scientific Instruments 2025 - American Institute of Physics
Authorship: Lead co-author
Content: This study integrates SABRE hyperpolarization with parallel coil arrays to accelerate NMR detection. Using a tube-in-tube reactor, hyperpolarized samples were continuously delivered through two parallel coils in a 1.05 T NMR spectrometer, enabling simultaneous multi-channel acquisition. SNR enhancements of 140 and 43 were achieved in each channel, demonstrating a detection acceleration factor of $2 \times \epsilon_{SNR}^2$. This approach improves NMR efficiency, enabling high-throughput and high-sensitivity spectroscopy with reduced acquisition times.
Contributions: Conceptualization, data curation, investigation, experiments, visualization, writing.

The steady-state ALTADENA RASER generates continuous NMR signals (Published) [JY02]
(This paper has being featured on the cover of the Journal.)
Journal: ChemPhysChem 2023 - Chemistry Europe
Authorship: Lead author
Content: This paper studies the a steady-state ALTADENA RASER system, which uses PHIP to achieve continuous RASER emission on a benchtop NMR. The study demonstrated five RASER operating regimes, including RASER startup, "normal NMR mode", period doubling, frequency combs, and chaotic behavior, depending on the level of population inversion. Experimental results matched well with simulations, providing a foundation for both precision NMR measurements and the study of nonlinear dynamics in NMR spectroscopy.

Contributions: Conceptualization, data curation, investigation, experiments, simulation, validation, visualization, writing, front cover design and drawing.

Development of a fully automated workstation for conducting routine SABRE hyperpolarization (Published) [JY03]
Journal: Scientific Reports 2024 - Springer Nature
Authorship: Lead author
Content: This paper introduces an automated lab workstation designed to perform SABRE hyperpolarization with high reproducibility. This system integrates a benchtop NMR spectrometer and a robotic arm-assisted shuttling system, enabling efficient transfer of hyperpolarized samples. The workstation is equipped with an automated bubbling unit to introduce *para*-H_2, and a magnetic field generator for optimizing polarization transfer, making it a versatile tool for both SABRE and SABRE-SHEATH experiments.
Contributions: Conceptualization, data curation, investigation, experiments, simulation, validation, software, visualization, writing.

Fundamental Background of Nuclear Magnetic Resonance Spectroscopy

2.1 Overview

NMR spectroscopy and MRI are powerful analytical techniques with broad applications in physical chemistry, drug discovery, structural biology, medical diagnostics, and food science, among other fields in materials and medical sciences. NMR is particularly valuable for providing detailed structural information at the atomic level, enabling insights into molecular interactions.

This chapter covers the fundamental principles of NMR measurements, providing an introduction to the key concepts of this technique. The first section introduces spin and nuclear magnetization, explaining how nuclear spins interact with magnetic fields. Subsequent sections discuss the Larmor frequency, which describes the precessional motion of nuclear spins in an external magnetic field, and examine Zeeman splitting, which explains the energy level differences that form the basis of NMR signal generation. Following this, the discussion moves to chemical shift, which helps distinguish between different nuclear environments. The next section focuses on T_1 and T_2 relaxation mechanisms, important for understanding signal dynamics in NMR. Finally, the analysis of J-coupling within a two-spin system, using a Hamiltonian-based perspective, provides an understanding of spin-spin interactions and their effects on NMR spectral features.

2.2 Spin and nuclear magnetization

Atomic nuclei exhibit intrinsic angular momentum, termed spin, quantized in units of $\hbar$ ($\hbar = h/2\pi$), with h representing the Planck constant, $h \approx 6.626 \times 10^{-34}$ J $\cdot$ s. The total spin angular momentum $\boldsymbol{S}$ of particles with spins is shown as follows:

$$|\boldsymbol{S}| = \sqrt{I(I+1)}\hbar \tag{2.1}$$

where I denotes the nuclear spin quantum number and is determined by its nucleus (number of protons and neutrons). For protons and neutrons, being fermions, each possess a spin

quantum number of $I = 1/2$. For atomic nuclei, the spin quantum number may assume integer ($I = 0, 1, 2, \ldots$) or half-integer ($I = 1/2, 3/2, \ldots$) values, contingent upon the combination of protons and neutrons within the nucleus. [28, 29, 30] The rules for determining the net spin of a nucleus are as follows:

1. When these particles appear in pairs (in even numbers), for example, ^{12}C, ^{16}O, and ^{32}S, their spins are paired against each other and canceled with each other out, resulting in an overall spin of zero.
2. If the number of neutrons and the number of protons are both odd, for example, ^{6}Li, ^{10}B and ^{14}N, the nucleus has an integer spin.
3. If the number of neutrons plus the number of protons is odd, the presence of unpaired particles leads to a half-integer total spin, for example ^{1}H, ^{13}C, ^{15}N, and ^{19}F.

The spin quantum number is pivotal in determining how particles respond to external magnetic fields, making it a critical parameter in the study of atoms, molecules, and their magnetic behaviors. [29, 30] In essence, the spin angular momentum $\boldsymbol{S}$ is a vector that has not only magnitude (described by the spin quantum number) but also direction. For nuclei with spin, the component of spin projected onto the z-axis, denoted as S_z, can be quantified by:

$$S_z = m_I \hbar \tag{2.2}$$

where m_I, the magnetic quantum number, has $2I + 1$ values in integral steps between $+I$ and -I:

$$m_I = I, I-1, I-2, \ldots, -I+1, -I \tag{2.3}$$

Each m_I represents a special spin state. For instance, nuclei with a spin quantum number of $I = 1/2$, such as ^{1}H, ^{13}C, and ^{19}F, exhibit two permissible orientations of spin angular momentum, corresponding to $S_z = \pm 1/2\hbar$. In the case of nuclei with a spin quantum number of $I = 1$, there are three potential states, specifically $S_z = -\hbar, 0,$ and $\hbar$. This space quantization is illustrated in Figure 2.1.

All nuclei with a non-zero spin have a magnetic moment, $\boldsymbol{\mu}$, given by:

$$\boldsymbol{\mu} = \gamma \boldsymbol{S} \tag{2.4}$$

where the proportionality constant γ between the magnetic moment and the spin angular momentum is the gyromagnetic ratio. The value of γ varies from nucleus to nucleus. Table 2.1 shows the different gyromagnetic ratios of several different spin isotopes and their corresponding natural abundances.

2.3 Precession and Larmor frequency

In NMR detection, a sample of the chemical compound contains lots of nuclei with spins is placed in a magnetic field, the nuclear magnetic moment $\boldsymbol{\mu}$ of the spins will couple to the external magnetic field $\boldsymbol{B_0}$, which produces a torque $\boldsymbol{\tau}$ on the nucleus and causes the precession around the direction of the magnetic field (Figure 2.2). The torque can be expressed in

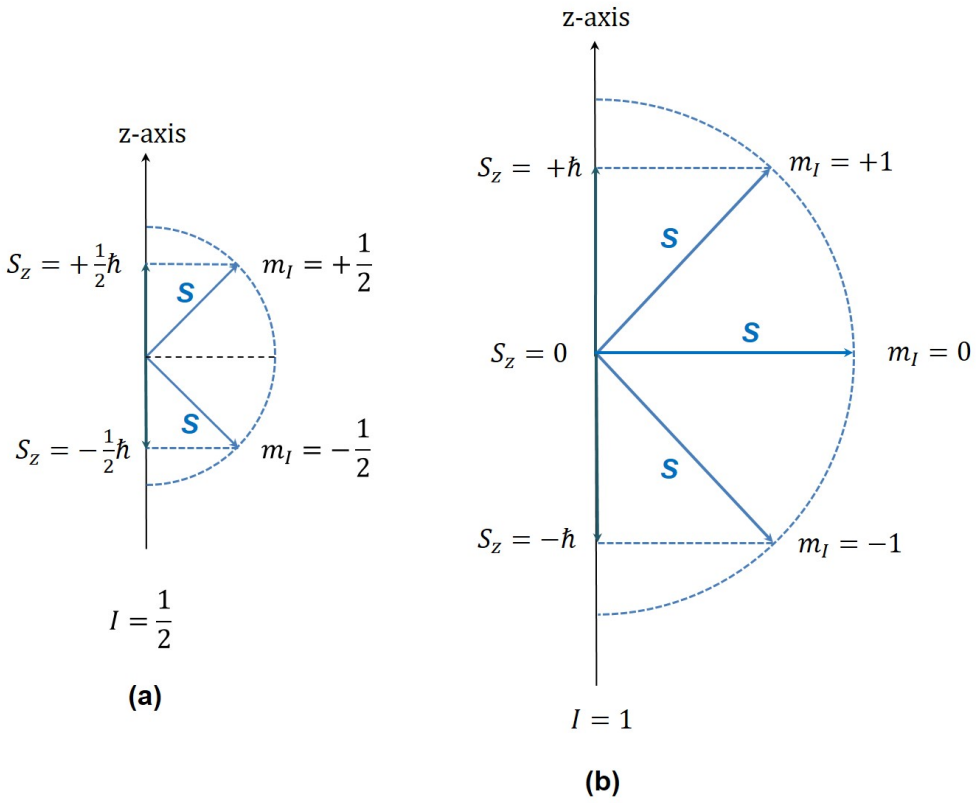

Figure 2.1: Illustration of quantum projection of the spin onto z-axis for nucleus with spin quantum number **(a)** $I = 1/2$ and **(b)** $I = 1$.

the form of a vector product as below:

$$\boldsymbol{\tau} = \boldsymbol{\mu} \times \boldsymbol{B_0} = |\boldsymbol{\mu}| \cdot |\boldsymbol{B_0}| \cdot sin\theta \tag{2.5}$$

For a static magnetic moment or a classical current loop, this torque tends to line up the magnetic moment with the magnetic field $\boldsymbol{B_0}$, so this represents its lowest energy configuration. However, if the magnetic moment arises from the motion of an electron orbiting a nucleus, it becomes proportional to the electron's angular momentum. The torque exerted then produces a change in angular momentum $\Delta \boldsymbol{S}$ which is perpendicular to that angular momentum $\boldsymbol{S}$ (Figure 2.2).

As a consequence, the nuclei line up like a compass needle aligning or anti-aligning to the magnetic field, and the spin magnetic moment starts to precess around the direction of the magnetic field rather than settle down in the direction of the magnetic field. The effect of this torque on spin angular momentum $\boldsymbol{S}$ can be described as follows:

$$\boldsymbol{\tau} = \frac{\Delta \boldsymbol{S}}{\Delta t} = \frac{|\boldsymbol{S}| \cdot sin\theta \cdot \Delta\phi}{\Delta t} \tag{2.6}$$

Substituting Equation (2.5) into Equation (2.6) yields:

$$|\boldsymbol{\mu}| \cdot |\boldsymbol{B_0}| \cdot sin\theta = \frac{|\boldsymbol{S}| \cdot sin\theta \cdot \Delta\phi}{\Delta t} \tag{2.7}$$

where θ is the precession angle. Therefore, the precession velocity is:

$$\omega_0 = \frac{\mathrm{d}\phi}{\mathrm{d}t} = -\gamma B_0 \tag{2.8}$$

Table 2.1: The gyromagnetic ratios for several common nuclei [28, 30]

Nuclei	Spin	Gyromagnetic Ratio (MHz/T)	Natural Abundance (%)
^{1}H	1/2	42.576	99.985
^{13}C	1/2	10.705	1.07
^{15}N	1/2	-4.361	0.368
^{19}F	1/2	40.078	100
^{31}P	1/2	17.235	100
^{27}Al	5/2	11.103	100
^{23}Na	3/2	11.262	100
^{7}Li	3/2	16.546	92.41
^{29}Si	1/2	-8.465	4.68
^{17}O	5/2	5.772	0.038

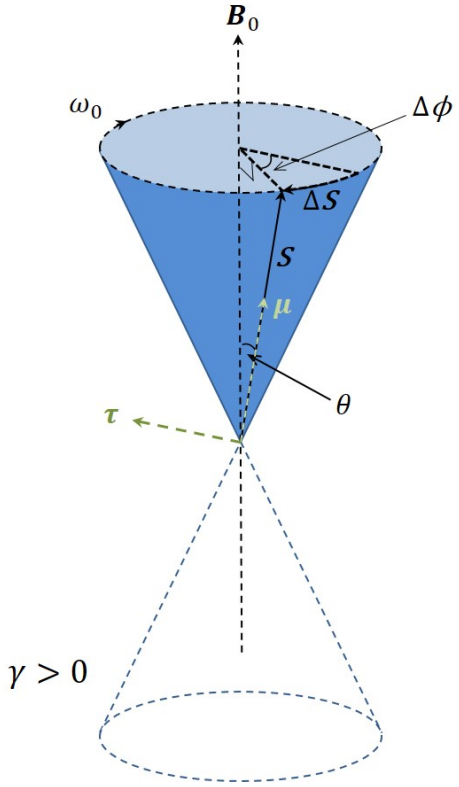

Figure 2.2: Illustration of Larmor precession. The nuclear magnetic moment $\boldsymbol{\mu}$ couples to the external magnetic field $\boldsymbol{B_0}$, which produces a torque $\boldsymbol{\tau}$ on the nucleus and causes the precession around the magnetic field with the Larmor frequency $\omega_0 = -\gamma B_0$.

where ω_0 is the Larmor frequency, describing the characteristic frequency of the precessional motion of spin at the magnetic field. ω_0 is in units of radians per second and it is proportional to the strength of the external magnetic field B_0.

The negative sign means, for nuclei with a positive gyromagnetic ratio, the Larmor precession occurs in the clockwise direction when observed from a perspective "upstream" relative

to the direction of the magnetic field (Figure 2.2). For nuclei with a negative gyromagnetic ratio, such as ^{15}N and ^{29}Si, their precession occurs in the anticlockwise direction. In NMR detection, the Larmor frequency is commonly expressed in unit of herz (Hz):

$$\nu_0 = -\frac{\gamma B_0}{2\pi} \tag{2.9}$$

2.4 Nuclear Zeeman splitting

In the absence of an external magnetic field, spin-1/2 particles such as protons or electrons possess two degenerate spin states, commonly referred to as "spin up" and "spin down" along any chosen axis. More generally, a spin with quantum number I exhibits a $(2I + 1)$-fold degeneracy when no external magnetic field is applied. Without a magnetic field to lift this degeneracy, these states are equally populated in thermal equilibrium, resulting in no net magnetization across a large ensemble of spins.

When a nucleus is placed in a static external magnetic field $\boldsymbol{B_0}$, its magnetic moment $\boldsymbol{\mu}$ interacts with the field, leading to a preferential alignment. The spin magnetic moment behaves as a tiny magnet or as a magnetic dipole. The energy of a such magnetic dipole moment in a magnetic field is given by

$$E = -\mu_z B_0 = -\gamma m_I \hbar B_0 \tag{2.10}$$

This interaction lifts the degeneracy of spin states: each m_I value corresponds to a distinct energy level. For a spin-1/2 nucleus ($I = 1/2$), there are two allowed states: $m_I = +1/2$ and $m_I = -1/2$, corresponding to spin orientations parallel and anti-parallel to the magnetic field, respectively (Figure 2.3). Their energies are given by:

$$E_\alpha = E_{+\frac{1}{2}} = -\frac{1}{2}\gamma\hbar B_0 \tag{2.11}$$

$$E_\beta = E_{-\frac{1}{2}} = \frac{1}{2}\gamma\hbar B_0 \tag{2.12}$$

The energy difference between these two levels is:

$$\Delta E = E_\alpha - E_\beta = -\gamma\hbar B_0 = \hbar\omega_0 = h\nu_0 \tag{2.13}$$

This splitting of energy levels under the influence of an external magnetic field is referred to as Zeeman splitting [28, 30, 31].

In NMR experiments, transitions between energy levels are induced by applying a radiofrequency (RF) pulse through a transmitting coil tuned to the Larmor frequency ν_0. As a result, spins in the lower energy state absorb energy and transition to the higher energy state, in which their magnetic moments become oriented antiparallel to the external magnetic field.

It should be noted that only a small proportion of the "target" nuclei reside in the lower energy state and are thus capable of absorbing radiation. Upon repeated excitation, the populations of the lower and higher energy states may equalize, leading to a condition known as saturation, in which no net absorption of radiation occurs.

When a sample containing numerous nuclei with spin-1/2 is placed in a magnetic field, the initial populations of the spins at low and high energy levels are denoted as $n_{1/2}$ and $n_{-1/2}$, respectively. These populations are determined by thermodynamics and obey the Boltzmann distribution:

$$\frac{n_{+1/2}}{n_{-1/2}} = \exp(\frac{\Delta E}{k_B T}) \tag{2.14}$$

where k_B is the Boltzmann constant ($k_B = 1.381 \times 10^{-23}$ J$\cdot$K^{-1}), T is the absolute temperature in unit of Kelvin. Equation (2.14) can be approximated as follows because $\Delta E \ll k_B T$:

$$\frac{n_{+1/2}}{n_{-1/2}} \approx 1 - \frac{\Delta E}{k_B T} \tag{2.15}$$

In a 500 MHz NMR spectrometer operating at a magnetic field of 11.7 T and a temperature of approximately 298 K, for every 100,000 proton spins, only about four more spin-1/2 nuclei are found at the lower energy level E_α than at the higher energy level E_β.

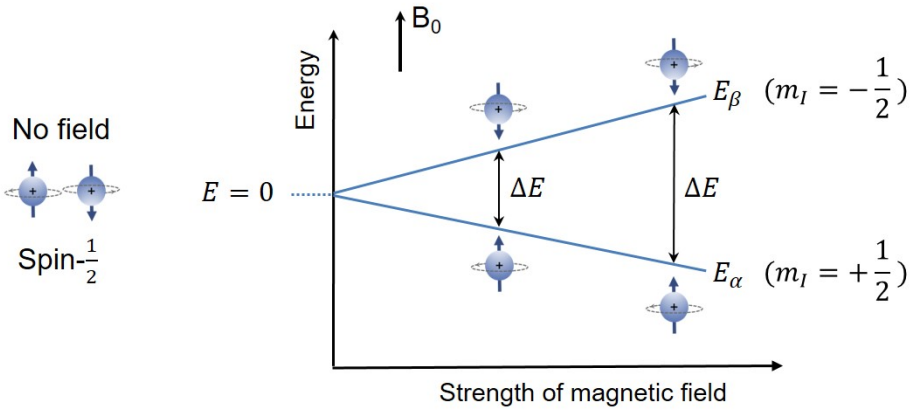

Figure 2.3: Illustration of Zeeman splitting of spin-1/2. When there is no external field is present, the energy level is the same regardless of nuclear orientation. When placing the nucleus in an external magnetic field, the spins tend to organize themselves into orientations either generally aligned with or opposed to the external field. The two spin states are often referred to as "spin-up" or "parallel" with energy of E_α and "spin-down" or "anti-parallel" with energy of E_β, leading to an energy difference ΔE between the two states.

2.5 Chemical shift

The most important feature in a NMR spectrum is the position of the resonance signal, also known as the resonance frequency ν_0 (or angular frequency ω_0), which depends on the specific molecular environment of the nucleus, the gyromagnetic value γ, and the strength of the magnetic field B_0 ($\nu_0 = -\gamma B_0/2\pi$ or $\omega_0 = -\gamma B_0$). It is the relationship between resonance frequency and molecular structure that determines the key characteristic of NMR spectra—the chemical shift. As electrons orbit the nucleus, they generate localized magnetic fields that shield the nucleus from the external magnetic field. This modulation of the actual magnetic field experienced by the nucleus depends on the nature of the surrounding electrons.

This modulation of the B_0 field by electrons is called shielding, which can be represented by the Greek letter σ. With the shielding effect, the effective magnetic field of the nucleus is changed into $B_{\text{eff}} = (1 - \sigma)B_0$. The shielding effect σ of the electrons on protons is given in a positive value.

Substituting B_{eff} into Equation (2.9), the relationship of the resonance frequency and shielding effect is given:

$$\nu_0 = \frac{-\gamma(1-\sigma)B_0}{2\pi} \tag{2.16}$$

when B_0 remains constant, the smaller σ is, the larger the resonance frequency ν_0. The same type of nuclei in different chemical environments can exhibit different resonance frequencies. For example, when an electron-withdrawing group is present on a molecule, the electron density around the proton decreases, and the shielding effect is reduced. In this case, the resonance frequency of the proton is higher than that of the protons without electron-withdrawing groups. For example, the proton resonance frequency of fluoromethane (CH_3F) is higher than that of methane (CH_4) due to the strong electron-withdrawing effect of the fluorine atom on the surrounding environment of proton.

The resonance frequency changes according to changes in B_{eff}, leading to a chemical shift. In NMR spectroscopy, chemical shift is used as a quantitative representation of the shielding effect, standardize the differences in resonance frequencies so that NMR signals of nuclei in different chemical environments can be uniformly compared. Chemical shift is defined as the difference between the actual resonance frequency of a nucleus and the resonance frequency of a standard reference, typically expressed in parts per million (ppm):

$$\delta = \frac{\nu_{\text{sample}} - \nu_{\text{ref}}}{\nu_{\text{ref}}} \times 10^6 \tag{2.17}$$

where ν_{sample} is the resonance frequency of the measured nucleus in the sample, and ν_{ref} is the resonance frequency of the reference material. In most ^{1}H NMR experiments, tetramethylsilane ($(CH_3)_4Si$), abbreviated as TMS, is used as the standard reference for chemical shifts. TMS is volatile, chemically inert, and soluble in most organic solvents. The protons in TMS produce a single, sharp resonance signal. Moreover, due to the low electronegativity of the silicon atom, the surrounding hydrogen and carbon nuclei experience a relatively high electron density, resulting in strong shielding. Consequently, the resonance signals of protons and carbons in TMS appear at the extreme right of the NMR spectrum, conveniently defining the zero point on the chemical shift scale.

2.6 Relaxation

In the absence of an external magnetic field, nuclear spins are randomly oriented, resulting in zero net macroscopic magnetization. When a static magnetic field B_0 is applied, the spin population becomes partially aligned, leading to a gradual build-up of longitudinal magnetization along the field direction. This magnetization component, denoted as M_z, increases

from zero and eventually reaches a thermal equilibrium value M_0, while the transverse components satisfy $M_x = M_y = 0$.

If the spin system is perturbed—typically by an applied RF pulse—the magnetization vector is displaced from equilibrium. In this non-equilibrium state, $M_z \neq M_0$ and $M_x, M_y \neq 0$. Once the perturbation is removed, the spin system relaxes back to equilibrium. This process, known as relaxation, is governed by interactions with the surrounding environment and occurs over a characteristic timescale that depends on the sample and environmental conditions.

For common liquids, the rates of M_z and $M_{x,y}$ return to their thermal equilibrium is proportional to the extent of their deviation from that equilibrium position. The time derivatives of these two components M_z and $M_{x,y}$ can be expressed as follows:

$$\frac{dM_z}{dt} = -\frac{M_z - M_0}{T_1} \tag{2.18}$$

$$\frac{dM_{x,y}}{dt} = -\frac{M_{x,y}}{T_2} \tag{2.19}$$

where the negative sign means the relaxation is the inverse process of the change in magnetization intensity. Integrating Equation (2.18) and Equation (2.19) and inserting the longitudinal relaxation $M_z(0)$ and the transverse relaxation $M_{x,y} = 0$ at $t = 0$ into the integration yields:

$$M_z(t) = M_0 \left(1 - e^{-t/T_1}\right) + M_z(0)e^{-t/T_1} \tag{2.20}$$

$$M_{x,y}(t) = M_{x,y}(0)e^{-t/T_2} \tag{2.21}$$

From the Equation (2.20) and Equation (2.21), the recovery of M_z and $M_{x,y}$ follows an exponential law, T_1 and T_2 possess the dimension of time, and thus are termed as relaxation time.

T_1 is the time constant characterizing the recovery process of the longitudinal component of the magnetization intensity M_z, called longitudinal relaxation time; while T_2 is the transverse relaxation time, representing the recovery rate of the transverse magnetization components $M_{x,y}$, called transverse relaxation time.

2.6.1 Spin-lattice relaxation

During NMR detection, a short RF pulse resonating at the same frequency as the measured nuclei is applied, generating a temporary magnetic field B_1 perpendicular to the direction of the B_0 field. This RF excitation enables the nuclei to absorb energy, causing the spins to flip from $+1/2$ (ground state) to $-1/2$ (excited state). This results in a decrease of the magnetization (M_z) along the $+z$ axis. As mentioned above, the spin system will relax to the thermal equilibrium state after the RF excitation, in which the energy will be transferred to the surroundings. The environment surrounding the atomic nuclei, whether in solid, liquid, or gas form, is collectively represented by the term "lattice".

Typically, the heat capacity of the lattice system is much larger than that of the spin system. [32, 33] Within the spin system, a matching electromagnetic field can be found in the lattice, allowing energy of the excited state to be transferred out. This facilitates the nuclear spins on the Zeeman energy levels to approach a Boltzmann distribution.

Since a molecule contains magnetic nuclei, their random motion generates fluctuating magnetic fields. When these fields are properly phased (to match the precessional frequency) and appropriately oriented, a nucleus in an upper spin state can relax to the ground state by transferring its excess energy to the lattice in the form of rotational and translational energy. The total energy level of the spin system remains unchanged, which is achieved through the exchange of energy between the spin system and the surrounding molecules, i.e., the lattice. Therefore, T_1 is also termed the spin-lattice relaxation time. The most common source of the local fluctuating field for spin-1/2 nuclei is direct dipolar interaction. For example, in solution the rapid reorientation of the dipolar interaction due to molecular motions provides fluctuating fields. This relaxation mechanism depends on the rate of molecular motion. Thus, T_1 is related to temperature.

The standard method for measuring T_1 is known as inversion recovery, in which the relaxation originates by creating a non-equilibrium distribution of spins, and then returns to equilibrium through a first-order rate process. [32, 34] First, a $180°_x$ is applied to rotate the entire spin system and generate a transient magnetization $-M_0$ along the $-z$ axis that is completely opposite to the magnetization at equilibrium state (Figure 2.4**a-c**). Following a short time period τ, during which spin-lattice relaxation occurs. After τ, the longitudinal magnetization is smaller than the initial magnetization (Figure 2.4**d**). A $90°_x$ pulse is then applied to flip the magnetization to xy-plane along y-axis for acquisition of the Free Induction Decay (FID) signal. Therefore, an NMR spectrum with inverse intensity is obtained (Figure 2.4**e**).

As the value of the time period τ increases, the relaxation time between the $180°_x$ and $90°_x$ pulses is extended, allowing M_z to transition from $-M_0$ through zero to its equilibrium value of M_0. The experiment is repeated with varying τ delays, facilitating the determination of the T_1 value using the curve fitting method. Substituting $M_z(0) = -M_0$ into Equation (2.20) gives:

$$M_z(t) = M_0 \left(1 - 2e^{-t/T_1}\right) \tag{2.22}$$

In practice, the following equation is used:

$$I = I_0 \left(1 - 2e^{-\tau/T_1}\right) \tag{2.23}$$

where I is the initial intensity of the signal after the $90°_x$ pulse, I_0 is the acquired signal intensity at thermal equilibrium for a very long interval of τ. Taking the natural logarithm of both sides of the Equation (2.23) yields:

$$ln\left(\frac{I}{I_0}\right) = -ln2 + \frac{\tau}{T_1} \tag{2.24}$$

where T_1 is determined from the slope of a plot of $ln(I/I_0)$ versus τ.

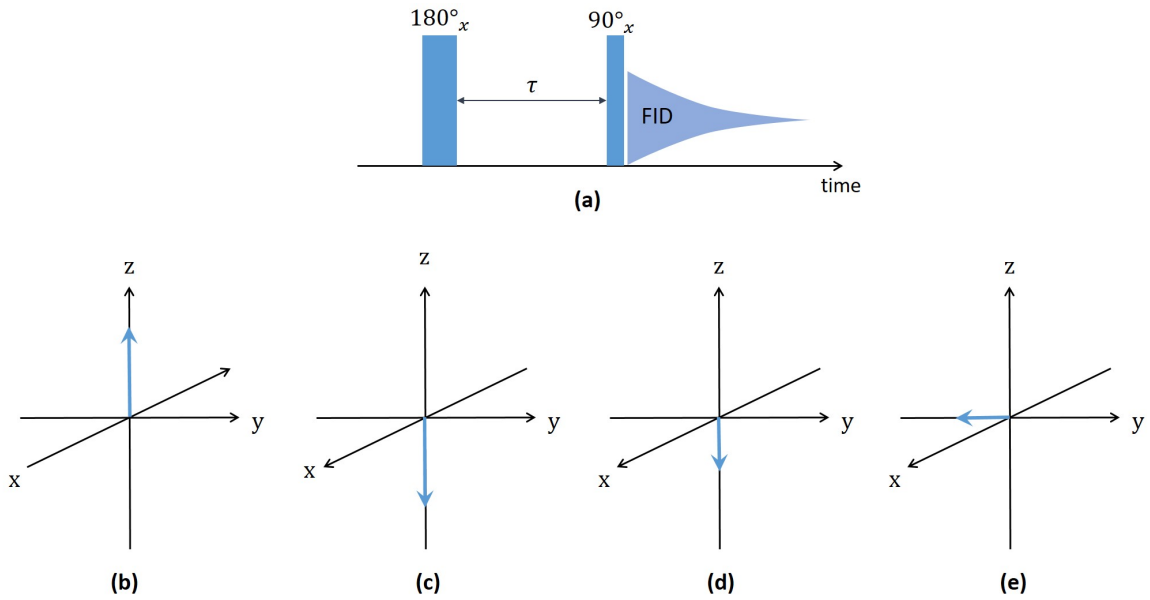

Figure 2.4: (**a**) Illustration of the pulse used in inverse recovery experiment to measure T_1-relaxation time. (**b-e**) Intensity of the magnetization changed during inverse recovery experiment: (**b**) before applying the pulse; (**c**) after applying the $180°_x$ pulse; (**d**) after waiting a period of τ for relaxation; (**e**) after applying the $90°_x$ pulse.

2.6.2 Spin-spin relaxation

Spin-spin (transverse) relaxation time T_2 is used to quantify the rate of the decay (or dephase) of the transverse component of the magnetization $M_{x,y}$. After a 90° excitation pulse, the nuclear spins are aligned in one direction, resulting a temporary statistical "phase coherence". However, this arrangement is gradually lost, for example, due to field inhomogeneities and direct interactions between the spins without energy transfer to the lattice. Hence, T_2-relaxation does not affect the total amount of magnetization M_z, but the degree of synchronization of the transverse magnetization components. The inhomogeneity of the B_0 field causes the phases of the spins on xy-plane to randomize. Therefore, T_2 is estimated to be much shorter than T_1 ($T_2 \ll T_1$).

Although T_1-relaxation is always accompanied by T_2-relaxation, T_2-relaxation can also occur independently without T_1-relaxation. A common scenario for this is when a spin is situated in a local environment that disturbs it with an additional static field B_{loc} besides the static magnetic field (B_0). For instance, consider a spin on a water molecule near a hemosiderin cluster with iron or adjacent to a molecule near an electronegative oxygen atom. If B_{loc} aligns with the same z-direction as B_0, the combined effect of the two static fields would cause the affected spin to precess at an altered frequency $-\gamma(B_0 + B_{loc})$, while other spins unaffected by B_{loc} continue at the standard Larmor frequency ($\omega_0 = -\gamma B_0$). After a time interval t, a phase difference $\Delta\phi = \gamma B_{loc} t$ emerges between the affected spin and its neighbors. This phase misalignment leads to reduced net transverse magnetization (M_{xy}), manifesting as T_2-relaxation.

Another mechanism of T_2-relaxation can occur independently of T_1-relaxation through a specific type of dipolar interaction, commonly referred to as a spin–spin "flip-flop" process. In this process, two neighboring spins exchange their longitudinal angular momentum components simultaneously (e.g. one spin flips from $+1/2$ to $-1/2$, while the other spin flips from $-1/2$ to $+1/2$). This exchange results in no overall change in T_1-relaxation but leads to a loss of T_2 coherence. This happens because while there is no net change in the energy state of the spins (hence no T_1 effect), their transverse components become misaligned, disrupting the T_2 coherence.

In practice, the transversal magnetization usually decays to zero quicker than is expected. ${T_2}^*$ is used to explain such observed shortened decay, as it considers both the natural T_2-relaxation (spin-spin interaction) and the relaxation due to magnetic field inhomogeneity (${T_2}'$), as described below:

$$\frac{1}{{T_2}^*} = \frac{1}{T_2} + \frac{1}{{T_2}'} \tag{2.25}$$

Therefore, ${T_2}^*$ is always shorter than or equal to T_2. In NMR experiments, the net magnetization is detected by using a RF pulse to flip it into the xy-plane, as it gives rise to the FID with the effective transversal relaxation time of ${T_2}^*$. While the ${T_2}^*$ value is related to the line-width at half-height of the detected NMR signal, the true T_2 value is crucial for various applications, including MRI and the study of protein dynamics, as it reflects the characteristics of individual spins and their immediate environments.

One of the methods used to determine pure T_2 is the CPMG (Carr-Purcell-Meiboom-Gill) experiment because dephase of the transverse component results from the field inhomogeneity effect can be refocused in this sequence. [28, 35]

In CPMG experiments, a ${90^\circ}_x$ pulse is first applied, rotating the magnetization from z-axis to xy-plane, followed by a specific delay time τ (Figure 2.5**a-b**). During the delay time, the transverse components decohere due to the inhomogeneity of the static magnetic field (Figure 2.5**c-d**). A ${180^\circ}_x$ pulse is then applied along x-axis rotating all the spins about that axis (Figure 2.5**e**). The flipped spins continue to precess at the same Larmor frequencies, allowing the slower spins to "catch up" and recohere with the faster rotating spins (Figure 2.5**f**). After a same delay time τ the spins re-cohere to form a spin echo at time T_E (Figure 2.5**g**). This refocusing action compensates for dephasing caused by inhomogeneities in the magnetic field and other local magnetic environments, allowing for the measurement of intrinsic spin-spin relaxation processes. By conducting the spin echo multiple times and measuring the amplitudes of the decaying spin-echo as a function of time, T_2 can be determined (Figure 2.6).

2.7 J-Coupling interaction in two spin$-1/2$ system

In a spin system, two main types of interactions exist between nuclear spins: the direct dipole–dipole interaction through space, typically with magnitudes on the order of kHz, and the indirect spin–spin coupling, commonly referred to as J-coupling or scalar coupling.

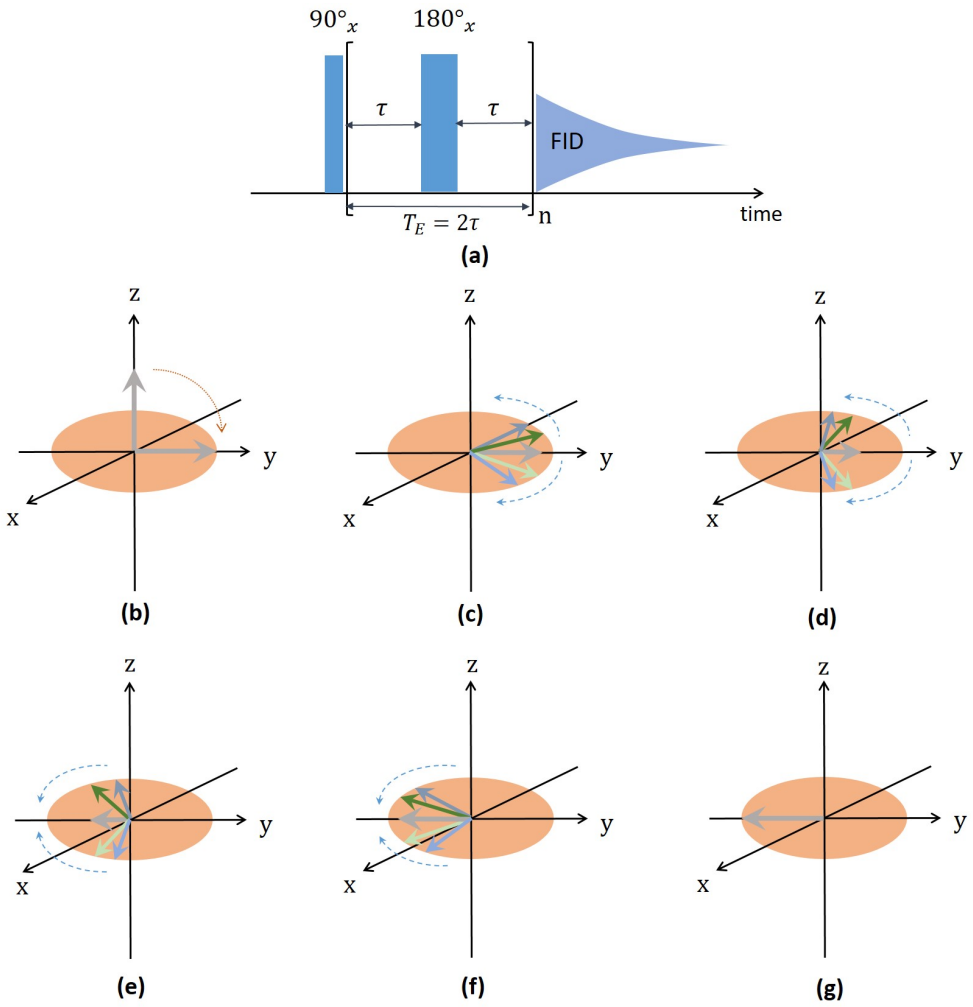

Figure 2.5: (**a**) Pulse sequence diagram used in CPMG experiment for measuring the T_2 time. (**b-g**) Schematic representation of magnetization on xy-plane in spin echo sequence. After a $90°_x$ pulse, the four example spin vectors begin to dephase because of differences in Larmor frequency. The gray color arrow represents the total transversal magnetization of the four spin vectors. The blue dotted arrows show the motions of the spins.

The dipolar-dipolar interaction is dependent on the internuclear distance and the relative orientation of the internuclear vector with respect to the external magnetic field. In solid-state NMR, dipolar couplings are preserved and often dominate the spectral features, whereas in solution-state NMR, they are averaged out due to rapid isotropic molecular tumbling. Despite being invisible in conventional solution NMR spectra, dipolar interactions underpin key relaxation mechanisms and are central to phenomena such as the Nuclear Overhauser Effect (NOE) and spin diffusion.

J-coupling interaction arises when nuclear magnetic moments within the same molecule affect each other through the electron cloud, which is shared among atoms due to chemical bonds in the molecule. Therefore, J-coupling is not a direct interaction between the two nuclear magnetic moments but an indirect interaction mediated by the bonding electrons. Unlike to the dipolar interaction, J-coupling is independent of the spatial orientation of the

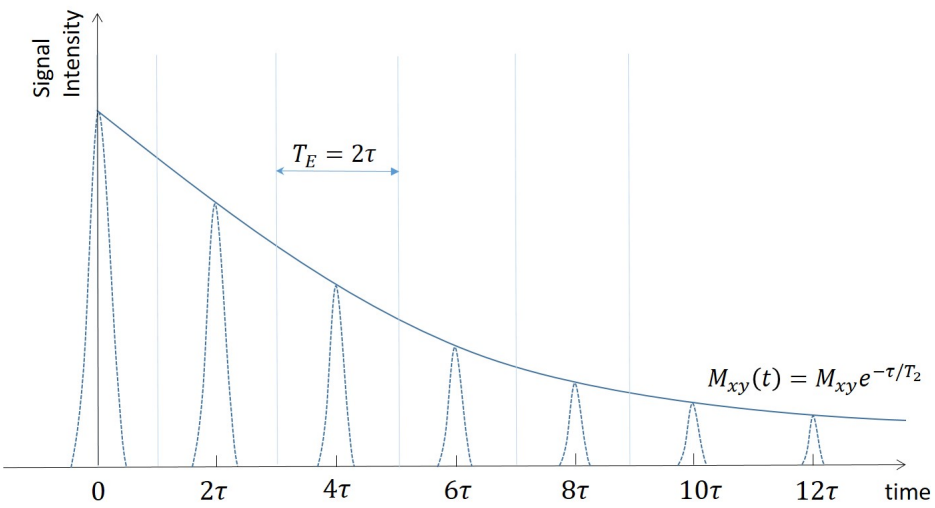

Figure 2.6: Graph of the relative intensity of the transversal magnetization (M_{xy}) versus time (t).

nuclei, the temperature, and the static magnetic field B_0. Spin-spin coupling splitting can be observed in a 1D-NMR spectrum when coupled nuclei are magnetically active, connected through chemical bonds, and sufficiently resolved in both frequency and line width.

Since this thesis focuses on liquid-state NMR, where dipolar interactions are averaged out by rapid molecular tumbling, only J-couplings are considered in the following discussions. The magnitude of J-coupling is generally in range from several to tens of Hz.

To gain an intuitive understanding of J-coupling, envision a molecule composed of two atoms linked by a chemical covalent bond. In a covalent bond, two electrons share the same molecular orbital, and they must have opposite spins according to the Pauli Exclusion Principle. For the spin-1/2 particles, the direction of their spin states can either be spin-up (usually denoted by $|\uparrow\rangle$ or abbreviated as $|\alpha\rangle$) or spin-down (usually denoted by $|\downarrow\rangle$ or abbreviated as $|\beta\rangle$). Therefore, in the absence of nuclear spin, the electron spin state is the mixture of the same quantities of the two basis states "up-down" ($\uparrow\downarrow$) and "down-up" ($\downarrow\uparrow$), with both states being degenerate (Figure 2.7**a**). The degeneracy is lifted when a nucleus with a positive γ is introduced near one side of the covalent electrons, resulting from the negative magnetic hyperfine interaction between the nuclear and electron spins. In a covalent bond scenario where the electron spin is aligned in the same direction as the nearby nuclear spin, their magnetic moments are opposed. This alignment is energetically favorable for the magnetic energy of the spin system, resulting in a lower energy state (Figure 2.7**b**).

In a molecule with two atoms connected by a covalent bond, the energy state depends on the orientations of the two nuclear spins (Figure 2.7**c**). If the two nuclear spins are antiparallel and each is opposed to the magnetic moments produced by the electron spins adjacent to them, a specific interaction dynamic occurs. In this scenario (Figure 2.7**c**, left), the energy states are both favorable for the two coupled nuclear spins and electron spins, leads to a lower energy state compared with the uncoupled state.

If the nuclear spin momentum of the two spins are aligned in the same direction—both pointing up (↑↑) or both down (↓↓), which are unfavorable for the magnetic energy of the spin system, the energy of these configurations is higher compared to the situation without J-coupling (Figure 2.7**c**, right).

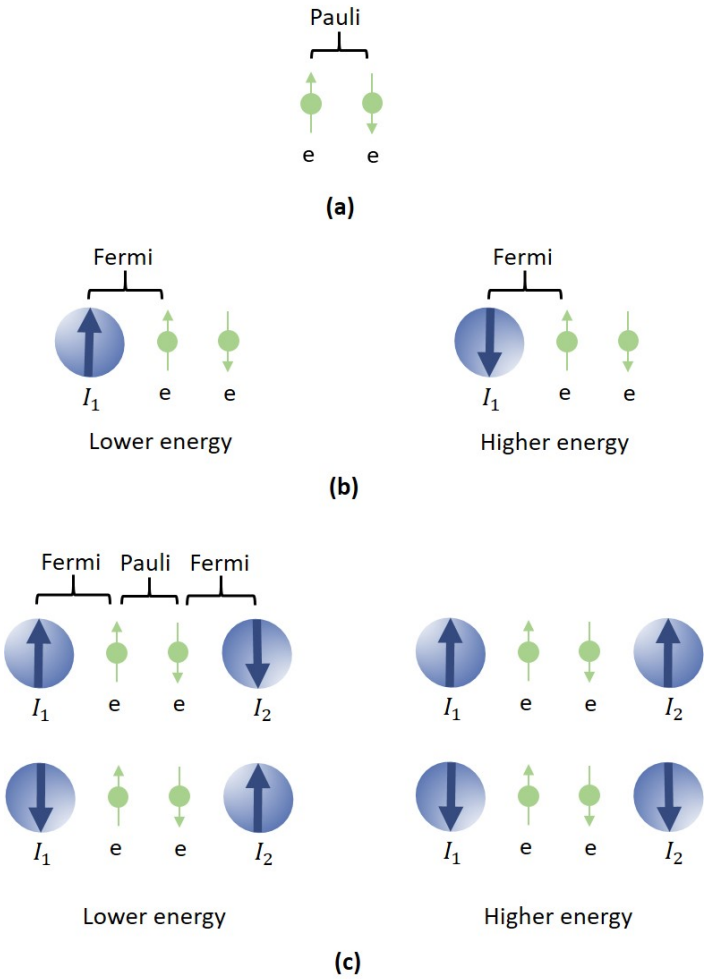

Figure 2.7: Illustration of the J-coupling mechanism mediated by the surrounding electrons. The arrows show the spin angular momentum of the nuclear spins with positive gyromagnetic ratios and the electron spins.

The energy of the J-coupling interaction between spins can be represented in its corresponding Hamiltonian operator $\hat{\mathcal{H}}_J$:

$$\hat{\mathcal{H}}_J = \sum_i \sum_j 2\pi\hbar J_{ij} \hat{\boldsymbol{I}}_i \hat{\boldsymbol{I}}_j \tag{2.26}$$

where J_{ij} is the J-coupling constant. The factor 2π in front of the J-coupling keeps the term $2\pi J_{ij}$ in angular frequency, as J_{ij} is measurable in Hz. $\hat{\boldsymbol{I}}_i$ is operator for the spin angular momentum of nucleus i. The interaction energy between the static magnetic field $\boldsymbol{B}_0$ along to z-axis and the magnetic moment $\boldsymbol{\mu} = \gamma\hbar\hat{I}_{iz}$ gives Zeeman Hamiltonian:

$$\hat{\mathcal{H}}_Z = -\sum_i \boldsymbol{\mu}_i \cdot \boldsymbol{B}_0 = -\sum_i \gamma\hbar\hat{I}_{iz} B_0 \tag{2.27}$$

where $\hat{I}_{iz}$ is the operator for its projection along the z-axis. Under the effect of chemical shielding, Equation (2.27) can be rewritten as follows:

$$\hat{\mathcal{H}}_Z = -\sum_i \gamma\hbar\hat{I}_{iz}(1-\sigma_i)B_0 = \sum_i \omega_i\hbar\hat{I}_{iz} \tag{2.28}$$

where σ_i is the shielding tensor, and ω_i is the Larmor frequency of nucleus.

This section takes a two-spin system as an example and discusses in detail, from the perspective of quantum mechanics, the effects of J-coupling in a two-spin system with different situations.

In NMR spectroscopy, the Hamiltonian of a system, encompassing both the chemical shift and J-coupling terms, provides a comprehensive description of the interactions affecting the nuclei in an NMR experiment. The chemical shift gives insight into the electronic environment of the nuclei, while the J-coupling reveals information about the molecular structure through the connectivity and arrangement of the nuclei [36]. Therefore, the total Hamiltonian that contributes to the NMR spectrum includes terms for both the chemical shifts of the individual spins and their spin-spin interactions through J-coupling, as given below:

$$\hat{\mathcal{H}} = \hat{\mathcal{H}}_Z + \hat{\mathcal{H}}_J \tag{2.29}$$

$$= \omega_1\hbar\hat{I}_{1z} + \omega_2\hbar\hat{I}_{2z} + 2\pi\hbar J_{12}\hat{\boldsymbol{I}}_1\hat{\boldsymbol{I}}_2 \tag{2.30}$$

To simplify, $\hbar = 1$ is set and the subscript from J_{12} is dropped, referring to it simply as J for clarity. The total Hamiltonian for the two-coupled spin system, expressed in terms of frequency with unit of Hz, is:

$$\hat{\mathcal{H}}_{\text{freq}} = \nu_1\hat{I}_{1z} + \nu_2\hat{I}_{2z} + J(\hat{I}_{1x}\hat{I}_{2x} + \hat{I}_{1y}\hat{I}_{2y} + \hat{I}_{1z}\hat{I}_{2z}) \tag{2.31}$$

As it is discussed above, the spin-1/2 points either up or down. Here, $|\alpha\rangle$ and $|\beta\rangle$ are used to represent the spin-up ($\uparrow$) and spin-down ($\downarrow$) state, respectively:

$$\hat{I}_{iz}|\alpha_i\rangle = \frac{1}{2}|\alpha_i\rangle \qquad \hat{I}_{iz}|\beta_i\rangle = -\frac{1}{2}|\beta_i\rangle \qquad (i=1,2) \tag{2.32}$$

The basis set of the two spin-1/2 system are $|\alpha_1\alpha_2\rangle$, $|\alpha_1\beta_2\rangle$, $|\beta_1\alpha_2\rangle$, and $|\beta_1\beta_2\rangle$. The subscribe 1 and 2 of the spin state can be dropped to make it cleaner. The z-component spin operators $\hat{I}_{1z}$ and $\hat{I}_{2z}$ act on the four basis spin states as follows:

$$\hat{I}_{1z}|\alpha\alpha\rangle = \frac{1}{2}|\alpha\alpha\rangle \qquad \hat{I}_{2z}|\alpha\alpha\rangle = \frac{1}{2}|\alpha\alpha\rangle \tag{2.33}$$

$$\hat{I}_{1z}|\alpha\beta\rangle = \frac{1}{2}|\alpha\beta\rangle \qquad \hat{I}_{2z}|\alpha\beta\rangle = -\frac{1}{2}|\alpha\beta\rangle \tag{2.34}$$

$$\hat{I}_{1z}|\beta\alpha\rangle = -\frac{1}{2}|\beta\alpha\rangle \qquad \hat{I}_{2z}|\beta\alpha\rangle = \frac{1}{2}|\beta\alpha\rangle \tag{2.35}$$

$$\hat{I}_{1z}|\beta\beta\rangle = -\frac{1}{2}|\beta\beta\rangle \qquad \hat{I}_{2z}|\beta\beta\rangle = -\frac{1}{2}|\beta\beta\rangle \tag{2.36}$$

To calculate the scalar product $\hat{\boldsymbol{I}}_1\hat{\boldsymbol{I}}_2 = \hat{I}_{1x}\hat{I}_{2x} + \hat{I}_{1y}\hat{I}_{2y} + \hat{I}_{1z}\hat{I}_{2z}$ in Equation (2.31), it is necessary to introduce the ladder operators

$$\hat{I}_{i+} = \hat{I}_{ix} + i\hat{I}_{iy} \tag{2.37}$$

$$\hat{I}_{i-} = \hat{I}_{ix} - i\hat{I}_{iy} \tag{2.38}$$

where $\hat{I}_{i+}$ is the raising operator that increases the spin state, i.e., from spin-down $|\beta\rangle$ to spin-up $|\alpha\rangle$, and $\hat{I}_{i-}$ is the lowering operator that decreases the spin state, i.e., from spin-up $|\alpha\rangle$ to spin-down $|\beta\rangle$. The x- and y-component of the spin operators can be represented by using the raising $\hat{I}_{i+}$ and lowering $\hat{I}_{i-}$ operators:

$$\hat{I}_{ix} = \frac{\hat{I}_{i+} + \hat{I}_{i-}}{2} \tag{2.39}$$

$$\hat{I}_{iy} = \frac{\hat{I}_{i+} - \hat{I}_{i-}}{2i} \tag{2.40}$$

Substituting Equation (2.39) and Equation (2.40) into the scalar product gives:

$$\hat{\boldsymbol{I}}_1\hat{\boldsymbol{I}}_2 = \hat{I}_{1x}\hat{I}_{2x} + \hat{I}_{1y}\hat{I}_{2y} + \hat{I}_{1z}\hat{I}_{2z} \tag{2.41}$$

$$= \frac{\hat{I}_{1+}\hat{I}_{2-} + \hat{I}_{1-}\hat{I}_{2+}}{2} + \hat{I}_{1z}\hat{I}_{2z} \tag{2.42}$$

To calculate the energy of the two-coupled spin system it can be discussed in three cases:

- if the two nuclei are chemically and magnetically equivalent, they will exhibit identical chemical shifts, denoted as $\nu_1 = \nu_2 = \nu$, and the spin system is referred to as A_2 system;
- if the two nuclei differ significantly in chemical shift ($\nu_1 \neq \nu_2$), the spin system is labeled with letters that are far apart in the alphabet, such as AX system;
- if the two nuclei exhibit similar but not identical chemical shifts ($\Delta\nu/J \leq 10$), the spin system can be classified as an AB-spin system, which is typically denoted by two consecutive letters of the alphabet.

2.7.1 A_2-spin system

The following three sections detail how the J-coupling effect influences the Hamiltonian of a two-spin system and affects the resulting spectra. For the first case, the Hamiltonian of the spin system A_2 (Equation (2.31)) can be rewritten as:

$$\hat{\mathcal{H}}(\mathrm{A}_2) = \nu(\hat{I}_{1z} + \hat{I}_{2z}) + J(\hat{I}_{1x}\hat{I}_{2x} + \hat{I}_{1y}\hat{I}_{2y} + \hat{I}_{1z}\hat{I}_{2z}) \tag{2.43}$$

The energy of corresponding basis states are:

$$\hat{\mathcal{H}}(\mathrm{A}_2)\,|\alpha\alpha\rangle = \left(\nu + \frac{J}{4}\right)|\alpha\alpha\rangle \tag{2.44}$$

$$\hat{\mathcal{H}}(\mathrm{A}_2)\,|\alpha\beta\rangle = -\frac{J}{4}\,|\alpha\beta\rangle + \frac{J}{2}\,|\beta\alpha\rangle \tag{2.45}$$

$$\hat{\mathcal{H}}(\mathrm{A}_2)\,|\beta\alpha\rangle = \frac{J}{2}\,|\alpha\beta\rangle - \frac{J}{4}\,|\beta\alpha\rangle \tag{2.46}$$

$$\hat{\mathcal{H}}(\mathrm{A}_2)\,|\beta\beta\rangle = \left(-\nu + \frac{J}{4}\right)|\beta\beta\rangle \tag{2.47}$$

Therefore, the Hamiltonian matrix of the A_2 spin system expressed in the basis states gives:

$$\mathcal{H}(A_2) = \begin{bmatrix} \nu + \frac{J}{4} & 0 & 0 & 0 \\ 0 & -\frac{J}{4} & \frac{J}{2} & 0 \\ 0 & \frac{J}{2} & -\frac{J}{4} & 0 \\ 0 & 0 & 0 & -\nu + \frac{J}{4} \end{bmatrix} \tag{2.48}$$

Since the off-diagonal elements $\mathcal{H}_{23}$ and $\mathcal{H}_{23}$ of the above Hamiltonian matrix are non-zero, diagonalizing the matrix is necessary to calculate the eigenvalues and corresponding eigenstates.

$$\mathcal{H}_{mn}(A_2) = \begin{bmatrix} \mathcal{H}_{22} & \mathcal{H}_{23} \\ \mathcal{H}_{32} & \mathcal{H}_{33} \end{bmatrix} \tag{2.49}$$

$$det(\mathcal{H}_{mn}(A_2) - E\mathbf{I}) = 0 \tag{2.50}$$

$$\begin{bmatrix} -\frac{J}{4} - E & \frac{J}{2} \\ \frac{J}{2} & -\frac{J}{4} - E \end{bmatrix} = 0$$

$$\left(-\frac{J}{4} - E\right)^2 - \left(\frac{J}{2}\right)^2 = E^2 + \frac{1}{2}JE - \frac{3}{16}J^2 = 0$$

$$E_{\pm} = \frac{-\frac{J}{2} \pm \sqrt{\frac{J^2}{4} + \frac{3J^2}{4}}}{2}$$

$$E_+ = \frac{J}{4} \qquad E_- = -\frac{3J}{4} \tag{2.51}$$

The eigenvalues $E_+ = J/4$ and $E_- = -3J/4$ correspond to the eigenstates $(|\alpha\beta\rangle + |\beta\alpha\rangle)/\sqrt{2}$ and $(|\alpha\beta\rangle - |\beta\alpha\rangle)/\sqrt{2}$, respectively. Therefore, the four eigenstates of the A_2-spin system, along with their corresponding total spin quantum numbers (m_I), and energies (E), are presented in Table 2.2.

Energy level	**Eigenstate**	m_I	E $(J = 0)$	E $(J \neq 0)$
I	$\|\alpha\alpha\rangle$	+1	ν	$\nu + \frac{1}{4}J$
II	$\frac{1}{\sqrt{2}}(\|\alpha\beta\rangle - \|\beta\alpha\rangle)$	0	0	$-\frac{3}{4}J$
III	$\frac{1}{\sqrt{2}}(\|\alpha\beta\rangle + \|\beta\alpha\rangle)$	0	0	$\frac{1}{4}J$
IV	$\|\beta\beta\rangle$	-1	$-\nu$	$-\nu + \frac{1}{4}J$

Table 2.2: Eigenstates and energies of A_2 spin system without and with J-coupling.

The transition between spin states is only allowed when $\Delta m_I = 1$ and the symmetry of their wave functions is consistent. A spin wave function is considered symmetric if it remains

unchanged upon the exchange of two particles. For the four eigenstates of the A_2-spin system, the wave functions $|\alpha\alpha\rangle$, $(|\alpha\beta\rangle + |\beta\alpha\rangle)\sqrt{2}$, and $|\beta\beta\rangle$ are symmetric, as their nuclear spin wave functions remain unchanged upon the exchange of the two nuclei. Therefore, it is allowed for the transitions from $|\alpha\alpha\rangle$ to $(|\alpha\beta\rangle + |\beta\alpha\rangle)\sqrt{2}$ with $\Delta E_{\mathrm{I}\to\mathrm{III}} = \nu - 0 = \nu$ for $J = 0$ (or $\Delta E_{\mathrm{I}\to\mathrm{III}} = (\nu + J/4) - J/4 = \nu$ for $J \neq 0$), and $(|\alpha\beta\rangle + |\beta\alpha\rangle)\sqrt{2}$ to $|\beta\beta\rangle$ with $\Delta E_{\mathrm{III}\to\mathrm{IV}} = 0 - \nu = \nu$ for $J = 0$ (or $\Delta E_{\mathrm{III}\to\mathrm{IV}} = J/4 - (-\nu + J/4) = \nu$) for $J \neq 0$). The two transitions occur at the same frequency ν, leads to a singlet in the spectrum (Figure 2.8).

The spin wave function $(|\alpha\beta\rangle - |\beta\alpha\rangle)/\sqrt{2}$ transforms into $(|\beta\alpha\rangle - |\alpha\beta\rangle)/\sqrt{2}$ upon exchanging the two nuclei, indicating a change in sign $(-(|\alpha\beta\rangle - |\beta\alpha\rangle)/\sqrt{2})$ and exhibiting anti-symmetric characteristics. Transitions from this antisymmetric spin state to the other three symmetric spin states are forbidden.

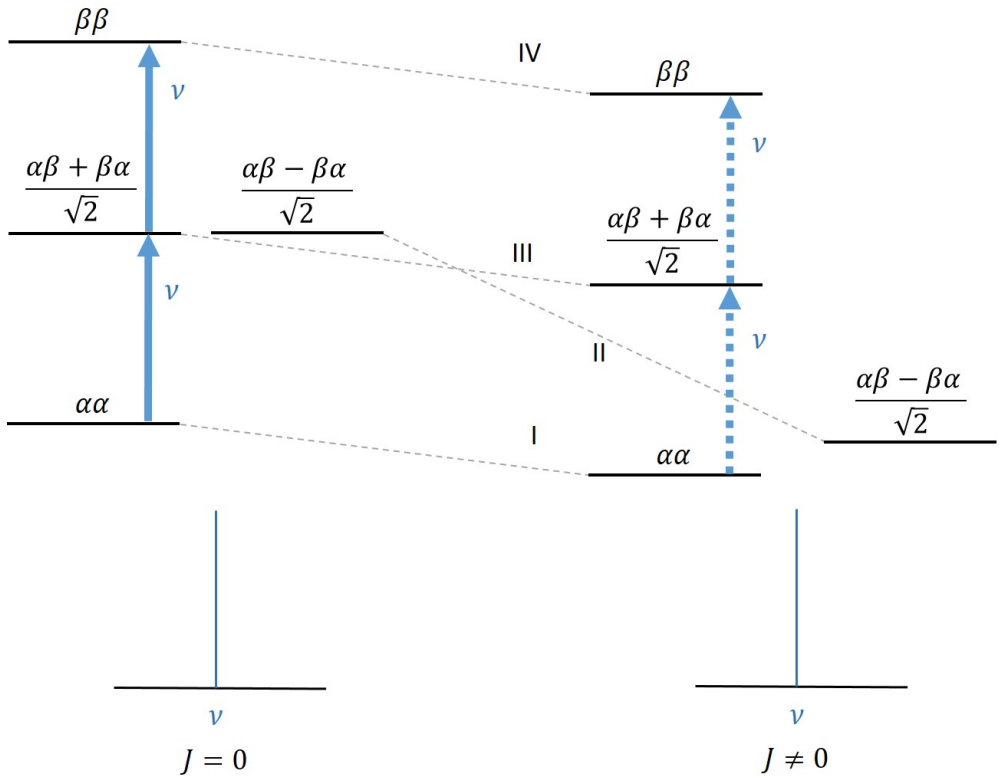

Figure 2.8: Energy level diagram of the A_2-spin system without and with J-coupling.

2.7.2 AX-spin system

The situation of the AX-spin system, characterized by different chemical shifts and relatively small coupling constants, is now discussed. This system is defined as a first-order spin system. The Hamiltonian of the AX-system is:

$$\hat{\mathcal{H}}(\mathrm{AX}) = \nu_1 \hat{I}_{1z} + \nu_2 \hat{I}_{2z} + J(\hat{I}_{1x}\hat{I}_{2x} + \hat{I}_{1y}\hat{I}_{2y} + \hat{I}_{1z}\hat{I}_{2z}) \tag{2.52}$$

In the scenario of the first-order spin system, the off-diagonal elements $\mathcal{H}_{mn} = 0$ $(m \neq n)$, the Hamiltonian matrix of the AX system gives as follows:

$$\mathcal{H}(\mathrm{AX}) = \begin{bmatrix} \frac{\nu_1}{2} + \frac{\nu_2}{2} + \frac{J}{4} & 0 & 0 & 0 \\ 0 & \frac{\nu_1}{2} - \frac{\nu_2}{2} - \frac{J}{4} & 0 & 0 \\ 0 & 0 & -\frac{\nu_1}{2} + \frac{\nu_2}{2} - \frac{J}{4} & 0 \\ 0 & 0 & 0 & -\frac{\nu_1}{2} - \frac{\nu_2}{2} + \frac{J}{4} \end{bmatrix} \tag{2.53}$$

The eigenstates can be expressed with the basis states and the corresponding energies of the AX-spin system are shown in Table 2.3.

Energy level	**Eigenstate**	m_I	$E\ (J = 0)$	$E\ (J \neq 0)$
I	$\|\alpha\alpha\rangle$	+1	$\frac{1}{2}(\nu_1 + \nu_2)$	$\frac{1}{2}(\nu_1 + \nu_2) + \frac{1}{4}J$
II	$\|\alpha\beta\rangle$	0	$\frac{1}{2}(\nu_1 - \nu_2)$	$\frac{1}{2}(\nu_1 - \nu_2) - \frac{1}{4}J$
III	$\|\beta\alpha\rangle$	0	$-\frac{1}{2}(\nu_1 - \nu_2)$	$-\frac{1}{2}(\nu_1 - \nu_2) - \frac{1}{4}J$
IV	$\|\beta\beta\rangle$	-1	$-\frac{1}{2}(\nu_1 + \nu_2)$	$-\frac{1}{2}(\nu_1 + \nu_2) + \frac{1}{4}J$

Table 2.3: Eigenstates and energies of AX spin system without and with J-coupling.

2.7.3 AB-spin system

If the chemical shift of the two nuclei are similar but not the same $(\Delta\nu/J \leq 10)$, the AX-spin system changed into AB-system. The stationary wave function $|\alpha\alpha\rangle$ and $|\beta\beta\rangle$ are still remain the same, but $|\alpha\beta\rangle$ and $|\beta\alpha\rangle$ are mixed with each other to form two different wave functions, represent in form of $c_a\,|\alpha\beta\rangle + c_b\,|\beta\alpha\rangle$ with two sets values of c_a and c_b.

In this scenario of AB-spin system, the off-diagonal elements of the Hamiltonian $\mathcal{H}_{mn}$ $(m \neq n)$, which represent the coupling between different energy levels of the system, can not be ignored anymore. Therefore, the Hamiltonian of the AB-spin system is:

$$\mathcal{H}(\mathrm{AB}) = \begin{bmatrix} \frac{\nu_1}{2} + \frac{\nu_2}{2} + \frac{J}{4} & 0 & 0 & 0 \\ 0 & \frac{\nu_1}{2} - \frac{\nu_2}{2} - \frac{J}{4} & \frac{J}{2} & 0 \\ 0 & \frac{J}{2} & -\frac{\nu_1}{2} + \frac{\nu_2}{2} - \frac{J}{4} & 0 \\ 0 & 0 & 0 & -\frac{\nu_1}{2} - \frac{\nu_2}{2} + \frac{J}{4} \end{bmatrix} \tag{2.54}$$

The calculation processes of diagonalizing the matrix $\mathcal{H}_{mn}$ to calculate the eigenvalues are

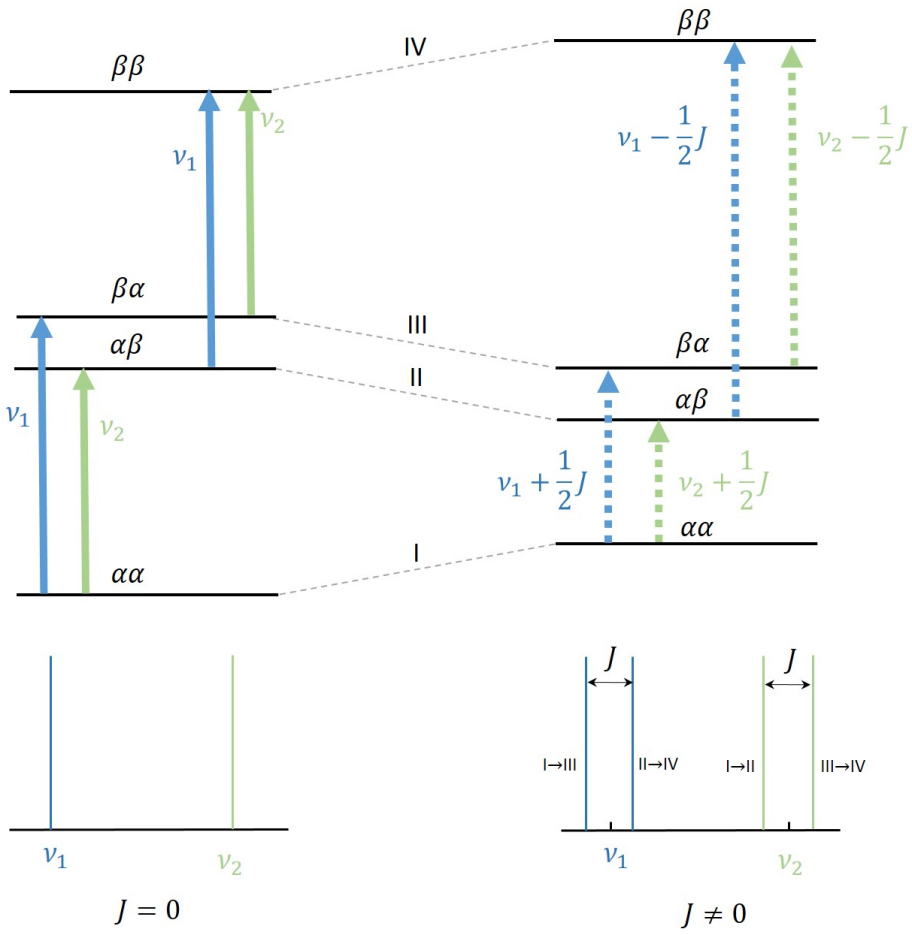

Figure 2.9: Energy level diagram of the AX-spin system without and with J-coupling.

shown as follows:

$$\mathcal{H}_{mn}(\mathrm{AB}) = \begin{bmatrix} \mathcal{H}_{22} & \mathcal{H}_{23} \\ \mathcal{H}_{32} & \mathcal{H}_{33} \end{bmatrix} \tag{2.55}$$

$$det(\mathcal{H}_{mn}(\mathrm{AB}) - E\mathbf{I}) = 0 \tag{2.56}$$

$$\begin{bmatrix} \frac{\nu_1}{2} - \frac{\nu_2}{2} - \frac{J}{4} - E & \frac{J}{2} \\ \frac{J}{2} & -\frac{\nu_1}{2} + \frac{\nu_2}{2} - \frac{J}{4} - E \end{bmatrix} = 0 \tag{2.57}$$

$$\left(-\frac{J}{4} - E\right)^2 - \frac{1}{4}(\nu_1 - \nu_2)^2 - \left(\frac{J}{2}\right)^2 = 0$$

$$E_{\pm} = \frac{-\frac{J}{2} \pm \sqrt{J^2 + (\nu_1 - \nu_2)^2}}{2} \tag{2.58}$$

$$= -\frac{J}{4} \pm \frac{1}{2}[J^2 + (\nu_1 - \nu_2)^2]^{1/2} \tag{2.59}$$

By setting the term $[J^2 + (\nu_1 - \nu_2)^2]^{1/2}/2 = C$, Equation (2.59) is rewritten as follows:

$$E_{\pm} = -\frac{J}{4} \pm C \tag{2.60}$$

where:

$$4C^2 = J^2 + (\nu_1 - \nu_2)^2$$
$$\nu_1 - \nu_2 = [4C^2 - J^2]^{1/2}$$

The energies of the AB-spin system are shown in Table 2.4:

Energy level	**Eigenstate**	m_I	E $(J \neq 0)$
I	$\|\alpha\alpha\rangle$	+1	$\frac{1}{2}(\nu_1 + \nu_2) + \frac{1}{4}J$
II	$c_a\|\alpha\beta\rangle + c_b\|\beta\alpha\rangle$	0	$C - \frac{1}{4}J$
III	$c'_a\|\alpha\beta\rangle + c'_b\|\beta\alpha\rangle$	0	$-C - \frac{1}{4}J$
IV	$\|\beta\beta\rangle$	-1	$-\frac{1}{2}(\nu_1 + \nu_2) + \frac{1}{4}J$

Table 2.4: Eigenstates and energies of AB spin system with J-coupling.

For the energy level transitions between the spin states and the corresponding spectrum of the AB-spin system, it is commonly to set the center of the spectrum as zero, i.e., $(\nu_1 + \nu_2)/2 = 0$. Thus, the four transition frequencies related to the center of the spectrum are: $\Delta E_{\mathrm{I}\to\mathrm{II}} = -C + J/2$ for transition from $|\alpha\alpha\rangle$ to $c_a|\alpha\beta\rangle + c_b|\beta\alpha\rangle$; $\Delta E_{\mathrm{I}\to\mathrm{III}} = C + J/2$ for transition from $|\alpha\alpha\rangle$ to $c'_a|\alpha\beta\rangle + c'_b|\beta\alpha\rangle$; $\Delta E_{\mathrm{II}\to\mathrm{IV}} = C - J/2$ for transition from $c_a|\alpha\beta\rangle + c_b|\beta\alpha\rangle$ to $|\beta\beta\rangle$; $\Delta E_{\mathrm{III}\to\mathrm{IV}} = -C - J/2$ for transition from $c'_a|\alpha\beta\rangle + c'_b|\beta\alpha\rangle$ to $|\beta\beta\rangle$. The spectrum of the AB-spin system is shown in Figure 2.10. The J-coupling is corresponding to the distance between the first peak (I $\to$ III) and second peak (II $\to$ IV), or between the third peak (I $\to$ II) and (III $\to$ IV) fourth peak.

To determine the peak intensities, the coefficient c_a and c_b need to calculated for obtaining the stationary-state wave functions of the spin states with $m_I = 0$. The ratio of the c_a and c_b can be represented by the ratio of their corresponding co-factors in Equation (2.57):

$$\frac{c_a}{c_b} = \frac{-\frac{1}{2}(\nu_1 - \nu_2) - \frac{1}{4} - E}{\frac{1}{2}J} \tag{2.61}$$

By substituting the values of E (Equation (2.60)), the above equation can be rewritten as:

$$\frac{c_a}{c_b} = \frac{-(\nu_1 - \nu_2) \pm 2C}{J} \tag{2.62}$$

To normalize the wave function, the relationship of the coefficient c_a and c_b needs to meet the following condition:

$${c_a}^2 + {c_b}^2 = 1 \tag{2.63}$$

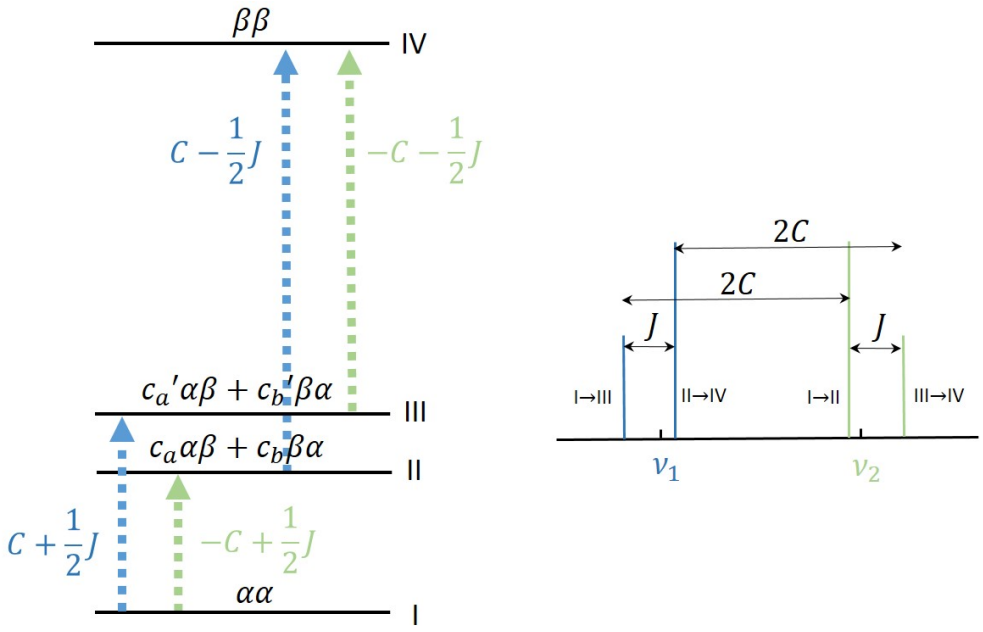

Figure 2.10: Energy level diagram of the AB-spin system.

The aforementioned formula readily evokes associations with the one of the formulas of trigonometric functions:

$$sin^2\theta + cos^2\theta = 1 \tag{2.64}$$

Therefore, it is possible to set $c_a = \cos\theta$, $c_b = \sin\theta$, $c_a' = -\sin\theta$, and $c_b' = \cos\theta$. The stationary-state wave functions are as follows:

$$\Phi_{II} = cos\theta|\alpha\beta\rangle + sin\theta|\beta\alpha\rangle \tag{2.65}$$

$$\Phi_{III} = -sin\theta|\alpha\beta\rangle + cos\theta|\beta\alpha\rangle \tag{2.66}$$

when $\theta = 0°$, $\Phi_{II} = |\alpha\beta\rangle$, $\Phi_{III} = |\beta\alpha\rangle$, which becomes into the situation of AX-spin system; when $\theta = 45°$, $\Phi_{II} = \sqrt{2}(|\alpha\beta\rangle + |\beta\alpha\rangle)/2$, $\Phi_{III} = \sqrt{2}(|\beta\alpha\rangle - |\alpha\beta\rangle)/2$, which are the stationary-state wave functions in situation of A_2-spin system.

The corresponding intensities of the four peaks are obtained by calculating the corresponding transition probabilities with raising operators. For I→II the transition probability is:

$$\begin{aligned}
&\{< \alpha\alpha|F_+|cos\theta\alpha\beta + sin\theta\beta\alpha >\}^2 \\
=&\{< \alpha\alpha|cos\theta\alpha\alpha > + < sin\theta\alpha\alpha >\}^2 \\
=&(cos\theta + sin\theta)^2 \\
=&1 + 2sin\theta cos\theta
\end{aligned}$$

For I→III the transition probability is:

$$\begin{aligned}
&\{< \alpha\alpha|F_+| - sin\theta\alpha\beta + cos\theta\beta\alpha >\}^2 \\
=&< \alpha\alpha|sin\theta\alpha\alpha > + < cos\theta\alpha\alpha >\}^2 \\
=&(-sin\theta + cos\theta)^2 \\
=&1 - 2sin\theta cos\theta
\end{aligned}$$

For III→IV the transition probability is:

$$\begin{aligned}
&\{< -sin\theta\alpha\beta + cos\theta\beta\alpha|F_+|\beta\beta >\}^2 \\
=&\{< -sin\theta\alpha\beta + cos\theta\beta\alpha|\alpha\beta + \beta\alpha >\}^2 \\
=&\{- < sin\theta\alpha\beta|\alpha\beta > - < sin\theta\alpha\beta|\beta\alpha > + < cos\theta\beta\alpha|\alpha\beta > + < cos\theta\beta\alpha|\beta\alpha >\}^2 \\
=&(-sin\theta + cos\theta)^2 \\
=&1 - 2sin\theta cos\theta
\end{aligned}$$

For II→IV the transition probability is:

$$\begin{aligned}
&\{< cos\theta\alpha\beta + sin\theta\beta\alpha|F_+|\beta\beta >\}^2 \\
=&\{< cos\theta\alpha\beta + sin\theta\beta\alpha|\alpha\beta + \beta\alpha >\}^2 \\
=&\{< cos\theta\alpha\beta|\alpha\beta > + < cos\theta\alpha\beta|\beta\alpha > + < sin\theta\beta\alpha|\alpha\beta > + < sin\theta\beta\alpha|\beta\alpha >\}^2 \\
=&(cos\theta + sin\theta)^2 \\
=&1 + 2sin\theta cos\theta
\end{aligned}$$

Thus, the ratio of the intensities of the inner and outer peaks in Figure 2.10 is $\frac{1 + 2sin\theta cos\theta}{1 - 2sin\theta cos\theta}$.

Parahydrogen-Based Hyperpolarization

3.1 Overview

This chapter begins by addressing the underlying reasons for the limited sensitivity of NMR detection, which naturally introduces the hyperpolarization techniques. It then delves into a detailed discussion on the spin source for both PHIP and SABRE methods—namely, parahydrogen (*para*-H_2)—from the perspectives of quantum mechanics and thermodynamics. The laboratory instruments used for producing and collecting *para*-H_2 are also described.

The subsequent section explains the signal enhancement in the two types of hydrogenative PHIP, namely PASADENA (Parahydrogen And Synthesis Allow Dramatically Enhanced Nuclear Alignment) and ALTADENA (Adiabatic Longitudinal Transport After Dissociation Engenders Nuclear Alignment). It then investigates the non-hydrogenative PHIP approach—SABRE, including a description of the catalytic cycle of the SABRE complex and an explanation of the spin order transfer mechanism via Level Anti-Crossings (LACs) in SABRE, represented using a three-spin system.

The final section reviews three experimental methods for conducting PHIP and SABRE: the bubbling method, the shake-and-drop method using a high-pressure NMR tube, and the utilization of membrane-based gas–liquid reactors.

3.2 Introduction

3.2.1 Sensitivity of NMR

Though NMR's wealth of information is undeniable, it does grapple with a fundamental sensitivity shortfall when compared with other conventional analytical methodologies, such as mass spectrometry. The inherently low sensitivity due to the small population differences between nuclear spin states at thermal equilibrium, where the population of these spins follows a Boltzmann distribution, with the spins aligned with the magnetic field marginally outnumbering those that are anti-aligned. This results in a relatively low net magnetic moment, which is what and NMR spectroscopy and MRIs detect.

For spin$-1/2$ species, the polarization P is defined the difference in population between the two energy levels relative to the total number of spins:

$$P = \frac{n_{1/2} - n_{-1/2}}{n_{1/2} + n_{-1/2}} \tag{3.1}$$

where $n_{1/2}$ and $n_{-1/2}$ are the number of the spins orient along and against the external magnetic field. As mentioned in Chapter 2.4, the populations of spins in the low- and high-energy levels follow the Boltzmann distribution, as describe with Equation (2.14). Therefore, the polarization at thermal equilibrium is obtained by inserting Equation (2.14) into Equation (3.1):

$$P_0 = \frac{n_{-1/2} \cdot \exp\left(\frac{\Delta E}{k_B T}\right) - n_{-1/2}}{n_{-1/2} \cdot \exp\left(\frac{\Delta E}{k_B T}\right) + n_{-1/2}} = \frac{\exp\left(\frac{\Delta E}{k_B T}\right) - 1}{\exp\left(\frac{\Delta E}{k_B T}\right) + 1} = \tanh\left(\frac{\Delta E}{2k_B T}\right) \tag{3.2}$$

By considering the nuclei ^{1}H ($\gamma_{^1H} = 2.675 \times 10^8$ rad $\cdot$ s$^{-1}\cdot$T^{-1}) and ^{13}C ($\gamma_{^{13}C} = 6.728 \times 10^7$ rad $\cdot$ s$^{-1}\cdot$T^{-1}), their thermal equilibrium spin polarizations in a 500 MHz (11.7 T) NMR magnet at room temperature (298 K) can be estimated as $P_0(^1\text{H}) \approx 4.0 \times 10^{-5}$ and $P_0(^{13}\text{C}) \approx 1.0 \times 10^{-5}$, respectively.

Over the past decades, several strategies have been developed to address this sensitivity bottleneck without altering the fundamental spin polarization. Hardware improvements in bulk NMR—such as ultra-high field magnets [37, 38], cryogenic probes [39, 40, 41], and advanced RF coil designs [42]—have substantially increased signal-to-noise (SNR) ratio, particularly for high-resolution applications. However, these approaches often involve high cost and system complexity.

In parallel, optimized pulse sequences such as INEPT (Insensitive Nuclei Enhanced by Polarization Transfer) and HSQC (Heteronuclear Single Quantum Coherence) have been widely adopted to maximize polarization transfer efficiency and suppress relaxation losses, enhancing sensitivity without requiring hardware changes [43, 44, 45]. For small sample volumes, microcoils provide another effective solution by increasing the filling factor and improving signal detection, especially in microfluidic or miniaturized NMR platforms [46, 47].

Although these methods have proven effective in a variety of applications, they ultimately operate within the constraints of thermal spin polarization. No matter how advanced the hardware, pulse sequence, or probe design becomes, the achievable signal intensity remains fundamentally limited by the extremely low population difference between spin states at thermal equilibrium—typically on the order of 10^{-5} at room temperature and clinical magnetic field strengths.

To transcend this intrinsic limitation, researchers have turned to a fundamentally different class of approaches: hyperpolarization techniques.

3.2.2 Hyperpolarization techniques

Hyperpolarization refers to a set of methods that deliberately drive nuclear spin systems into highly polarized, non-equilibrium states, thereby enhancing NMR signal intensities by up to

four to five orders of magnitude. These techniques temporarily overcome the Boltzmann-imposed polarization limits and enable the detection of low-concentration species or rapid dynamic processes that are otherwise beyond the reach of conventional NMR. A key figure of merit for characterizing the efficiency of hyperpolarization is the enhancement factor. In practical NMR applications, the signal enhancement ϵ of a hyperpolarized signal is defined as the ratio of the measured signal intensities of the hyperpolarized (HP) and thermal equilibrium states:

$$\epsilon = \frac{I_{\mathrm{HP}}}{I_{\mathrm{thermal}}} \tag{3.3}$$

For spin-1/2 species, the ratio of $I_{\mathrm{HP}}/I_{\mathrm{thermal}}$ in Equation 3.3 is proportional to $P_{\mathrm{X}}/P_{\mathrm{thermal}}$, where P_{X} is the polarization of a nucleus X achieved with hyperpolarization method. [48]

Having defined the enhancement factor, the prominent hyperpolarization methods—DNP, SEOP, and parahydrogen-based approaches including PHIP and SABRE—are briefly introduced below. Each technique is based on a distinct principle and requires specific instrumentation, exhibiting varying degrees of polarization efficiency, sample compatibility, and practical accessibility.

DNP is performed by introducing free radicals or other paramagnetic agents into the sample, which possess unpaired electrons with a much higher gyromagnetic ratio compared to nuclei ($\gamma_e/\gamma_{\mathrm{H}} \approx -658$). Under microwave irradiation, the polarization of these electrons is transferred to nearby nuclei, resulting in a dramatic increase in nuclear polarization.

A typical DNP spectrometer comprises three core components: a high-power, high-frequency terahertz source to drive electron spin transitions; a low-loss transmission line to efficiently deliver the microwave energy to the sample; an cryogenic DNP-NMR probe capable of simultaneous terahertz and radio-frequency irradiation. [49, 50] Moreover, DNP requires a paramagnetic polarizing agent that present in the sample as the source of highly polarized unpaired electrons. These paramagnetic species can be either exogenous radicals, which can be intentionally added to the sample, or endogenous radicals that are naturally present under specific physiological or chemical conditions. The selection criteria for suitable polarizing agents primarily include electron paramagnetic resonance linewidth, solubility, toxicity, chemical stability, reactivity, and relaxation times. Currently, nitroxide-based biradicals are among the most commonly employed exogenous polarizing agents. [51] In contrast, common endogenous radicals can be semiquinone species [52] or isotope enriched metabolites and drug molecules, such as^{15}N-choline [53], ^{15}N-carnitine [54], and permethylated, perdeuterated ^{15}N-amino acids [55, 56]. DNP can achieve spin polarization levels ranging from several percent to tens of percent, depending on factors such as magnetic field strength, temperature, electron-spin concentration, and microwave irradiation strategies. These capabilities make DNP particularly valuable in diverse applications, including solid-state NMR for structural characterization of complex materials [57], biomolecules [58], and pharmaceuticals [59, 60]; liquid-state NMR for real-time monitoring of chemical reactions and metabolic processes [61, 62, 63, 64]; and real-time *in vivo* metabolic imaging for investigating diseases such as cancer and cardiovascular disorders [65, 66, 67].

Despite its broad applicability, DNP remains technically demanding due to the need for specialized components—such as high-power microwave sources, cryogenic cooling infrastructure, custom probes, and polarizing agent doping—which not only increases experimental complexity but also leads to significantly higher operational costs.

SEOP is another powerful hyperpolarization technique, which is used to polarize noble gases such as ^{3}He or ^{129}Xe. SEOP involves optically pumping alkali metal atoms (such as rubidium) with circularly polarized light, resulting in highly polarized electron spins. [20, 21] These polarized electrons then collide with noble gas atoms, transferring polarization through spin exchange. The polarized noble gases with high polarization level ($P \sim 50\% - 90\%$) can subsequently be used for a variety of imaging and diagnostic applications, particularly in the context of lung imaging, where hyperpolarized ^{129}Xe is used to visualize gas exchange and lung function. [68, 69, 70] Nonetheless, the reliance on high-power and narrow-linewidth lasers, circular polarization optics, and carefully controlled optical pumping cells makes SEOP more technically demanding than some other hyperpolarization techniques. Besides, SEOP is ineffective for solid or liquid samples, which limits its applicability and makes it less versatile compared to other polarization methods.

Parahydrogen (*para*-H_2)-based hyperpolarization techniques, namely PHIP and SABRE, exploit *para*-H_2 to generate hyperpolarization on target nuclei at room temperature [12, 13]. As a spin isomer of molecular hydrogen, *para*-H_2 consists of two hydrogen atoms with antiparallel aligned nuclear spins, forming a singlet spin state with a total nuclear spin of zero. This singlet nature renders *para*-H_2 inherently NMR silent, as it has no net magnetic moment and does not produce an NMR signal. However, this singlet spin state can be exploited for efficient polarization transfer, making *para*-H_2 an excellent source of hyperpolarization. Modern cryogenic methods enable the efficient enrichment of nearly 100% pure *para*-H_2, and its storage is straightforward in non-ferromagnetic containers, such as aluminum gas cylinders, where it can retain its spin order for weeks to months. This technological accessibility makes PHIP and SABRE easily accessible and practical compared to other hyperpolarization techniques.

PHIP can achieve spin polarization levels of 20%–50% under optimal conditions [22, 71, 72], while SABRE reaches highest polarization level of 50% for ^{1}H with field-cycling strategy [73], with heteronuclear targets such as ^{13}C and ^{15}N attaining 1%–35% polarization [74, 75, 76] .

Although the polarization mechanisms differ, PHIP and SABRE achieve polarization levels comparable to those of DNP and SEOP under optimized conditions. What makes PHIP and SABRE particularly attractive is their operational simplicity: they operate at room temperature, require only inexpensive *para*-H_2 gas, and generate hyperpolarized products within seconds via a straightforward gas–liquid mixing process. These features make them uniquely suited for rapid, cost-effective, and scalable hyperpolarization applications.

Given these advantages, this PhD thesis focuses on the engineering development and optimization of PHIP and SABRE hyperpolarization platforms. Before delving directly into PHIP and SABRE, the following chapter introduces the fundamental spin properties and

physical characteristics of *para*-H_2, which serve as the foundation for these techniques.

3.3 Properties of parahydrogen

3.3.1 Discovery of the two spin isomers of hydrogen molecules

The hydrogen atom is one of the most extensively studied entities in chemistry, featured in virtually every introductory chemistry textbook. It consists of a single proton at its nucleus, orbited by a lone electron. Hydrogen gas, composed of two hydrogen atoms, is the lightest molecule and originates from the most abundant element in the universe. In the field of chemistry, hydrogen gas is not only crucial for studying basic reactions but also plays a key role in energy science, particularly in the development of sustainable energy and fuel technologies. [77, 78, 79, 80]

Normal hydrogen gas consists of two types of hydrogen molecules: ortho-H_2 and para-H_2. These are spin isomers of the hydrogen molecule, distinguished by the relative orientation of the nuclear spins of the two protons. Initial studies on the properties of hydrogen did not directly address the distinction between *ortho*-H_2 and *para*-H_2. Scientists observed some anomalies by measuring the physical properties of hydrogen, such as specific heat and thermal conductivity. For example, they found that the specific heat of hydrogen at low temperatures was significantly lower than expected, suggesting a mechanism that restricted the excitation of internal energy levels within the molecules. [81]

The discovery of ortho- and para-H_2 represents a significant milestone in the intersection of quantum mechanics, experimental chemistry, and thermodynamics. In 1925, Wolfgang Pauli formulated the Pauli exclusion principle, establishing that identical fermions (such as protons) must occupy distinct quantum states. In 1926, Werner Heisenberg introduced the exchange interaction in quantum mechanics, describing how symmetry affects the total wavefunction of a system. [82] In 1927, Friedrich Hund applied quantum mechanics to molecular hydrogen, proposed the molecular orbital theory and highlighted the role of wavefunction symmetry in molecular spin states, suggesting the possible existence of nuclear spin isomers in hydrogen molecules. [83] In the same year, Robert Mulliken formally established the relationship between nuclear spin states and rotational quantum numbers, identifying ortho-H_2 with parallel spin alignment and para-H_2 with antiparallel spin alignments as distinct molecular species. [84] In 1928, Heisenberg expanded on the exchange symmetry principle, explaining why ortho-H_2 is associated with odd rotational states, whereas para-H_2 corresponds to even rotational states.

In 1929, German physicists Konrad Bonhoeffer and Paul Harteck first verified the existence of the spin isomer of hydrogen through experimentally isolated para-H_2, confirming its stability and lower energy state. [85] Their research experiment used the cooling process of liquefied hydrogen and confirmed the existence of positive hydrogen and negative hydrogen by measuring the different heat capacities of hydrogen at different temperatures. In 1934,

the Farkas brothers directly observed the spin isomers of hydrogen in a gas sample using spectroscopic methods. [86] They cooled the hydrogen sample and measured its absorption spectrum, discovering two distinct sets of spectral lines corresponding to different rotational energy levels within the hydrogen molecule. These experimental results provided the first direct evidence of the existence of two different spin states in hydrogen molecules: *para*-H_2 and *ortho*-H_2.

3.3.2 Nuclear spin states of parahydrogen and orthohydrogen

Hydrogen molecule consists of two identical hydrogen atoms, which are fermions particles with half-integral spin quantum number. The total molecular wave function of H_2 molecule is

$$\Psi_{\text{tot}} = \Psi_{\text{elec}}\Psi_{\text{trans}}\Psi_{\text{vib}}\Psi_{\text{rot}}\Psi_{\text{spin}} \tag{3.4}$$

in which the 5 components of this wave function are as following:

- Ψ_{elec}, the electronic component;
- Ψ_{trans}, the translational component;
- Ψ_{vib}, the vibrational component;
- Ψ_{rot}, the rotational component;
- Ψ_{spin}, the nuclear spin component.

Following Pauli's Exclusion Principle, the Ψ_{tot} must be antisymmetric under the exchange of the two atomic positions, meaning the wave function changes sign when the two hydrogen atoms are exchanged.

When analyzing the five factors in total wave function of hydrogen molecule individually, it is demonstrated that the first three components (Ψ_{elec}, Ψ_{trans}, and Ψ_{vib}) are symmetric with respect to the proton exchange. Considering that the total wave function is antisymmetric, one of the last two factors Ψ_{rot} and Ψ_{spin} necessitates to be antisymmetric while the other is symmetric.

Now comes the question: what are the corresponding nuclear spin states and rotational states of *para*-H_2 and *ortho*-H_2?

In an H_2 molecule, the two protons, each with spin-1/2, can align either parallel (spin-up, $|\alpha\rangle$) or antiparallel (spin-down, $|\beta\rangle$) to the external magnetic field, resulting in the following four basis spin states:

- One spin is in the spin-up state and the other in the spin-down state, which can be $|\alpha\beta\rangle$ or $|\beta\alpha\rangle$. Both of these states indicate that the spins have antiparallel spins with a total spin quantum number of 0, forming a spin singlet state.
- Both spins are in the spin-up state, $|\alpha\alpha\rangle$, or both are in the spin-down state, $|\beta\beta\rangle$. These two states indicate that the spins have parallel spins with a total spin quantum number of 1, forming a spin triplet state.

It is evident that the basis states $|\alpha\alpha\rangle$ and $|\beta\beta\rangle$ are symmetric. However, the other two basis states $|\alpha\beta\rangle$ and $|\beta\alpha\rangle$ are neither symmetric nor antisymmetric. As a consequence, these two non-symmetric basis states cannot serve as the spin wave functions. By taking the linear combination of $|\alpha\beta\rangle$ and $|\beta\alpha\rangle$, an antisymmetric spin wave function $(|\beta\alpha\rangle - |\alpha\beta\rangle)/\sqrt{2}$ and a symmetric spin wave function $(|\alpha\beta\rangle + |\beta\alpha\rangle)/\sqrt{2}$ are constructed.

For *para*-H_2, the two spin-$\frac{1}{2}$ nuclei are aligned in opposite directions ($m_I = 0$), forming an antisymmetric nuclear spin wavefunction (Figure 3.1**a**). This results in a singlet spin state with total nuclear spin quantum number $I = 0$, and the corresponding nuclear spin wavefunction is given by:

$$|\psi\rangle_{\text{para}} = \frac{1}{\sqrt{2}}(|\beta\alpha\rangle - |\alpha\beta\rangle) = |S_0\rangle\,, \quad m_I = 0 \tag{3.5}$$

Since the total wavefunction must be antisymmetric, the rotational wavefunction must be symmetric for *para*-H_2. Consequently, *para*-H_2 is restricted to even rotational quantum numbers, with the lowest energy state given by $J_{\text{rot}} = 0$. [87, 88]

Analogously, ortho-hydrogen, with two spin-1/2 nuclei aligned in parallel, has a symmetric nuclear spin wavefunction (Figure 3.1**b**). This corresponds to a total nuclear spin quantum number $I = 1$, which is associated with the triplet spin states. These states have magnetic spin quantum numbers $m_I = -1, 0, +1$ along the z-axis, with their corresponding spin wavefunctions given by:

$$|\psi\rangle_{1,\text{ortho}} = |\alpha\alpha\rangle = |T_+\rangle\,, \quad m_I = +1 \tag{3.6}$$

$$|\psi\rangle_{2,\text{ortho}} = |\beta\beta\rangle = |T_-\rangle\,, \quad m_I = -1 \tag{3.7}$$

$$|\psi\rangle_{3,\text{ortho}} = \frac{1}{\sqrt{2}}(|\alpha\beta\rangle + |\beta\alpha\rangle) = |T_0\rangle\,, \quad m_I = 0 \tag{3.8}$$

Consequently, the rotational wavefunction of ortho-hydrogen must be antisymmetric, which restricts it to odd rotational quantum numbers ($J_{\text{rot}} = 1, 3, 5, \ldots$).

3.3.3 Statistical thermodynamics of parahydrogen and orthohydrogen

The composite quantum state of multiple particles can be expressed as a tensor product of single particle states. [89] For instance, if $|z_1\rangle$ and $|z_2\rangle$ represent the quantum states of two particles, then the composite state can be represented as $|Z\rangle = |z_1\rangle \otimes |z_2\rangle$.

Due to the coupling of the rotational states of the hydrogen molecule with nuclear spin states, both are considered together. The complete rotational partition function is denoted by

$$Z^{rn} = Z^r \cdot Z^n \tag{3.9}$$

it is also simply referred as the molecular rotational partition function. [90] Assuming that the nuclei are in the ground state, and setting the energy of the nuclear ground state to zero, the nuclear partition function for a single atom is given by:

$$z^n = g_n \tag{3.10}$$

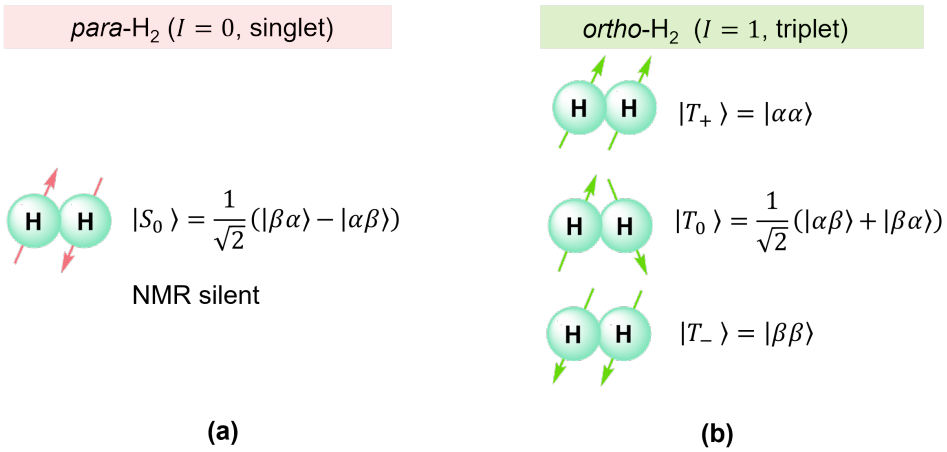

Figure 3.1: Schematic representation of the nuclear spin states of *para*-H_2 and *ortho*-H_2. **(a)** For *para*-H_2 (singlet state) the the wave function is antisymmetric with respect to the exchange of two hydrogen atoms, which can be described by $|\psi\rangle_{\text{para}} = (|\beta\alpha\rangle - |\alpha\beta\rangle)/\sqrt{2}$. The two spins are oriented in opposite directions: one within the upper half of the cone and the other within the lower half, resulting in the magnetic spin number $M_I = 0$. **(b)** For the *ortho*-H_2 (triplet states), there are symmetric wave functions corresponding to each of the three possible orientations, $M_I = +1, -1, 0$, with the corresponding spin wave functions of $|\alpha\alpha\rangle$, $|\beta\beta\rangle$ and $(|\alpha\beta\rangle + |\beta\alpha\rangle)/\sqrt{2}$.

where g_n represents the spin degeneracy of the nuclear ground state. Denoting the nuclear spin quantum number as i, then $g_n = 2i + 1$. Hence:

$$z^n = 2i + 1 \tag{3.11}$$

The rotational partition function for a diatomic gas molecule is given by:

$$Z^r = \sum_{J=0}^{\infty} (2J_{\text{rot}} + 1) \exp\left(-\frac{J_{\text{rot}}(J_{\text{rot}} + 1)\hbar^2}{2\Theta k_B T}\right) \tag{3.12}$$

where T is the temperature, J_{rot} the rotational quantum number, $\hbar$ is the reduced Planck's constant $1.054 \times 10^{-34}\,\text{J} \cdot \text{s}$, Θ is the moment of inertia of the hydrogen molecule $4.583 \times 10^{-48}\,\text{kg} \cdot \text{m}^2$, and k_B is the Boltzmann constant $1.381 \times 10^{-23}\,\text{J} \cdot \text{K}^{-1}$.

Therefore, the complete rotational partition function of a heteronuclear diatomic molecule is

$$Z^{rn} = Z^r \cdot Z^n = z^r \cdot z^{n'} \cdot z^n \tag{3.13}$$

$$= (2i + 1)\left(2i' + 1\right) \sum_{J=0}^{\infty} (2J_{\text{rot}} + 1) \exp\left(-\frac{J_{\text{rot}}(J_{\text{rot}} + 1)\hbar^2}{2\Theta k_B T}\right) \tag{3.14}$$

Similarly, the complete rotational partition function of a homonuclear diatomic molecule is

$$Z^{rn} = Z^r \cdot Z^n = z^r \cdot z^n \cdot z^n = z^r \cdot (z^n)^2 \tag{3.15}$$

$$= (2i + 1)^2 \sum_{J=0}^{\infty} (2J_{\text{rot}} + 1) \exp\left(-\frac{J_{\text{rot}}(J_{\text{rot}} + 1)\hbar^2}{2\Theta k_B T}\right) \tag{3.16}$$

Homonuclear diatomic molecules are divided into *ortho*- and *para*-states, and their nuclear spin degeneracy are:

$$g_{n_o} = (i+1)\,(2i+1) \tag{3.17}$$

$$g_{n_p} = i\,(2i+1) \tag{3.18}$$

with their sum of:

$$g_{n_o} + g_{n_p} = (i+1)(2i+1) + i(2i+1) = g_n^2 \tag{3.19}$$

In the above section, the symmetry of the nuclear spin states of *para*-H_2 and *ortho*-H_2 is discussed. The antisymmetric spin state of *para*-H_2 has even rotational quantum numbers ($J_{\mathrm{rot}} = 0, 2, 4, \ldots$) and the symmetric spin state of *ortho*-H_2 has odd rotational quantum numbers ($J_{\mathrm{rot}} = 1, 3, 5, \ldots$). Therefore, the complete rotational partition function of hydrogen molecules is

$$\begin{aligned} Z^{rn} &= Z_o^{rn} + Z_p^{rn} \\ &= (i+1)\,(2i+1) \sum_{J_{\mathrm{rot}}=1,3,5,\ldots}^{\infty} (2J_{\mathrm{rot}}+1) \exp\left(-\frac{J_{\mathrm{rot}}(J_{\mathrm{rot}}+1)\hbar^2}{2\Theta k_B T}\right) \\ &\quad + i\,(2i+1) \sum_{J_{\mathrm{rot}}=0,2,4,\ldots}^{\infty} (2J_{\mathrm{rot}}+1) \exp\left(-\frac{J_{\mathrm{rot}}(J_{\mathrm{rot}}+1)\hbar^2}{2\Theta k_B T}\right) \\ &= g_{n_o} Z_o^r + g_{n_p} Z_p^r \end{aligned} \tag{3.20}$$

where the rotational partition functions of *ortho*-H_2 and *para*-H_2 are shown as following respectively:

$$Z_o^r = \sum_{J_{\mathrm{rot}}=1,3,5,\ldots}^{\infty} (2J_{\mathrm{rot}}+1) \exp\left(-\frac{J_{\mathrm{rot}}(J_{\mathrm{rot}}+1)\hbar^2}{2\Theta k_B T}\right) \tag{3.21}$$

$$Z_p^r = \sum_{J_{\mathrm{rot}}=0,2,4,\ldots}^{\infty} (2J_{\mathrm{rot}}+1) \exp\left(-\frac{J_{\mathrm{rot}}(J_{\mathrm{rot}}+1)\hbar^2}{2\Theta k_B T}\right) \tag{3.22}$$

By taking the normalized nuclear spin statistical weights with $g'_{n_o} + g'_{n_p} = 1$, the relative regeneracy of *ortho*-H_2 and *para*-H_2 are $g'_{n_o} = \frac{i+1}{2i+1}$, and $g'_{n_p} = \frac{i}{2i+1}$. For hydrogen molecule, $i = \frac{1}{2}$, $g'_{n_o} = \frac{3}{4}$, $g'_{n_p} = \frac{1}{4}$, hence, Equation (3.20) can be rewritten as

$$Z^{rn} = \frac{3}{4} Z_o^r + \frac{1}{4} Z_p^r \tag{3.23}$$

The ratio of *para*-H_2 and *ortho*-H_2 at thermal equilibrium is,

$$\frac{N_p}{N_o} = \frac{g'_{n_p} Z_p^r}{g'_{n_o} Z_o^r} = \frac{Z_p^r}{3 Z_o^r} \tag{3.24}$$

$$= \frac{\sum_{J_{\mathrm{rot}}=0,2,4,\ldots}^{\infty} (2J_{\mathrm{rot}}+1) \exp\left(-\frac{J_{\mathrm{rot}}(J_{\mathrm{rot}}+1)\hbar^2}{2\Theta k_B T}\right)}{3 \sum_{J=1,3,5,\ldots}^{\infty} (2J_{\mathrm{rot}}+1) \exp\left(-\frac{J_{\mathrm{rot}}(J_{\mathrm{rot}}+1)\hbar^2}{2\Theta k_B T}\right)} \tag{3.25}$$

Therefore, hydrogen can be taken as a binary mixture of two different species of molecules (*para*-H_2 and *ortho*-H_2) with different physical properties and their equilibrium ratio in this

mixture is temperature dependent. The calculation of the terms in Equation (3.25) reveals the relationship between the percentages of the two isomers (*para*-H_2 and *ortho*-H_2) in hydrogen gas at equilibrium, as a function of temperature. As shown in Figure 3.2, the equilibrium ratio of the *para*-H_2 and *ortho*-H_2 concentrations in the hydrogen gas mixture is approximately 0.25 : 0.75 at elevated temperature ($T > 300$ K). This mixture is named as "normal hydrogen". At liquid nitrogen temperature (77 K), more than half (52.28 %) of the hydrogen molecules is *para*-H_2. With the temperature cooling down to 23 K, the enrichment of *para*-H_2 exceeds 99%.

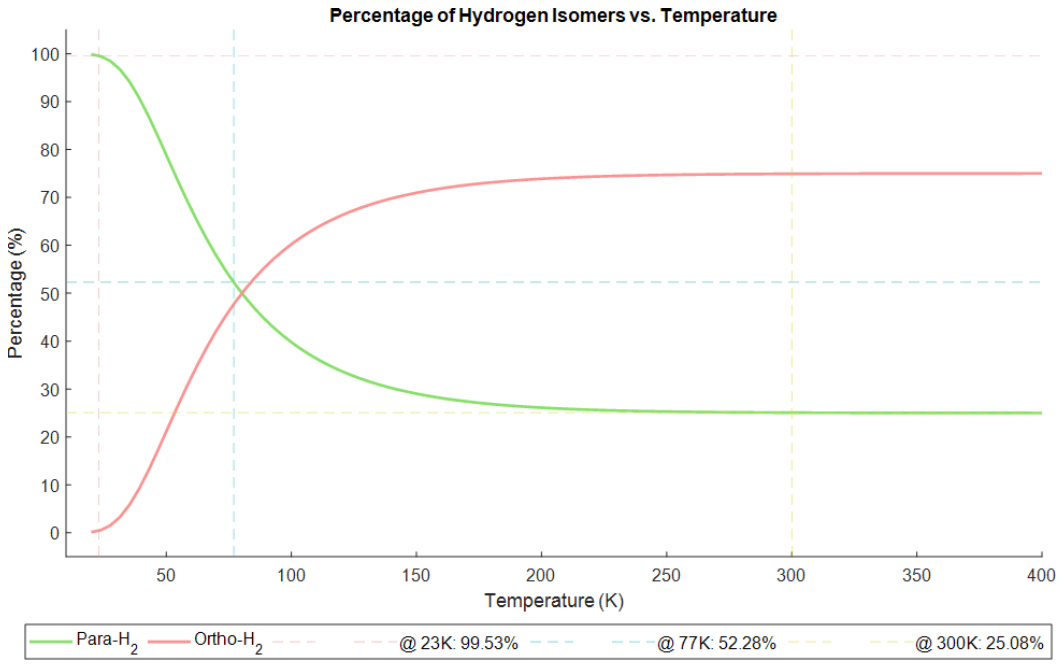

Figure 3.2: Equilibrium percentage of *para*-H_2 as a function of temperature. More details of the calculation in MATLAB can be found in Appendix A.1.

3.3.4 Laboratory apparatus for parahydrogen enrichment

Since *para*-H_2 is in a lower energy state compared to *ortho*-H_2, there is a slow spontaneous transition from *ortho*-H_2 to *para*-H_2 when the temperature decreases (Figure 3.2). This slow transformation from ortho-H_2 to para-H_2 is driven exclusively by weak perturbations involving nuclear spin interactions. Nevertheless, this interconversion process can be effectively accelerated in the presence of a proper catalyst. Normal hydrogen gas, when cooled with liquid nitrogen and catalyzed by active charcoal or iron (III) oxide catalyst (or other ferromagnetic materials), can achieve a 50% enrichment of *para*-H_2. By further cooling to 22 K with a cryogenic system (Figure 3.3), the enrichment of *para*-H_2 can exceed 98%.

The procedure for generating *para*-H_2 in the laboratory involves using a commercial water-cooled helium compressor (ARS-4HW Compressor, USA) as the cooling source for the cryostat (cold head). A vacuum pump evacuates the remaining air from the chamber of the cold head to accelerate the cooling process. A PID controller monitors the temperature in real

time and precisely maintains the target temperature in the cold head during the *para*-H_2 collection process. Normal hydrogen gas flows along the pipeline with an appropriate flow rate (0.5 L/min) controlled by a mass flow controller. After contact with the paramagnetic hydrated Iron (III) oxide catalyst ($Fe_2O_3 \cdot H_2O$) in the chamber at the bottom of the cold head, *para*-H_2 gas is generated and collected within an aluminum gas bottle.

Figure 3.3: *para*-H_2 enrichment apparatus in laboratory. **(a)** Helium compressor with PID controller on the top. **(b)** Control unit of mass flow controller. **(c)** Vacuum pump. **(d)** Gas cabinet for *para*-H_2 collection. Right bottom: cryostat (cold head).

3.4 Parahydrogen Induced Polarization

Since quantum mechanics was first established in the 1920s, the properties of dihydrogen have been accurately predicted. This including correct calculation of the heat capacities of hydrogen, which aligning theoretical predictions closely with experimental results. [91, 92, 93]

In 1986, Weitekamp et al. [94, 95] introduced a groundbreaking concept involving dihydrogen: transferring *para*-H_2 into unsaturated molecules through hydrogenation could significantly enhance NMR signals. Prior to this proposal, researchers in organometallic chemistry had already observed anomalous NMR spectra when they stored their samples in liquid nitrogen overnight. These samples, which were intended for studies on hydrogenation reactions of organometallic complexes, retained unusual spectral characteristics, likely due to the preservation of high levels of *para*-H_2 under cryogenic conditions. This phenomenon was only later understood and exploited in NMR spectroscopy following Weitekamp's insights.

Before introducing the signal enhancement of PHIP, the case where normal hydrogen is

used for the hydrogenation reaction is first discussed, focusing on the resulting NMR spectrum and signal enhancement.

In the absence of a magnetic field, the energy levels of the four spin states of normal hydrogen, with wave functions $|S_0\rangle$, $|T_+\rangle$, $|T_0\rangle$, and $|T_-\rangle$, are degenerate at the same energy level and each possesses an equal population of $P_0 = 25\%$ (Figure 3.4**a**). By applying a non-zero static magnetic field, the energy level of $|T_+\rangle = |\alpha\alpha\rangle$ is decreased by δ and $|T_-\rangle = |\beta\beta\rangle$ increases the energy level with the same amount of δ, hence, the population of $|T_+\rangle$ and $|T_-\rangle$ gains and looses with the amount proportional to δ due to the Boltzmann distribution. However, the population of the two states $|S_0\rangle$ and $|T_0\rangle$ with linear combinations of $|\alpha\beta\rangle$ and $|\beta\alpha\rangle$ remains the same (Figure 3.4**b**).

In this case, there's no transition between singlet and triplet spin states (more details can be found in Chapter 2.7.1), thus the population P_0 in *para*-H_2 is trapped. As a consequence, the singlet state of *para*-H_2 renders NMR silence. However, in the triplet spin states of *ortho*-H_2, there are two energy gaps with the transition probability proportional to 2δ and this yields the total NMR spectrum of *ortho*-H_2 with intensity of 4δ. Here should be noticed, the value of δ/P_0 is very small and only in the order of $\sim 10^{-5}$ at room temperature and 11.7 T field.

After hydrogenation of the normal hydrogen on unsaturated bonds, the symmetry of dihydrogen is broken and forms a AX-spin system (Figure 3.4**c**). The four spin states $|\alpha\alpha\rangle$, $|\alpha\beta\rangle$, $|\beta\alpha\rangle$, and $|\beta\beta\rangle$ are equally distributed, and there are four energy transitions with the same probability proportional to δ. Therefore, the generated spectrum of the formed AX-spin system are two doublets at the two chemical shifts of nuclei A (ν_A) and X (ν_X) with the corresponding J-coupling constant of J_{AX}, the ratio of the intensity of the four peaks is 1:1:1:1.

3.4.1 Parahydrogen And Synthesis Allow Dramatically Enhanced Nuclear Alignment (PASADENA)

As mentioned in the previous section, *para*-H_2 can be enriched by cooling normal hydrogen in the presence of an appropriate catalyst. Therefore, the populations of enriched-*para*-H_2 and *ortho*-H_2 in hydrogen are $P_0 + \Delta$ and $3P_0 - \Delta$, respectively. Here, $P_0 = 0.25$ is the equal population fraction of the four spin states in normal hydrogen gas, and Δ is an excess population generated from conversion of *ortho*-H_2 to *para*-H_2. As a consequence, Δ is related to temperature ($\Delta/P_0 \in [0, 3]$ when $T \in [300\text{ K}, 0\text{ K}]$). At liquid nitrogen temperature (77 K), the value of the ratio Δ/P_0 is approximately 1. Upon further cooling to 23 K, this ratio increases to approximately 3, corresponding to enrichment of more than 99% *para*-H_2.

Without applying a magnetic field, the singlet spin state of *para*-H_2, with a population of $P_0 + \Delta$, and the three triplet spin states of *ortho*-H_2, each with a population of $P_0 - \Delta/3$, are depicted in Figure 3.5**a**.

In the presence of a static magnetic field, the energy levels are no longer degenerate. The

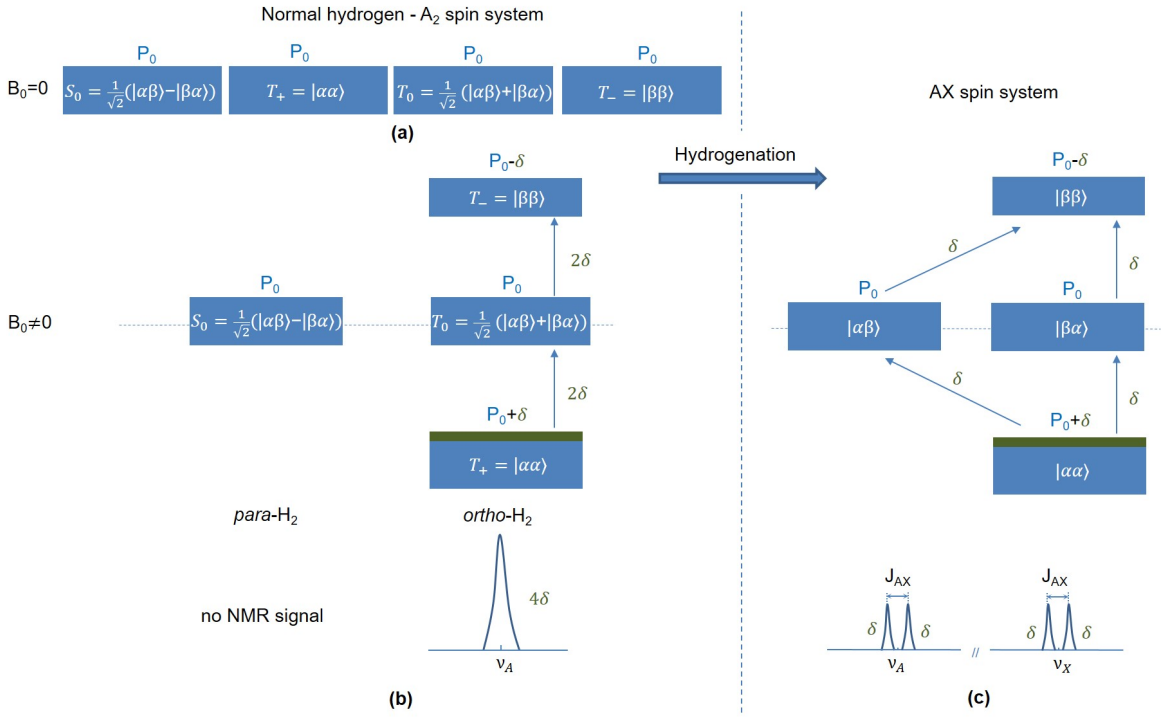

Figure 3.4: Population for the spin states of normal hydrogen gas with a A_2-spin system and of a AX-spin system after hydrogenation. (**a**) At zero magnetic field, all the four states have the same energy level and same population. (**b**) At non-zero field, the energy levels of the triplet states splits in three different levels, the population of $|S_0\rangle$ and $|T_0\rangle$ remain unchanged, but $|T_+\rangle$ and $|T_-\rangle$ increased and decrease with the amount of δ respectively. (**c**) The formed AX spin system after hydrogenation of normal hydrogen. The four transitions in this AX system yield 4 peaks two chemical shift ν_A and ν_X with the J-coupling constant of J_{AX} and equal signal intensities proportional to δ.

population of the spin states $|T_+\rangle$ and $|T_-\rangle$ increases and decreases with the amount of δ' ($\delta' < \delta$) respectively by taking the population of $|T_0\rangle$ as a reference (Figure 3.5**b**). Given that the hydrogenation of *para*-H_2 enriched hydrogen on unsaturated C=C bonds under high-field conditions, the spin states of $|\alpha\beta\rangle$ and $|\beta\alpha\rangle$ in the formed AX-spin system are significantly overpopulated, which benefits from the hyperpolarized singlet spin states $|S_0\rangle$ of *para*-H_2. The transitions of $|\alpha\beta\rangle \rightarrow |\beta\beta\rangle$ and $|\beta\alpha\rangle \rightarrow |\beta\beta\rangle$ generate two enhanced absorption peaks, while the transitions from the two overpopulated states back to the ground state $|\alpha\alpha\rangle$ showcase two enhanced emission peaks. As a results, the four transitions in this AX system yield two antiphased doublets at two chemical shift ν_A and ν_X with the J-coupling constant of J_{AX}. As depicted in Figure 3.5**c**, the intensities of the four peaks are proportional to $2\Delta/3 \pm \delta'$. The enhancement compared to the spectrum of after hydrogenation of normal hydrogen can be up to 20,000 folds when using nearly 100% enriched *para*-H_2 ($\Delta/P_0 \approx 3$).

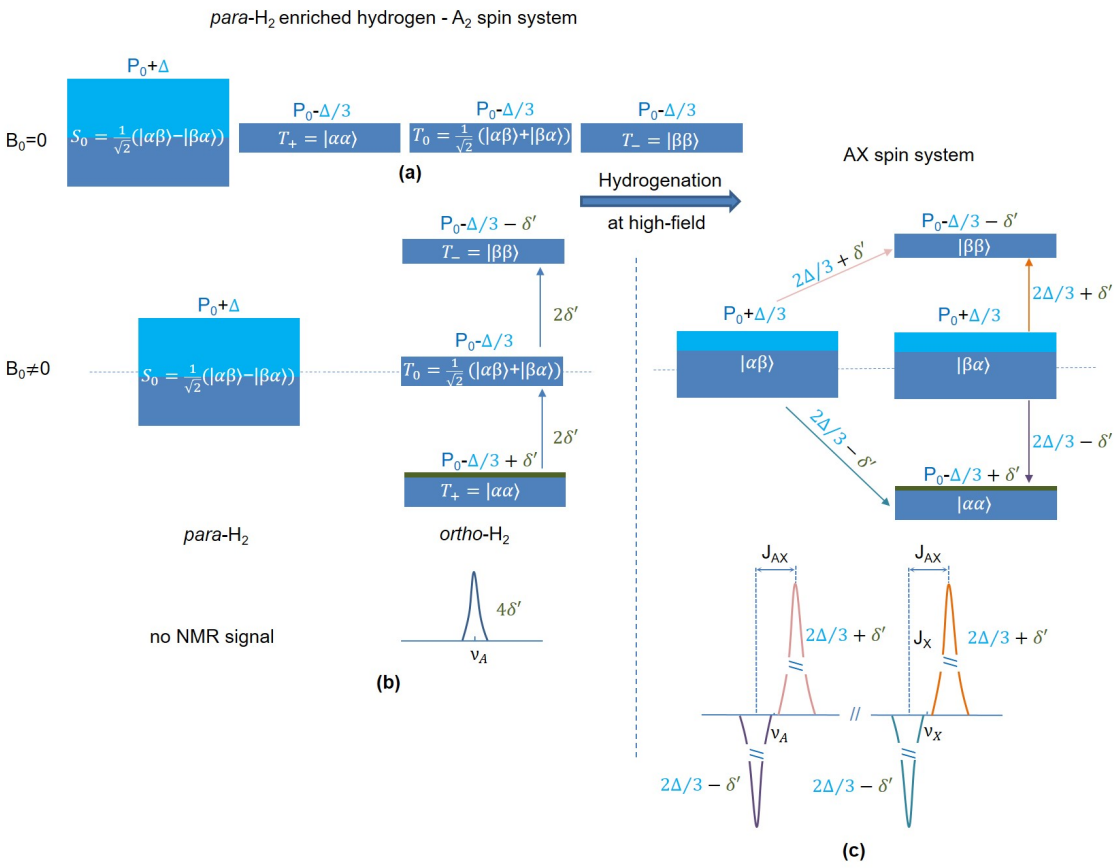

Figure 3.5: Population for the spin states of *para*-H_2 enriched hydrogen gas with a A_2-spin system and of a AX-spin system after hydrogenation (PASADENA protocol). **(a)** At zero magnetic field, all the four states have the same energy level. The singlet spin states of *para*-H_2 is overpopulated with an excess of Δ after enrichment. As a consequence of conversion, each spin states of triplet processes the population of P_0-$\frac{1}{3}\Delta$. **(b)** At non-zero field, the energy levels of the triplet states split in three different levels. By taking the population of the spin state $|T_0\rangle$ as a reference, the population of $|T_+\rangle$ and $|T_-\rangle$ increased and decrease with the amount of δ' respectively. δ' is smaller than δ in Figure 3.4 with the relationship $\delta'/\delta = (P_0 - \frac{1}{3}\Delta)/P_0$. **(c)** The formed AX spin system after hydrogenation of the *para*-H_2 enriched hydrogen at high-field (PASADENA). The two spin states of $|\alpha\beta\rangle$ and $|\beta\alpha\rangle$ overpopulated with the non-thermal equilibrium population of P_0+$\frac{1}{3}\Delta$. The four allowed energetic transitions in the AX-spin system and the generated spectrum represents two antiphased doublets with enhanced intensities proportional to $\frac{2}{3}\Delta \pm \delta'$.

3.4.2 Adiabatic Longitudinal Transport After Dissociation Engenders Nuclear Alignment (ALTADENA)

This section discusses another situation of PHIP, in which the hydrogenation of *para*-H_2 performed at low-field conditions, such as the Earth's magnetic field or even weaker. In these scenarios, the J-coupling between the two spins in the products is in the same order of magnitude as their chemical shift difference ($J \sim \nu_A - \nu_B$). As a result, the two spins are strongly coupled and exhibit coherence (correlation).

Considering a simple situation of molecular addition of 100% *para*-H_2 with singlet spin states $((|\beta\alpha\rangle - |\alpha\beta\rangle)/\sqrt{2})$ at low-field, the generated hydrogenated products are populated with the singlet character (Figure 3.6). With adiabatically transport the sample to a subsequent high-field for NMR signal detection, or under the adiabatic conditions, the gradual change in the external magnetic field allows the field-dependent eigenstates of the system to adapt to the evolving field. This ensures that the quantum state of the system evolves smoothly along with the changes, without losing coherence between spin states.

As a consequence of the conditions described, the singlet-like low-field spin states of the hydrogenated AX-spin system are adiabatically transferred into one high-field spin state, which is restricted to either $|\alpha\beta\rangle$ or $|\beta\alpha\rangle$ (Figure 3.6**a**). This process leads to two possible transitions of the occupied spin states to the spin states $|\alpha\alpha\rangle$ and $|\beta\beta\rangle$, corresponding to emissive and absorptive peaks respectively (Figure 3.6**b**). Under ALTADENA conditions, the overpopulated spin state allows only one spin to emit while the other absorbs, which results in two antiphase peaks with greater intensity compared to PASADENA. [96]

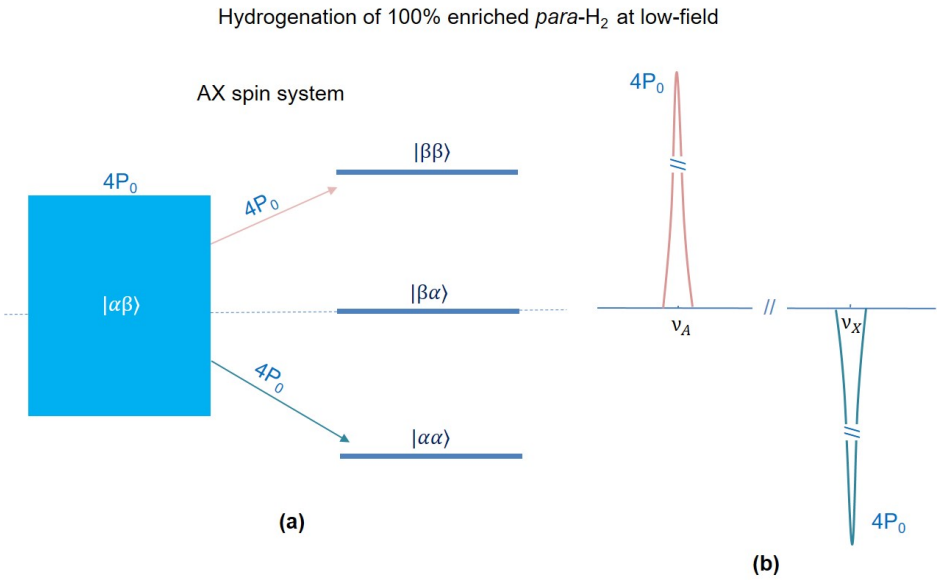

Figure 3.6: Population of the hydrogenative products spin states under condition of ALTADENA. **(a)** After molecular addition of 100% para-H_2 at low-field, the spin state $|\alpha\beta\rangle$ in the hydrogenated AX-spin system becomes populated with a relative population of $4P_0$. This allows only the spin of nucleus A to absorb and the spin of nucleus X to emit. **(b)** The generates two intense peaks at each chemical shift with opposite amplitudes.

3.5 Signal Amplification By Reversible Exchange

In PHIP method, *para*-H_2 molecules are chemically and pairwisely introduced into an unsaturated precursor via a hydrogenation reaction, thereby the magnetic asymmetry of the dihydride derived from *para*-H_2 on the products release the overpopulated latent spin order from *para*-H_2. However, the need for a suitable precursor with unsaturated bonds, or

the chemical modification from the perspective of the substrates limit the applications of PHIP techniques. In 2009, a subclass of PHIP methods terms in SABRE was discovered and developed. [97, 98]

SABRE works through the formation of a temporary complex involving *para*-H_2, the target substrate, and a transient metal catalyst, which facilitates the scalar coupling network between *para*-H_2 and the to-be-polarized nuclei in the target substrate. As a derivative of PHIP, SABRE has shown considerable potential in extending the range of applications for PHIP methodologies, including SABRE-RELAY for different molecular scaffolds [24, 99, 100], SABRE-SHEATH for different heteronuclei [26, 27, 101]. This section describes the catalytic cycle for the reversible mechanism in SABRE and the explains the formation of Level Anti-Crossings (LACs) for spin order transfer in SABRE.

3.5.1 Catalytic cycle in SABRE hyperpolarization

SABRE was discovered by investigating Crabtree's catalyst [Ir(COD)(PCy_3)(Py)][BF_4] (COD = cyclooctadiene; PCy_3 = tricyclohexylphosphine; Py = pyridine) for direct hyperpolarization under low magnetic field conditions [102]. Besides, this study also investigated into various phosphine ligands to elucidate the correlation between the signal enhancement of pyridine. It was revealed that employing phosphines such as PCy_2Ph and PCy_3, which possess both strong electron-donating capabilities and substantial steric bulk, leads to increased signal enhancement of free pyridine in bulk solution. With Crabtree's catalyst, the active polarization transfer catalyst fac,cis-[$Ir(H)_2(PCy_3)(Py)_3$][BF_4] is temporary formed upon the addition of *para*-H_2 and pyridine. [97] Thus, the symmetry of the two nascent hydrides derived from *para*-H_2 is broken and allows for the singlet-triplet spin state interconversion. The use of a low magnetic field in SABRE is essential because it reduces the chemical shift difference between the coupled nuclei (typically between the hydrides and the in-plane ligand nuclei) to the same order of magnitude as the scalar coupling constant. This condition leads to a strong coupling regime, which facilitates coherent polarization transfer within the spin network, and therefore enhances hyperpolarization efficiency. [103]

The other commonly used homogeneous SABRE pre-catalyst is [IrCl(COD)(IMes)] (IMes = 1,3-bis(2,4,6-trimethylphenyl)-imidazole-2-ylidene; COD = 1,5-cyclooctadiene) (**(1)** in Figure 3.7), in which the phosphine ligand is substituted with an N-Heterocyclic Carbene (NHC) ligand IMes with stronger electron-donating property [104]. The Ir-IMes catalyst has been established as the optimal SABRE catalyst, achieving the high efficiency in the polarization of pyridine and various pyridine derivatives, and is often referred to as the standard SABRE pre-catalyst. [104, 15] The following content of this subsequent section will explore the chemical mechanisms involved in typical SABRE hyperpolarization processes.

Generally, the SABRE experiments start with the activation process of this pre-catalyst. Figure 3.7 depicts the formation of the SABRE active complex for polarization transfer [97].

Firstly, the SABRE sample stock solution is prepared under Argon gas atmosphere and

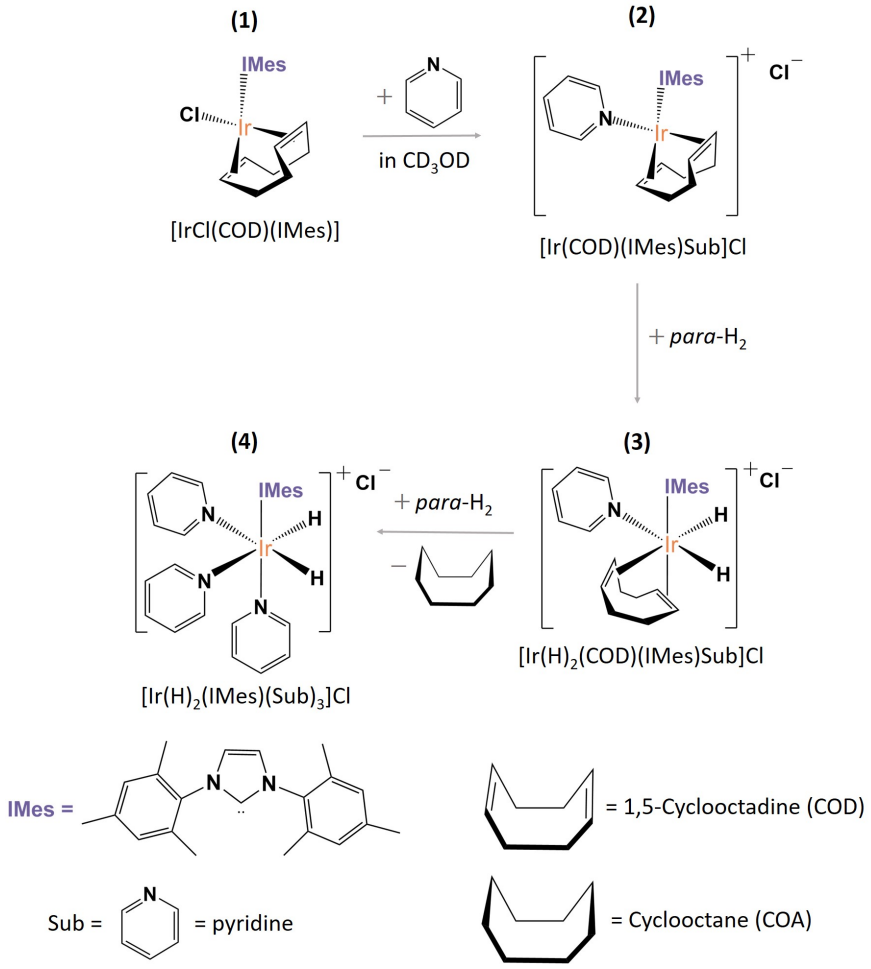

Figure 3.7: Scheme of the activation mechanism of the SABRE precatalyst **(1)** ([IrCl(COD)(IMes)]). The activation process start with a typical SABRE stock solution contains **(1)** and the substrate dissolved in the degassed methanol-d_4 solution. By bubbling H_2 in the stock solution, complex **(2)** forms an intermediate complex **(3)**. **(4)** Completely activated SABRE complex.

it contains the pre-catalyst **(1)**, the target substrate (here is pyridine) and three pump-freeze-thaw cycles degassed methanol-d_4 as solvent. By bubbling normal H_2 or fresh *para*-H_2 into the sample solution, the two hydrides originate from H_2 bind to the Ir-center results in conversion from complex **(2)** to **(3)** with an octahedral structure. With even longer bubbling of hydrogen, COD is further hydrogenated and forms COA, which is not stable within the Ir-complex and dissociates from the catalyst. Two more substrate molecules bind to the catalyst and forms the SABRE active complex **(4)**. With fresh *para*-H_2 dissolved in the activated sample solution, the polarization is propagated to the nuclei on the target substrate via the formed J-coupling networks between the two hydrides and the substrates on the equatorial plane of the complex **(4)**.

The catalytic cycle for propagating hyperpolarization from *para*-H_2-derived hydrides to the target substrates and the reversible binding process of them are shown in Figure 3.8. The activated SABRE complex **(4)** facilitates the J-coupling network between the two hydrides and

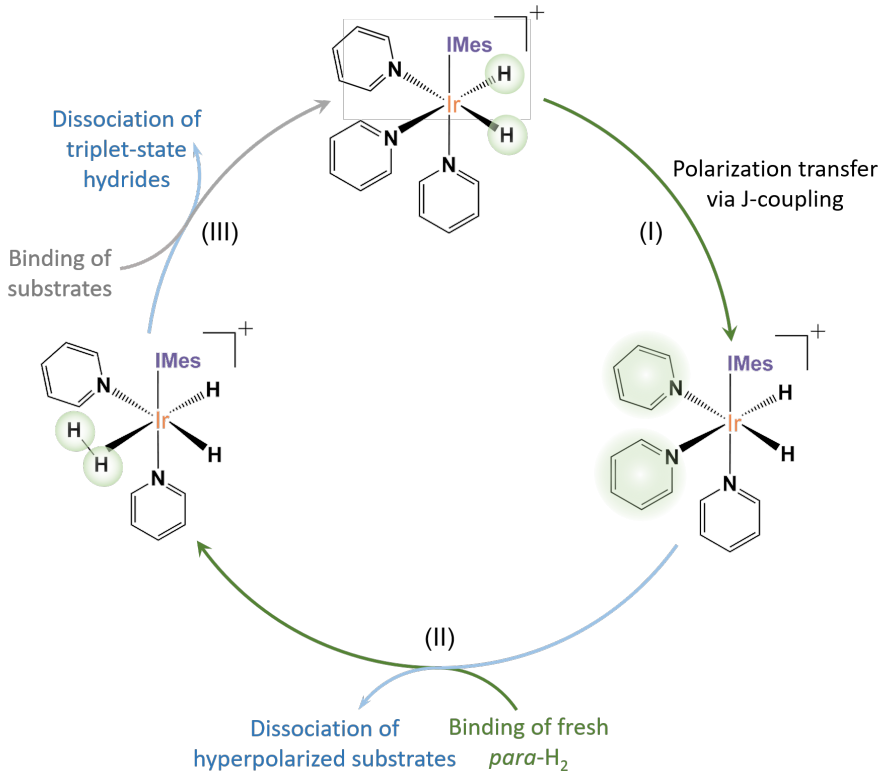

Figure 3.8: Schematic diagram of the catalytic cycle in SABRE hyperpolarization. The cycle can be divided in three stages. (I) Polarized spin orders from the hydrides are transferred to the substrates on the equatorial plane through the J-coupling network. (II) The hyperpolarized substrates with boosted magnetization dissociate from the catalyst, and form the free substrates in solution without chemical modification. The vacant position is then bound with *para*-H_2. (III) Dissociation of the hydrides, and binding of thermal equilibrium substrates for rehyperpolarization.

the equatorial substrates at low-field. In this J-coupling network, the different *cis* and *trans* J-couplings across the metal center break hydride symmetry, resulting in a coherent polarization transfer from *para*-H_2-derived hydrides to the nuclei of the substrates. Subsequently, the hyperpolarized catalyst-bound substrates dissociate into the solution, forming free hyperpolarized substrates with enhanced NMR signal intensity. The vacant site is then bound with fresh *para*-H_2 molecule with singlet spin state, follows by the exchange of the triplet-state hydrides and the thermal equilibrium substrate for completing the cycle for rehyperpolarization. Hence, SABRE allows for continuous hyperpolarization as long as replenishing the sample with fresh *para*-H_2.

3.5.2 Mechanisms of polarization transfer in SABRE

With the development of SABRE technology, two theory methods have been established to explain the mechanism of polarization transfer across spins in SABRE. These theory methods are density matrix theory and Level Anti-Crossings (LACs).

3.5.2.1 Density matrix theory and its limitations

SABRE was initially conceptualized by Adams et al. [105] using density matrix theory, based on a four-spin system comprising two hydride spins derived from the para-H_2 molecule and two additional spins originating from nuclei on the bound substrate. According to this theoretical framework, the process of polarization transfer and the measurement of the hyperpolarized sample are segmented into three distinct phases.

The initial phase includes the formation of the metal-organic complex and the consequent evolution of the four-spin system containing ^{1}H nuclei originating from *para*-H_2 and the ligated target substrates at a mixing field. This mixing field is typically low-field with strength < 250 mT. The second phase spans from the disassociation of the hyperpolarized substrate from the complex, and the two-spin system on the free substrates continue to evolve at the mixing field until the sample is transferred into the magnet of the NMR spectrometer. The final stage extends from this point until the sample reaches the detection area with static magnetic field. Throughout the experiment, the magnetic field strength undergoes a dramatic increase from the spin mixing field to the measurement field, following a diabatic transition.

The density matrix formalism enables the modeling of the time evolution of nuclear spin systems during polarization transfer. It accounts for the effects of J-couplings, chemical exchange, and relaxation processes, providing a quantitative description of how the singlet spin order of parahydrogen is converted into observable magnetization on the target nuclei [106, 107, 108, 105].

Despite these advantages, the density matrix approach is often simplified and truncated in practical implementations to maintain computational tractability. Such simplifications may neglect coupling terms and spin interactions that, although subtle, can be critical—especially under varying magnetic field conditions, ultimately preventing an accurate capture of the sign changes observed in the SABRE signal.

3.5.2.2 Level Anti-Crossings and the role of J-coupling

In recent years, an alternative theoretical framework based on Level Anti-Crossings (LACs) has provided valuable insight into the spontaneous polarization transfer process in SABRE [109, 103]. Unlike the density matrix approach, the LAC model offers a more intuitive and physically transparent picture of energy-level interactions, particularly under low-field conditions, making it a useful complementary tool for understanding SABRE dynamics.

The concept of LAC, also referred to as "avoided crossing" in the literature, is foundational in the field of quantum mechanics and has played a crucial role in shaping the understanding of quantum systems. This phenomenon was first observed and discussed in the early 20th century, during the broader investigation into the quantum properties of atoms and molecules. LAC refers to a phenomenon where energy levels in a quantum system, which would typically intersect when a parameter such as a magnetic or electric field is varied, instead seem to repel each other and avoid intersecting. This behavior is observed in plots of energy versus the parameter, illustrating the quantum mechanical non-crossing rule. [110] This effect of LAC

is a direct consequence of the system's underlying quantum mechanical interactions and is particularly prominent in systems where there are non-negligible interactions or couplings between different states.

For simplicity, a two-level system is considered to illustrate how perturbations in a two-state Hamiltonian manifest as avoided crossings. The two-state Hamiltonian can be written as follows:

$$\hat{\mathcal{H}} = |\Psi_a\rangle \mathcal{E}_a \langle\Psi_a| + |\Psi_b\rangle \mathcal{E}_b \langle\Psi_b| \tag{3.26}$$

$$= \begin{pmatrix} \mathcal{E}_a & 0 \\ 0 & \mathcal{E}_b \end{pmatrix} \tag{3.27}$$

in which $\mathcal{E}_a$ and $\mathcal{E}_b$ are the eigenvalues. The two eigenvectors $\begin{pmatrix} 1 \\ 0 \end{pmatrix}$ and $\begin{pmatrix} 0 \\ 1 \end{pmatrix}$ denoted the two states of the system. If $\mathcal{E}_a$ equals $\mathcal{E}_b$ at a point, the two energy levels are crossed termed as Level Crossing (LC). In this situation, the Hamiltonian exhibits a twofold degeneracy, and any superposition of the degenerate eigenstates also serves as an eigenstate of the Hamiltonian. Consequently, a system prepared in any of these states will remain in that state indefinitely. However, when the states interact through coupling $\hat{\mathcal{V}}$, the matrix elements of the Hamiltonian are "perturbed". For the sake of simplification, the coupling effect is Hermitian and affects only the off-diagonal elements of the Hamiltonian matrix.

$$\hat{\mathcal{V}} = |\Psi_a\rangle \mathcal{V}_{ab} \langle\Psi_b| + |\Psi_b\rangle \mathcal{V}_{ba} \langle\Psi_a| \tag{3.28}$$

$$= \begin{pmatrix} 0 & \mathcal{V}_{ab} \\ \mathcal{V}_{ab}^* & 0 \end{pmatrix} \tag{3.29}$$

where $\mathcal{V}_{ab} = \mathcal{V}_{ba}^* = \mathcal{V}e^{-i\varphi}$. Given that the overall Hamiltonian must remain Hermitian, the revised Hamiltonian can be succinctly expressed as follows:

$$\hat{\mathcal{H}}' = \hat{\mathcal{H}} + \hat{\mathcal{V}} \tag{3.30}$$

$$= \begin{pmatrix} \mathcal{E}_a & 0 \\ 0 & \mathcal{E}_b \end{pmatrix} + \begin{pmatrix} 0 & \mathcal{V}e^{-i\varphi} \\ \mathcal{V}e^{+i\varphi} & 0 \end{pmatrix} \tag{3.31}$$

$$= \begin{pmatrix} \mathcal{E}_a & \mathcal{V}e^{-i\varphi} \\ \mathcal{V}e^{+i\varphi} & \mathcal{E}_b \end{pmatrix} \tag{3.32}$$

where $\hat{\mathcal{V}}$ is Hermitian fixes its off-diagonal components. The coupling are often real and the phase φ can be neglected. Therefore, the actual state energies $\mathcal{E}_+$ and $\mathcal{E}_-$, i.e., the eigenvalues of the modified Hamiltonian can be determined by diagonalising $\hat{\mathcal{H}}'$. Consequently, the following equation is derived for solving the actual energy $\mathcal{E}$:

$$\begin{vmatrix} \mathcal{E} - \mathcal{E}_a & \mathcal{V} \\ \mathcal{V} & \mathcal{E} - \mathcal{E}_b \end{vmatrix} = 0 \tag{3.33}$$

and the two energies are

$$\mathcal{E}_+ = \frac{1}{2}(\mathcal{E}_a + \mathcal{E}_b) + \frac{1}{2}\sqrt{(\mathcal{E}_a - \mathcal{E}_b)^2 + 4\mathcal{V}^2} \tag{3.34}$$

$$\mathcal{E}_- = \frac{1}{2}(\mathcal{E}_a + \mathcal{E}_b) - \frac{1}{2}\sqrt{(\mathcal{E}_a - \mathcal{E}_b)^2 + 4\mathcal{V}^2} \tag{3.35}$$

By plotting the curve of the actual energies and the half of the difference between the two original energy values $(\mathcal{E}_a - \mathcal{E}_b)/2$, two branches of a hyperbola are avoided crossing shown in Figure 3.9 illustrate the LAC effect.

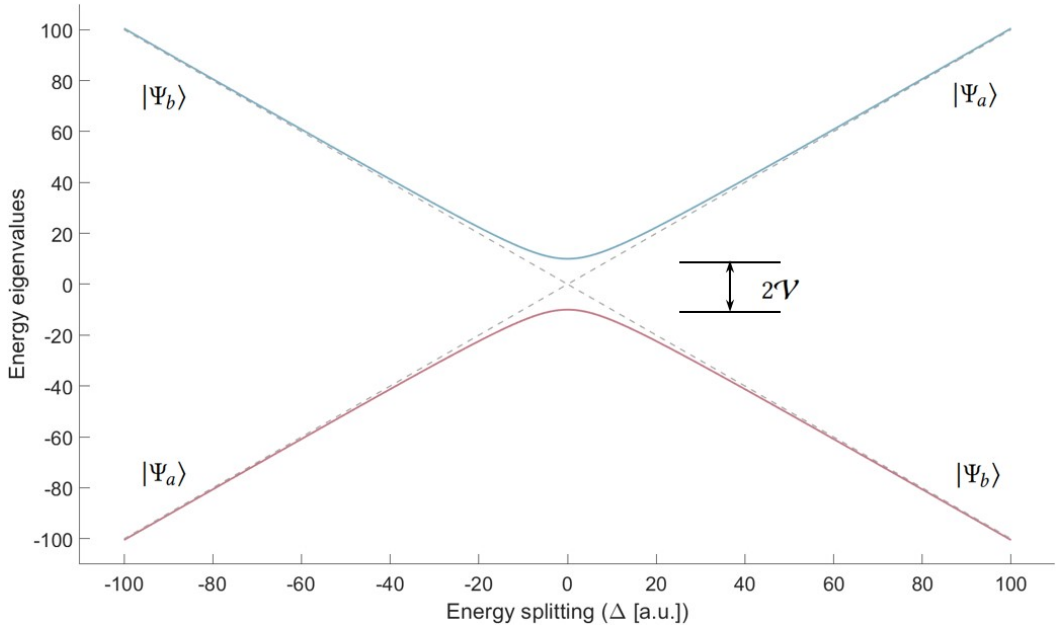

Figure 3.9: Schematic illustration of LC and LAC of a two-level system. If there is no the perturbation $\hat{\mathcal{V}} = 0$, the two energy states will cross and degenerate (dashed lines). By the presence of a small "perturbation" $\hat{\mathcal{V}} \neq 0$, the two levels repel each other with distance of $2\mathcal{V}$ instead of crossing (solid lines).

The two energy states $|\Psi_a\rangle$ and $|\Psi_b\rangle$ of the "unperturbed" Hamiltonian $\hat{\mathcal{H}}$ with their corresponding energies of $\mathcal{E}_a$ and $\mathcal{E}_b$ can cross at a point. However, with the coupling $\hat{\mathcal{V}}$, the the actual eigenstates $\mathcal{E}_+$ and $\mathcal{E}_-$ are no longer equal and remain split by the strength of interaction $2\mathcal{V}$. The curves of the energies asymptotically approaches the original unperturbed energy levels. Here, the energy splitting Δ and the mean energy $\overline{E}$ and the are defined as following:

$$\Delta = \frac{\mathcal{E}_a - \mathcal{E}_b}{2} \tag{3.36}$$

$$\overline{E} = \frac{\mathcal{E}_a + \mathcal{E}_b}{2} \tag{3.37}$$

By substituting Δ and $\overline{E}$ in Equation (3.34) and (3.35), the following results can be obtained:

$$\mathcal{E}_\pm = \overline{E} \pm \sqrt{\Delta^2 + \mathcal{V}^2} \tag{3.38}$$

To simplify the above equation, another variable Ω is defined as:

$$\Omega = \sqrt{\Delta^2 + \mathcal{V}^2} \tag{3.39}$$

Therefore, Equation (3.38) represents the eigenvalues of the Hamiltonian $\hat{\mathcal{H}}'$ can be rewritten as:

$$\mathcal{E}_\pm = \overline{E} \pm \Omega \tag{3.40}$$

To understand the coupling effect in LAC, another variable termed mixing angle θ of LAC is defined as:

$$\tan 2\theta = \frac{\mathcal{V}}{\Delta} \tag{3.41}$$

and it describes the relative magnitude of the coupling and the energy splitting. The relationship of $\mathcal{V}$, Δ, $\overline{E}$, Ω, and θ are shown in Figure 3.10. The value of mixing angle θ is in range of $0 \leq \theta \leq \frac{\pi}{4}$.

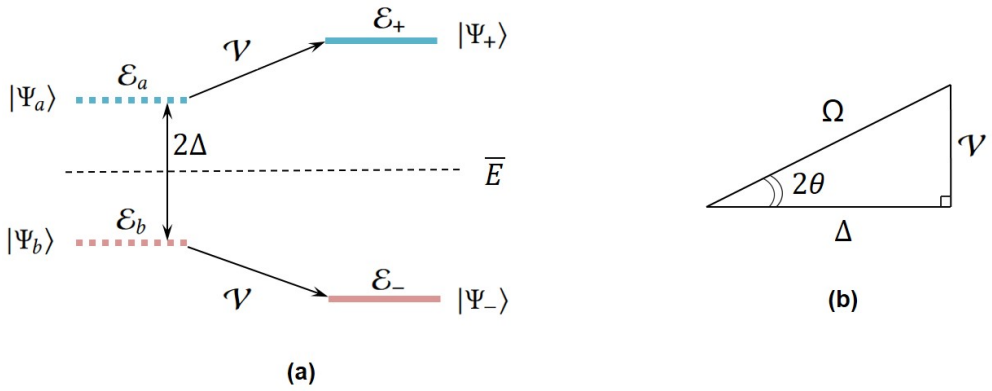

Figure 3.10: Representation of the coupling effect. **(a)** Relationship of the zero-order states and the eigenstates of Hamiltonian $\hat{\mathcal{H}}'$. The coupling brings the spin system to LAC and mixing the two zero-order, leading to two eigenstates $|\Psi_+\rangle$ and $|\Psi_-\rangle$ with their corresponding eigenvalues of $\mathcal{E}_+$ and $\mathcal{E}_-$. **(b)** Relationship of the mixing angle θ, the coupling $\mathcal{V}$, the energy splitting Δ.

It is important to emphasize that the coupling between spin states is critical for effective coherent mixing, which facilitates polarization transfer at LACs. To rationalize this, understanding the eigenstates of the full Hamiltonian is necessary. The two eigenstates corresponding to the energy levels $|\Psi_+\rangle$ and $|\Psi_-\rangle$ are superposition states of $|\Psi_a\rangle$ and $|\Psi_b\rangle$:

$$|\Psi_\pm\rangle = c_a\,|\Psi_a\rangle \pm c_b\,|\Psi_b\rangle \tag{3.42}$$

where, c_a and c_a are the mixing coefficients at the region of LAC. This equation can be written in matrix form as

$$\begin{pmatrix} \mathcal{E}_+ \\ \mathcal{E}_- \end{pmatrix} = S \begin{pmatrix} \mathcal{E}_a \\ \mathcal{E}_b \end{pmatrix} \tag{3.43}$$

where S is the transformation that diagonalizes the Hamiltonian and which transforms the coefficients of the wavefunction from the zero-order basis to the eigenbasis. By substitution Equation (3.43) in Schrödinger's equation $\hat{\mathcal{H}}'\,|\Psi\rangle_\pm = \mathcal{E}_\pm\,|\Psi\rangle_\pm$, the transformation S is obtained as:

$$S = \begin{pmatrix} \cos\theta e^{-i\varphi/2} & \sin\theta e^{i\varphi/2} \\ -\sin\theta e^{-i\varphi/2} & \cos\theta e^{i\varphi/2} \end{pmatrix} \tag{3.44}$$

Hence, the eigenstates of the full Hamiltonian $\hat{\mathcal{H}}'$ are

$$|\Psi_+\rangle = c_a\,|\Psi_a\rangle + c_b\,|\Psi_b\rangle = \cos\theta\,|\Psi_a\rangle + \sin\theta\,|\Psi_b\rangle \tag{3.45}$$

$$|\Psi_-\rangle = -c_b\,|\Psi_a\rangle + c_a\,|\Psi_b\rangle = -\sin\theta\,|\Psi_a\rangle + \cos\theta\,|\Psi_b\rangle \tag{3.46}$$

where $c_a = \cos\theta$ and $c_b = \sin\theta$. The mixing coefficients $|c_a|^2$ and $|c_b|^2$ change upon the energy splitting Δ are shown in Figure 3.11.

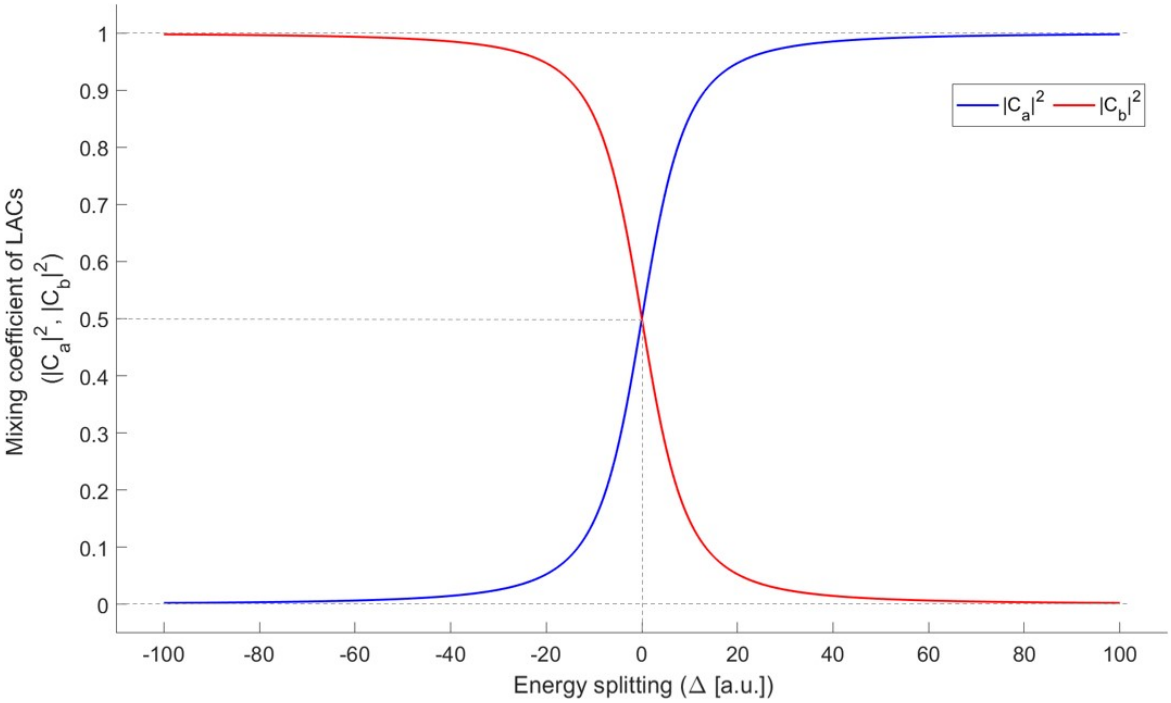

Figure 3.11: Mixing coefficients $|c_a|^2$ and $|c_b|^2$ of LAC in a two-level system. When the system is far away from the LAC region, one of the mixing coefficients turns to 1 and the other goes to 0.

When the mixing angle θ is zero, the perturbation term $\mathcal{V}$ (i.e., the coupling) is also zero, and the states $|\Psi_a\rangle$ and $|\Psi_b\rangle$ are the two eigenstates of the system. In this case, the energy levels can cross when their eigenvalues are equal. This situation is referred to as LC and is schematically represented by dashed lines in Figure 3.9.

However, in the case of LAC, the coupling $\mathcal{V} \neq 0$, and the eigenstates are the superposition of the zero-order basis $|\Psi_a\rangle$ and $|\Psi_b\rangle$. If the initial state $|\Psi_a\rangle$ is populated, the spin system will not stay in this state but oscillate between the states $|\Psi_a\rangle$ and $|\Psi_b\rangle$. From Equation (3.45) and Equation (3.46), it can be determined that the mixing effect is most significant when $|\theta| = \pi/4$. In this case, $|\Psi_\pm\rangle = (|\Psi_a\rangle \pm |\Psi_b\rangle)/\sqrt{2}$, indicating that the complete population transfer between $|\Psi_+\rangle$ and $|\Psi_-\rangle$ becomes possible. Hence, strong coupling can drive the spin system into the region of LACs, where coherent mixing enables full population transfer between the involved quantum states.

Here, Equations (3.38)–(3.46) directly relate to the discussion of the J-coupling effect in the AB-spin system presented in Chapter 2.7.3 (Equations (2.60)-(2.66)). In an AB-spin system, J-coupling (i.e., spin-spin coupling) describes the magnetic interaction between two spins transmitted indirectly via bonded electrons. This coupling leads to the appearance of multiple peaks in NMR spectra, and the interaction strength is determined by the coupling constant. The LAC phenomenon involves situations where the energy levels approach and interact under changing external conditions. In this scenario, spin-spin coupling can be

treated as a perturbation, leading to the mixing and splitting of energy levels. In a two-spin system, with the strength of the perturbation $\mathcal{V} = J/2$, the distance of the splitting between the two energy levels is $2\mathcal{V} = J$ (Figure 3.9), the stronger the J-coupling, the larger splitting distance at the anticrossing.

3.5.2.3 Level Anti-Crossing of a AB-spin system

As it is discussed above, the off-diagonal element in the Hamiltonian, i.e., the perturbation turns the LC into LAC. In this section, an example of the AB-spin system is presented, where the two nuclei have different gyromagnetic ratios. The Hamiltonian for this system is introduced in Equation (2.52), where the terms for Zeeman interaction and the secular part of the J-coupling contribute to the diagonal elements of the Hamiltonian.

$$\hat{\mathcal{H}}_0(\mathrm{AB}) = \nu_1 \hat{I}_{1z} + \nu_2 \hat{I}_{2z} + J \hat{I}_{1z} \hat{I}_{2z} \tag{3.47}$$

The non-secular part of the J-coupling

$$\hat{\mathcal{H}}'(\mathrm{AB}) = J(\hat{I}_{1x} \hat{I}_{2x} + \hat{I}_{1y} \hat{I}_{2y}) \tag{3.48}$$

can be transferred to the secular products by utilizing the ladder operators (Equation (2.42)) to form the off-diagonal elements of the Hamiltonian as the perturbation term:

$$\hat{\mathcal{V}} = \hat{\mathcal{H}}'(\mathrm{AB}) = \frac{J}{2}(\hat{I}_{1+} \hat{I}_{2-} + \hat{I}_{1-} \hat{I}_{2+}) \tag{3.49}$$

The energy of the four basis state $|\alpha\alpha\rangle$, $|\alpha\beta\rangle$, $|\beta\alpha\rangle$, and $|\beta\beta\rangle$ are as follows:

$$\hat{\mathcal{H}}(\mathrm{AB})\,|\alpha\alpha\rangle = \left(\frac{\nu_1}{2} + \frac{\nu_2}{2} + \frac{J}{4}\right)|\alpha\alpha\rangle \tag{3.50}$$

$$\hat{\mathcal{H}}(\mathrm{AB})\,|\alpha\beta\rangle = \left(\frac{\nu_1}{2} - \frac{\nu_2}{2} - \frac{J}{4}\right)|\alpha\beta\rangle + \frac{J}{2}|\beta\alpha\rangle \tag{3.51}$$

$$\hat{\mathcal{H}}(\mathrm{AB})\,|\beta\alpha\rangle = \left(-\frac{\nu_1}{2} + \frac{\nu_2}{2} - \frac{J}{4}\right)|\beta\alpha\rangle + \frac{J}{2}|\alpha\beta\rangle \tag{3.52}$$

$$\hat{\mathcal{H}}(\mathrm{AB})\,|\beta\beta\rangle = \left(-\frac{\nu_1}{2} - \frac{\nu_2}{2} + \frac{J}{4}\right)|\beta\beta\rangle \tag{3.53}$$

The complete Hamiltonian of the two-spin system in matrix form is shown in Equation (2.54).

In this analysis, MATLAB software is utilized to solve the eigenvalues of the Hamiltonian for a spin system affected by J-coupling. The resulting simulated diagram (Figure 3.12) illustrates the relationship between energy (expressed in Hz) and magnetic field strength, comparing scenarios both without and with J-coupling as a perturbation. When there's no perturbation (Figure 3.12**a**), the energy level $|\alpha\alpha\rangle$ crosses with the one of $|\beta\beta\rangle$, and $|\alpha\beta\rangle$ crosses with $|\beta\alpha\rangle$ at the magnetic filed strength of $B = 0$. However, the first LC cannot turn into LAC since there's no perturbation between these two basis states ($\langle\alpha\alpha|\hat{\mathcal{V}}|\beta\beta\rangle = 0$). The second LC can turn into LAC since $\langle\alpha\beta|\hat{\mathcal{V}}|\beta\alpha\rangle = J/2$ (Figure 3.12**b**).

3.5.2.4 Level Anti-Crossing of a three-spin system in SABRE

Now, a more complex example of a three-spin system (AA'S) is considered to investigate the spin order transfer in SABRE from *para*-H_2 to heteronuclei such as ^{13}C or ^{15}N. The

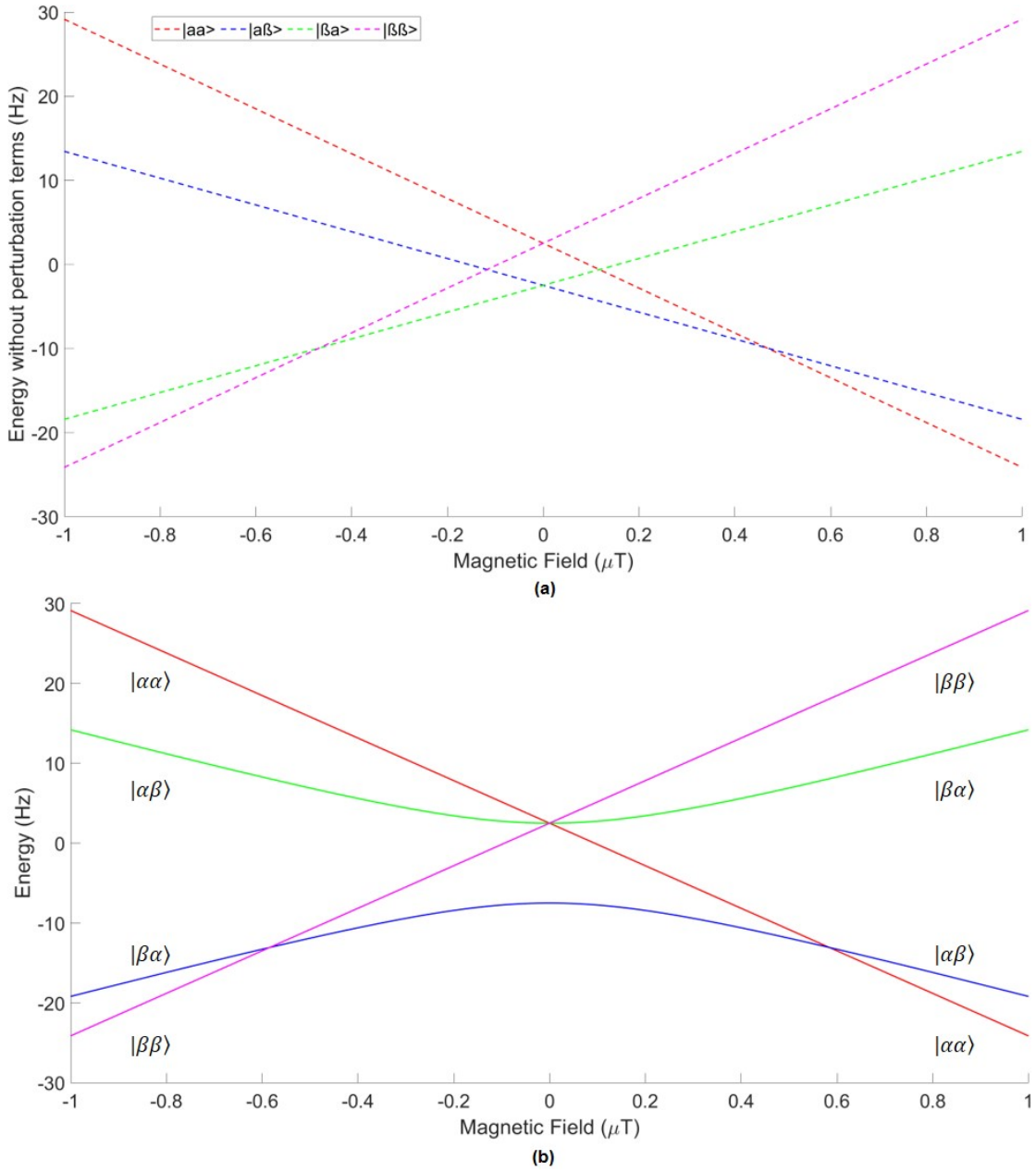

Figure 3.12: Energy level diagram of the AB-spin system. **(a)** Without J-coupling as perturbation. **(b)** With non-secular J-coupling term between spin states $|\alpha\beta\rangle$ and $|\beta\alpha\rangle$ as perturbation to turn the LA to LAC. Simulation parameters: $\gamma_{\mathrm{H}} = 2.675 \times 10^8$ rad $\cdot$ T$^{-1} \cdot$ s^{-1}, $\gamma_{\mathrm{C}} = 6.728 \times 10^7$ rad $\cdot$ T$^{-1} \cdot$ s^{-1}, and $J_{\mathrm{CH}} = 10$ Hz.

Hamiltonian for this three-spin system is as follows:

$$\hat{\mathcal{H}} = \nu_{\mathrm{H}}(\hat{I}_{\mathrm{a}z} + \hat{I}_{\mathrm{b}z}) + \nu_{\mathrm{C}}\hat{S}_z + J_{\mathrm{ab}}\hat{\boldsymbol{I}}_{\mathrm{a}}\hat{\boldsymbol{I}}_{\mathrm{b}} + J_{\mathrm{aS}}\hat{\boldsymbol{I}}_{\mathrm{a}}\hat{\boldsymbol{S}} + J_{\mathrm{bS}}\hat{\boldsymbol{I}}_{\mathrm{b}}\hat{\boldsymbol{S}} \tag{3.54}$$

The two spins, I_{a} and I_{b}, represent the two hydrides originating from the *para*-H_2 molecule, while the spin S corresponds to the heteronucleus on the to-be-polarized substrate (in this case is ^{13}C) (Figure 3.13).

As discussed in section 3.3.2, the spin state of the H_2 molecule can be represented as

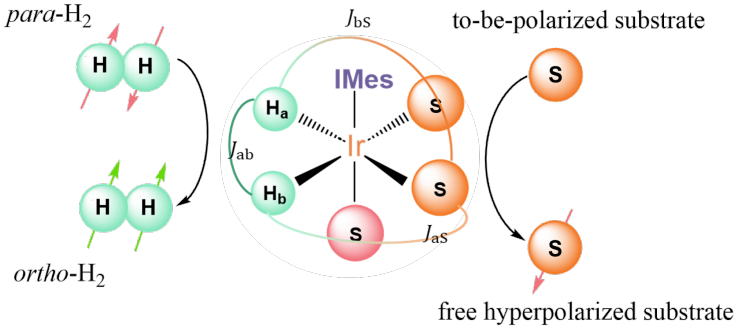

Figure 3.13: Schematic of a three-spin system (AA'S) in SABRE.

follows:

$$\begin{bmatrix} T_+ \\ T_0 \\ S_0 \\ T_- \end{bmatrix} = \begin{bmatrix} 1 & 0 & 0 & 0 \\ 0 & 1 & 1 & 0 \\ 0 & -1 & 1 & 0 \\ 0 & 0 & 0 & 1 \end{bmatrix} \begin{bmatrix} \alpha\alpha \\ \alpha\beta \\ \beta\alpha \\ \beta\beta \end{bmatrix} \tag{3.55}$$

By calculating the Kronecker product of triplet-singlet state (Equation (3.55)) and the Zeeman basis of each spin, the eigenstates of the three-spin system are:

$$\begin{matrix} T_+ \otimes \alpha & T_+ \otimes \beta \\ T_0 \otimes \alpha & T_0 \otimes \beta \\ S_0 \otimes \alpha & S_0 \otimes \beta \\ T_- \otimes \alpha & T_- \otimes \beta \end{matrix} \tag{3.56}$$

These spin states of the three-spin system AA'S in SABRE written in matrix form of the Zeeman basis is:

$$\begin{bmatrix} S_0\alpha \\ T_+\beta \\ T_0\alpha \\ S_0\beta \\ T_-\alpha \\ T_0\beta \\ T_-\beta \\ T_+\alpha \end{bmatrix} = \underbrace{\begin{bmatrix} 0 & 0 & -\frac{\sqrt{2}}{2} & 0 & \frac{\sqrt{2}}{2} & 0 & 0 & 0 \\ 0 & 1 & 0 & 0 & 0 & 0 & 0 & 0 \\ 0 & 0 & \frac{\sqrt{2}}{2} & 0 & \frac{\sqrt{2}}{2} & 0 & 0 & 0 \\ 0 & 0 & 0 & -\frac{\sqrt{2}}{2} & 0 & \frac{\sqrt{2}}{2} & 0 & 0 \\ 0 & 0 & 0 & 0 & 0 & 0 & 1 & 0 \\ 0 & 0 & 0 & \frac{\sqrt{2}}{2} & 0 & \frac{\sqrt{2}}{2} & 0 & 0 \\ 0 & 0 & 0 & 0 & 0 & 0 & 0 & 1 \\ 1 & 0 & 0 & 0 & 0 & 0 & 0 & 0 \end{bmatrix}}_{T} \begin{bmatrix} \alpha\alpha\alpha \\ \alpha\alpha\beta \\ \alpha\beta\alpha \\ \alpha\beta\beta \\ \beta\alpha\alpha \\ \beta\alpha\beta \\ \beta\beta\alpha \\ \beta\beta\beta \end{bmatrix} \tag{3.57}$$

where T is the normalized transformation matrix.

The Hamiltonian of the eight Zeemann basis states can be calculated by substituting $J_{\mathrm{ab}} = J_{\mathrm{HH'}}$, $J_{\mathrm{aS}} = J_{\mathrm{CH}}$, $J_{\mathrm{bS}} = J_{\mathrm{CH'}}$, $\nu_{\mathrm{H}} = -\gamma_{\mathrm{H}}B$, and $\nu_{\mathrm{C}} = -\gamma_{\mathrm{C}}B$ in Equation (3.54):

$$\hat{\mathcal{H}}\,|\alpha\alpha\alpha\rangle = \left(-\gamma_{\mathrm{H}}B - \frac{1}{2}\gamma_{\mathrm{C}}B + \frac{1}{4}J_{\mathrm{HH'}} + \frac{1}{4}(J_{\mathrm{CH}} + J_{\mathrm{CH'}})\right)|\alpha\alpha\alpha\rangle \tag{3.58}$$

$$\begin{aligned}\hat{\mathcal{H}}\,|\alpha\alpha\beta\rangle = &\left(-\gamma_{\mathrm{H}}B + \frac{1}{2}\gamma_{\mathrm{C}}B + \frac{1}{4}J_{\mathrm{HH'}} - \frac{1}{4}(J_{\mathrm{CH}} + J_{\mathrm{CH'}})\right)|\alpha\alpha\beta\rangle \\ &+ \frac{1}{2}J_{\mathrm{CH}}\,|\beta\alpha\alpha\rangle + \frac{1}{2}J_{\mathrm{CH'}}\,|\alpha\beta\alpha\rangle\end{aligned} \tag{3.59}$$

$$\hat{\mathcal{H}}\,|\alpha\beta\alpha\rangle = \left(-\frac{1}{2}\gamma_{\mathrm{C}}B - \frac{1}{4}J_{\mathrm{HH'}} + \frac{1}{4}(J_{\mathrm{CH}} - J_{\mathrm{CH'}})\right)|\alpha\beta\alpha\rangle + \frac{1}{2}J_{\mathrm{HH'}}\,|\beta\alpha\alpha\rangle + \frac{1}{2}J_{\mathrm{CH'}}\,|\alpha\alpha\beta\rangle \tag{3.60}$$

$$\hat{\mathcal{H}}\,|\alpha\beta\beta\rangle = \left(\frac{1}{2}\gamma_{\mathrm{C}}B - \frac{1}{4}J_{\mathrm{HH'}} - \frac{1}{4}(J_{\mathrm{CH}} - J_{\mathrm{CH'}})\right)|\alpha\beta\beta\rangle + \frac{1}{2}J_{\mathrm{HH'}}\,|\beta\alpha\beta\rangle + \frac{1}{2}J_{\mathrm{CH}}\,|\beta\beta\alpha\rangle \tag{3.61}$$

$$\hat{\mathcal{H}}\,|\beta\alpha\alpha\rangle = \left(-\frac{1}{2}\gamma_{\mathrm{C}}B - \frac{1}{4}J_{\mathrm{HH'}} - \frac{1}{4}(J_{\mathrm{CH}} - J_{\mathrm{CH'}})\right)|\beta\alpha\alpha\rangle + \frac{1}{2}J_{\mathrm{HH'}}\,|\alpha\beta\alpha\rangle + \frac{1}{2}J_{\mathrm{CH}}\,|\alpha\alpha\beta\rangle \tag{3.62}$$

$$\hat{\mathcal{H}}\,|\beta\alpha\beta\rangle = \left(\frac{1}{2}\gamma_{\mathrm{C}}B - \frac{1}{4}J_{\mathrm{HH'}} + \frac{1}{4}(J_{\mathrm{CH}} - J_{\mathrm{CH'}})\right)|\beta\alpha\beta\rangle + \frac{1}{2}J_{\mathrm{HH'}}\,|\alpha\beta\beta\rangle + \frac{1}{2}J_{\mathrm{CH'}}\,|\beta\beta\alpha\rangle \tag{3.63}$$

$$\hat{\mathcal{H}}\,|\beta\beta\alpha\rangle = \left(\gamma_{\mathrm{H}}B - \frac{1}{2}\gamma_{\mathrm{C}}B + \frac{1}{4}J_{\mathrm{HH'}} - \frac{1}{4}(J_{\mathrm{CH}} + J_{\mathrm{CH'}})\right)|\beta\beta\alpha\rangle + \frac{1}{2}J_{\mathrm{CH}}\,|\alpha\beta\beta\rangle + \frac{1}{2}J_{\mathrm{CH'}}\,|\beta\alpha\beta\rangle \tag{3.64}$$

$$\hat{\mathcal{H}}\,|\beta\beta\beta\rangle = \left(\gamma_{\mathrm{H}}B + \frac{1}{2}\gamma_{\mathrm{C}}B + \frac{1}{4}J_{\mathrm{HH'}} + \frac{1}{4}(J_{\mathrm{CH}} + J_{\mathrm{CH'}})\right)|\beta\beta\beta\rangle \tag{3.65}$$

By substituting $\Sigma_{J_{\mathrm{CH}}} = J_{\mathrm{CH}} + J_{\mathrm{CH'}}$ and $\Delta_{J_{\mathrm{CH}}} = J_{\mathrm{CH}} - J_{\mathrm{CH'}}$ in the above Hamiltonian of each basis state, the total Hamiltonian of the three-spin states can be written in matrix form as follows:

$$\hat{\mathcal{H}} = \begin{Bmatrix} -\nu_{\mathrm{H}} - \frac{\nu_{\mathrm{C}}}{2} + \frac{J_{\mathrm{HH'}} + \Sigma_{J_{\mathrm{CH}}}}{4} & 0 & 0 & 0 \\ 0 & -\nu_{\mathrm{H}} + \frac{\nu_{\mathrm{C}}}{2} + \frac{J_{\mathrm{HH'}} - \Sigma_{J_{\mathrm{CH}}}}{4} & \frac{J_{\mathrm{CH'}}}{2} & 0 \\ 0 & \frac{J_{\mathrm{CH'}}}{2} & -\frac{\nu_{\mathrm{C}}}{2} - \frac{J_{\mathrm{HH'}} - \Delta_{J_{\mathrm{CH}}}}{4} & 0 \\ 0 & 0 & 0 & \frac{\nu_{\mathrm{C}}}{2} - \frac{J_{\mathrm{HH'}} + \Delta_{J_{\mathrm{CH}}}}{4} \\ 0 & \frac{J_{\mathrm{CH}}}{2} & \frac{J_{\mathrm{HH'}}}{2} & 0 \\ 0 & 0 & 0 & \frac{J_{\mathrm{HH'}}}{2} \\ 0 & 0 & 0 & \frac{J_{\mathrm{CH}}}{2} \\ 0 & 0 & 0 & 0 \end{Bmatrix}$$

$$\begin{pmatrix}
0 & 0 & 0 & 0 \\
\frac{J_{CH}}{2} & 0 & 0 & 0 \\
\frac{J_{HH'}}{2} & 0 & 0 & 0 \\
0 & \frac{J_{HH'}}{2} & \frac{J_{CH}}{2} & 0 \\
-\frac{\nu_C}{2} - \frac{J_{HH'}+\Delta_{J_{CH}}}{4} & 0 & 0 & 0 \\
0 & \frac{\nu_C}{2} - \frac{J_{HH'}-\Delta_{J_{CH}}}{4} & \frac{J_{CH'}}{2} & 0 \\
0 & \frac{J_{CH'}}{2} & \nu_H - \frac{\nu_C}{2} + \frac{J_{HH'}-\Sigma_{J_{CH}}}{4} & 0 \\
0 & 0 & 0 & \nu_H + \frac{\nu_C}{2} + \frac{J_{HH'}+\Sigma_{J_{CH}}}{4}
\end{pmatrix} \tag{3.66}$$

To gain a more intuitive understanding of the evolution of the spin states in the three-spin system, a similarity transformation ($\hat{\mathcal{H}}_{ST} = T\hat{\mathcal{H}}T^{\dagger}$) can be applied to convert the matrix of $\hat{\mathcal{H}}$ (Equation (3.66)) into a matrix described with singlet-triplet spin states. This is achieved using the transformation matrix T (Equation (3.57)). The calculation process is done by using MATLAB, more details can be found in Appendix A.5. The obtained $\hat{\mathcal{H}}_{ST}$ is:

$$\hat{\mathcal{H}}_{ST} = \begin{pmatrix}
-\frac{3J_{HH'}}{4} - \frac{\nu_C}{2} & \frac{\sqrt{2}\Delta_{J_{CH}}}{4} & -\frac{\Delta_{J_{CH}}}{4} \\
\frac{\sqrt{2}\Delta_{J_{CH}}}{4} & \frac{J_{HH'}-\Sigma_{J_{CH}}}{4} + \frac{\nu_C-2\nu_H}{2} & \frac{\sqrt{2}\Sigma_{J_{CH}}}{4} \\
-\frac{\Delta_{J_{CH}}}{4} & \frac{\sqrt{2}\Sigma_{J_{CH}}}{4} & \frac{J_{HH'}}{4} - \frac{\nu_C}{2} \\
0 & 0 & 0 \\
0 & 0 & 0 \\
0 & 0 & 0 \\
0 & 0 & 0 \\
0 & 0 & 0
\end{pmatrix}$$

$$\begin{pmatrix}
0 & 0 & 0 & 0 & 0 \\
0 & 0 & 0 & 0 & 0 \\
0 & 0 & 0 & 0 & 0 \\
\frac{\nu_C}{2} - \frac{3J_{HH'}}{4} & -\frac{\sqrt{2}\Delta_{J_{CH}}}{4} & \frac{\Delta_{J_{CH}}}{4} & 0 & 0 \\
-\frac{\sqrt{2}\Delta_{J_{CH}}}{4} & \frac{J_{HH'}-\Sigma_{J_{CH}}}{4} - \frac{\nu_C-2\nu_H}{2} & \frac{\sqrt{2}\Sigma_{J_{CH}}}{4} & 0 & 0 \\
\frac{\Delta_{J_{CH}}}{4} & \frac{\sqrt{2}\Sigma_{J_{CH}}}{4} & \frac{J_{HH'}}{4} + \frac{\nu_C}{2} & 0 & 0 \\
0 & 0 & 0 & \frac{J_{HH'}+\Sigma_{J_{CH}}}{4} + \frac{\nu_C+2\nu_H}{2} & 0 \\
0 & 0 & 0 & 0 & \frac{J_{HH'}+\Sigma_{J_{CH}}}{4} - \frac{\nu_C+2\nu_H}{2}
\end{pmatrix} \tag{3.67}$$

where two blocks of 3×3 can be identified. In each block, the diagonal elements are the energies of the spin states without the effect of J-coupling, while the off-diagonal elements describes the J-coupling interactions (perturbation). Figure 3.14 illustrates all the LCs of the eigenstates without perturbations. Among these, only the one related to coherence and J-coupling perturbed can be transformed into LACs for population transfer. More details of the simulation can be found in Appendix A.6.

To determine the conditions for Level Anti-Crossings (LACs) of the Hamiltonian ($\hat{\mathcal{H}}_{ST}$) in the singlet-triplet basis, the two diagonal sub-matrices are analyzed separately. The first sub-matrix corresponds to the population transfer pathways of the spin states $|S_0\alpha\rangle$, $|T_+\beta\rangle$,

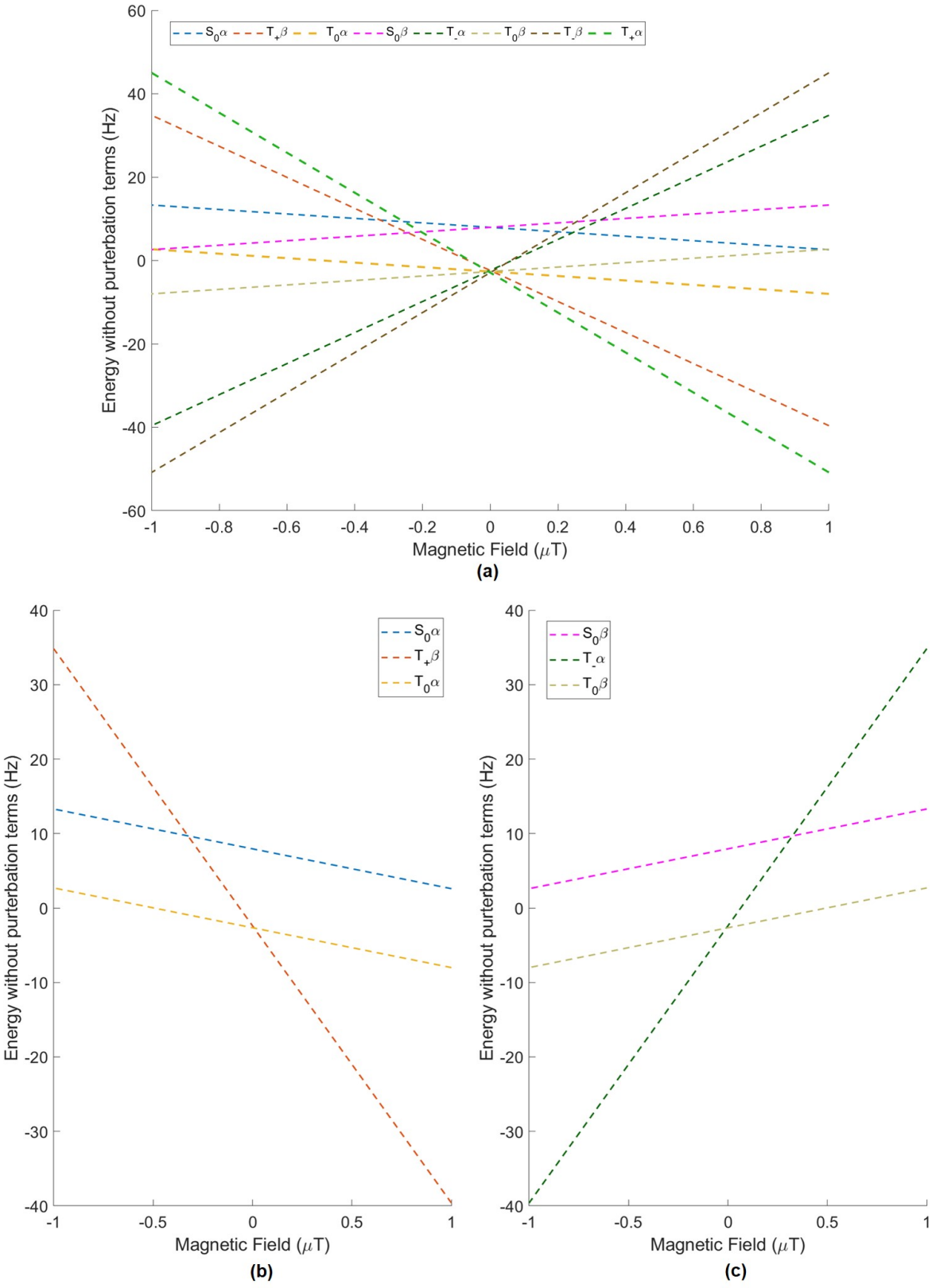

Figure 3.14: **(a)** LCs of three-spin system simulated with MATLAB. **(b-c)** Zoom-in of the LCs corresponding to the spin states in the two on-diagonal sub-matrices.

and $|T_0\alpha\rangle$. The conditions for generating the LACs between any two of these three spin states

is the equalization of their on-diagonal elements:

$$|S_0\alpha\rangle \rightarrow |T_+\beta\rangle \qquad \hat{\mathcal{H}}_{\mathrm{ST},11} = \hat{\mathcal{H}}_{\mathrm{ST},22} \Rightarrow \nu_{\mathrm{H}} - \nu_{\mathrm{C}} = J_{\mathrm{HH'}} - \frac{\Sigma_{J_{\mathrm{CH}}}}{4} \tag{3.68}$$

$$|T_+\beta\rangle \rightarrow |T_0\alpha\rangle \qquad \hat{\mathcal{H}}_{\mathrm{ST},22} = \hat{\mathcal{H}}_{\mathrm{ST},33} \Rightarrow \nu_{\mathrm{C}} - \nu_{\mathrm{H}} = \frac{\Sigma_{J_{\mathrm{CH}}}}{4} \tag{3.69}$$

$$|S_0\alpha\rangle \rightarrow |T_0\alpha\rangle \qquad \hat{\mathcal{H}}_{\mathrm{ST},11} = \hat{\mathcal{H}}_{\mathrm{ST},33} \Rightarrow J_{\mathrm{HH'}} = 0 \tag{3.70}$$

However, the population transfer between the spin states $|S_0\alpha\rangle$ and $|T_0\alpha\rangle$ is not possible, i.e., Equation (3.70) cannot be established, since the J-coupling constant of the di-hydride in SABRE system is non-zero ($J_{\mathrm{HH'}} \neq 0$).

Similarly, the second sub-matrix describes the evolution of the spin states $|S_0\beta\rangle$, $|T_-\alpha\rangle$, and $|T_0\beta\rangle$. The conditions for the corresponding Level Anti-Crossings (LACs) can be determined as follows:

$$|S_0\beta\rangle \rightarrow |T_-\alpha\rangle \qquad \hat{\mathcal{H}}_{\mathrm{ST},44} = \hat{\mathcal{H}}_{\mathrm{ST},55} \Rightarrow -(\nu_{\mathrm{H}} - \nu_{\mathrm{C}}) = J_{\mathrm{HH'}} - \frac{\Sigma_{J_{\mathrm{CH}}}}{4} \tag{3.71}$$

$$|T_-\alpha\rangle \rightarrow |T_0\beta\rangle \qquad \hat{\mathcal{H}}_{\mathrm{ST},55} = \hat{\mathcal{H}}_{\mathrm{ST},66} \Rightarrow -(\nu_{\mathrm{C}} - \nu_{\mathrm{H}}) = \frac{\Sigma_{J_{\mathrm{CH}}}}{4} \tag{3.72}$$

$$|S_0\beta\rangle \rightarrow |T_0\beta\rangle \qquad \hat{\mathcal{H}}_{\mathrm{ST},44} = \hat{\mathcal{H}}_{\mathrm{ST},66} \Rightarrow J_{\mathrm{HH'}} = 0 \tag{3.73}$$

It is obviously that the population transfer from the spin states $|S_0\beta\rangle$ to $|T_0\beta\rangle$ (Equation (3.73)) is not possible due to $J_{\mathrm{HH'}} \neq 0$.

Additionally, the conditions for the LACs of $|S_0\alpha\rangle \rightarrow |T_+\beta\rangle$ and $|S_0\beta\rangle \rightarrow |T_-\alpha\rangle$ are opposite in sign (Equation (3.68) and Equation (3.71)), which describes the population transfer pathway starting from either the α or β state of the singlet order stemming from *para*-H_2. A similar situation occurs for the LACs between $|T_+\beta\rangle \rightarrow |T_0\alpha\rangle$ and $|T_-\alpha\rangle \rightarrow |T_0\beta\rangle$ (Equation (3.69) and Equation (3.72)). Figure 3.15 illustrates the possible LACs in the three-spin system by using MATLAB to solve the eigenvalues of the sub-matrices corresponding to each pair of possible spin states in the 3×3 blocks. Additionally, the visualization of the population transfer between spin states via LACs is shown in Figure 3.16, obtained by taking the partial derivative of the energy levels with respect to the magnetic field strength. (More details of the MATLAB simulation can be found in Appendix A.7.)

3.6 Experimental methods for conducting PHIP and SABRE

In the previous section, the exploration focused on how the polarization transfer across spins in PHIP and SABRE. These two methods utilize a straightforward gas-liquid reaction, wherein *para*-H_2 catalytically reacts with substrates dissolved in a solution. This reaction is conducted under appropriate magnetic field and temperature conditions, or using a specific pulse sequence, to effectively transfer the spin order from *para*-H_2 to the substrate nuclei. Once hyperpolarized, these substrates are then transported to the NMR detector for signal acquisition. A system or unit that facilitates these processes is commonly termed a "polarizer" in the realms of PHIP and SABRE [111, 112].

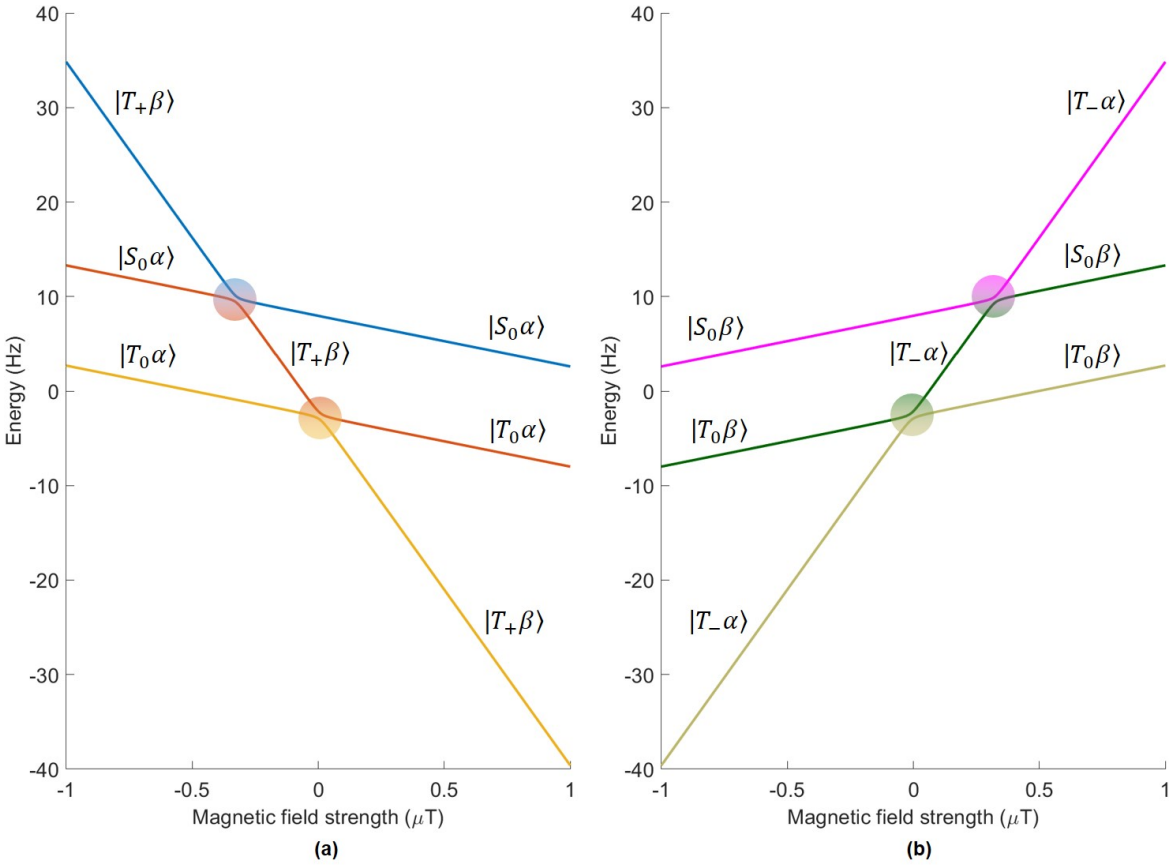

Figure 3.15: LACs of three-spin system simulated with MATLAB. **(a)** LACs for transitions of $|S_0\alpha\rangle \leftrightarrow |T_+\beta\rangle$ and $|T_+\beta\rangle \leftrightarrow |T_0\alpha\rangle$. **(b)** LACs for transitions of $|S_0\beta\rangle \leftrightarrow |T_-\alpha\rangle$ and $|T_-\alpha\rangle \leftrightarrow |T_0\beta\rangle$.

This section discusses polarizer design from two critical perspectives that are pivotal for optimizing hyperpolarization. The first is the efficiency of hydrogen gas solubility, which directly influences the polarization level achieved in the substrate. The second concerns the delivery of hyperpolarized substrates from the production site to the NMR apparatus, where preserving polarization during transfer is essential for effective signal detection.

Moreover, various polarizers implemented in the literature to deliver the hyperpolarized *para*-H_2 substances into bulk or microscale solutions are described and discussed. This chapter aims to provide a standardized evaluation framework to assist researchers in selecting or designing the most appropriate polarizer based on their specific needs.

3.6.1 Design considerations for PHIP and SABRE polarizers

A brief procedure of conducting PHIP or SABRE experiments involves several key steps: firstly, the dissolution of *para*-H_2 gas into the sample solution; followed the addition reaction of hydrogen with the substrate for PHIP, or the ligation of hydride and substrate to the organometallic the catalyst for SABRE; then the transfer of spin order to the target nuclei on the substrate at an optimal magnetic field. Therefore, a polarizer used in PHIP or SABRE

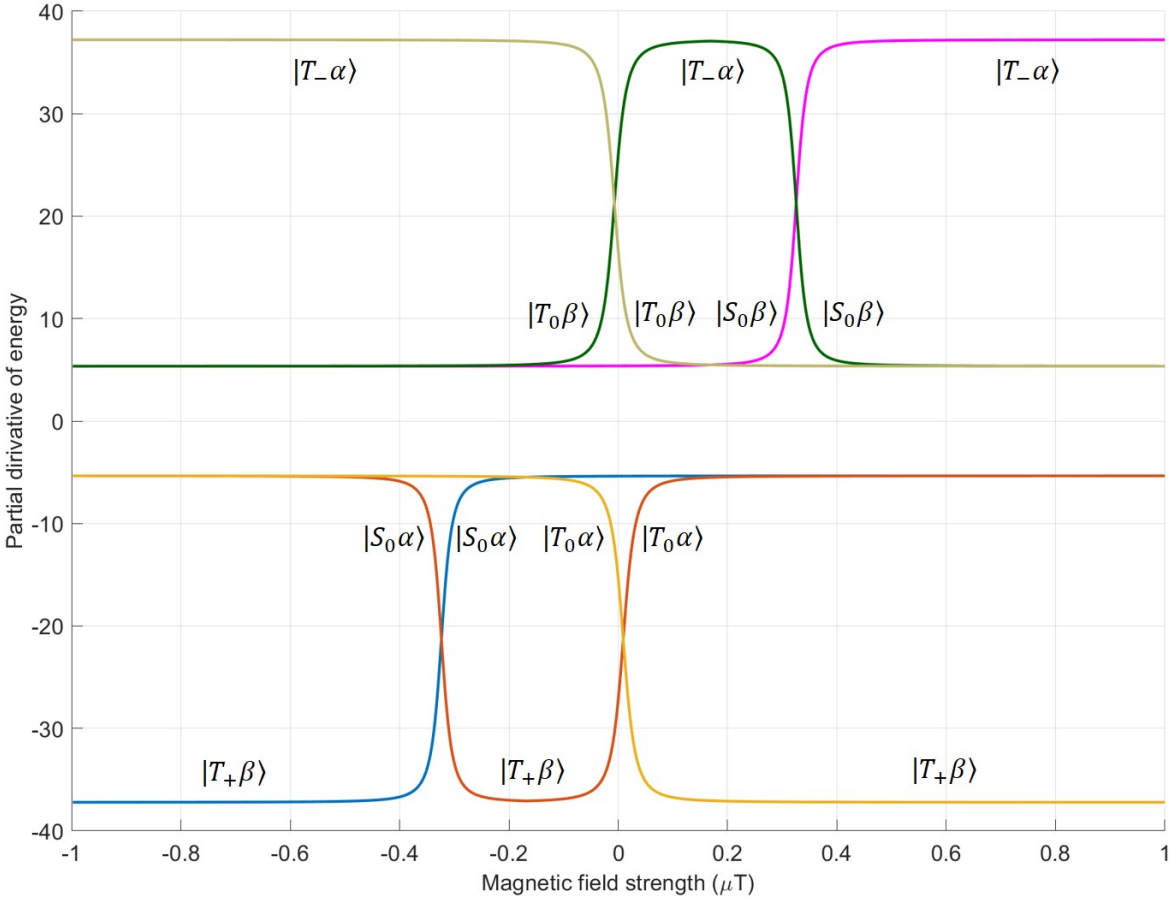

Figure 3.16: Partial derivation of energies for visualizing variation in the population status of the spin states with respect to changes in the magnetic field.

is compromised with:

- a fluidic unit, which is responsible for efficiently introducing *para*-H_2 into the sample solution. From a chemical engineering perspective, this fluidic unit functions as a gas-liquid reactor. Different types of gas-liquid reactors reported in published works of PHIP and SABRE can be classified as high-pressure NMR tubes, bubbling device, and membrane gas-liquid reactor
- a magnetic field generation equipment for generating the optimal magnetic field required for polarization transfer. The strength of the magnetic field can range from several microteslas to several teslas, depending on the polarization technique used and the type of target nuclei. For instance: the ultra-low fields range from near-zero tesla to microtesla for SABRE hyperpolarization of heteronuclei, such as ^{13}C and ^{15}N, can be generated by using electromagnetic coils within a magnetic shielding chamber; for ^{1}H SABRE and ALTADENA-PHIP the field usually in low-field range from geomagnetic field to several millitesla can be the Earth's magnetic field itself, the stray fields from NMR equipment, or generated by electromagnetic coils; high-fields ranging from several hundred millitesla to a few tesla for PASADENA-PHIP can be generated by permanent magnets or the magnets inherent in NMR equipment.

Although this chapter mentions magnetic field generation equipment, the focus is not on the generators themselves but rather on analyzing their impact on the efficiency of PHIP and SABRE hyperpolarization from the perspective of the gas-liquid reactor.

Applying SABRE and PHIP in liquid-state NMR requires one to dissolve the *para*-H_2 gas into the liquids containing the target molecules, followed by efficient detection of the enhanced molecules. The following factors are considered as the main challenges in the process to be faced:

- **Efficiency of *para*-H_2's solubility in solution**

At 298 K and 1 atm, the solubility of hydrogen in water is about 0.8 mmol/L [113]. Under the same conditions, its solubility in methanol is higher—approximately 3.9 mmol/L, because methanol's weaker hydrogen-bond network and hydrophobic methyl group reduce the free-energy cost of cavity formation and afford stronger dispersion interactions with H_2. Even so, the overall solubility remains low, which limits the dissolution of *para*-H_2 in polar media and constrains hyperpolarization performance.[114, 115, 116, 117]

Various approaches have been applied to improve the uptake of gas in solutions. The most straightforward method is increasing the injected gas pressure or the temperature. Laili et al. [118] observed the signal gains of SABRE hyperpolarization with increased *para*-H_2 gas pressure from 2 bar to 4 bar, and 40% improved response with the overall polarization level by raising the temperature from 289 K to 308 K. Lehmkuhl et al. [119] also reported the correlation of signal enhancement with higher *para*-H_2 pressure in SABRE experiments. In addition to optimizing the experimental conditions (pressure, temperature), increasing the gas-liquid interface can enhance the dissolution process and will be discussed in detail later.

- **Delivery of hyperpolarized compounds to the detection field**

The detection of magnetic resonance signals of the hyperpolarized compounds is usually carried out in an NMR spectrometer, where the magnetic field is typically stronger than 1 T. However, the optimal polarization transfer field (PTF) in SABRE experiments is in milliTesla range, which is much lower than the magnetic field of conventional NMR spectrometers. For instance, the magnetic field strength of 6.5 mT is sufficient for spin order derived from *para*-H_2 spontaneously transferred to the ^{1}H sites on co-ligand substrates with SABRE. [120] For efficient direct polarization of heteronuclei, such as ^{13}C, ^{15}N, and ^{31}P, a near-zero or ultralow field is applied to achieve a strong coupling between between heteronuclei and proton. [74, 121, 122]

It should be kept in mind that, unless the spin order is converted to a long-lived state, the hyperpolarized samples usually readily relax towards thermal equilibrium populations. The lifetime of liquid-state hyperpolarization is typically within a few tens of seconds. Therefore, the transfer of hyperpolarized compounds from the polarization field to the detection field needs to be performed as quickly as possible. This rapid transfer is a prerequisite for measuring the hyperpolarized signal with sufficient intensity.

3.6.2 Overview of methods for conducting PHIP and SABRE

This section provides a brief overview of three main methods commonly used in PHIP and SABRE experiments: shaking, bubbling, and the use of membrane-based gas–liquid reactors. Additionally, the configurations, compatibility, and performance of various types of gas–liquid contactors employed in each method are discussed. The content presented in this methodological review forms part of the published article entitled *"Integrating Micro Process Chemistry into an NMR Spectrometer"* in the journal ***Chemie Ingenieur Technik*** [JY01].

3.6.2.1 Shaking method

Shaking method provides a simple and fast way for conducting *para*-H_2-based hyperpolarization. In shaking method, a commercial high-pressure NMR tube is typically used for mixing the *para*-H_2 with sample solution. Before each experiment, *para*-H_2 gas is pressurized via tubing into the headspace of the high-pressure NMR tube, which is capped and sealed with either a Young's valve or a quick pressure valve (Figure 3.17**a**). Subsequently, PHIP and SABRE experiments can be conducted manually by shaking this tube by hand for tens of seconds at the geomagnetic field or near the stray field of a high-field NMR magnet. After shaking, the tube is rapidly inserted into the NMR spectrometer (typically within 3 s) for detection. [123, 124, 125]

Another commercial high-pressure NMR tube (Wilmad-LabGlass, Norell®) with a thick glass wall can reach up to 300 psi (≈ 20.68 bar) (Figure 3.17**b**). With increased pressure and vigorous shaking, *para*-H_2 effectively dissolves into and mixes with the sample solution, thereby enhancing the reaction rate and achieving high-level polarization.

Aside from the high-pressure NMR tube made of glass, Duchowny et al. [126] utilized a sapphire high-pressure NMR tube allowing for much higher pressure up to 200 bar (Figure 3.17**c**). With this setup, the correlation between the *para*-H_2 pressure and the enhancement of pyrazine signals via SABRE hyperpolarization was explored. The study revealed that within a pressure range up to 10 bar, the relationship was quasi linear. However, beyond 10 bar, this relationship ceased to be linear; instead, signal enhancement plateaued as the pressure increased, with only a three-fold increase observed at 200 bar. In addition to exploring the pressure-signal enhancement relationship, the team also utilized this setup to validate the use of liquefied carbon dioxide under high pressure as an alternative solvent for SABRE. This approach avoids the need for typical organic solvents such as methanol used in SABRE processes. Consequently, the elimination of organic solvent potentially makes SABRE hyperpolarization more suitable for applications like molecular medical research.

The manual "shake and drop" method offers a convenient and rapid way in many studies of new catalytic system, substrates, and newly proposed concepts for PHIP and SABRE. However, the manual nature of the process leads to variability in results due to differences in the force and the time for transfer the tube into NMR detector. These variations in this procedure contribute to inconsistent signal enhancements and result in low reproducibility of experimental outcomes. Furthermore, the "shake and drop" method is only suitable for

Figure 3.17: Photo of different commercial high-pressure NMR tubes. **(a)** A 5 mm thin wall quick pressure valve NMR tube (Wilmad-LabGlass). The upper portion of the quick pressure valve is fitted with 1/16 inch PTFE tubing. The maximal pressure is 100 psi. **(b)** A 5 mm heavy wall NMR pressure tube for medium range pressure ($\leq$ 300 psi) (Wilmad-LabGlass). The valve is designed to connect to a 1/8 inch tubing using Swagelok® fittings. **(c)** A 5 mm sapphire NMR tube for high-pressure ranging up to 200 bar.

hyperpolarization experiments conducted within the range of the Earth's magnetic field or stray magnetic fields. For other magnetic field environments, for example, a high-field for PASADENA-PHIP or a micro-tesla field for heteronuclei hyperpolarization, it is challenging to shake the tube *in-situ*.

The typical procedure involves initially shaking the tube within the geomagnetic field in the laboratory for a few seconds to mix the gas and liquid. This is immediately followed by insertion into the appropriate magnetic fields to allow for another a few seconds of spin evolution. Subsequently, the tube is inserted into an NMR spectrometer for signal acquisition. It is important to note that the uptake of fresh *para*-H_2 ceases during the evolution time, resulting in a corresponding loss of signal.

3.6.2.2 Bubbling method

PHIP and SABRE is also experimentally achieved by bubbling the *para*-H_2 gas into the sample solution to achieve intense gas-liquid contacting at the macroscale. The simplest and most accessible technique involves bubbling *para*-H_2 gas through a capillary into the NMR sample tube. However, the high-pressure gas jetting from the capillary at the onset of

bubbling can cause liquid to splash, leading to unnecessary evaporation and loss of sample volume. Reducing the pressure and slowing the flow rate during bubbling can minimize splashing to a certain extent, but this may compromise signal enhancement. [127]

Adelabu et al. [128] developed a custom bubbling setup using a standard 5 mm NMR tube to facilitate high-pressure bubbling without causing splashing (Figure 3.18**a**). In this system, the NMR tube is connected to a Y-shaped quick-connect pneumatic fitting via a PTFE tubing (OD: 1/4 inch, ID: 3/16 inch). This fitting is designed with two pipelines (PTFE tubing, OD: 1/8 inch, ID: 1/16 inch): one for bubbling with a capillary tubing (PTFE tubing, OD: 0.9 mm, ID: 0.5 mm) inserted in it, and the other one for releasing the gas. Additionally, a bypass path is established between the two pipelines via T-junctions. By controlling the open and close status of the bypass valve, bubbling can be halted or initiated, respectively. This bypass path balances the pressures at the bubbling gas inlet and the releasing gas outlet, thus enabling splash-free bubbling under high-pressure conditions.

Unlike the shaking method in scenarios of hyperpolarization at ultralow- and high-fields, which requires a wait time at such magnetic fields for spin evolution, this bubbling setup permits simultaneous gas-liquid mixing and spin evolution across all environments. Therefore, it provides a convenient way for studying *in-situ* SABRE and PHIP experiments by simply placing the modified NMR tube at the location of the desired magnetic field strength, whether in zero-and ultralow-field (ZULF) NMR spectrometer [129] or in conventional NMR spectrometer.

In addition to its compatibility with a wide range of magnetic fields, this setup enables the exploration of the effects of various parameters, such as temperature, bubbling time, flow rate, and pressure, on the level of polarization, thereby aiding in the optimization of the hyperpolarization process. However, one drawback of this bubbling setup is that the capillary remaining inside the tube can interfere with the homogeneity of the magnetic field, particularly in high-field NMR measurements, resulting in broader linewidth of the NMR spectrum. This magnetic field inhomogeneity caused by the susceptibility of capillary tubing can be mitigated through shimming procedures performed prior to the hyperpolarization experiments.

Compared to high-field environments, the impact of bubbling tubing left in the mixing chamber on magnetic field homogeneity is much less significant in low-field NMR measurements. Hill-Casey et al. [130] explored a bubbling unit for *in situ* SABRE experiments inside of a commercial Earth's field NMR spectrometer (Terranova-MRI, Magritek). This bubbling unit comprised of a customized glass cylindrical reaction chamber (OD: 28 mm, ID: 24 mm, Length: 24 mm) with an inlet port and outlet port (OD: 4 mm) (Figure 3.18**b**). The *para*-H_2 gas was bubbled through a VitraPOR frit (Robu, Hattert, Germany) with an approximate pore size distribution of 40–100 µm.

During the experiments, the reaction chamber horizontally located inside of the bore of the Earth's field NMR spectrometer, the pressure of *para*-H_2 was maintained at 3.2 bar and 2.8 bar at the inlet and outlet, respectively. With this setup, the polarization transfer process

of SABRE in the low-field regime was explored, including the build-up of polarization as a function of the duration of the PTF, measuring the polarization decay time at the Earth's field, and determination the optimal PTF for ^{1}H SABRE of different substrates.

Although hyperpolarization techniques have expanded the application range of economically viable, portable, and easy-to-operate low-field NMR, these systems still suffer from low resolution in NMR spectra, particularly with crowded chemical shifts. In the analysis of samples with complex components, high-field NMR, offering higher resolution spectra with detailed information of chemical structure and a wider range of pulse sequence options, remains the preferred choice for researchers.

As mentioned previously, the tubing or capillary used for bubbling that remains inside the NMR tube can cause line broadening during high-field measurements. Bruker has developed an automated polarizer, which is still based on the bubbling method but addressed the issue. This polarizer allows for SABRE hyperpolarization at millitelsa field and automated shuttling the hyperpolarized sample solution via helium gas in high-field NMR spectrometer for signal acquisition with different NMR pulse sequences.

Cowley et al. [131] initially used this automated polarizer to validate the performance of their developed iridium N-heterocyclic carbene complexes ([IrCl(COD)(IMes)]) for efficient SABRE hyperpolarization. These catalysts later became as the standard catalyst in SABRE experiments.

As the schematic representation of the polarizer shown in Figure 3.18**c**, the gas-liquid reaction cell is located in a solenoid copper coil for generating the PTF in range from -15 mT to 15 mT . The *para*-H_2 gas is bubbled through into the solution from the bottom of the reaction cell. After a predetermined bubbling time period, the hyperpolarized solution was shuttled to the NMR flow probe for signal acquisition via a liquid transfer line connected to the chamber. The flow rate and the bubbling time of this automated polarizer was computer controlled and thus ensured a high level of reproducibility. Taking these benefits, this setup is also exploited for studying the impact of experimental variables, such as the bubbling time, the pressure of *para*-H_2 in the mixing chamber, and the magnetic field strength on efficiency of SABRE hyperpolarization [120].

Several years later, the automated polarizer was modified to be compatible with Spinsolve benchtop NMR spectrometer [132]. In this work, the *para*-H_2 gas was bubbled through SABRE sample solution in the external mixing chamber, which is connected to a home-built flow cell with fluorinated ethylene propylene (FEP) tubing (Figure 3.18**d**). After a 15 s bubbling period, there is a 3 s delay to release the *para*-H_2. The hyperpolarized sample is then transferred pneumatically with nitrogen gas into a home-built flow cell at the NMR detection area in 0.9 s, followed by a 0.1 s waiting period for the sample to settle for signal acquisition. After each measurement, the pneumatic system drives the sample solution back to the mixing chamber for re-polarization. This automated polarizer offers high reproducibility and facilitates SABRE hyperploarized multi-dimensional spectroscopy.

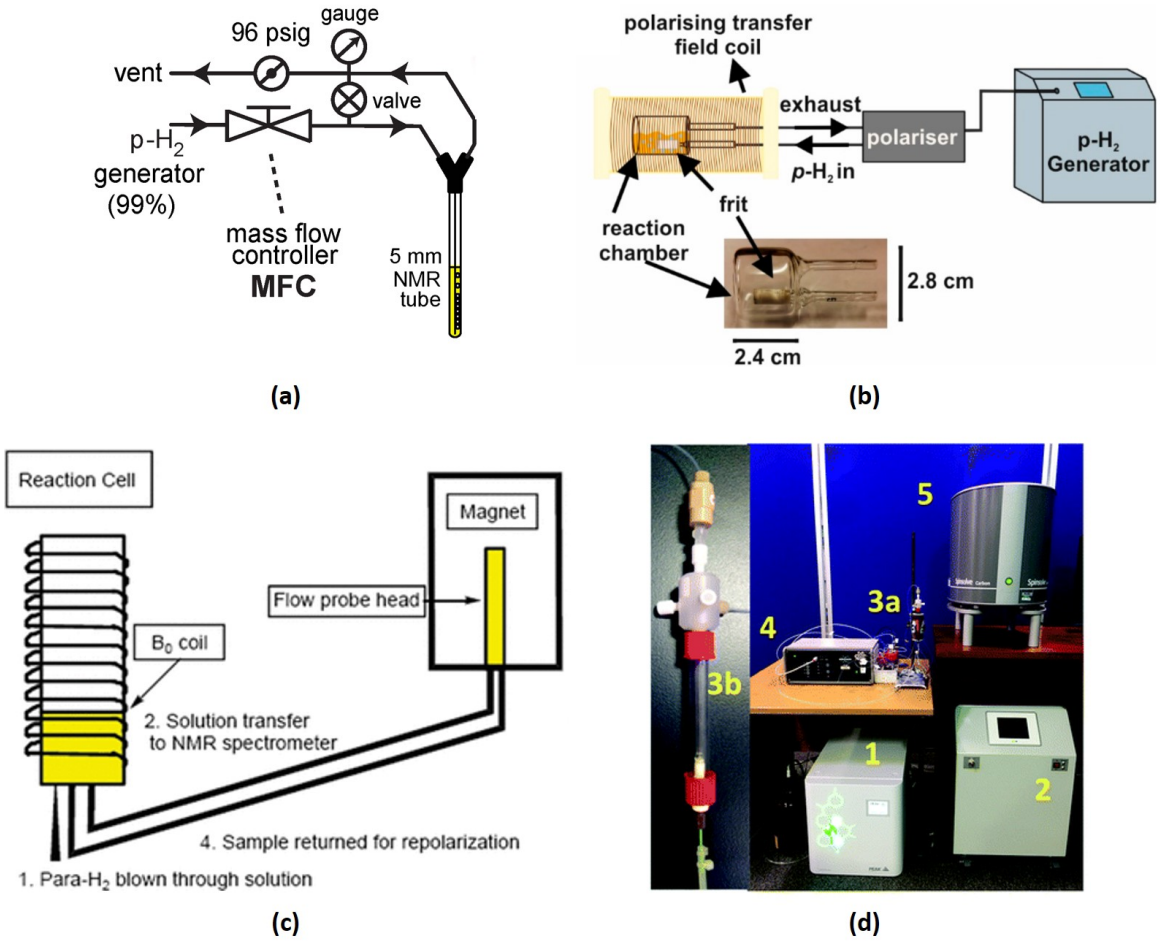

Figure 3.18: Overview of bubbling apparatus used in gas-based hyperpolarization technologies. **(a)** A bubbling setup for SABRE hyperpolarization, consisting of capillary tubing inserted into a 5 mm NMR tube, equipped with valves and a mass flow controller. [128] Copyright © Licensee MDPI, Basel, Switzerland. **(b)** Schematic of a polarizer based on the bubbling method for *in situ* SABRE hyperpolarization and detection at the Earth's magnetic field. [130] *para*-H_2 was bubbled via a porous frit into a reaction chamber located in a commercial Earth's field NMR spectrometer. Copyright © Licensee MDPI, Basel, Switzerland. **(c)** Schematic of an automated polarizer compatible with high-field NMR spectrometer. [131] *para*-H_2 gas was introduced from the bottom of through the solution in the mixing chamber. After a certain bubbling time, the hyperpolarized solution was automated transferred to the high-field NMR spectrometer using helium gas. Copyright © John Wiley & Sons, Ltd. **(d)** An automated polarizer compatible with Spinsolve benchtop NMR. [132] The hyperpolarized sample solution in the mixing chamber (left) is pneumatically shuttled into the flow cell inside of benchtop NMR for signal acquisition. Copyright © The Royal Society of Chemistry 2018. (Adopted from [JY01].)

Although gas bubbling utilizing batch-type hyperpolarization offers its own merits for gas-liquid reaction and for producing hyperpolarized MRI contrast agent [133, 16], the bubbling method at the macroscale still faces the following limitations. Firstly, gas bubbles create havoc with magnetic field homogeneity because the magnetic susceptibility of *para*-H_2 differs from that of the surrounding liquid sample phase. Therefore, the spectral resolution deteriorates significantly. The stop flow strategy has been used to maintain spectral resolution at the cost of losing polarization, due to delay caused by switching off the flow [134] (Figure 3.18**c**). Secondly, it suffers from an inherent gas-liquid mass transfer limitation due to low interfacial areas, which is determined by the surface area of the capillary generated bubbles. Finally, handling flammable and hazardous hydrogen gas in batch hyperpolarization can harbor a severe safety issue.

3.6.2.3 Membrane gas-liquid reactor

With the development of flow chemistry and MEMS technology, the use of membrane-based gas-liquid reactors has been increasingly affirmed in many applications, such as gas stripping, water treatment, and fundamental research such as studying kinetics and mechanisms gas-liquid reactions. [135, 136, 137, 138, 139, 140] These reactors utilize a semi-permeable membrane—often porous or selectively permeable—to separate the reacting media, allowing gases and liquids to flow on opposite sides of the membrane without direct contact. [141, 142, 143]

The membrane provides a stable and significantly larger gas-liquid interface for enhanced mass transfer, reducing the limitations associated with conventional gas bubbling methods. This section gives a brief introduction of strategy utilizing membrane-based gas-liquid reactors for PHIP and SABRE. With various configurations, the membrane reactors demonstrate the ability to achieve continuous and efficient hyperpolarization across a range of NMR detection scenarios.

Roth et al. [144] employed a hollow fiber-based membrane reactor for PHIP experiments at high-field (Fig. 3.19**a**). The hollow fiber membrane acts like a micro sieve, in which the hydrophobicity prevents fluids from wetting the wall of the fibers. The gas diffused through the micropores distributed in the membrane and dissolved in the liquid phase inside the hollow fiber. It has been demonstrated that utilizing the hollow fiber membrane reactors for dissolving hyperpolarized gas substances is fast, robust, and without the formation of foam or bubbles, thus diminishing the deleterious effects on NMR spectral resolution.

In addition to the hollow fiber reactor, a flat membrane configuration has also been explored to accomplish *para*-H_2-based hyperpolarization. Lehmkuhl et al. [119] utilized a flat membrane reactor for continuously achieving high polarization of target molecules via the SABRE method using benchtop NMR systems (Figure 3.19**b**). Moreover, the influence of experimental conditions, such as the flow rate and pressure of both phases, on signal enhancement was studied in detail. In this work, a membrane reactor with meandered microchannels was fabricated by 3D printing, and a composite membrane (poly(ethylene oxide)- poly(butylene

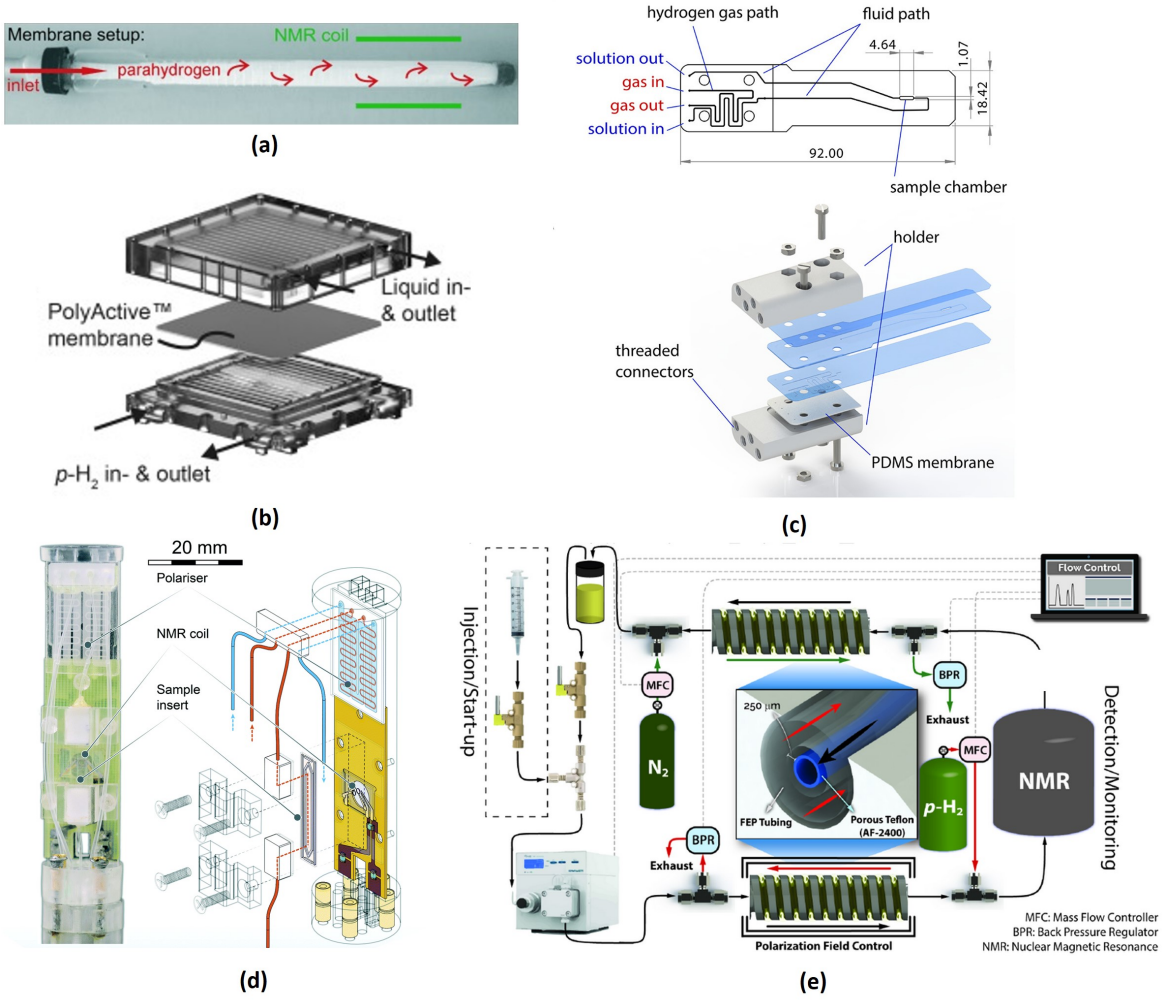

Figure 3.19: Overview of micro gas-liquid reactors in gas-based hyperpolarization technologies. (**a**) A hollow fiber membrane implemented in PHIP [144]. Copyright © 2010 Wiley-VCH Verlag GmbH & Co. KGaA, Weinheim. **(b)** A flat membrane reactor consist of 3D printed channel structure and an embedded PolyActive^{TM} membrane [145]. Copyright 2018 Elsevier Inc. (**c**) Schematic of an on-chip gas-liquid reactor for PHIP with a three-layer configuration of PMMA-PMMA-PDMS [146]. Copyright © 2019 American Chemical Society. (**d**) A micro-SABRE platform consisted of a membrane gas-liquid reactor, a microfluidic chip and a micro-Helmholtz coil for chemosensing [147]. Copyright © The Royal Society of Chemistry 2019. (**e**) A flow reactor system consisted of two tube-in-tube reactors, tee unions, mass flow controllers and pump for producing continuous SABRE hyperpolarization [148]. Copyright © 2021 Wiley-VCH GmbH. (Adopted from [JY01].)

terephthalate) (PEO-PBT) copolymer) was used to separate the gas and liquid phase. During the experiments, the membrane reactor was located near the NMR spectrometer, and the polarized solution was transported to the detection area by a short length of tubing, to minimize loss of polarization via relaxation.

Eills et al. [146] conducted PHIP experiments on a micro gas-liquid reactor compatible with a custom transmission line probe. Thin PMMA sheets with cut channel structures were directly bonded together with a solvent plasticizer (Fig. 3.19**c**). Unlike the sandwich layout of the flat membrane reactor mentioned before, the silicon elastomer PDMS membrane layer attached at the liquid channel side acted as both diffusion media and fluid sealing. *para*-H_2 gas flowing in the gas channel diffused throughout the bulk PDMS membrane and contacted the solution in the liquid channel above the membrane. The performance of PHIP hyperpolarization could achieve high resolution with picomole sensitivity.

Bordonali et al. [147] designed and fabricated a micro gas-liquid reactor for *in situ* chemosensing SABRE processes at a high-field (11.7 T) (Fig. 3.19**d**). The reactor featured a sandwich structure consisting of glass-PDMS membrane-glass. The gas and liquid microchannels with dimensions 300 µm × 100 µm = width×depth were engraved on two 210 µm thick glass substrates respectively by nanosecond laser cutting. A 20 µm thick PDMS membrane fabricated by spin coating was plasma bonded between the channel faces of the two glass layers. This micro gas-liquid reactor was connected via polyethylene (PE) tubing to a microfluidic chip inserted in a custom micro-Helmholtz coil for NMR signal detection. Due to the flexibility of the PDMS membrane, which may deform and block the channels under excessive pressure, a safe working pressure of 2 bar was applied to the gas phase during experiments for safety reasons. This lower pressure difference also leads to a reduced polarization efficiency. Despite these challenges, the signal of the dihydride on the hyperpolarized substrate can still be detected with the highly sensitive micro-Helmholtz coil. The sufficient signal intensity allows it to be effectively exploited as a probe for SABRE-driven chemosensing.

More recently, TomHon et al. [148] utilized a gas-liquid reactor system with a tube-in-tube configuration to yield continuous ^{1}H, ^{13}C, and ^{15}N hyperpolarization on various substrates by SABRE (Fig. 3.19**e**). The highly gas-permeable AF 2400 tubing inserted in an outer FEP tubing significantly increased the mass transfer rate of *para*-H_2. The two tube-in-tube gas-liquid reactors were arranged both upstream and downstream to efficiently deliver and subsequently remove the hydrogen gas. In the secondary tube-in-tube reactor, inert gas with lower pressure with respect to the liquid phase was delivered in the outer tubing to reduce the concentration of the remaining *para*-H_2 gas in the solution flowing in the inner AF 2400 tube. The degassing process enabled a better saturation of the fresh *para*-H_2 gas in the primary reactor, and thus optimized the polarization level. The scalable overlapped length of the inner and outer tubing provides extremely contacting area of the gas and liquid phase. [149, 150] This facilitates highly efficient reaction rate and sufficient polarization level.

In this work, a similar tube-in-tube reactor was employed for hydrogenation of *para*-H_2 on

vinyl acetate at the Earth's field. [JY02] The achieved polarization level of ^{1}H of the generated ethyl acetate molecules was sufficiently high to exceed the RASER threshold. Compared with the bubbling method, the tube-in-tube reactor enables continuous hyper-polarization without the need to introduce a phantom. This feature allows the acquisition of steady-state RASER signals rather than brief RASER bursts that decay within seconds. More detailed information of this work can be found in Chapter 6.

Continuous-Flow Platforms for SABRE and PHIP

4.1 Overview

In the preceding chapter three methods for implementing SABRE and PHIP were compared. Among these, membrane gas-liquid reactors as continuous-flow platforms stand out, offering the unique advantages of enabling in-line measurement of the hyperpolarized signal in continuous flow conditions and flexible control of gas and liquid phases.

This chapter therefore focuses on the design and evaluation of several membrane gas–liquid reactors optimized for *para*-H_2-based hyperpolarization, together with one membrane-free reactor that produces a sandwich multiphase flow by direct gas–liquid contact.

Each continuous-flow platform prototype is outlined from fabrication through proof-of-concept testing using CO_2 gas and a pH indicator solution. While all prototypes underwent initial validation, only a subset were further evaluated in preliminary SABRE hyperpolarization experiments, some of which delivered encouraging results. A concluding feasibility assessment summarizes the remaining challenges and identifies key refinements needed to advance continuous-flow SABRE and PHIP platforms.

4.2 Introduction

In a gas-liquid reactor (contactor), the gas and liquid phases come into contact under stable flow conditions. Based on the flow behavior of the two phases, gas-liquid contactors can be classified into two categories: those with continuous phases and those with dispersed phases.

In continuous-phase gas-liquid contactors, the gas and liquid phases are introduced separately into distinct regions of the contactor. This configuration is typically achieved through two primary methods: falling film and membrane-based systems. In a falling film contactor, the gas and liquid phases interact through a thin, falling liquid film—only a few tens of micrometers thick—that flows down vertical open channels under the influence of gravity. [151] These channels are typically grooved into the surface of a plate using advanced microfabri-

cation techniques, such as dry etching; or using precision 3D-printing to obtain the desired channel structure. Typically, the liquid film measures approximately 100 µm in thickness. This thin, stable film creates a large surface-to-volume ratio, enhancing mass transfer efficiency. However, this approach can also have certain drawbacks, such as partial vaporization. The resulting flow regimes are influenced by various factors, including viscosity, wettability, flow rate, and surface tension. [152]

The second type, membrane gas–liquid contactors, separate the gas and liquid phases into two channels divided by a membrane or mesh. These structures function as selective barriers that, depending on their permeability, allow specific molecules or ions to pass while blocking others. Membranes can be fabricated from dense metals (e.g., nickel), ceramics (e.g., silicon nitride), or polymers (e.g., Teflon, PTFE, or PVDF) [140, 153]. Microstructured meshes created via etching or laser processing typically feature dimensions on the order of 10 µm, while porous membranes such as PTFE or Teflon exhibit pore sizes ranging from tens to hundreds of nanometers.

In a membrane contactor, the gas phase diffuses into the liquid phase through the pores on the membrane. The small size of these pores helps prevent liquid from breaking through into the gas phase, primarily due to capillary forces. However, careful control of operating parameters—such as the pressure difference between the gas and liquid phases—is necessary to avoid such breakthroughs.

In dispersed-phase gas-liquid contactors, the dispersion is achieved by an inlet that combines the gas and liquid streams. [154] The two phases in such system can form different flow regimes, such as bubble flow, slug flow, churn flow, annular flow, mist flow and so on. [155, 156]

The flow regime in a dispersed-phase contactor depends on the operating conditions, including channel dimensions, inlet conditions, phase superficial velocities, liquid surface tension, and the wettability of the channel surface (hydrophilic or hydrophobic). Among these, the gas-to-liquid flow rate ratio is the most critical. If the ratio becomes too high, the flow regime transitions from discrete bubbles and slugs to annular flow. In many practical studies, slug flow is highlighted for especially intense local mass transfer due to the strong recirculation in the slugs and the vigorous interfacial renewal at the Taylor bubble boundaries. Meanwhile, annular flow can achieve comparable or higher overall mass transfer rates if a large fraction of the liquid is entrained as droplets, thereby increasing the effective interfacial area.

In the context of *para*-H_2-based hyperpolarization, once the sample solution has mixed and reacted with *para*-H_2, it is typically analyzed using liquid NMR. Nonetheless, any residual gas bubbles can disrupt the magnetic field's homogeneity, leading to broadening of the NMR signal's linewidth. Therefore, when employing a falling film contactor or a dispersed-phase contactor for SABRE and PHIP, it is necessary to first separate the bubbles from the liquid before introducing the solution into the NMR spectrometer for measurement.

The following sections introduce the different prototypes of gas–liquid contactors fabricated

for continuous-flow SABRE and PHIP platforms during this PhD project. These include three membrane-based gas–liquid contactors for continuous-phase operation, and a direct-contact gas–liquid reactor designed for dispersed-phase systems.

4.3 Membrane-based gas-liquid contactor

The membrane-based contactor offers a particularly advantageous approach, as the membrane consistently isolates the liquid throughout the entire mixing and reaction process. Its simplified operation for both gas and liquid phases make it a more practical choice compared to falling film or dispersed-phase contactors. By employing a membrane design, this approach not only simplifies operations but also provides the flexibility to independently control the gas and liquid phases. This independent control enables more adaptable experimental setups, making it easier to optimize conditions and streamline the overall process.

Typically, a membrane gas-liquid contactor consists of the following parts:

- the membrane, as the core component of the contactor to separate the gas and liquid phases. The porous pores on the membrane only allows for the gas molecule diffuse through and dissolved in the liquid phase.
- the distinct channels for gas and liquid phases, in which the gas and liquid flow on opposite sides of the membrane.
- fluidic distribution system including an inlet distributor and an outlet collector. The inlet distributor ensures the fluid is evenly spread over the membrane surface, preventing areas of excessively high or low flow. The outlet collector guides the processed gas or liquid out of the contactor;
- sealing components such as sealing rings or bonded seals are used around the membrane to prevent gas or liquid leaks. Effective sealing ensures that the gas and liquid phases exclusively interact through the membrane.

The following sections introduce two categories of fabricated membrane gas–liquid contactors, classified according to the configuration of the membrane: flat-sheet membranes and tubular membranes. The structural design and fabrication process of each type will be discussed in detail.

4.3.1 Flat PTFE membrane gas-liquid contactor

4.3.1.1 Configuration of the prototypes

This design employs a commercial porous, hydrophobic PTFE membrane (Aspire QL217, Sterlitech, USA). The membrane has a pore size of 0.2 µm and a porosity of 70%–80%. It is a laminated structure composed of a functional PTFE layer and a polypropylene support layer. The total membrane thickness is 250 µm. The water entry pressure and gas breakthrough pressure are 4 bar and 1.2 bar, respectively.

The first version of the flat PTFE membrane gas-liquid contactor is shown in Figure 4.1. The flat membrane gas-liquid contactor comprises two poly(methyl methacrylate) PMMA

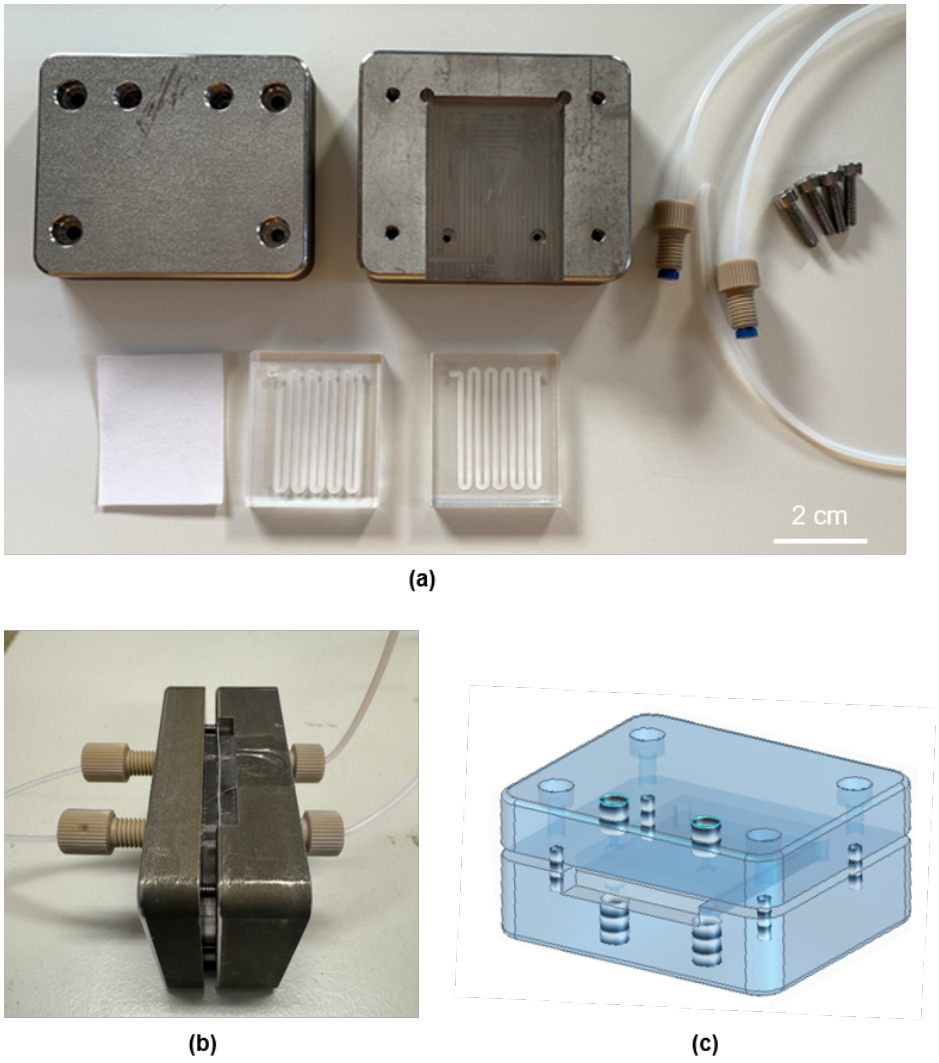

Figure 4.1: **(a)** The main components of the first version flat membrane gas-liquid contactor. **(b)** The assembled gas-liquid contactor with four fluidic connectors (IDEX XP-215) for fitting with the PTFE tubing with OD of 1.6 mm. **(c)** 3D drawing of the assembled gas-liquid contactor.

layers featuring a meandering channel structure (width: 1.5 mm, depth: 1 mm), fabricated using a micro-milling process. A PTFE membrane is sandwiched between these PMMA layers. This PMMA-PTFE-PMMA sandwich structure is clamped in place by the stainless steel upper and lower holders with four screws for sealing of the reactor. In addition, four rubber rings are placed at both top surfaces of each holder to seal the liquid and gas channel inlets and outlets.

However, this configuration is not optimal for fluidic flow because the reactor must remain vertical during experiments (Figure 4.1**b**). Moreover, the stainless steel holder can produce a magnetic field, which may interfere with hyperpolarization experiments conducted in the spin transfer field.

As a result, a second version of the PTFE membrane gas-liquid reactor was developed with improvements in both holder material and fitting arrangement. The aluminum holders, manufactured via CNC machining, each feature two circular observation windows. The four fittings were repositioned to the side surfaces of each holder (Figure 4.2). Additionally, a 3D printed positioner is made for alignment of the two channel layers. Two tailored designed set screws replaced the four smaller screws used in the first version of the reactor, simplifying the assembly process.

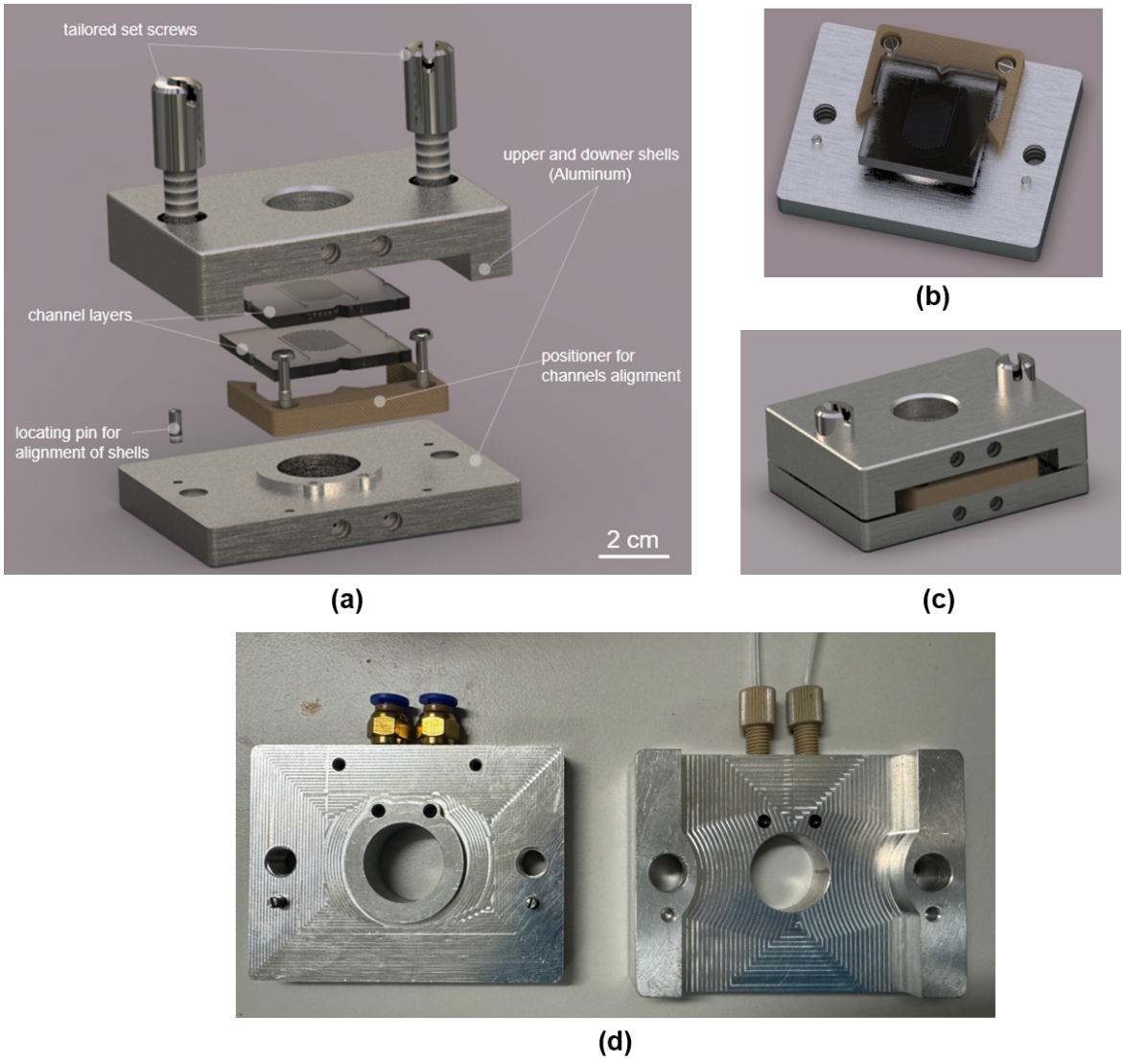

Figure 4.2: **(a)** Explosion view of the flat membrane gas-liquid contactor. **(b)** The channel layers aligned with the 3D-printed PEEK positioner. **(c)** 3D drawing of the assembled flat-membrane contactor. **(d)** Photo of the manufactured holder parts connected with fittings for gas and liquid solution.

4.3.1.2 Test of the prototype with SABRE hyperpolarization

Here, the prototype of the second version was preliminarily tested with ^{1}H SABRE hyperpolarization of pyridine at Earth's field.

The SABRE sample solution contained 3 mmol/L standard homogeneous SABRE pre-catalyst [IrCl(COD)(IMes)] and 60 mmol/L of pyridine dissolved in degassed methanol-d_4. The prepared sample solutions were deposited in two Falcon tubes and capped tightly until activation. The pre-catalyst in the sample solution was activated by bubbling normal H_2 at a flow rate of 20 sccm, ambient pressure, and room temperature (25°C) for 10 minutes. The *para*-H_2 with an enrichment level of 50% was generated using a liquid nitrogen *para*-H_2 generator (HyperSpin Scientific, Germany).

Throughout the experiments, the sample solution was initially pumped into the liquid channel of the prototype using a peristaltic pump (BT100-2J, LongerPump, China) at a flow rate of 1 mL/min. The sample solution was then directed towards the detection area of the Spinsolve NMR spectrometer using PTFE tubing (OD: 1.6 mm, ID: 0.8 mm) inserted into the bore of the magnet. Subsequently, the sample solution was subjected to NMR analysis in reaction monitoring mode. Here, a 90-degree pulse was applied every 15 seconds. After acquiring the NMR signal at thermal equilibrium as a reference, 50% *para*-H_2 was introduced into the gas channel in a counter-current flow at a controlled rate of 10 mL/min via a mass flow controller (MFC).

As depicted in the figure, a total of 20 acquisitions were recorded over a period of less than 8 minutes. The spectra of the sample solution, hyperpolarized using SABRE at Earth's magnetic field, display two enhanced antiphase peaks corresponding to the proton nuclei at the *ortho* (highlighted in red) and *para* (highlighted in green) sites on pyridine (Figure 4.3).

4.3.1.3 Challenges of the flat PTFE membrane gas-liquid reactor in SABRE and PHIP hyperpolarization applications

Firstly, the poor spectral resolution observed during the proof-of-concept experiments is primarily attributed to the mismatch between the inner diameter of the PTFE tubing (0.8 mm) and the detection region of the NMR coil (5 mm). This size disparity results in a low filling factor, thereby reducing the signal quality. This limitation can be mitigated by incorporating a glass flow cell with an expanded internal diameter (see more details in section 4.3.4.4), providing a larger detection volume and improving the filling factor of the NMR coil, ultimately enhancing signal acquisition.

Besides, the prototype of the second version encountered sealing issues after being used multiple times. Gas bubbles were observed at the interface between the PMMA and the PTFE membrane, suggesting that the sealing provided by mechanical force through screws is inadequate for maintaining airtight integrity. This issue highlights the need for revising the sealing approach to ensure reliable performance of the reactor under operational conditions.

4.3.2 Micro gas-liquid contactor with flat PDMS membrane

This section describes a flat PDMS membrane micro gas-liquid contactor designed to be compatible with a custom micro-NMR detector (LiquidVoxel^{TM}, Voxalytic GmbH, Germany) for

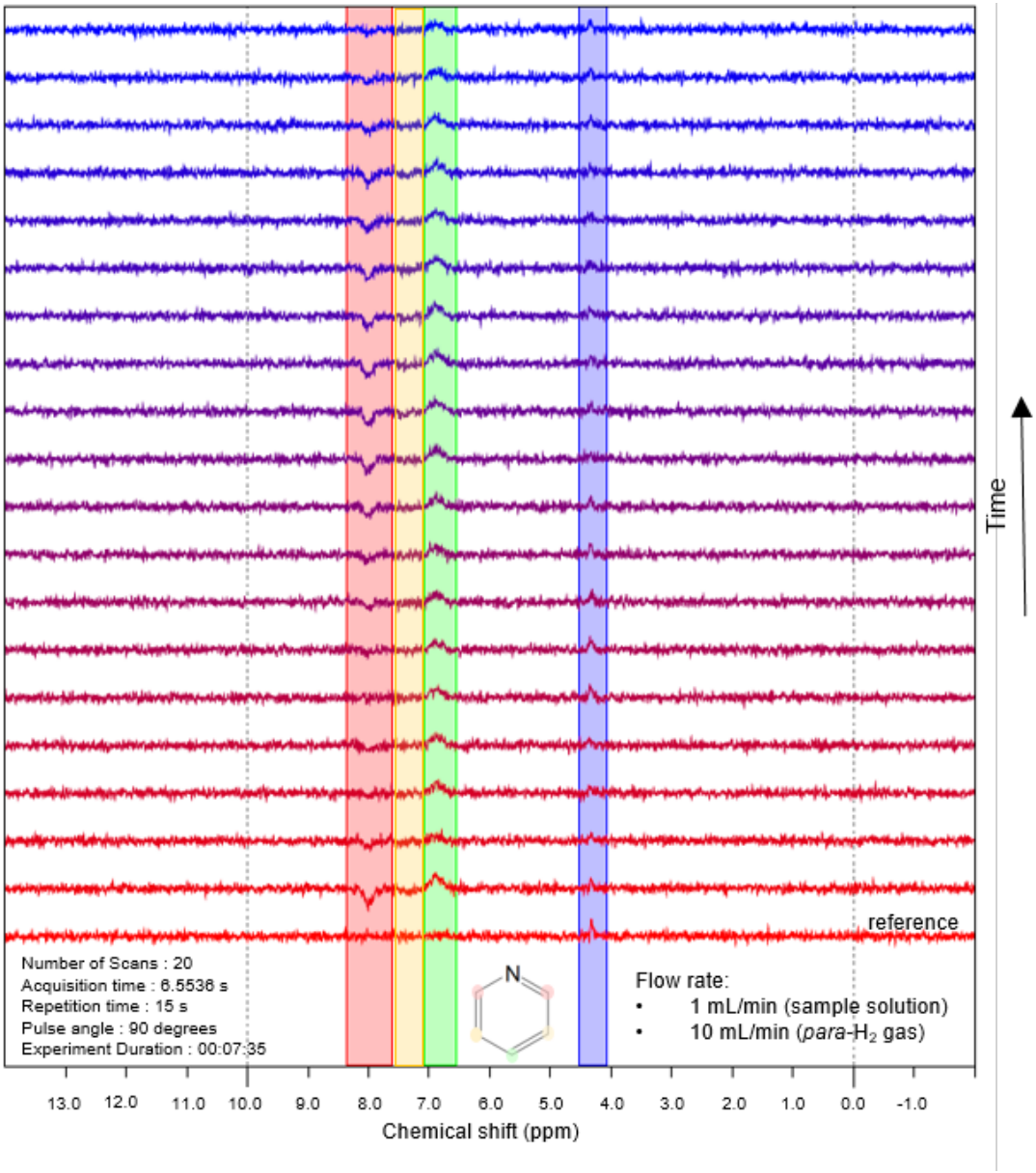

Figure 4.3: Stacked NMR spectra of the sample solution hyperpolarized using SABRE in a prototype flat PTFE gas-liquid reactor. The bottom spectrum serves as a reference and represents the sample solution at thermal equilibrium, acquired before introducing *para*-H_2 into the reactor. The sample solution consisted of 3 mmol/L pyridine and 60 mmol/L standard Ir-IMes SABRE catalyst, all dissolved in deuterated methanol.

measurements in an 11.74 T magnet (ELMAR, Bruker, Germany) (Figure 4.4). The micro-Helmholtz coil pair is embedded between two glass chips. The vertical spacing between the coils is 0.5 mm, allowing for the insertion of a chip with dimensions of 5 mm × 0.5 mm (width × height). Due to these dimensional constraints, the compatible microfluidic gas-liquid contactor integrates two functional components: a gas-liquid contactor positioned outside the micro-Helmholtz coil, optimizing the contacting area for the gas and liquid channels, and a microfluidic chip with a circular reservoir for sample measurement inserted into the micro-Helmholtz coil. (Figure 4.5).

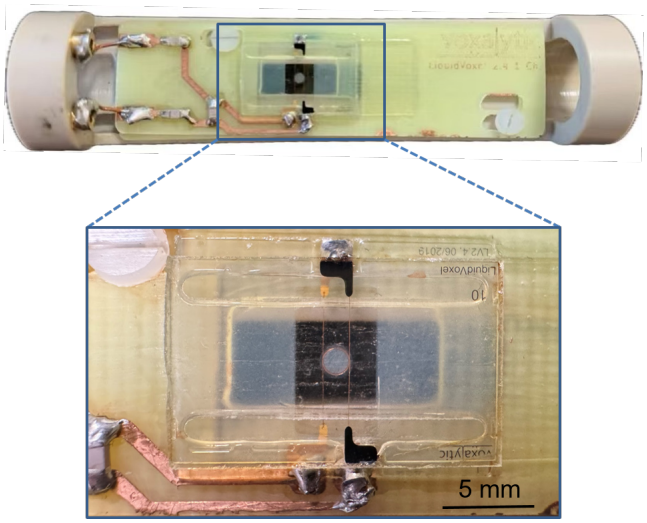

Figure 4.4: The micro-NMR detector (LiquidVoxel^{TM}) equipped with 1.2 mm diameter micro-Helmholtz coil pair.

In the micro gas-liquid reactor, the liquid channel features 185 mm long meandering channel with a cross-section of 0.2 mm×0.1 mm = width×depth while the gas channel is 85 mm long with the cross-section of 1.2 mm×0.1 mm = width×depth (Figure 4.5). The two channels are arranged in a crisscross pattern to provide sufficient bonding area for the PDMS membrane. The total area available for the exchange of gaseous species is 16.18 mm^2. The reservoir on the inserted chip has a diameter of 1.5 mm and a depth of 0.1 mm, providing a detection volume of 0.18 µL (Figure 4.5). The 50 µm-thick PDMS membrane serves as both a porous membrane for gas exchange and a sealing basket for the gas and liquid channels on the glass substrate.

4.3.2.1 Fabrication of micro gas-liquid reactor

The patterns for the meandering channels on the gas and liquid sides of the reactor were engraved on a 4-inch, 210 µm-thick square borosilicate glass wafer (263D-Eco Schott) using a nanosecond UV laser (PIRANHA, ACSYS, Germany) pulsing at 30 kHz. Two inlet and two outlet holes (0.5 mm diameter) were fabricated by completely cutting through the glass layer of the gas sides with the laser. The wafer was diced by laser around the perimeter of the reactor halves (Figure 4.5**a**). After fabrication, the two halves with engraved channels were sequentially cleaned in an ultrasonic bath with acetone, isopropyl alcohol (IPA), and deionized (DI) water. Subsequently, the two glass halves with engraved channels were dried under pressurized nitrogen flow and baked at 200 °C for 2 hours. Completely drying the surfaces intended for bonding is essential to achieve a strong glass-PDMS bond.

Meanwhile, the thin PDMS membrane was fabricated by spin coating of the PDMS elastomer solution prepared using the standard 10:1 elastomer-to-binding agent ratio. A 125 µm Kapton film sheet was cut into a 4-inch round shape, cleaned with IPA and dried under nitrogen gas flow at 70 °C for 10 min. The Kapton film was vacuum-clamped on a spin-coater (SCC-200, Quantum Design GmbH, Germany) and 2.5 mL of PDMS solution was statically

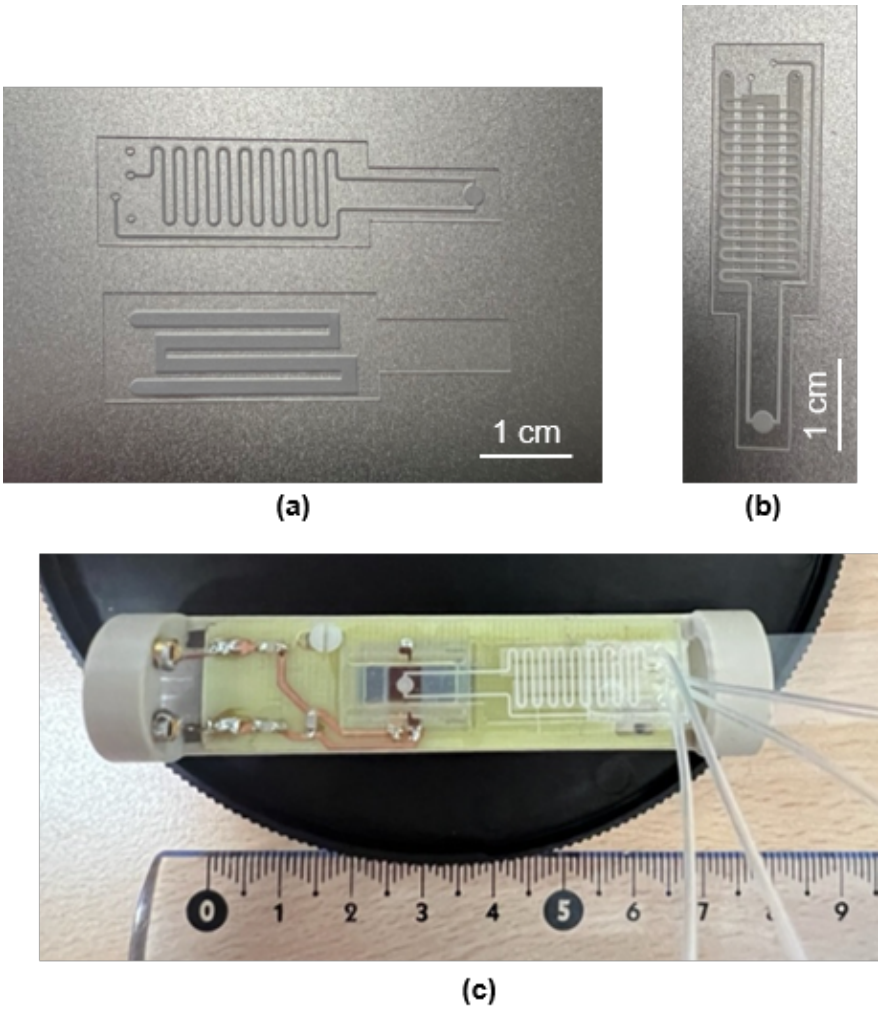

Figure 4.5: **(a)** The gas and liquid channels fabricated on borosilicate glass wafer with nanosecond laser cutting system. **(b)** The alignment of the two glass substrate layers. **(c)** The bonded micro gas-liquid reactor as a chip inserted in the micro-NMR detector. The circular reservoir with detection volume of 0.18 µL located in the center of the micro-Helmholtz coil.

dispensed and spun at 1500 rpm for 3 min to achieve a uniform layer of 50 µm thick PDMS film. The Kapton handling film was transferred to a hot plate and baked at 120 °C for 5 min for curing the silicon film.

The bottom half of the reactor (gas side) was prepared for bonding to the PDMS membrane by activating the contact glass surface in an oxygen plasma cleaner at 200 W RF power for 10 min. The PDMS was similarly activated by driving the plasma cleaner at 50 W RF power for 60 s. After the plasma treatment, the Kapton-supported PDMS film was then immediately attached to the activated surface of the gas side under a standard laminator (Mylam 12, GMP, Germany) at room temperature and roll speed of 1 cm/s. After a waiting time of 10 min the Kapton film layer was peeled off from the bonded PDMS film. The exposed PDMS and the second glass half (liquid side) were then treated with oxygen plasma under the same conditions for PDMS and glass surface activation, respectively. Finally, the top half (liquid side) was aligned to the bottom half (gas side) under a microscope and brought into contact

with the activated PDMS layer. The completed stack with the sandwich configuration of glass-PDMS-glass was placed on a hot plate set at 90°C for 2 h under mechanical pressure, to further increase bond strength at the glass-PDMS interfaces (Figure 4.5**b**).

A PDMS block fitting was tailor-cut to couple the polyethylene tubing (OD: 0.97 mm, ID: 0.51 mm, BTPE25, Instech Laboratories, Germany) to the contactor inlets and outlets, secured in place by oxygen plasma bonding (Figure 4.5**c**).

4.3.2.2 Proof of the prototype

To demonstrate the performance of the fabricated prototype, the pH indicator bromothymol blue (BTB) solution and CO_2 gas were used to visualize the pH change as CO_2 dissolved into the sample solution, indicated by a change in color. In solutions with a pH of 6.4 or lower, BTB appears yellow, whereas in solutions with less dissolved CO_2 (pH above 7.1), it appears blue. The BTB sample solution was prepared by dissolving 0.1 g of BTB powder into 3.2 mL of a 0.05 mol/L NaOH solution, and then diluting with DI water to a total volume of 200 mL, resulting in a pH of 8.1.

During the experiment, the BTB sample was delivered to the micro gas-liquid reactor at a flow rate of 200 µL/min using a syringe pump, while CO_2 gas was introduced into the gas channel at a flow rate of 10 mL/min and a pressure of 23 psi, regulated by a mass flow controller (MFC) and a back-pressure regulator (BPR). As shown in Figure 4.6, the blue BTB sample solution is introduced into the liquid channel of the micro gas-liquid reactor successfully demonstrated that CO_2 gas diffused through the PDMS membrane and dissolved into the BTB solution, resulting in a pH decrease and a corresponding color change from blue to greenish yellow.

4.3.2.3 Challenges of micro gas-liquid reactor in application of SABRE and PHIP hyperpolarization

Although the prototype of the micro gas-liquid reactor was successfully demonstrated using CO_2 gas and aqueous BTB solution, it faces several challenges when applied to SABRE and PHIP hyperpolarization experiments.

A significant issue is the deformation of the thin PDMS membrane when subjected to gas pressures exceeding 2.5 bar. Such deformation often leads to clogging of the liquid channel with the height of 100 µm. Consequently, the allowable pressure difference between the gas and liquid phases is restricted, which in turn limits the mass transfer efficiency of *para*-H_2 into the sample solution.

Additionally, methanol, the solvent most commonly used in SABRE and PHIP hyperpolarization experiments, aggressively attacks the covalent Si–O–Si bonds formed during the oxygen plasma bonding of PDMS to glass, thereby weakening the adhesion at the bonding interface. When the sample solution flows for more than 5 minutes, the bond between the PDMS and the glass chip fails, resulting in a compromised seal of the micro gas-liquid reactor.

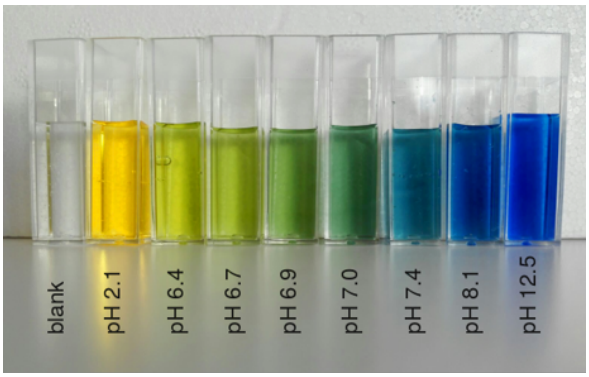

(a)

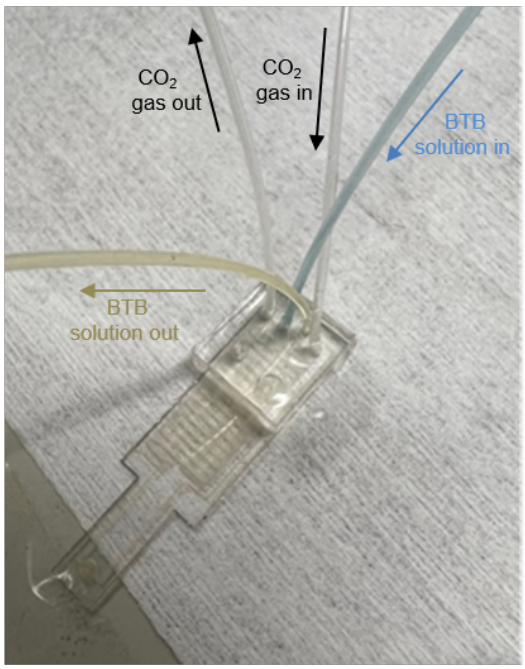

(b)

Figure 4.6: Proof of the micro gas-liquid reactor prototype by measuring dissolved CO_2 gas with a BTB sample solution as a pH indicator. **(a)** Different colors of BTB solution at different pH values. [157] Copyright © John Wiley & Sons, Ltd. **(b)** Testing the fabricated micro gas-liquid reactor prototype, the dissolved CO_2 caused the color of BTB solution changes from blue to greenish yellow as it flowed through the liquid channel.

4.3.3 Gas-liquid reactor based on PDMS matrix with bonded PMMA layers

In this section, a new version of gas-liquid reactor compatible with the 10 mm saddle coil at high-field NMR spectrometer (11.74 T, Bruker) was fabricated. The gas-liquid reactor comprises a microfluidic chip, a PDMS matrix, and a chip holder with microfluidic fittings (Figure 4.7**a**). The PDMS matrix with the thickness of 1 mm serves a dual purpose: it functions as both the membrane material and a sealing gasket for the microfluidic chip.

The microfluidic chip is composed of three layers of PMMA sheet (0.5 mm × 10 mm ×

150 mm = height×width×length). The meandering gas on the bottom layer of the microfluidic chip features a width of 300 µm and a total length of 55 mm. The liquid channel with the same meandering manner located on the same layer parallel to the gas channel with distance of 600 µm (Figure 4.7**b**). This differs from conventional flat membrane gas-liquid reactors, where the gas and liquid channels are positioned on opposite sides of the membrane. In this design, gas molecules first diffuse into the PDMS block, then spread throughout the entire PDMS matrix, and ultimately diffuse into the liquid phase. After coming into contact with the gas molecules, the liquid sample flows along the channel into the middle layer, where it reaches a 5 mm-wide reservoir for NMR detection. The open channel on the middle layer was sealed by another piece of blank PMMA sheet as a cover layer. As illustrated in the assembly drawing in Figure 4.7**c**, half of the reservoir's length is positioned within the 10 mm saddle coil, providing a detection volume of 25 µL for the sample solution.

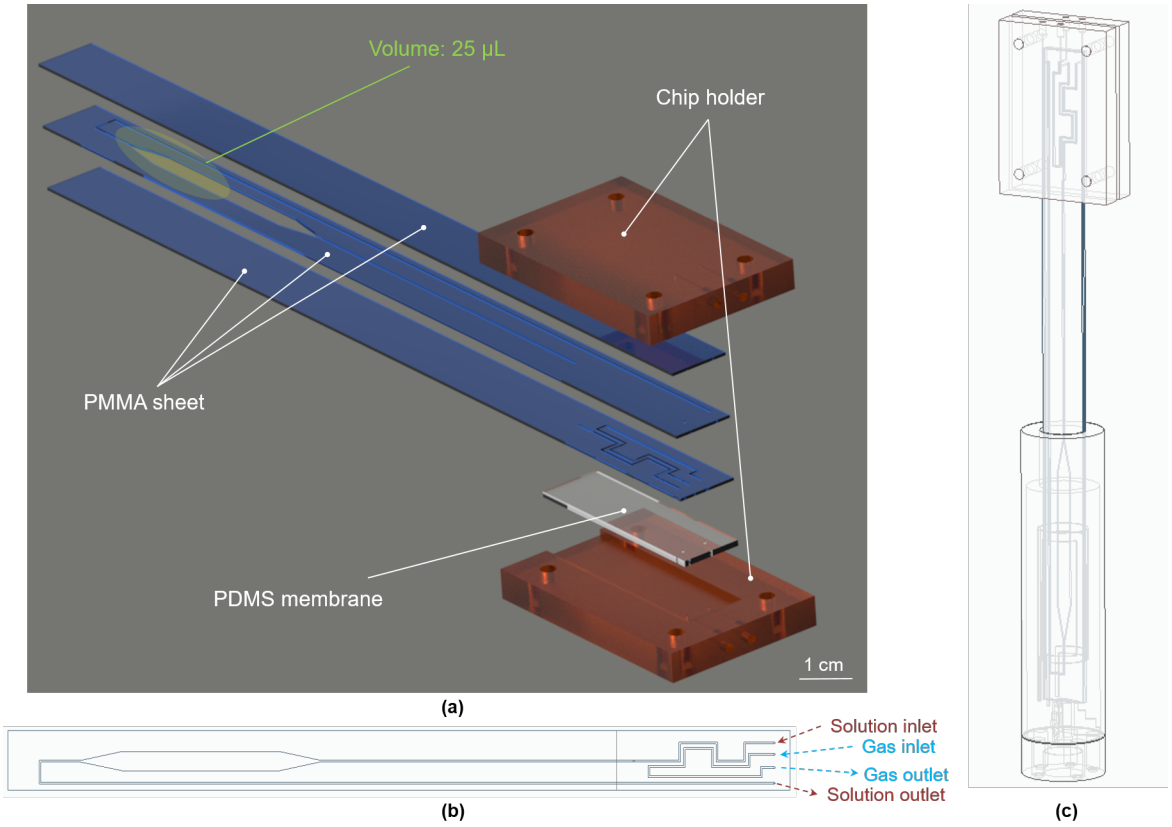

Figure 4.7: **(a)** Explosive drawing of the gas-liquid reactor based on PDMS block and PMMA sheet. **(b)** Assembly drawing of the gas-liquid reactor located in the 10 mm saddle coil. **(c)** Top view of the microfluidic chip.

4.3.3.1 Fabrication of the prototype

The single layer PMMA sheet of the microfluidic chip were fabricated using a CO_2 laser cutter (Universal Laser Systems, VLS 3.50) equipped with a laser diode operating at a wavelength of 630–680 nm and a maximum power of 1 mW. The 2D design of the channel structure for each layer was created using CorelDraw software. These patterns were then laser-cut onto the 0.5 mm thick PMMA sheets using cutting parameters of 8% power intensity and a

cutting speed of 4 mm/s, which were sufficient to achieve a clean and precise cut through the material.

Prior to the bonding experiments, the thermoplastic substrates were ultrasonically cleaned (Sonorex Super RK 100 H, Bandelin, Germany) using isopropyl alcohol (IPA) solution for 10 min for the removal of debris and dust. The substrates were then rinsed and washed using DI water and dried on a hotplate at 70°C for 10 min.

The cleaned, laser-cut PMMA sheets were then assembled using the solvent bonding method, which employs specific organic solvents to dissolve polymer chains at the surface. The dissolved polymer chains diffuse across the interface and re-crosslink with those from the opposing substrate, creating entanglement through mechanical interlocking of the diffusing chains, and ultimately forms a durable and permanent physical bond. [158] Solvent bonding method enables strong adhesion at low temperatures with minimal equipment requirements compared to other bonding methods (thermal bonding, ultrasonic bonding, and adhesive bonding). [159]

In this bonding process, ethanol was selected as the bonding solvent due to its low toxicity and widespread use with thermoplastic substrates such as PMMA, cycloolefin copolymer (COC), polycarbonate (PC), and polyethylene terephthalate (PET). Ethanol can effectively dissolve these materials without compromising their optical properties.

During the bonding process, ethanol was applied to the surface of the PMMA sheet by dispensing 0.1 mL per square centimeter of bonding area onto the blank cover layer. The middle layer was then aligned and placed in contact with the treated surface. The same procedure was repeated to bond the middle and top layers. After assembly, the three-layer chip was placed in an oven at 90°C and pressed under a metal weight overnight to ensure a strong and uniform bond.

The rectangular chip holder was fabricated using CNC machining, with microfluidic fittings (thread size: $1/4 - 28$ UNF) arranged perpendicular to the chip surface (Figure 4.8**b**). However, this design requires a large lateral space for the fittings, making it unsuitable for insertion into the NMR probehead. To address this limitation, a redesigned chip holder was developed with a cylindrical outer shape and microfluidic fittings (thread size: 10-32 UNF) oriented longitudinally along the chip's length, minimizing space requirements (Figure 4.8**c**).

4.3.3.2 Proof of the prototype

The prototype of the fabricated gas-liquid reactor, incorporating a PDMS matrix and a bonded PMMA chip, was demonstrated using CO_2 gas and the BTB solution as a pH indicator. The prepared BTB solution with a pH of 8.1 exhibited a blue color. More details about the preparation of BTB solution can be found in section 4.3.2.2.

The BTB sample solution was continuously pumped with a syringe pump with flow rate of 100 µL/min into the reactor until filling all the liquid channel. The CO_2 gas was then introduced into the gas channel with flow rate of 10 mL/min controlled with a MFC.

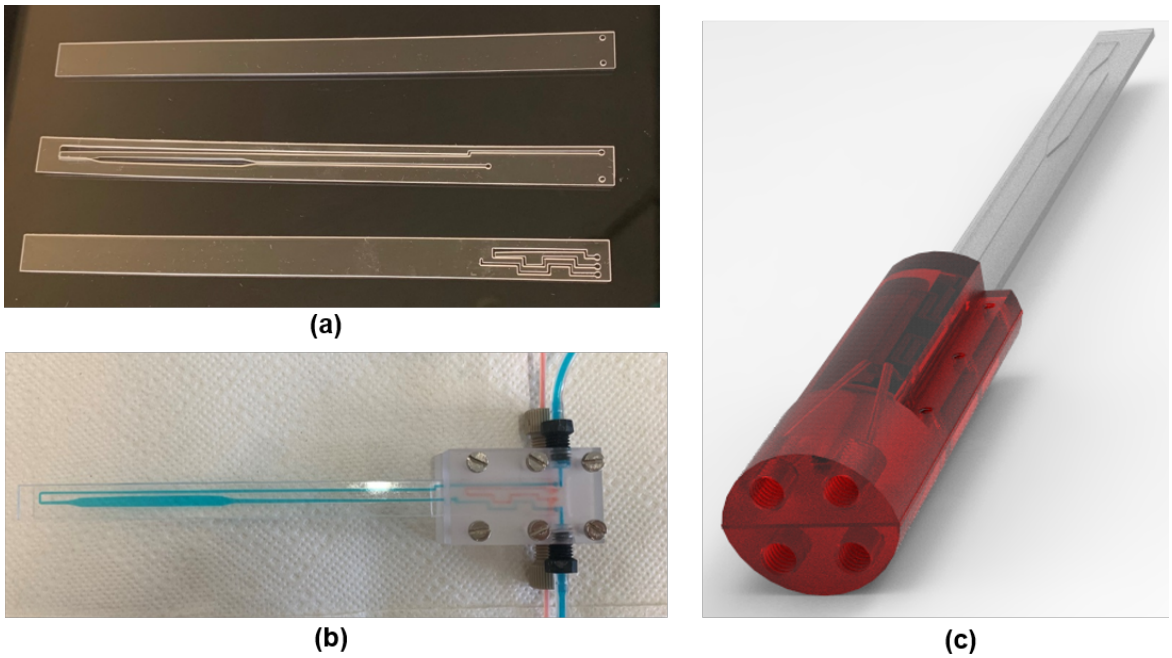

Figure 4.8: **(a)** Three laser-cut PMMA sheets with the corresponding channel patterns. **(b)** Bonded microfluidic chip integrated with a CNC-machined chip holder. The channels are filled with red and blue ink solutions, representing the gas and liquid flow paths, respectively. **(c)** 3D structure of the new version chip holder with more compact arrangement for microfluidic fittings.

As shown in the captured images of the reactor during the experiment (Figure 4.9**a-c**), the color of the solution in the reservoir gradually shifts from blue to greenish-yellow as the BTB sample solution is continuously pumped through the channel after interacting with CO_2 gas.

Another set of experiments was conducted with a lower liquid flow rate of 10 µL/min, while keeping the gas flow rate unchanged. After interacting with CO_2 gas, the BTB solution exhibited a bright yellow color (Figure 4.9**d**). The reduced flow rate resulted in a longer residence time of the BTB solution within the reactor, allowing for more efficient mass transfer and increased CO_2 dissolution in the solution.

4.3.3.3 Challenges of the prototype in application of SABRE and PHIP hyperpolarization

The prototype test for SABRE hyperpolarization failed due to leakage issues, which occurred after less than 30 min of sample flow with a methanol-based SABRE or PHIP sample solution. The primary cause was the insufficient strength of the solvent-bonded PMMA, which was unable to withstand prolonged exposure to methanol.

Additionally, in this design, *para*-H_2 diffuses into the PDMS matrix and disperses throughout before interacting with the sample solution in the liquid channel. This configuration may pose a potential safety concern, as part of the PDMS matrix is exposed to air, allowing *para*-H_2 to escape from the reactor.

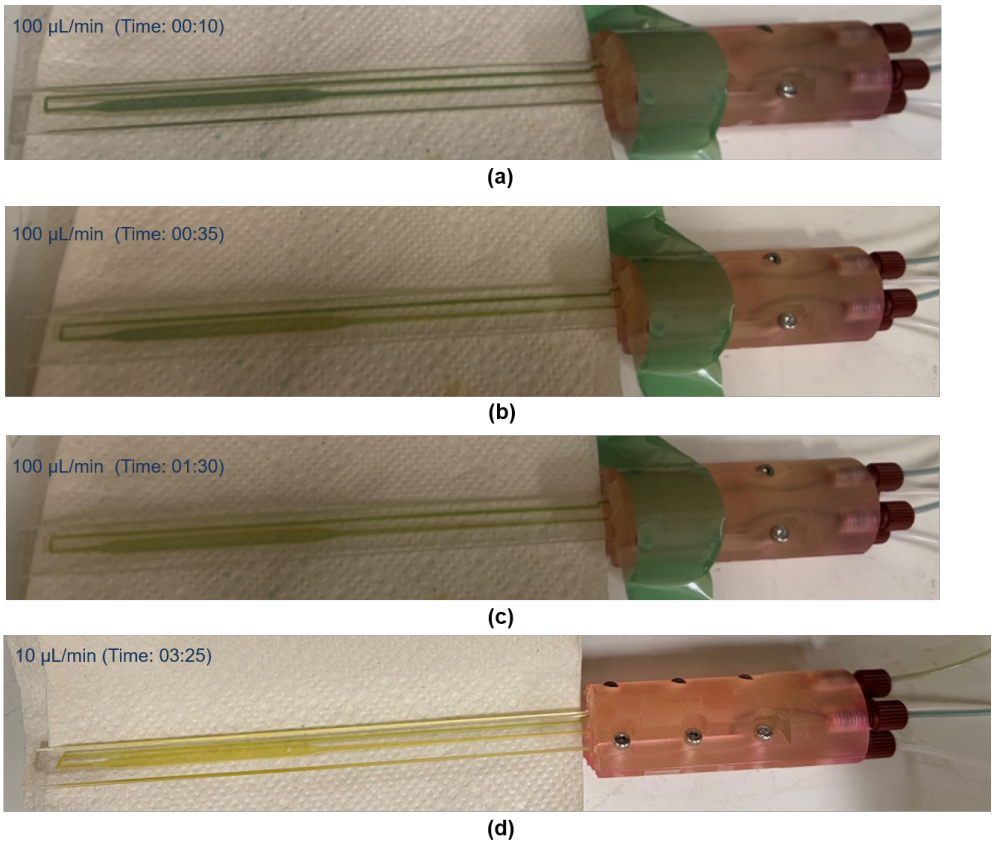

Figure 4.9: **(a)**–**(c)** Photos of the gas-liquid reactor with a BTB sample solution flowing at 100 µL/min. **(d)** At a lower BTB solution flow rate of 10 µL/min, the solution entering the reservoir exhibited a more intense yellow color.

Furthermore, the long mass transfer distance for gas diffusion results in lower gas-liquid reaction efficiency. This issue can be mitigated by reducing the liquid flow rate to extend the residence time, thereby enhancing gas dissolution. However, a lower flow rate also increases the delivery time of the HP sample solution to the detection reservoir, leading to signal loss due to relaxation, ultimately reducing the detected NMR signal intensity.

4.3.4 Tubular membrane gas-liquid reactor

Membrane reactors can be classified based on their configuration into several types, including flat-sheet membranes, spiral-wound membranes, and tubular membranes. Among these, tubular membrane reactors, characterized by their cylindrical geometry, offer distinct advantages over other configurations.

Due to their structural and operational versatility, tubular membrane reactors have been widely adopted in both industrial and biological applications. Their modular design enhances flexibility and scalability; the number of membrane modules (such as hollow fiber membranes) or the total length of the tubing can be easily adjusted to accommodate different throughput and operational demands. [141, 160]

Furthermore, the unique tubular architecture of these reactors enables the emulation of tissue-like environments, analogous to networks of arteries, veins, and lymphatics in living systems. [161] This makes them particularly valuable in bioreactor applications, where such conditions are essential for mimicking physiological processes and improving the efficiency of biochemical reactions. [162]

In this section, a gas-liquid reactor with configuration of tube-in-tube based on a commercial tubular membrane (Teflon^{TM} AF 2400) is introduced. First, the gas permeable property of AF 2400 is explained, followed by the configuration of a tube-in-tube gas-liquid reactor using AF 2400 tubing.

4.3.4.1 Material properties of AF 2400 membrane

The material of the tubular membrane AF 2400 is an amorphous glassy copolymer of fluoroethylene and perfluorodioxolane. It is known for the excellent gas permeability for various gases (i.e., NH_3, H_2, O_2, CO_2) and resistance to aqueous and organic solvents due to their unique molecular structure. For instance, the H_2 gas permeability of AF 2400 tubing is more than 220 times greater than that of PTFE tubing [163]. The amorphous fluoropolymers lack the tightly packed crystalline regions typical of semi-crystalline polymers, which allows for more free volume within the material. This free volume creates pathways that facilitate the easier transport of gases, contributing to their high permeability. The highly electronegative fluorine atoms in these polymers form a protective barrier around the polymer chains, providing a shield that resists interaction with other molecules. Therefore, amorphous fluoropolymer material is hydrophobic (water-repellent) and oleophobic (oil-repellent), which is impermeable to (non-fluorinated) liquids and resistant to a wide range of corrosives.

Moreover, fluoropolymers are generally chemically inert due to the strong carbon-fluorine bonds. [164] These bonds are among the strongest in organic chemistry and resist breaking down or reacting with most other chemicals, including organic solvents. These properties make amorphous fluoropolymers as ideal material for applications of continuous flow chemical reactions that require precise control over the contact time and conditions between gases and liquids, such as catalytic hydrogenation reactions, gas absorption processes.

In addition to its high gas permeability and chemical resistance, AF 2400 also features a low refractive index, which minimizes light scattering and reflection. This characteristic is especially advantageous for applications that require optical clarity and minimal light interference, such as protective coatings and anti-reflective coatings for optical devices. [165, 166]

4.3.4.2 Configuration of tube-in-tube gas-liquid reactors based on AF 2400 tubular membrane

As it shown in Figure 4.10**a**, the AF 2400 tubing (ID: 0.8 mm, OD: 1 mm) as an inner tubing inserted in an outer PTFE tubing (ID: 1.6 mm, OD: 3.2 mm). Their concentric inner and outer ends are typically connected with Swagelok tee union or T-type connectors with thread

compatible to microfluidic flangeless fittings (Figure 4.10**b**). The overlapped length of the inner and outer tubings is extendable to provide extremely large interfacial area between the gas and liquid phases and can be wrapped to be more compact. Furthermore, the wall thickness of the AF 2400 tubing is approximately 100 µm, and the inner radius is 400 µm, resulting in a short mass transfer distance.

Therefore, the high gas permeability, large interfacial area, and short mass transfer distance of the tube-in-tube reactor contribute to significantly higher liquid volumetric mass transfer coefficients, ranging from 0.1 to 1.0 s^{-1} [149], and enable efficient gas-liquid contact.

Generally, for the implementation of gas-liquid reactions, the liquid flows within the inner tubing while the gas flows in the outer tubing. The flow directions of the gas and liquid can be configured either in countercurrent or co-current flow arrangements. With a positive pressure differential between the gas and liquid phases, the gas molecule diffused across the tubular membrane (wall of inner tubing) and dissolved in the liquid phase.

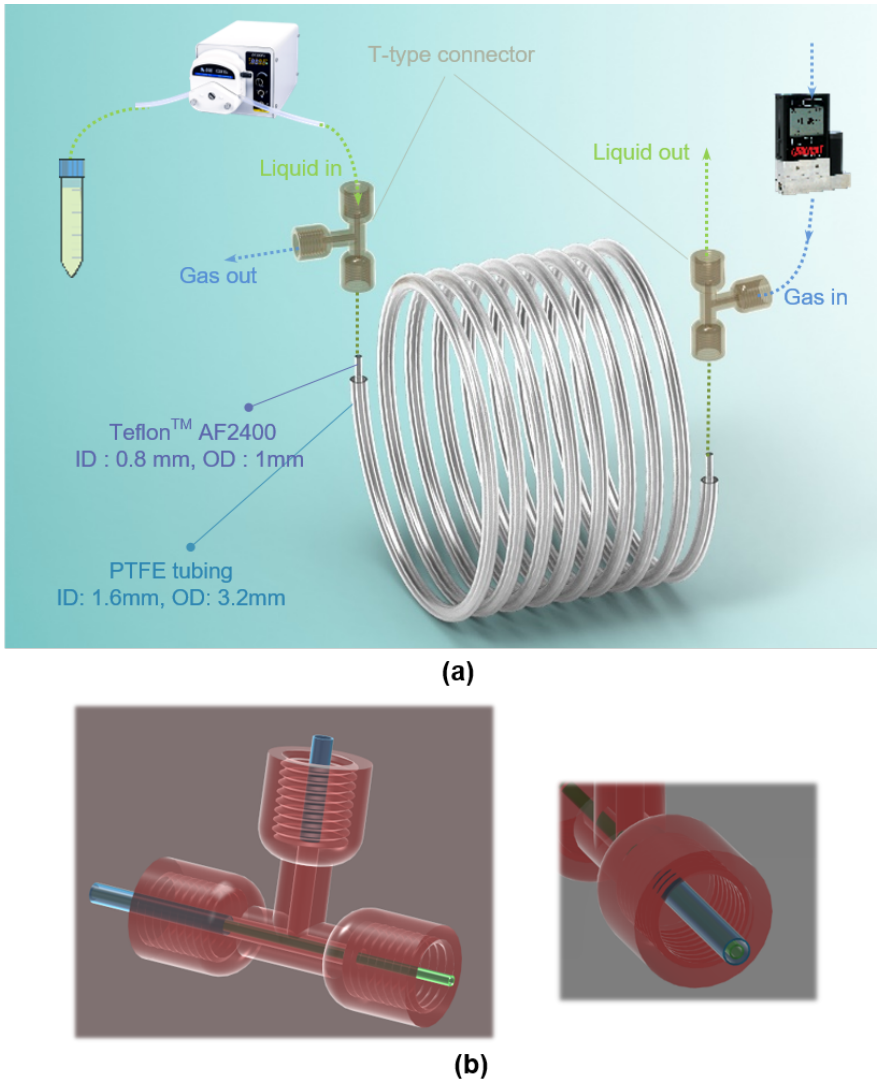

Figure 4.10: **(a)** Representation of a continuous flow setup based on tube-in-tube gas-liquid reactor.**(b)** Sketch of the T-type connector for assembling the inner and outer tubings.

4.3.4.3 Proof of the prototype

To assemble the tube-in-tube reactor, two T-type connectors with female thread size of 1/4 − 28 UNF were 3D printed using an SLA 3D printer (Photon Mono 4K, Anycubic, China). A 510 mm long inner tubing AF 2400 and a 450 mm long PTFE outer tubing were fitting with the microfluidic fittings (ID-XP-230X, IDEX), and then concentrically assembled with the T-type connectors to form the tube-in-tube reactor with an overlapped tubing length of 450 mm.

To demonstrate the performance of the tube-in-tube reactor, a BTB solution was employed as the pH indicator in the liquid phase, and CO_2 gas was used as the gas phase. The BTB solution was prepared at a pH value of 8.1, exhibiting a blue color. More details on the preparation of the BTB solution can be found in Section 4.3.2.2.

The BTB solution was initially pumped into the AF 2400 tubing using a peristaltic pump (BT100-2J, LongerPump, China), prior to the introduction of CO_2 gas. The inner tubing appeared blue, indicating a basic pH value (Figure 4.11**a**).

Subsequently, CO_2 gas was introduced into the PTFE outer tubing of the reactor at a flow rate of 5 mL/min in a countercurrent direction. Shortly thereafter, the BTB solution exhibited a color gradient from yellow to blue along the gas flow direction (Figure 4.11**b**). This gradient reflects the mass transfer of CO_2 within the reactor, with reduced CO_2 dissolution near the liquid inlet due to shorter contact time.

Next, the flow of the liquid phase was stopped while maintaining the gas flow at 5 mL/min. As a result, the solution near the liquid inlet also turned yellow, since no fresh BTB solution was supplied to the reactor (Figure 4.11**c**).

4.3.4.4 Flow rate dependence of SABRE using a tube-in-tube reactor

The advantages of the tube-in-tube reactor, including its high gas permeability, large interfacial surface area with scalable length, and resistance to chemicals (notably to methanol, a common solvent in SABRE samples), make it particularly suitable for investigating SABRE hyperpolarization. Additionally, the ability to independently control the flow dynamics of the gas and liquid phases renders the tube-in-tube reactor ideal for real-time monitoring SABRE reactions under continuous flow condition.

As mentioned in Section 3.6.1, the delivery time of the hyperpolarized substrate to the NMR detection region needs to be carefully considered when performing SABRE using a continuous-flow gas–liquid reactor. In the tube-in-tube reactor, there is a trade-off between the delivery time and retention time of the sample solution, which impacts the intensity of the NMR signal.

On one hand, a short delivery time, resulting from a fast flow rate of the sample solution, leads to a shorter retention time of the sample inside the reactor. This reduces the amount of *para*-H_2 that dissolves into the sample solution, thereby decreasing the efficiency of the SABRE reaction. On the other hand, the rapid transport of the sample to the NMR spec-

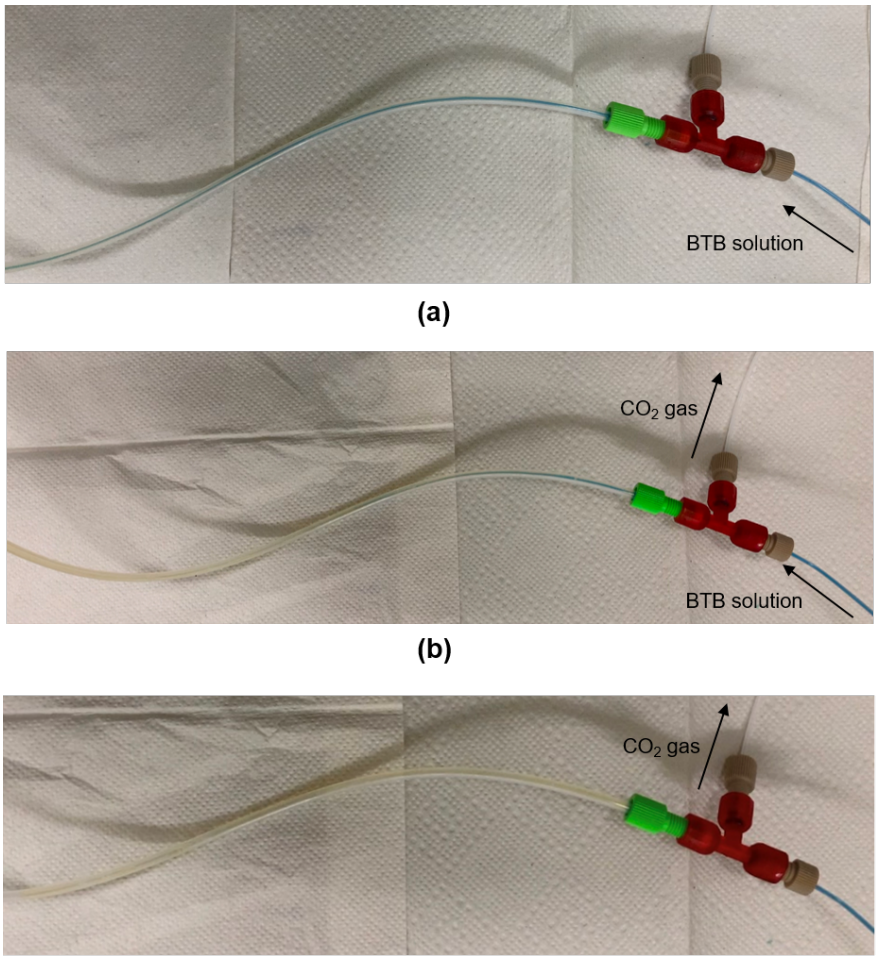

Figure 4.11: Photos of the tube-in-tube reactor at the section near the T-type connector (gas: CO_2, liquid: BTB solution). **(a)** Prior to the introduction of CO_2 gas into the reactor. **(b)** Introducing CO_2 while maintaining the flow rates of both gas and liquid at 5 mL/min. **(c)** Stop the flow of the liquid while maintaining the CO_2 at a flow rate of 5 mL/min.

trometer minimizes relaxation decay of the hyperpolarized substrate, which in turn allows for greater signal intensity to be detected. Therefore, it is essential to determine the optimal gas and liquid flow rates in a tube-in-tube reactor used in SABRE hyperpolarization to balance these factors effectively.

Here, the SABRE hyperpolarization of pyrazine was performed in the custom-built tube-in-tube reactor, where the inner and outer tubing had an overlapping length of 450 mm (Figure 4.12a). The reactor was spiral-wound around a holder and placed inside a homemade electromagnetic coil. A magnetic field strength of 6.5 mT for optimal spin transfer of ^{1}H SABRE was achieved at the center of the coil by adjusting the voltage applied on it (Figure 4.12**b**).

Three different sample solution flow rates were investigated. The flow rate of the *para*-H_2 was 40 sccm for all three sets of experiments. A positive pressure difference between the gas and liquid phases was set to 55 psi to facilitate the mass transfer efficiency of *para*-H_2.

The 5 mL activated SABRE solution was firstly pumped into the reactor with flow rate of 1.5 mL/min. The hyperpolarized sample was then directed out of the reactor and delivered through PTFE tubing (OD: 1.8 mm, ID: 1 mm) to the bottom of a glass flow cell (OD: 5 mm, ID: 1 mm) positioned inside the Spinsolve NMR spectrometer. The central section of the flow cell featured an expanded inner diameter of 4 mm, where the sample solution was detected by the NMR coil, ensuring an improved filling factor for signal acquisition (Figure 4.12**c**). Subsequently, the sample exited from the top of the glass flow cell and was recirculated via PTFE tubing back to the reservoir, forming a closed liquid loop for continuous rehyperpolarization using the SABRE method.

After running the experiment for 5 min, the signal of the hyperpolarized solution was measured using a single scan. Following each NMR acquisition, the sample was degassed and allowed to return to thermal equilibrium.

Adhering to this protocol, measurements of pyrazine sample solutions hyperpolarized via SABRE in the same tube-in-tube reactor were conducted at liquid flow rates of 1.5 mL/min, 2.5 mL/min, and 3.5 mL/min. As the results shown in Figure 4.13, the signal intensity of the hyperpolarized pyrazine reached its maximum at a flow rate of 2.5 mL/min. At a higher flow rate of 3.5 mL/min, the observed NMR signal intensity decreased, suggesting a reduced SABRE hyperpolarization efficiency in the tube-in-tube reactor despite the shorter delivery time.

4.4 Direct contact gas-liquid reactor

In the previous section, it was discussed how planar and tubular membrane gas-liquid contactors achieve gas-liquid separation while facilitating mass transfer through a membrane structure. Although effective for specific applications, the efficiency of mass transfer in these systems is limited by the membrane area and its properties (porosity and the pore size).

In contrast, direct contact gas-liquid reactors employ a fundamentally different approach, the two phases interact without the separation afforded by membranes or other solid media. The absence of such physical barriers allows for immediate and direct contact between the phases, typically resulting in higher mass and heat transfer efficiencies compared to contactors that utilize membrane structures. The design of these contactors is relatively straightforward, facilitating easier fabrication and maintenance. This simplicity, combined with enhanced operational efficiency, makes direct contact contactors favorable for a wide range of industrial applications.

For a two-phase flow system in direct contact gas-liquid reactor, the flow patterns such as slug flow, churn flow, and annular flow differ significantly in their structure and thus in their gas-liquid interfacial area. [167]

The slug flow typically occurs at moderate gas and liquid flow rates, it consists of alternating sequences of liquid slugs and gas bubbles. The liquid slugs often carry a film of liquid on

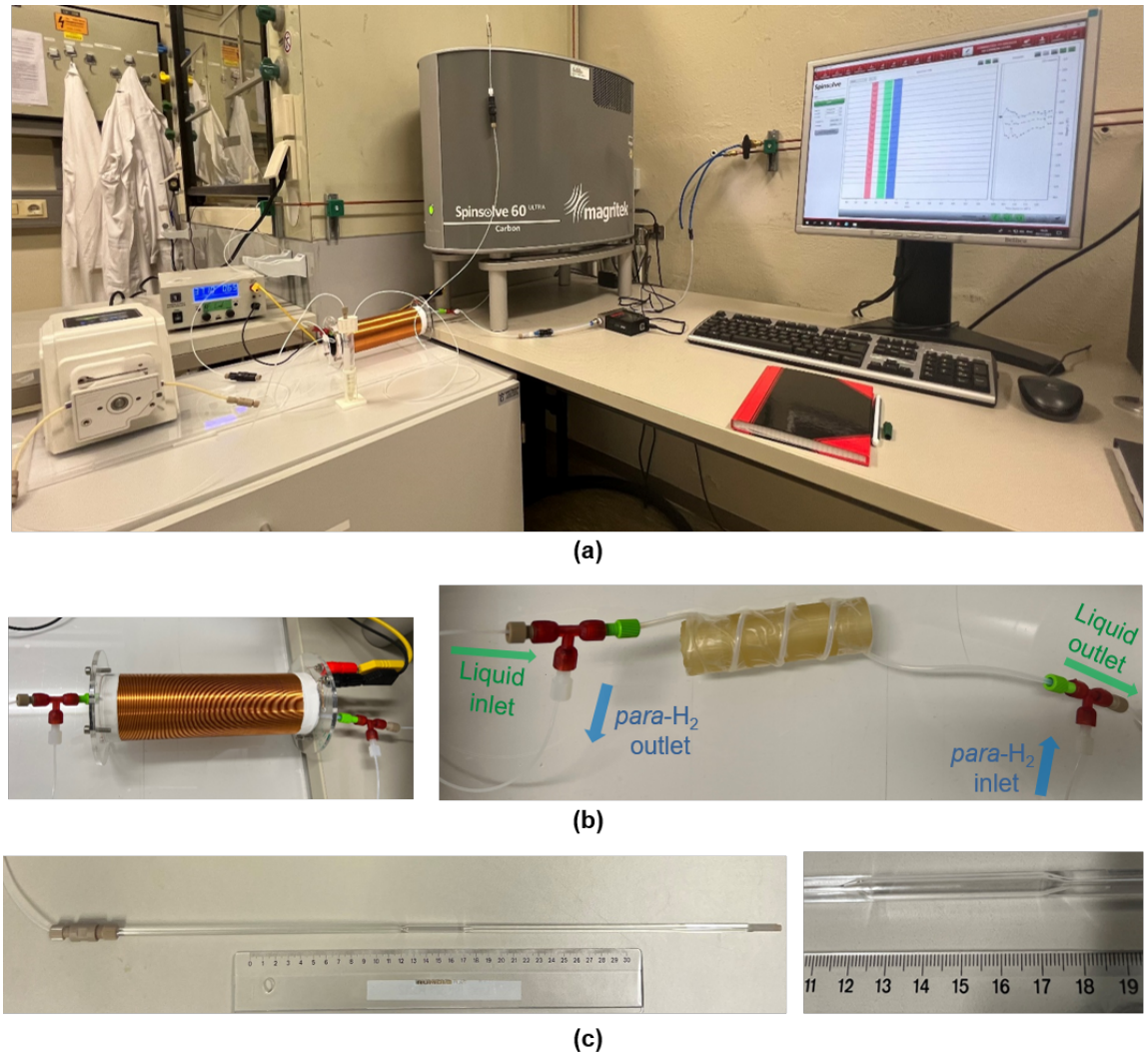

Figure 4.12: **(a)** Photo of the experimental setup for SABRE hyperpolarization using a tube-in-tube reactor. **(b)** Left: The reactor is positioned within an electromagnetic coil to generate the optimal PTF (6.5 mT) for ^{1}H SABRE. Right: The tube-in-tube reactor with an overlapped length of 450 mm is spiral-wound around a 3D printed holder. Arrows indicate the countercurrent flow direction of *para*-H_2 and the sample solution within the reactor. **(c)** Photo of the glass flow cell with a total length of 500 mm and an outer diameter of 5 mm used for flow measurements on the Spinsolve NMR. The internal diameter of the flow cell at its central part is expanded from 1 mm to 4 mm, designated as the detection region within the NMR coil.

the pipe walls and encapsulate large gas bubbles or gas slugs (Figure 4.14**a**). Therefore, the surface of the bubbles provides the main interface of contact between the gas slugs and the surrounding liquid. These bubbles or gas slugs typically move within the liquid, completely or partially enveloped by it, causing vigorous mixing in the liquid slug ahead of and behind each bubble. This dynamic interaction between the gas and liquid phases creates fluctuating boundaries, which leads to frequent renewal of the gas–liquid interface, enhancing local mass transfer.

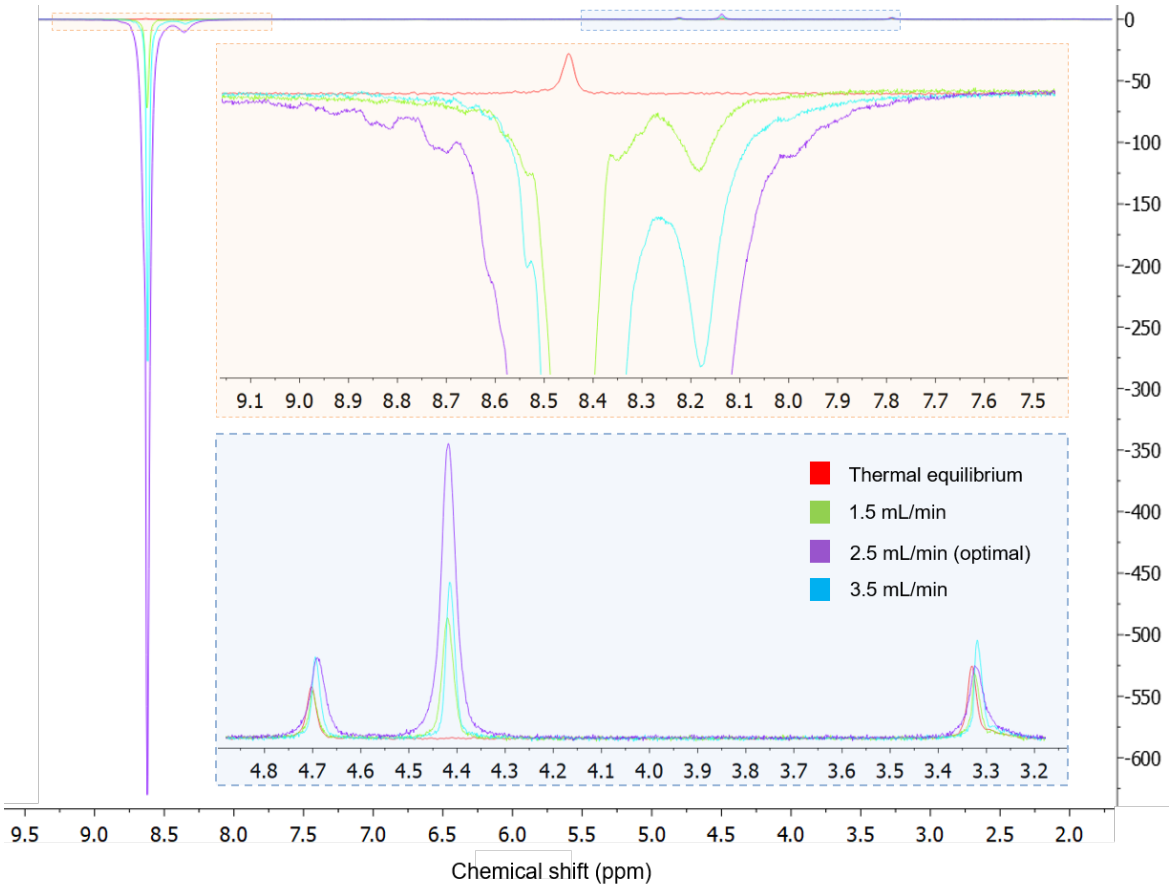

Figure 4.13: NMR spectra of pyrazine measured at thermal equilibrium and static fluidic condition (red) as reference, and hyperpolarized by SABRE in tube-in-tube reactor at different flow rates of the sample solution. The pyrazine peak (7.6-8.7 ppm) and the *ortho*-H_2 peak (4.3-4.5 ppm) are magnified to facilitate a clearer comparison. Sample solution: 60 mmol/L pyrazine with 3 mmol/L standard Ir-IMes catalyst in deuterated methanol.

As the velocity of the gas phase increases, the gas slugs begin to interact more turbulently with the liquid slugs. The kinetic energy of the gas phase becomes sufficient to disrupt the liquid slugs more violently. With further increases in gas flow rate, the liquid slugs start to break down into smaller fragments. These fragments are less capable of maintaining a coherent slug structure and begin to mix more chaotically with the gas. The breakdown of liquid slugs leads to increased turbulence within the pipe. The flow becomes more mixed and chaotic, with no distinct large gas or liquid slugs. This mixed and chaotic state is characteristic of churn flow (Figure 4.14**b**). In churn flow, the flow is highly turbulent, consisting of a frothy, churned mixture of gas and liquid without any orderly structure. The interface between the gas and liquid phases increases significantly, enhancing mass and heat transfer, although the interfacial area becomes less predictable due to the chaotic nature of the flow. [168]

As gas velocity increases beyond the churn flow regime, the momentum of the gas is sufficient to push most of the liquid phase towards the pipe walls. With the gas phase dominating the core of the pipe, it forces the liquid into a thin film along the walls. This film

may initially appear wavy and uneven but tends to stabilize into a smoother, more continuous film as gas velocity continues to increase and stabilize, thus initiating the formation of annular flow (Figure 4.14**c**). In the annular flow regime, the gas needs to flow at high velocity through the center since the gaseous void fraction is very high, and the liquid, primarily in the form of a film, lines the walls. Droplets may be entrained in the gas stream, but the main body of the liquid remains at the periphery. The annular flow offers efficient heat and mass transfer because of the large surface area of the liquid film and the rapid gas flow in the core. [169]

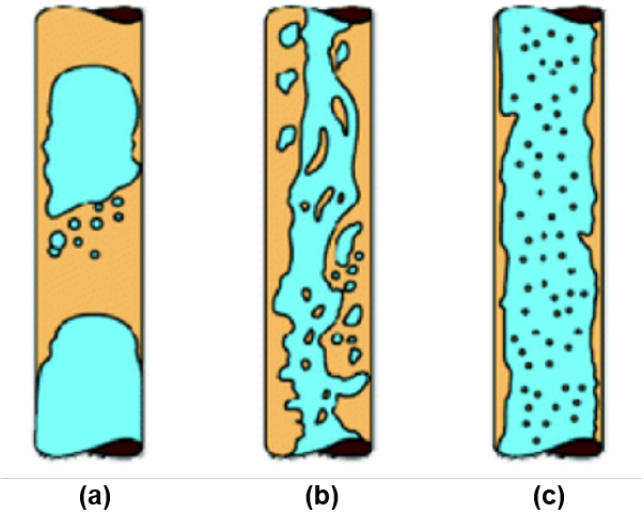

Figure 4.14: Representation of flow patterns of gas-liquid two phase system in vertical pipe. [170] **(a)** Slug flow. **(b)** Churn flow. **(c)** Annular flow. Copyright © 2012 American Chemical Society.

4.4.1 On-chip sandwich flow gas-liquid reactor

Among the formed flow patterns (such as slug flow, churn flow and annular flow) in a direct contact gas-liquid reactors, the annular flow exhibits large interface between the two phases. Nevertheless, annular flow gas-liquid reactors place higher demands on control of the flow dynamics, particularly regarding the meticulous management of gas-liquid flow rate and balanced gas-liquid ratio.

In this subsection, a 3D-printed prototype of annular flow gas-liquid reactor based on a microfluidic chip is introduced. Unlike conventional reactors that achieve annular flow in circular channels, this design utilizes a channel with a rectangular cross-section to form a sandwich flow with multi-phases of liquid-gas-liquid, which adapts from the traditional concept of annular flow.

4.4.1.1 Fabrication of the on-chip sandwich flow gas-liquid reactor

The on-chip gas-liquid reactor features a compact footprint measuring 2 cm in width and 10 cm in length. The liquid phase inlets are arranged in a Y-shaped configuration on both

sides of the central gas inlet, each forming a 30° angle with the main axis (Figure 4.15). This configuration leads to three inlet channels, each 1 mm wide, which converge to form a main channel with a width of 1.82 mm. This arrangement facilitates the formation of a sandwich flow pattern, where the gas layer is effectively sandwiched between two layers of liquid along the length of the channel. With a stable sandwich flow established in the main channel, the total gas-liquid interface effectively doubles the channel length. This maximizes the contact area between the phases, thereby enhancing mass and heat transfer between the gas and liquid phases within the compact microfluidic platform.

To accommodate the high flow rate of the gas, the ports of the chip were custom-designed and 3D-printed to connect seamlessly with flangeless microfluidic fittings (Model LVF-KFI-29, ELVEFLOW, France). These connections support rigid PTFE tubing with OD of 1/16 inch, ensuring stable and efficient gas delivery to the reactor. As shown in Figure 4.15**c**, both the microfluidic ports and the sandwich flow gas-liquid reactor were 3D printed using an SLA printer (Photon Mono 4K, Anycubic, China). The cured 3D-printed ports were aligned with the corresponding inlets and outlet on the chip and then assembled using UV glue (PHOTOBOND 4436, DELO, Germany). The assembly required a curing time of 90 s under the 100% power setting of a high-intensity UV lamp (DELOLUX 20, DELO, Germany).

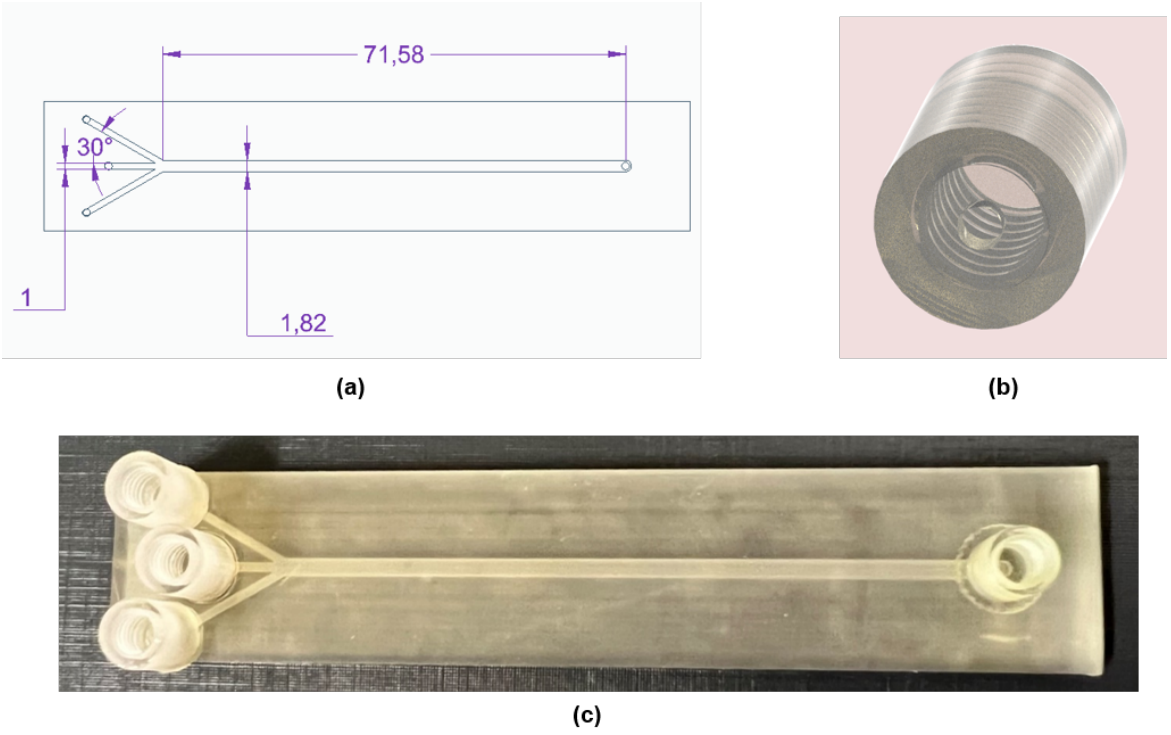

Figure 4.15: **(a)** Dimensions of the on-chip sandwich flow gas-liquid reactor (unit in mm). **(b)** 3D rendering of the ports with 10-32 UNF thread size for microfluidic fittings. **(c)** Assembled 3D-printed on-chip sandwich flow gas-liquid reactor.

4.4.1.2 Proof of the prototype

To demonstrate the performance of the sandwich flow gas-liquid reactor, BTB solution was employed as the pH indicator for the liquid phase, and CO_2 gas was used as the gas phase.

The BTB sample solution was prepared with pH value of 8.1 and the color was blue. More details of the BTB solution preparation can be found in section 4.3.2.2.

Here, three different gas-liquid flow rate ratios were tested on the gas-liquid reactor. All flow photos shown in Figure 4.16 were captured 30 s after the stable sandwich flow had been established. As illustrated, a well-defined sandwich flow was successfully formed in all three experiments.

In the first experiment, the flow rates for the gas and liquid phases were set at 10 mL/min and 1000 µL/min respectively, resulting in a gas-liquid flow rate ratio of 10:1. The two layers of the solution predominantly occupied the channel space, leaving only a narrow gap for the gas in the center. At the outlet terminal, the color of the blue BTB solution remained almost unchanged. (Figure 4.16**a**).

As deducing the flow rate of the liquid phase to 150 µL/min in the second experiment, the gas-liquid flow rate ratio increased to 200:3 (Figure 4.16**b**). Consequently, the BTB solution was pushed further towards the both sidewalls of the main channel, and the blue color began to transition to greenish-yellow halfway down the channel, indicating increased CO_2 dissolution due to the longer residual time of the solution in channel. A clear color gradient from yellow to blue was observed from the center to the sidewalls in the cross-section of the channel.

In the third experiment, while the flow rate of the BTB solution was maintained, the gas flow rate was increased to 30 mL/min, resulting in the color transition occurring before reaching halfway along the channel (Figure 4.16**c**). At the outlet port, the BTB solution displayed a bright yellow color. Despite the unchanged residence time of the solution, the higher gas-liquid flow rate ratio—caused by the faster flow of the gas—resulted in thinner liquid films along the sidewalls. Consequently, this produced a shorter diffusion path for CO_2 gas across the cross-section of the main channel, which explains the earlier transition of the BTB solution compared to the other two experiments. Furthermore, the increased flow rate of the gas also led to higher pressure inside the channel, which enhanced the dissolution of the gas into the liquid.

The on-chip sandwich flow design offers a simple reactor configuration that is scalable and compatible with various fabrication processes. While 3D printing is used for prototyping, this design can also be integrated with other manufacturing techniques, such as soft lithography for PDMS chips or UV lithography on glass substrates. This flexibility enhances the reactor's applicability across different research and industrial contexts.

4.4.1.3 Challenges of the sandwish flow gas-liquid reactor in application of SABRE and PHIP hyperpolarization

Despite the advantages in perspective of design, challenges persist, particularly in applying PHIP and SABRE hyperpolarization. A critical issue is the separation of gas and liquid after they flow from the reactor towards the NMR detector. Although installing a bubble remover can facilitate degassing, it introduces a drawback: the additional time required for

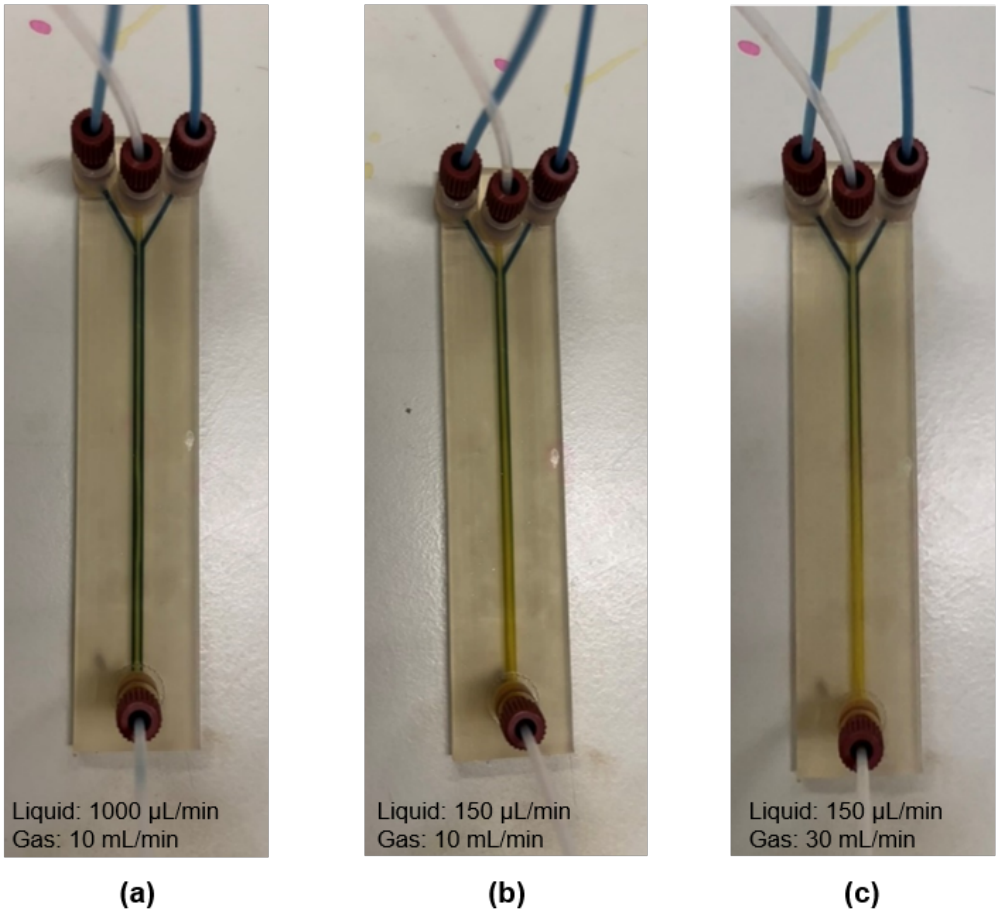

Figure 4.16: The sandwich flow formed with different flow rates of gas (CO_2) and liquid (BTB solution) phases in the 3D-printed gas-liquid reactor. Different colors indicate the interaction of CO_2 dissolved in the BTB solution. Gas-liquid flow rate ratio: **(a)** 10:1 **(b)** 200:3 **(c)** 200:1.

degassing may substantially reduce the NMR signal intensity of the hyperpolarized sample due to relaxation decay during this period.

Additionally, establishing a stable sandwich flow within the reactor typically requires several seconds. During this interval, the fast-flowing gas propels the sample solution out of the reactor, necessitating a larger volume of the sample solution. This issue becomes particularly problematic when testing SABRE and PHIP sample solutions that involve expensive catalysts or isotope-labeled substrates, as the increased volume leads to higher costs.

Furthermore, unlike membrane contactors with a physical barriers facilitate phase separation, the operation of such sandwish flow reactor requires careful management of the dynamic balance between gas and liquid phases to ensure efficient mass transfer while avoiding instabilities such as bubble formation or liquid accumulation. The high level of flow condition control makes the design and operation of sandwish flow reactors more complex; however, in applications where high mass transfer efficiency is critical, these additional efforts are often justified by the performance gains.

Parallelization of SABRE under Continuous-Flow Conditions

5.1 Overview

Building on the preliminary evaluation of the fabricated continuous-flow platforms for PHIP and SABRE presented in the previous chapter, this chapter introduces an NMR acceleration strategy that integrates SABRE hyperpolarization in tube-in-tube gas-liquid reactors with parallel detection using dual NMR cells (NCs).

The chapter begins by outlining the motivation for combining SABRE hyperpolarization and parallel detection to accelerate NMR analysis, particularly for low-concentration analytes. It then provides a detailed description of the two main components of the system: (i) parallel printed circuit board (PCB)-based NCs consisting of two spatially separated, locally shimmed saddle coils, and (ii) a continuous-flow SABRE setup using tube-in-tube reactors to ensure stable and uninterrupted delivery of hyperpolarized solution.

The performance of the integrated platform is evaluated through a series of experiments, including flow rate optimization to balance polarization efficiency and throughput, comparison of MRI measurements using thermally polarized reference samples and hyperpolarized analytes at low concentrations, and simultaneous single-scan detection of such hyperpolarized samples in both channels. These results collectively demonstrate the feasibility and effectiveness of the parallelized SABRE approach in enabling high-throughput NMR measurements. The results presented in this chapter are part of a manuscript entitled "*Accelerating NMR spectroscopy via parallel SABRE in a continuous-flow system*", which has been submitted to the journal ***Review of Scientific Instruments*** and is currently under peer review [JY04].

5.2 Introduction

NMR is one of the most powerful analytical tools, capable of extracting enormous amounts of information from the spin of a target sample, widely used in chemistry, medicine, and physical sciences. However, when measuring low-concentration samples, NMR typically requires

extended acquisition times due to the need for multiple scans to improve the signal-to-noise ratio (SNR). [171, 32] This is a limitation for time-dependent effects, such as occurring in fast chemical reactions, or for low-concentration analytes such as arising in biological settings. Consequently, there is growing interest in developing fast and cost-effective screening methods using NMR coil arrays. [172, 173, 174, 175] These arrays consist of multiple coils that are arranged and operated either in a time-interleaved or synchronized manner, achieving an n-fold reduction in detection time. For instance, an NMR coil array comprising two identical, parallel NCs integrated with local shimming coils—as described in previous work [176]—enables the simultaneous measurement of two independent samples with precise field homogeneity. This configuration effectively doubles the detection throughput. However, the sensitivity of NMR detection using such NCs remains fundamentally limited by the inherently low nuclear spin polarization at thermal equilibrium—a constraint that becomes particularly pronounced when analyzing small sample volumes or low-concentration analytes.

A common but time-consuming approach is to acquire multiple replicate spectra for signal averaging to increase the SNR. This method leads to prolonged experiment's duration, for example, achieving a twofold enhancement in SNR necessitates quadrupling the number of replicate measurements. Other hardware-perspective approaches to increase the sensitivity of NMR detection involve the use of ultra-high field superconducting magnets, which operate in the GHz range and enhance the population difference between spins at different energy levels, potentially improving the SNR. Additionally, employing cryoprobes to cool the RF coil and preamplifier can significantly reduce thermal noise from the electronics, potentially enhancing the SNR by up to fourfold. However, these methods are costly and the capacities of increasing the sensitivity are limited. Furthermore, the cooling systems may complicate the implementation of RF coil arrays due to the constrained space within typical magnet bores and the challenge of maintaining precise temperature control for each RF coil.

Hyperpolarization techniques provide an alternative and efficient way to overcome the fundamentally low sensitivity by breaking the thermal equilibrium state through physical or chemical means and establishing the non-equilibrium polarization with large population difference at different energy states, thereby boosting the sensitivity of NMR and MRI. [48, 72, 177]

As previously mentioned in Chapter 3.5, SABRE as a non-hydrogenative variant of PHIP, has its own merits of rapid generation substantial polarization of substrates within seconds by harnessing the spin order from *para*-H_2 (Figure 5.1**a**). [98, 102] Consequently, it enables the acquisition of an NMR spectrum or MR imaging with dramatically enhanced SNR from a single scan experiment, thereby greatly accelerating NMR detection. Additionally, the unpolarized substrates can rebind to the catalyst and re-hyperpolarize as long as the sample solution is replenished with fresh *para*-H_2, allowing SABRE to continuously produce HP substrates.

Inspired by capabilities of SABRE, this study integrates NMR detection coils with SABRE hyperpolarization to enable rapid, high-throughput NMR measurements. Here, the first

demonstration of parallel ^{1}H SABRE hyperpolarization under continuous-flow conditions is presented, achieved by combining a parallel NMR detector system with SABRE hyperpolarization on a commercial 1.05 T MRI system for real-time NMR and MRI sensing. Two different sample solutions were hyperpolarized using SABRE in gas–liquid reactors with a tube-in-tube configuration (Figure 5.1**b**), where the optimal flow rate was initially determined using both NMR and MRI techniques.

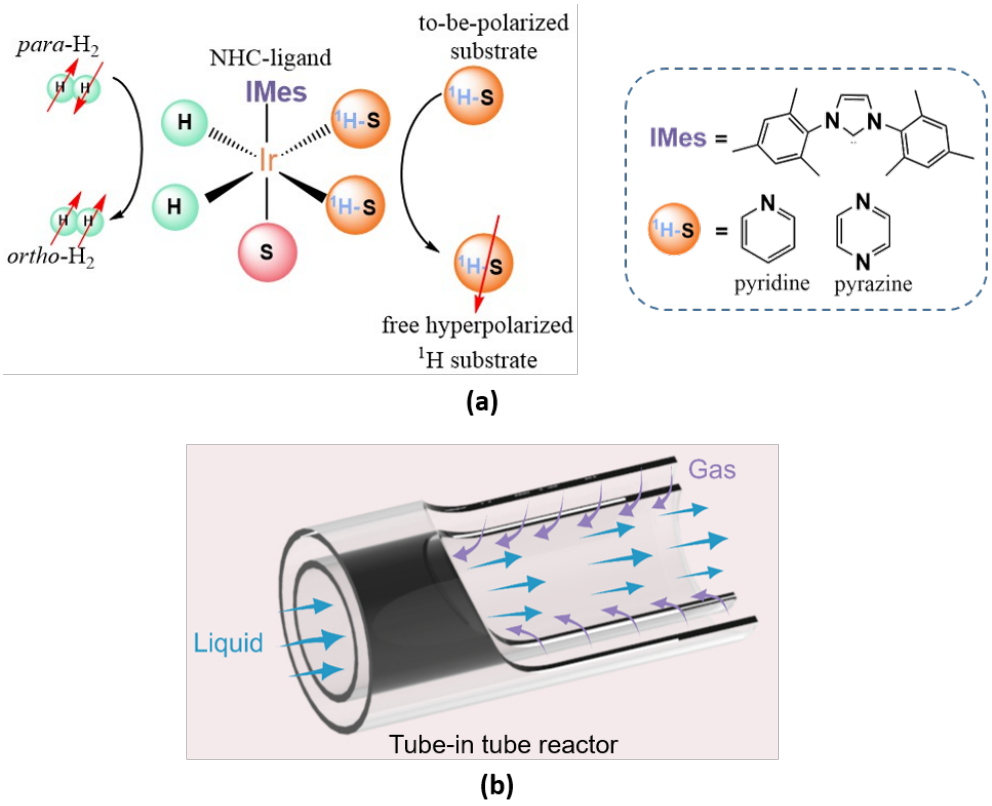

Figure 5.1: **(a)** Schematic representation of SABRE hyperpolarization on a catalytic complex. The spin orders derived from *para*-H_2 are transferred to the substrates (pyridine and pyrazine) on the equatorial plane through the J-coupling network. The hyperpolarized substrates with boosted magnetization dissociate from the catalyst form free substrates without chemical modification. **(b)** Section view of the tube-in-tube reactor under countercurrent condition.

To evaluate the feasibility of parallelized SABRE hyperpolarization, single-scan acquisitions were performed simultaneously on two distinct SABRE solutions—one containing pyridine and the other pyrazine—measuring their signals in both thermal equilibrium and hyperpolarized states. By applying different pressure conditions in the tube-in-tube reactors, variations in hyperpolarization efficiency were observed, with SNR enhancements of 140-fold for pyridine and 43-fold for pyrazine. These results provide a direct comparison of SABRE efficiency under varying conditions and lay the groundwork for implementing multi-sample parallel NMR detection.

This study establishes a framework for integrating SABRE hyperpolarization with parallel NMR detection, allowing for single-scan acquisition of hyperpolarized signals from multiple

samples. Through the implementation of continuous-flow conditions and parallel coil detection, high-quality spectral acquisition is achieved without the need for signal averaging, significantly accelerating NMR detection.

5.3 System design and setup for parallel SABRE measurement

The experimental setup consists of two main components: parallel PCB-based NCs and a continuous-flow SABRE system (Figure 5.2).

The parallel PCB-based NCs are designed to enable simultaneous acquisition of NMR signals from multiple samples, effectively doubling the throughput and improving the overall efficiency of NMR detection. The core of continuous-flow SABRE system is two tube-in-tube gas–liquid reactor housed within two electromagnetic solenoid coils. Each tube-in-tube reactor hyperpolarizes the SABRE sample solution under continuous-flow conditions at the optimal magnetic field provided by the solenoid coils. The following two subsections provide a detailed description of each component.

5.3.1 Parallel NCs with local shimming coils

Commercial NMR magnet systems are conventionally designed with a single RF coil and a single shim set, restricting measurements to one sample at a time. These shim systems rely on co-located spherical harmonics to achieve field homogeneity, but their effectiveness is inherently limited to a single coordinate origin. Additionally, practical deviations arise due to the non-ideal spherical geometry of both the sample and the RF coil.

To overcome this limitation, a parallel NMR detection system was adapted for a 1.05 T MRI system, incorporating localized field correction to enable independent and simultaneous NMR signal acquisition from multiple samples. This system consists of two modular NCs, each functioning as an independent measurement unit, denoted as CH 1 and CH 2. The design allows for scalable parallelization while maintaining signal integrity. Each NC comprises an RF coil responsible for both excitation and detection, along with a dedicated set of shim coils for localized magnetic field correction. The B_1 field orientations of the two NCs are deliberately arranged orthogonally to minimize mutual magnetic flux interference.

As illustrated in Figure 5.3, both the RF and shim coils are fabricated using flexible PCB technology and assembled onto cylindrical 3D-printed PLA-based supports. The sample holder is designed for glass tubes with an inner diameter of 5 mm, while the RF detector coil is a saddle coil with an optimized 8 mm diameter. The shim coils are positioned around the outer support structure, which has a radius of 8.5 mm. The RF coil geometry follows the design principles outlined by Ginsberg et al. [178], ensuring uniform excitation fields.

By implementing localized shim coils, the conventional isocenter of the magnet is effectively subdivided into multiple, sample-specific isocenters, allowing for precise spatial field correction in each NC. The key advantage of this approach lies in the independent control of

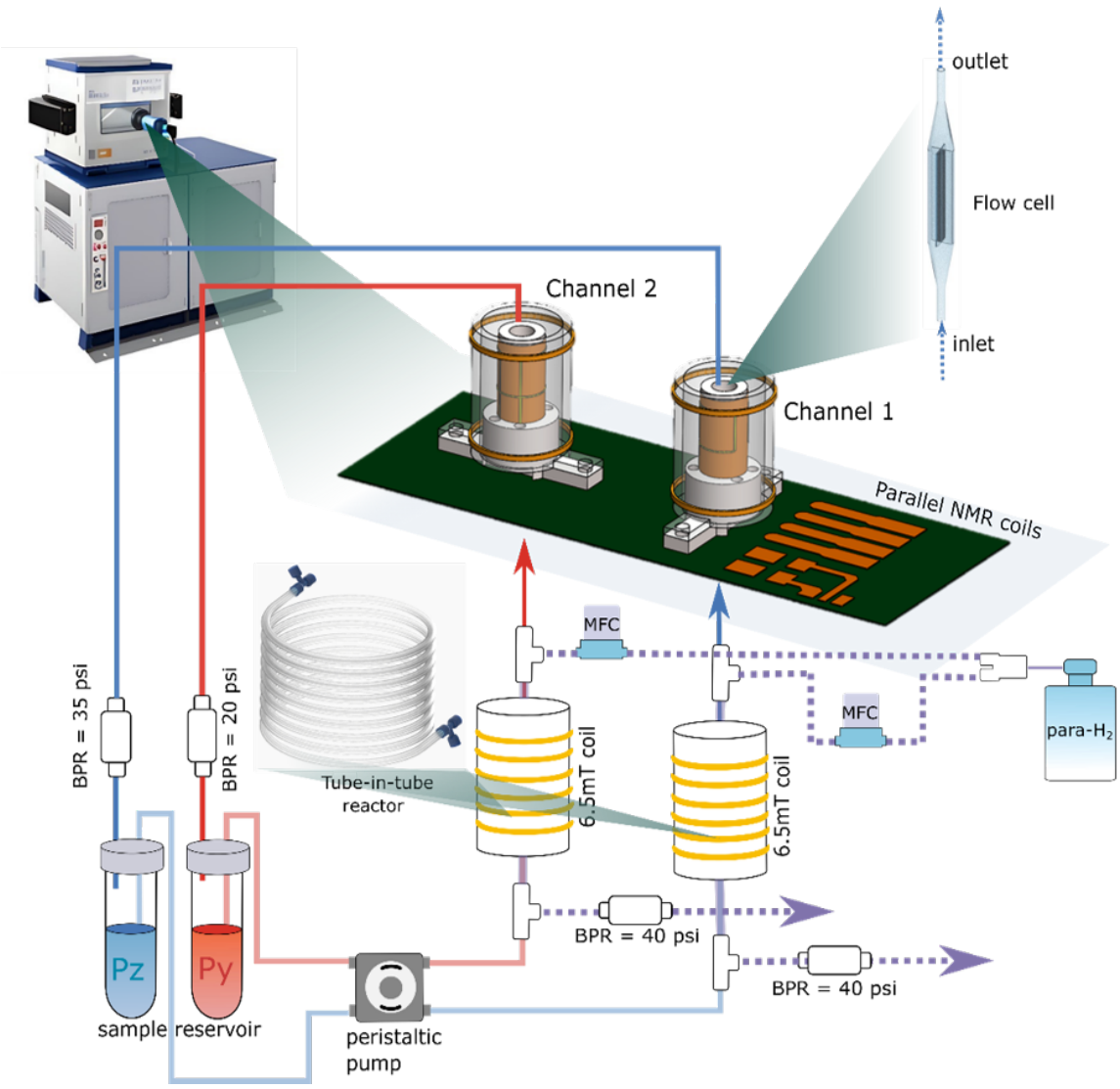

Figure 5.2: Overview of continuous parallel SABRE experiment setup. The tube-in-tube reactors for continuous SABRE hyperpolarization are wrapped and located inside of the electromagnetic coils with the generated magnetic field of 6.5 mT. The SABRE sample solutions (pyrazine in red color, pyridine in blue color) are continuously hyperpolarized within the tube-in-tube reactors at different pressure differences of the gas and liquid phase. The HP solutions are pumped into the 3D-printed conical-sided flow cells located inside of the RF coils on the NC-based parallel probe positioned at the 1.05 T horizontal field magnet. (Adopted from [JY04].)

the orthogonal spherical harmonic shim fields, enabling flexible and effective compensation for inhomogeneities within the measurement regions (details on the design of the NC shim can be found in previews work [176]).

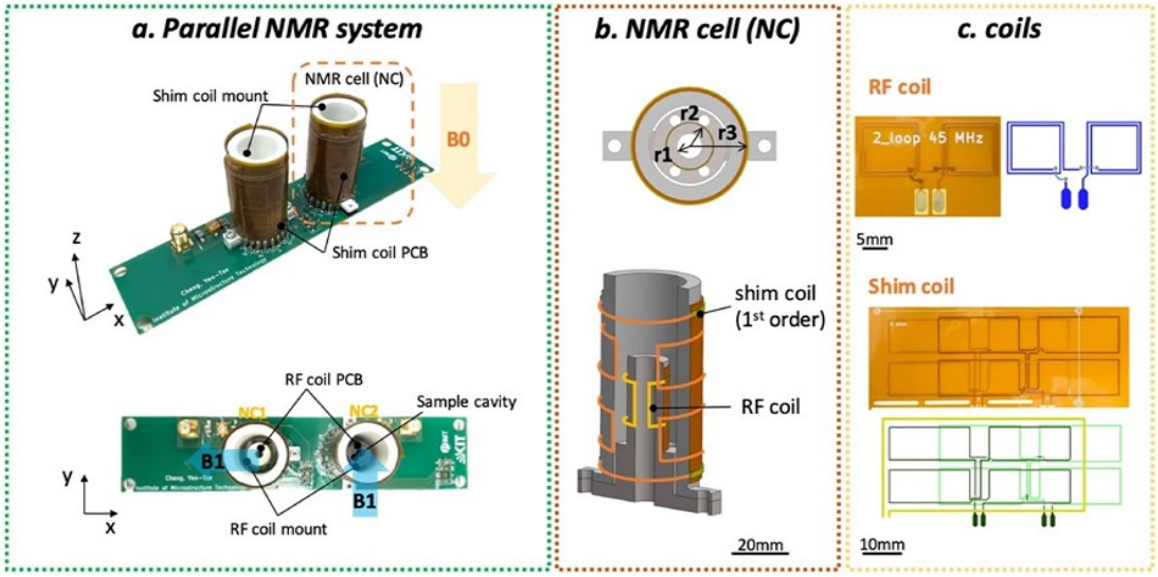

Figure 5.3: **(a)** Photograph of the proposed parallel system, featuring two NCs mounted on a PCB. **(b)** 3D model of a single NC, featuring an inner holder for the RF signal detection coil and an outer surrounding holder for shimming coil ($r_1 = 2.5$ mm, $r_2 = 4$ mm, $r_3 = 8.5$ mm.) **(c)** Photograph and schematic of a flexible substrate RF coil PCB, and a shim coil stack PCB, prior to wrapping the PCBs onto the coil support. [176] Copyright © Springer Nature Limited 2022.

5.3.2 Continuous flow SABRE in tube-in-tube reactor

The continuous SABRE hyperpolarization setup featured two identical gas-liquid reactors in a tube-in-tube configuration, as shown in Figure 5.2. The inlets and outlets of the outer and inner tubing were assembled via two T-junctions (P-713, IDEX Science&Health) and microfluidic tubing fittings (1/4-28 flat-bottom, XP-348 and XP-245, IDEX Science&Health). An extended contacting surface of gas and liquid was provided by 1.5 m overlapping length of the outer and inner tubing.

To achieve efficient polarization of ^{1}H via SABRE, the tube-in-tube reactors were coiled and positioned inside two home-made solenoid electromagnetic coil, each providing an optimal magnetic field strength of 6.5 mT for optimal polarization transfer.

SABRE sample solutions were pumped through the highly gas-permeable inner tubing (Teflon^{TM} AF 2400, OD: 0.8 mm, ID: 0.6 mm) using two peristaltic pumps, establishing a counter-flow between the gas and liquid phases. Additionally, two back-pressure regulators (IDEX Science&Health, JR-BPR1 and P-791) were installed downstream of the liquid flow in the reactors, maintaining pressures of 35 psi and 20 psi (1 psi $\approx$ 6.89 kPa) for the pyridine and pyrazine sample solutions, respectively (Figure 5.2).

Para-H_2 supply was evenly split into two paths and directed through the outer PTFE tubing (OD: 3.2 mm, ID: 2 mm) of each reactor at a flow rate of 20 mL/min, regulated by a mass flow controller (MFC). Two identical back-pressure regulators with 40 psi cartridges

were installed downstream of the gas flow in each reactor. This setup ensured consistent pressure differences Δp between the gas and liquid phases: $\Delta p = 5$ psi was applied on the reactor for hyperpolarization pyrazine, while $\Delta p = 20$ psi was applied to the reactor used for pyridine. The positive Δp facilitated the diffusion of parahydrogen molecules through the inner tubing wall and into the sample solutions, ensuring efficient mass transfer of *para*-H_2.

The HP sample solutions were continuously fed into the 3D-printed flow cells centered within the RF saddle coils. The flow cell was designed with a cylindrical middle section (5 mm in OD) to achieve a high filling factor for the detection coils. The ends of the cell were conically shaped, tapering to 2 mm in diameter, to facilitate easy connection to tubing, minimize dead volume, and conserve sample solution. The middle section of the flow cell was modified with a cross-shaped flow cross-section for better visualization for MRI detection. After traversing the detection area, the sample solutions were continuously pumped to their respective sample reservoirs forming a closed loop for subsequent regeneration of hyperpolarization.

5.4 Experiments and results

5.4.1 Chemical preparation

- Preparation of SABRE sample solution

All SABRE sample solutions were prepared under inert gas conditions. For SABRE hyperpolarization of ^{1}H pyrazine and pyridine, each sample solution contained 3 mmol/L of standard homogeneous SABRE pre-catalyst [IrCl(COD)(IMes)] (IMes=1,3-bis(2,4,6- trimethylphenyl) imidazole-2-ylidene; COD=cyclooctadiene) and 60 mmol/L of each substrate dissolved in degassed methanol-d_4. The prepared sample solutions were deposited in two Falcon tubes and capped tightly until activation. The pre-catalyst in each sample solution was activated by bubbling fresh *para*-H_2 at a flow rate of 20 mL/min, ambient pressure, and room temperature (25 °C) for 10 min.

- Enrichment of *para*-H_2

Normal hydrogen gas (ALPHAGAZ^{TM} H_2, 99.999%) flows along the pipeline with an appropriate flow rate (0.5 L/min) controlled by a mass flow controller. A commercial water-cooled helium compressor (Advanced Research System, Model ARS-4HW) offers the cooling source to the cryostat (cold head) at 23 K. After contacting the paramagnetic hydrated iron (III) oxide catalyst ($Fe_2O_3 \cdot H_2O$) in the chamber at the bottom of the cold head, the *para*-H_2 fraction of 98% was generated and collected within an aluminum gas bottle.

5.4.2 Dependency of volume flow on the rate of continuous SABRE hyperpolarization

The hyperpolarization of a substrate in a gas-liquid reactor is critically influenced by the volumetric flow rate and the size of the fluidic circuit. Upon leaving a reactor, the sample's

level of polarization relaxes during transport to the detection volume, and the remaining polarization passing through a detection coil of average traversal length $\bar{l}_c$ will have time $t = \bar{l}_c/\bar{v}_c$ for acquisition, where $\bar{v}_c$ is the average fluid velocity. High volumetric flow rates, which would compensate for loss of polarization during transport between a reactor and the detection coil, but suffer from reduced residence time in the reactor, leading to a decreased *para*-H_2 uptake and consequently less efficient polarization transfer, and loss of detection time in the coil. In contrast, lower volumetric flow rates allow to generate more HP substrate in the reactor, while needing longer transfer time to reach the detection coil, which again results in polarization loss. Therefore, an optimal volume-flow rate needs to be determined to obtain the best compromise between short transport time, and a long enough residence time to both maximize the polarization level, and have sufficient time for detection.

In this work, the flow rate dependency on the signal intensity of the generated HP pyrazine was studied using a 3D printed flow cell with a cross-shaped cross-section. The sample flow rates varied from 1 mL/min to 10 mL/min, while the pressure difference between the gas and liquid phases in the tube-in-tube reactor was maintained at 20 psi.

For this flow rate study, NMR measurements were performed in single-scan mode using a single detection channel on the parallel NC probe. As shown by the stacked NMR spectra of HP pyrazine in Figure 5.4**a**, the signal intensity initially increased and reached a maximum as the flow rate increased from 1 mL/min to 6 mL/min (Figure 5.4**b**). Upon further increasing the flow rate, the signal intensity decreased again due to the shorter residence time of the sample in the reactor, which resulted in a less efficient SABRE process.

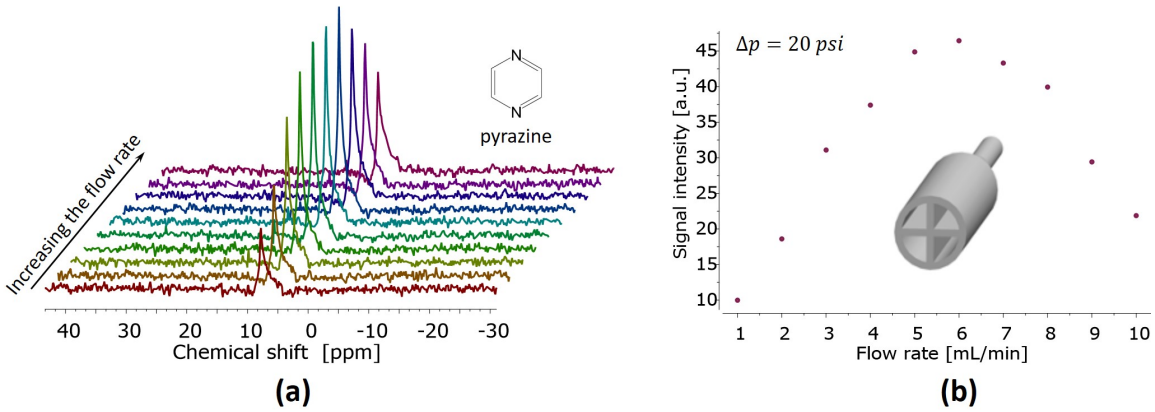

Figure 5.4: (**a**) ^{1}H NMR spectra of HP pyrazine as a function of the volumetric flow rate in the tube-in-tube reactor, with a positive pressure difference of 20 psi (137 kPa) between the gas and liquid phases. The sample solution contained 60 mmol/L pyrazine and 3 mmol/L Ir-IMes catalyst dissolved in methanol-d_4. (**b**) Signal intensities of HP pyrazine with different flow rates. Middle: 3D-model of the flow cell with a cross-shaped cross section.

5.4.3 SNR enhancement analysis based on MRI comparison

To quantitatively assess the sensitivity enhancement enabled by SABRE hyperpolarization under low-concentration conditions, a comparative MRI study was conducted using thermally polarized methanol and SABRE-hyperpolarized pyrazine solutions. The corresponding proton concentrations were $c_{^1\mathrm{H,Ref}} = 98.88$ mol/L for the methanol reference sample (accounting for four protons per methanol molecule) and $c_{^1\mathrm{H,HP}} = 0.24$ mol/L for the hyperpolarized pyrazine sample (60 mM pyrazine, four protons per molecule).

Both samples were imaged under identical acquisition parameters, differing only in the number of signal averages: $N_{\mathrm{REF}} = 16$ scans for the thermally polarized methanol reference and $N_{\mathrm{HP}} = 2$ scans for the hyperpolarized pyrazine sample. All MRI measurements were performed under continuous flow conditions at a flow rate of 6 mL/min, which was determined as the optimal flow rate based on the flow rate versus signal intensity analysis discussed in the preceding section. Both reference and hyperpolarized measurements were conducted at this optimized flow rate.

The SNR of each MR imaging were determined by manually selecting four signal-dominant regions and four background regions within each MRI dataset (Figure 5.5). Circular ROIs of identical physical area were used to ensure consistent sampling.

For each ROI, the mean pixel intensity was extracted, and SNR of MR imaging was calculated according to the relation

$$\mathrm{SNR_I} = \frac{\overline{S}}{\sigma_{\mathrm{N}}}, \tag{5.1}$$

where $\overline{S}$ indicates mean values for the signal and σ_{N} represent the standard deviation of the background noise. This approach emphasizes the practical detectability of low-concentration signals, which is the primary objective of hyperpolarization-enhanced detection, rather than assessing instrument-limited noise characteristics.

Therefore, the calculated SNR values were

$$\mathrm{SNR_{I,Ref}} = \frac{696.3}{22.07} \approx 31.6,$$

and

$$\mathrm{SNR_{I,HP}} = \frac{491.88}{8.39} \approx 58.6.$$

To account for differences in proton concentration and acquisition time, the per-proton normalized sensitivity enhancement factor ($\varepsilon_{^1\mathrm{H}}$) is introduced by

$$\varepsilon_{^1\mathrm{H}} = \frac{\mathrm{SNR_{I,HP}} \cdot c_{^1\mathrm{H,Ref}} \cdot \sqrt{\mathrm{N_{Ref}}}}{\mathrm{SNR_{Ref}} \cdot c_{^1\mathrm{H,HP}} \cdot \sqrt{\mathrm{N_{HP}}}}. \tag{5.2}$$

Substituting the experimental values yields

$$\varepsilon_{^1\mathrm{H}} = \frac{58.6 \times 98.88 \times \sqrt{16}}{31.6 \times 0.24 \times \sqrt{2}} = \frac{58.6 \times 98.88 \times 4}{31.6 \times 0.24 \times 1.414} \approx 2161.$$

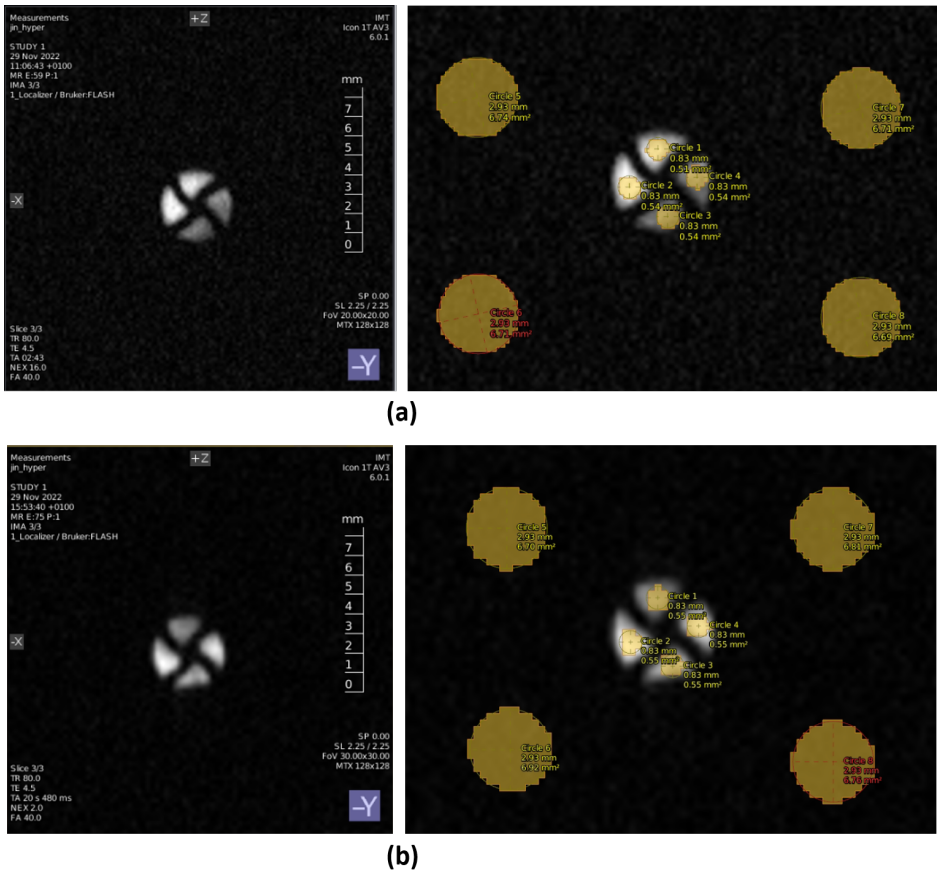

Figure 5.5: MR images and corresponding ROI selections for SNR analysis under continuous flow conditions at a flow rate of 6 mL/min. **(a)** Thermally polarized methanol reference sample ($c_{^1\mathrm{H,Ref}} = 98.88$ mol/L, 16 scans); **(b)** SABRE HP pyrazine sample ($c_{^1\mathrm{H,HP}} = 0.24$ mol/L, 2 scans). Left: Original MRI images acquired using identical imaging parameters. Right: ROI selections for SNR calculation, where central small ROIs represent signal-dominant regions and peripheral ROIs represent background noise regions.

This result indicates that, after normalizing for proton concentration and scan time, SABRE hyperpolarization provides approximately a 2161-fold improvement in detection sensitivity per proton compared to thermal equilibrium conditions. Such a enhancement demonstrates the particular suitability of SABRE hyperpolarization for the detection of metabolites and biochemical intermediates that typically exist from nano to milli molar concentrations in biological systems. In these scenarios, conventional NMR and MRI methods are often inadequate due to insufficient sensitivity and prohibitively long acquisition times.

5.4.4 Parallel SABRE hyperpolarization of pyrazine and pyridine

Parallel ^{1}H SABRE hyperpolarization of pyrazine and pyridine was performed with simultaneous NMR detection in two parallel channels using the dual RF coils on the NC-based probe. With tube-in-tube gas-liquid reactors, HP pyrazine and pyridine were continuously fed into parallel RF coils (CH 1 and CH 2), at an optimized flow rate of 6 mL/min, as determined

		Reference (Methanol, 16 scans) $c_{^1\mathrm{H,Ref}} = 98.88$ M	**HP** (Pyrazine, 2 scans) $c_{^1\mathrm{H,HP}} = 0.24$ M
Signal region (Mean value, $\overline{S}$)	1	217.0	85.18
	2	246.7	159.50
	3	102.9	104.20
	4	129.7	143.00
Background region (Std Dev, σ_N)	5	5.50	1.99
	6	5.43	2.29
	7	5.42	2.18
	8	5.72	1.93

Table 5.1: Comparison of mean signal and standard deviation of background noise levels for a reference sample (methanol) and hyperpolarized pyrazine under different proton concentrations and scan numbers.

from preliminary experiments (Figure 5.4**b**).

One RF coil was connected to the ICON MRI system to perform a standard ^{1}H single-pulse experiment using the ParaVision software interface (version 6.0.1, Bruker), while the second coil was connected to a separate NMR spectrometer system (Kea2, Magritek). A transistor-transistor logic (TTL) line connected the two systems to ensure precise synchronization of RF pulse excitation and signal acquisition, enabling truly parallel data collection from both hyperpolarized samples.

Four sets of experiments were conducted to simultaneously acquire signals from the samples fed into the flow cells in CH 1 and CH 2. The results are presented as stacked spectra in Figure 5.6. In the initial set of experiments, the supply of *para*-H_2 was turned off in the gas pathways of both tube-in-tube reactors to measure the thermal equilibrium signals of pyrazine and pyridine. However, due to the low millimolar-range concentrations in the single-scan experiments, the peaks in the recorded spectra were scarcely discernible (Figure 5.6**a**).

In the second set of experiments, *para*-H_2 delivery was then commenced to both reactors, which initiated the hyperpolarization of substrates via SABRE. After 60 s of *para*-H_2 exposure, NMR signals from both channels were acquired simultaneously within a single scan. Notably, a distinct singlet peak at 8.5 ppm with an amplitude-based SNR of 43 was observed in the pyrazine spectrum, while peaks between 7.0 to 8.6 ppm were resolved in the pyridine spectrum. The expected triplet splitting of pyridine in the NMR spectrum was not fully resolved under our experimental conditions. Instead, the signals from the protons at the

para and meta positions coalesced into a broader peak, resulting in an apparent doublet-like pattern. The most intense peak, originating from the ortho proton, exhibited an SNR of 140 (Figure 5.6**b**). The higher SNR value of the pyridine peak, compared to that of pyrazine, resulted from the greater pressure difference ($\Delta p = 20$ psi) applied to the tube-in-tube reactor for hyperpolarizing the pyridine sample solution, relative to that used ($\Delta p = 5$ psi) for the pyrazine sample.

Subsequently, the *para*-H_2 supply in CH 1 was discontinued, while it remained constant in CH 2. The absence of *para*-H_2 caused the pyridine sample in CH 1 to revert to its thermal equilibrium state, rendering it undetectable with a single scan. In contrast, CH 2 still contained hyperpolarized pyrazine solution, which produced a sufficiently strong signal to be observed with an SNR of 120 (Figure 5.6**c**).

In the fourth set of experiment, the *para*-H_2 supply was reactivated in CH 1 and turned off in CH 2, resulting in rehyperpolarization of pyrazine and relaxation of the HP pyridine to its thermal equilibrium state. However, the signal intensity of hyperpolarized pyridine was weaker than in the second set of experiments, possibly due to magnetic field drift of the non cryo-cooled MRI system. Meanwhile, in the CH 2 spectrum, the thermally equilibrated pyridine resonance was too weak to be detected (Figure 5.6**d**).

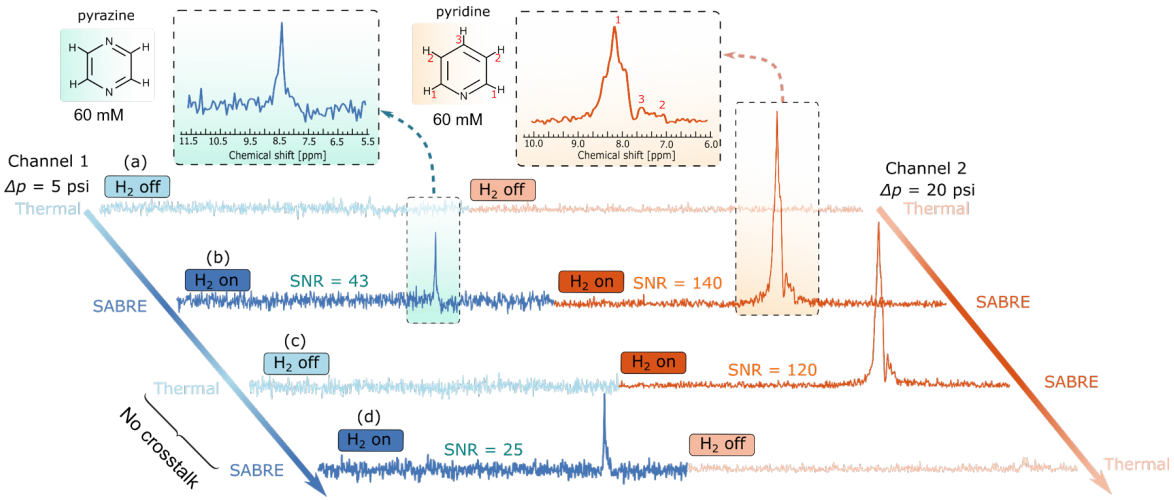

Figure 5.6: Parallel ^{1}H NMR spectra of pyrazine and pyridine, acquired under SABRE hyperpolarization or thermal equilibrium conditions, with sample solutions continuously flowing from tube-in-tube gas-liquid reactors under different *para*-H_2 supply conditions ($\Delta p = 5$ psi in pyrazine channel and $\Delta p = 20$ psi in pyridine channel). **(a)** CH 1: *para*-H_2 off, CH 2: *para*-H_2 off **(b)** CH 1: *para*-H_2 on, CH 2: *para*-H_2 on **(c)** CH 1: *para*-H_2 off, CH 2: *para*-H_2 on **(d)** CH 1: *para*-H_2 on, CH 2: *para*-H_2 off.

The experimental results demonstrated that, following SABRE hyperpolarization, the main peak of each HP substrate became discernible from a single scan—an outcome that was unattainable under thermal equilibrium conditions with the parallel coils and samples at such low concentrations. While both pyridine and pyrazine samples were hyperpolarized in each channel, no coupling effect was observed in the parallel coil pair, which is attributed

to an effective parallel shimming approach. Since the thermal signal was undetectable in a single scan in our case, we use an amplitude-based SNR definition to quantify enhancement, where we assigned $\mathrm{SNR}_{\mathrm{thermal}} = 1$ for reference. The enhancement factor is then given by $\epsilon_{\mathrm{SNR}} = \mathrm{SNR}_{\mathrm{HP}}/\mathrm{SNR}_{\mathrm{thermal}}$, which provides a practical metric for quantifying signal gain achieved through hyperpolarization.

In our experiments, hyperpolarized signals corresponding to enhancement factors of 140 and 43 were achieved from a single scan. This implies that, approximately $140^2 = 19,600$ and $43^2 = 1,849$ scans, respectively, would be required under thermal conditions to reach equivalent signal levels. Therefore, it demonstrates that SABRE hyperpolarization effectively reduces the acquisition time by several orders of magnitude. When combined with a parallel coil array, the measurement throughput is further increased, enabling simultaneous acquisition of multiple hyperpolarized samples. This dual approach not only accelerates data collection but also extends the applicability of high-throughput NMR to analytes present at concentrations previously undetectable by conventional methods.

It is worth noting that, while the MRI experiments in a single channel presented earlier provided a direct quantitative comparison between thermal signal from a pure protonated methanol solution and hyperpolarized signal from a low-concentration sample solution, the NMR experiments in this section highlight a complementary advantage of hyperpolarization—the ability to achieve rapid single-scan detection even when thermal signals are completely undetectable.

5.5 Conclusion

A continuous-flow SABRE hyperpolarization system integrated with parallel NMR detection was developed and demonstrated, enabling real-time, high-throughput acquisition of hyperpolarized signals from low-concentration liquid samples. The successful implementation of parallel SABRE under continuous-flow conditions also establishes a practical foundation for future plug-flow-based hyperpolarization of diverse samples, facilitating the development of scalable platforms for advanced NMR analysis.

Despite these achievements, the current setup remains limited to ^{1}H detection. Expanding its capability to additional nuclei such as ^{13}C would significantly broaden its applicability for multi-channel, multi-sample high-throughput NMR measurements. Furthermore, simultaneous MRI imaging of both channels is currently restricted by the requirement for independent gradient fields at each detector. Potential solutions include the incorporation of localized gradient coils or the application of RF encoding techniques to overcome this limitation.

While SABRE hyperpolarization inherently depends on reversible substrate binding, ongoing efforts in catalyst and ligand design continue to expand the range of polarizable substrates. Several biologically and pharmaceutically relevant molecules—such as isoniazid, pyrazinamide [179], ^{15}N-imidazole [101], and ^{13}C-pyruvate [16]—have already been successfully hyperpolarized, further highlighting the growing potential of SABRE in biomedical and pharmaceutical

applications.

In conclusion, the developed parallel SABRE hyperpolarization system provides a robust foundation for designing scalable and specialized hardware platforms aimed at the rapid characterization of low-concentration samples. This advancement holds promise for future applications in biomolecular research, metabolic studies, and pharmaceutical screening.

PHIP-Pumped Steady-State RASER

6.1 Overview

This chapter explores how continuous-flow PHIP can be advanced beyond mere signal enhancement, creating a self-sustained source of coherent radio-frequency emission—a phenomenon termed RASER (Radio-frequency Amplification by Stimulated Emission of Radiation). In a RASER system, a large population inversion among nuclear spin states is typically established through hyperpolarization techniques such as SABRE or PHIP. Under suitable conditions, stimulated emission occurs, leading to long-term NMR signals with high intensity. This process generates coherent radiation in the RF range, analogous to coherent optical emission in LASER systems (Light Amplification by Stimulated Emission of Radiation).

The work presented in this chapter investigates the steady-state ALTADENA-RASER phenomenon through a combination of experimental observations and numerical simulations. It begins with a brief review of the historical background of related stimulated emission techniques—specifically MASER and LASER—to contextualize the emergence of RASER in NMR spectroscopy. Subsequently, the chapter describes how the RASER effect in NMR fundamentally arises from radiation damping.

Following this foundational discussion, a method to precisely control the operational regime of the RASER is introduced. By manipulating pressure differential applied on the gas and liquid phases of a tube-in-tube reactor, various RASER regimes emerge over extended durations at elevated polarization levels. These regimes exhibit nonlinear dynamic phenomena, including frequency combs, chaos, and period doublings.

To provide a comprehensive interpretation of these experimental findings, numerical simulations based on a theoretical model of two nonlinearly coupled RASER modes are presented. The resulting bifurcation diagram offers a clear visualization and predictive capability regarding the accessible operational regimes of the continuous-flow RASER system. The results which are presented within this chapter are published under title "*The steady-state ALTADENA RASER generates continuous NMR signals*" in the journal ***ChemPhysChem*** [JY02].

6.2 Introduction

6.2.1 Development of MASER and LASER techniques

RASER technique is analogue to MASER or LASER. The similarity of the three techniques are electromagnetic wave amplification by stimulated emission of radiation. Before delving deeper into the study of RASERs, a brief introduction about the development of MASER and LASER is worth to depict here since both of the two discoveries have obtained the Nobel Prices for their outstanding contributions to the field of MASER and LASER. [180]

The principle of LASER dates back to 1917, when Albert Einstein first described the theory of stimulated emission, in which he had deduced theoretically the existence of stimulated emission–the process by which electromagnetic waves of the right frequency can "stimulate" an excited atom or molecule to fall to a lower energy state and emit more waves. Subsequently, several scientists continued to explore this avenue of research extensively.

By the late 1940s and early 1950s, it was recognized that stimulated emission and population inversion—the redistribution of particles such that higher energy states become more populated than lower ones—are essential prerequisites for the coherent amplification of microwave radiation. Inspired by this concept, Charles Townes, along with Arthur Schawlow of Bell Laboratories, published a paper in 1958 proposing a system that would work at infrared and optical wavelengths. [181] This development paved the way for the invention of the first light-emitting MASER, known as the LASER, by Theodore Maiman in 1960 using a synthetic ruby crystal [182]. LASER technology operates in the visible, infrared, or ultraviolet regions and delivers a highly coherent and directional beam of light, enabling widespread applications in fields such as communication, medicine, and industry. [183, 184, 185]

Historically, the MASER was the first technology to demonstrate stimulated emission, later followed by the LASER, which gained broader recognition and more widespread applications. More recently, the RASER has emerged in NMR research, utilizing stimulated emission in the radiofrequency (RF) range. It enables a variety of advanced applications, including the generation of continuous NMR signals without decay for precise J-coupling measurements, spontaneous signal acquisition without excitation pulses, background noise-free MRI, and the study of nonlinear spin dynamics, among others.[186, 187, 188, 189, 190]

6.2.2 Radiation damping and negative polarization in RASER

While the previous section highlighted the similarities between the RASER and conventional MASER or LASER systems, this section focuses on the distinctive characteristics of the RASER. Unlike MASER and LASER, RASER exploits the phenomenon of stimulated emission in RF range to enhance the NMR signals of certain molecules, providing a novel approach to NMR spectroscopy. Additionally, the RF-emission is spontaneous due to the interaction of the large negative magnetization and the detection coil.

In a standard NMR procedure, transverse magnetization is induced by applying RF pulses. This magnetization arises from nuclear spins within a static magnetic field and proceeds to precess at the Larmor frequency. The coherence duration in traditional NMR is constrained by the decay of this transverse magnetization, characterized by the time constant T_2^*, which sets the limit for resolution (Figure 6.1**a**).

When the magnetization of a sample is significant, an interaction occurs between the RF-circuit and the nuclear spin system, termed radiation damping. [191, 192] This phenomenon involves the current generated by the precession of transverse magnetization in the coil, which in turn produces a magnetic field. This field influences the magnetization to rotate towards thermal equilibrium, namely towards the $+z$ direction, characterized by a time constant τ_{rd}, given by:

$$\tau_{rd} = \frac{2}{\mu_0 \eta Q \gamma M} \tag{6.1}$$

where μ_0 is the magnetic permeability of vacuum, η represents the filling factor of the NMR detection coil, Q is the quality factor of the RF circuit on the coil, γ denotes the nuclear gyromagnetic ratio, and M stands for the magnitude of the nuclear magnetization. After a 90° pulse, radiation damping reorients the magnetization away from the transverse plane, thereby contributing to the decay of transverse magnetization and acting as a source of broadening (Figure 6.1**a**). This phenomenon is commonly encountered in liquid-state NMR analyses involving samples with high proton concentrations, leading to substantial magnetization. [193]

Conversely, if the initial magnetization of the sample is negative, the radiation damping effect on any transverse component functions to pivot the magnetization towards the transverse plane, as depicted in Figure 6.1**b**. This mechanism facilitates the generation of spontaneous transverse magnetization within a RASER.

As a self-organized system, the stimulated emission in RASERs of a spin-1/2 system begins spontaneously after the system is "pumped" to a state where the population inversion between the two Zeeman levels is achieved by hyperpolarization techniques. In this case, the population inversion generates a negative magnetization. [186]

In RASER, the equilibrium negative magnetization M_0 is used to define the initial radiation damping constant $\tau_{rd,0}$:

$$M = |M_0| = \frac{1}{2}\hbar\gamma_s n_s |P_0| \tag{6.2}$$

where $|P_0|$ is the negative polarization at thermal equilibrium of the spin system, n_s is the density of spin species. Therefore, the functional relationship of the radiation damping in terms of the negative polarization in RASER is:

$$\frac{1}{\tau_{rd,0}} = \frac{1}{4}\mu_0 \eta Q \hbar \gamma^2 n_s |P_0| \tag{6.3}$$

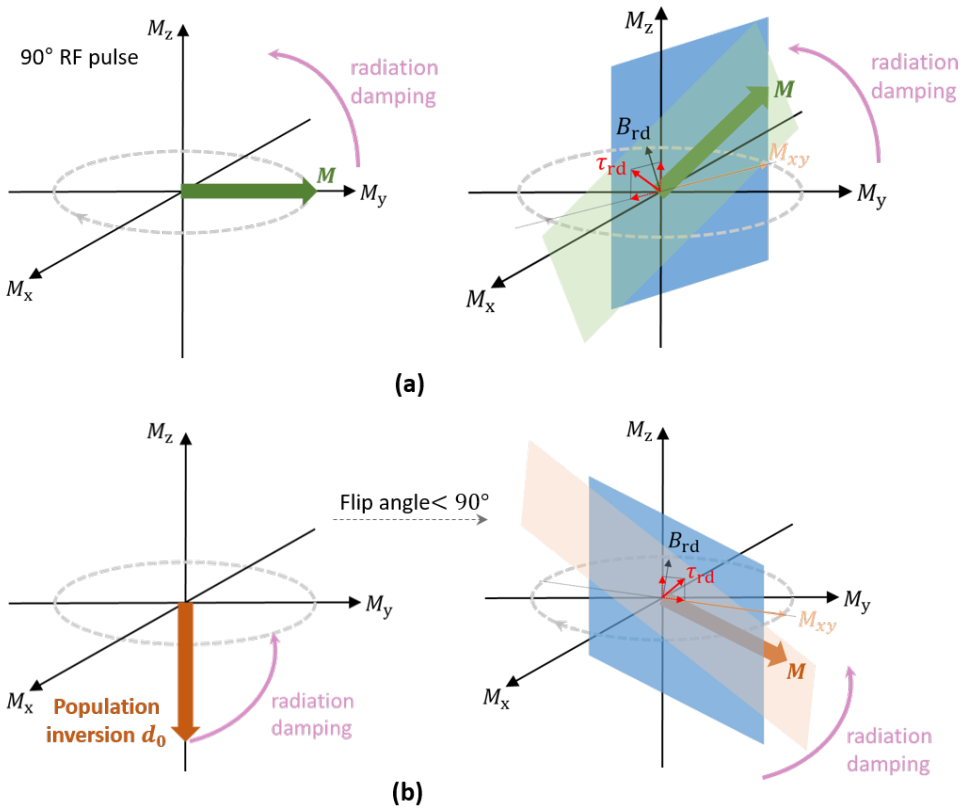

Figure 6.1: Schematic showing the effect of radiation damping (τ_{rd}) in the case of **(a)** normal NMR detection with a 90° RF pulse applied on a positive magnetization and **(b)** negative longitudinal magnetization with a small flip-angle.

If the generation rate of this transverse magnetization through radiation damping exceeds its relaxation rate ($1/\tau_{d,0} > 1/T_2^*$), the spin system can develop the transverse magnetization spontaneously and it is RASER active.

6.3 Hyperpolarization pumped RASER

NMR is a versatile and powerful analytical tool in many fields, such as chemistry, biology, pharmacy, and beyond. However, the resolution of any NMR experiment is still limited by the effective transverse relaxation time T_2^*. In this way, any NMR experiment has a minimum natural linewidth, and higher frequency resolution can only be gained at low speed through signal averaging. This limitation can be overcome by a RASER with sub-mHz NMR resolution. [194]

Additionally, a RASER can be used to study nonlinear phenomena in coupled spin systems [189, 186], or to transfer polarization to molecules-of interest (e.g. amino acids) using a PRINOE (Para-hydrogen and RASER Induced Nuclear Overhauser Effect) [195, 187].

As mentioned above, to operate a RASER of the spin-1/2 system, a population inversion between the two Zeeman splitting energy levels is required. This can be generated for example

by hyperpolarization methods. The most common hyperpolarization methods are SEOP, DNP and PHIP. RASERs have been demonstrated with all these techniques: previous work has shown RASERs of ^{1}H, ^{17}O and ^{17}Al by using DNP in solid-state at low temperature and at high magnetic field. [196, 188, 197] The innovation of dissolution-DNP makes the measurement of DNP-RASER in liquid-state more favorable. [198] Alternatively, the liquid-state RASERs are observed by dissolving SEOP hyperpolarized nobel gases (^{3}He and ^{129}Xe). [199, 200] However, SEOP and DNP are currently mostly limited to single-mode operation, and require sophisticated equipment. [201, 202]

With parahydrogen fueled RASERs, various new use-cases were unveiled in recent years, all based on RASERs with multiple frequencies. These included a chemical reaction tracked by a ^{13}C RASER, [203] the study of nonlinear phenomena, [186, 189] and background-free NMR, [204, 205, 206] reaching a frequency resolution below the mHz regime. [194] Additionally, by introducing magnetic field gradients, RASER modes were used to encode spatial information, i.e., RASER MRI. [207]

Despite all these advantages, a *para*-H_2 fueled RASER operating at a high magnetic field is burdened by the *para*-H_2 pumping itself. *para*-H_2 bubbles formed in a solution generate susceptibility artifacts that broaden the RASER signals. [206] Turning off the pumping during acquisition alleviates this problem, but limits RASER signals to bursts that only last until the polarization is depleted. [189, 207] Additionally, over the course of a RASER burst, it passes through different operating regimes and features different types of nonlinear phenomena due to the decaying polarization.

6.3.1 Continuous steady-state ALTADENA PHIP-pumped RASER

This work presents a steady-state RASER operating in different regimes. Utilizing two nonlinear-coupled RASER modes, various operational states are demonstrated, including a starting RASER, a "normal NMR" RASER, a RASER dominated by frequency combs, a RASER dominated by period doublings, and a chaotic RASER (Figure 6.2**a**).

To achieve the steady-state RASER, highly polarized ethyl acetate (EA) is continuously supplied to the NMR magnet (Figure 6.2**b**). Continuous flow reactors for *para*-H_2 applications can avoid susceptibility artifacts caused by bubbles and continuously generate a highly polarized liquid. [145, 208, 184, 209] The hyperpolarized EA is generated within a tube-in-tube reactor [209, 210] by hydrogenating vinyl acetate (VA) with *para*-H_2 (Figure 6.2**c**).

A convenient alternative to hydrogenative PHIP is SABRE [98], which allows for repetitive polarization of the same solution. [210] However, the polarizations at high concentrations is often lower than in hydrogenative PHIP. [186, 204] Therefore, a hydrogenation reaction is chosen as a model system to access higher population inversions, and with it a broader range of RASER regimes.

In this work, VA is hydrogenated with *para*-H_2 in a tube-in-tube reactor at the Earth's magnetic field with detection at 1.45 T, and thus under ALTADENA condition [96]. Hydro-

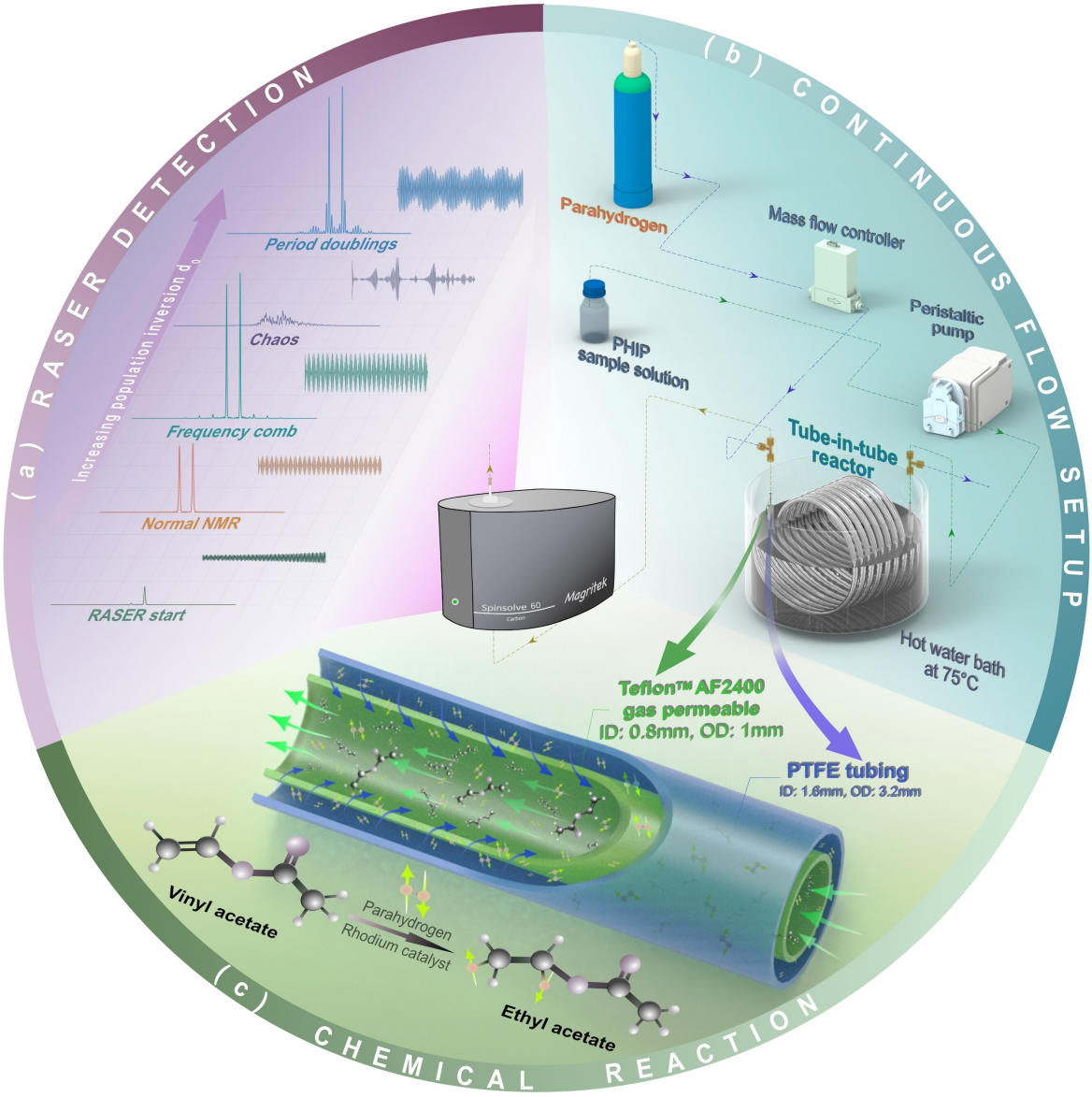

Figure 6.2: Controlling and monitoring continuous-flow RASERs pumped by *para*-H_2. The experimental setup (cyan) features a chemical reaction at its core (green) to detect RASER signals precisely over long periods of time (purple). Five different RASER regimes were acquired on a 60 MHz benchtop spectrometer. At the heart of the experimental setup is a tube-in-tube gas-liquid reactor. Within this reactor, the liquid flow (green arrows) as well as the *para*-H_2 pressure and flow rate (blue arrows) can be controlled. The chosen chemical system is a hydrogenation reaction of vinyl acetate (VA) to ethyl acetate (EA). (Adopted from [JY02].)

genation under PASADENA condition is possible with this setup for example by adding a coil to generate a higher magnetic field around the reactor. [204] However, ALTADENA provides an ideal condition for observing different RASER regimes: an antiphase ^{1}H spectrum of the hydrogenation product ethyl acetate (EA) is obtained in this work, characterized by a positively polarized ethyl group and a negatively polarized methyl group (Figure 6.3). The triplet of the methyl group (highlighted in green) can fuel a RASER, as the negative polarization constitutes a population inversion. If the population inversion is high enough, the RASER threshold d_{th} is surpassed and a RASER initiates. [186] The triplet entails three potential RASER modes $d_{0,\mu}$ ($\mu = 1, 2, 3$) separated by a 7.10 Hz J-coupling. Only two of these modes are RASER active, as the mode with the smallest polarization does not surpass the RASER threshold, but can fuel the other modes as described previously. [204] The identification of the two RASER-active modes will be detailed discussed later in section 6.4.1

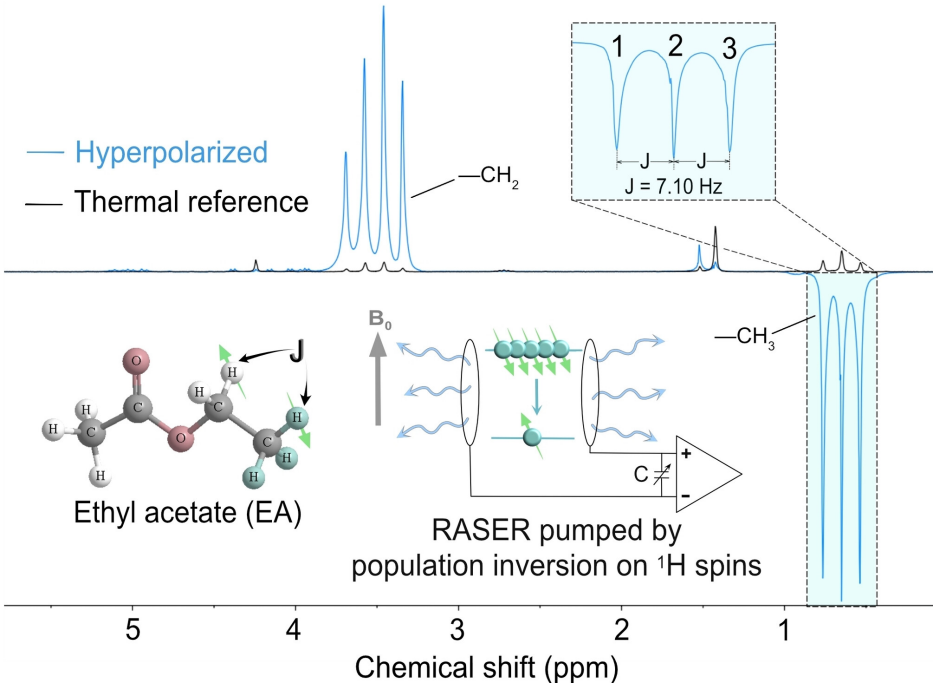

Figure 6.3: ^{1}H NMR spectrum of ALTADENA-PHIP hyperpolarized EA at the Earth's field (blue) compared to a thermal reference spectrum recorded at 1.45 T (grey). The methyl group (highlighted in cyan) is negatively polarized and its resonances can therefore be RASER active. The two modes with the highest intensity (the middle and right mode) surpass the RASER threshold, yielding the two RASER active modes shown in Figure 6.4-Figure 6.9. Details on the RASER-active modes and the threshold can be found in section 6.4.1. (Adopted from [JY02].)

6.3.2 Experiments

6.3.2.1 Chemical preparation

- Preparation of PHIP sample solution

All PHIP sample solutions were prepared under inert gas conditions. Each solution contained 400 mmol/L VA and 4.0 mmol/L [Rh(dppb)(COD)]BF_4 in methanol-d_4. The deuterated methanol was degassed by three freeze-pump-thaw cycles using a bath of liquid nitrogen and argon. All other chemicals were purchased from Sigma-Aldrich and used without further purification. VA (CAS number: 108-05-4, Sigma-Aldrich, 100 mL) and [1,4-Bis-(diphenylphosphino)-butan]-(1,5-cyclooctadien)-rhodium(I)-tetrafluoroborat (CAS number: 79255-71-3, Sigma-Aldrich, 500 mg).

- Enrichment of *para*-H_2

Normal hydrogen gas (ALPHAGAZ^{TM} H_2, 99.999%) flows along the pipeline with an appropriate flow rate (0.5 L/min) controlled by a mass flow controller. A commercial water-cooled helium compressor (Advanced Research System, Model ARS-4HW) offers the cooling source to the cryostat (cold head) at 23 K. After contacting the paramagnetic hydrated iron (III) oxide catalyst ($Fe_2O_3 \cdot H_2O$) in the chamber at the bottom of the cold head, the *para*-H_2 fraction of 98% was generated and collected within an aluminum gas bottle.

6.3.2.2 Experimental setup

The basic experimental setup used for exploring the PHIP-RASER phenomenon is shown in Figure 6.2. The PHIP experiments were conducted using the ALTADENA protocol.

The main parts of the continuous flow experimental setup are: a mass flow controller for *para*-H_2 gas, a peristaltic pump (BT100-2J, LongerPump, China) for pumping the PHIP sample solution, two back pressure regulators for control the pressure applied in gas and liquid phase, and a tube-in-tube gas-liquid reactor that introduces the *para*-H_2 into the solution for the PHIP hyperpolarization.

The tube-in-tube gas-liquid reactor consists of an outer PTFE tubing (ID: 1.6 mm, OD: 3.2 mm) with an inserted inner tubing (Teflon^{TM} AF 2400, ID: 0.8 mm, OD: 1 mm). The inner tubing is a semi-permeable membrane with high gas permeability. It allows for gas transfer from one side to according to the pressure difference. The inner and outer tubing have an overlapped length of 1.5 m to achieve a high contacting area. More details of tube-in-tube reactor can be found in Chapter 4.3.4.

Here, the PHIP solution and *para*-H_2 gas flow in opposite directions in the outer and inner tubing. To increase the conversion of the hydrogenation reaction, the tube-in-tube reactor is wrapped into a compact winding, and immersed in a hot water bath at 75 °C. To halt the reaction after the reactor and enhance the quality of the spectra, an ice-water bath was placed immediately after the tube-in-tube reactor to cool the sample solution before NMR signal acquisition.

6.4 Results and discussion

In this study, a series of ^{1}H RASER signals were recorded at 1.45 T under continuous flow conditions (Figure 6.4-Figure 6.9). To explore different operating regimes, the pressure differential Δp between the gas and liquid phases in the tube-in-tube reactor was varied. Higher gas uptake efficiency enhanced the conversion of the hydrogenation reaction, thereby increasing the amount of hyperpolarized EA.

To ensure that Δp was the sole experimental variable, the sample flow rate was kept constant at 4 mL/min throughout all experiments. The flow rate affects both the residence time in the reactor and the transport time to the detection zone. Any variation would influence the efficiency of the hydrogenation reaction and the extent of relaxation losses, thereby altering the effective pumping level of d_0. Therefore, this Δp-controlled method enabled quantitative control over the pumping of the RASER, with the amount of population inversion d_0 reaching the magnet given by Equation (6.4):

$$d_0 = N_\mathrm{A} \cdot V_s \cdot c \cdot P_H \tag{6.4}$$

where N_A is Avogadro's number, V_s is the sensitive volume of the NMR detection coil, c is the concentration, and P_H is polarization of the RASER active ^{1}H spins.

6.4.1 Identifying different RASER regimes

The identification of each measured RASER signal was performed through analysis of the corresponding NMR spectrum. To obtain spectra from a five-second time slice, a Hamming filter was applied to the RASER signal to suppress Sinc wiggles. The selected time-domain segment was zero-filled with twice the signal length, both before and after the slice. The final RASER spectra were obtained by applying a Fast Fourier Transform (FFT) and are displayed in absolute mode.

For longer time slices, correction for magnetic field drift, as described by TomHon et al. [209] and Nelson et al. [203], or for magnetic field fluctuations, as in the method by Suefke et al. [194], would be required. However, a five-second time window of the RASER signal is sufficient to analyze the spectral features characteristic of each RASER regime. In this way, the five RASER spectra in Figure 6.4-6.9 are generated. The corresponding time slices are depicted in the insets of each regimes. (A composite version combining all measured five RASER regimes is shown in Appendix B.1.)

- RASER startup

The startup of a RASER was initiated by applying a small pressure differential of $\Delta p =$ 5 psi. The corresponding pumping level d_0 was sufficient to sustain a steady-state RASER. The steady-state population inversion during RASER emission was measured by applying a 90° pulse. After the FID decayed ($t > 5$ s), RASER activity resumed (Figure 6.4**a**), illustrating the competition between two RASER-active lines during the initial stage of RASER

formation (Figure 6.4**b**). The RASER spectrum between $t = 10-15$ s shows two RASER-active modes separated by their J-coupling, with differing signal intensities; one mode is more highly polarized and therefore extends further above the RASER threshold. At $t > 20$ s, the RASER signal reaches a steady state, in which only two components of the methyl proton triplet persist.

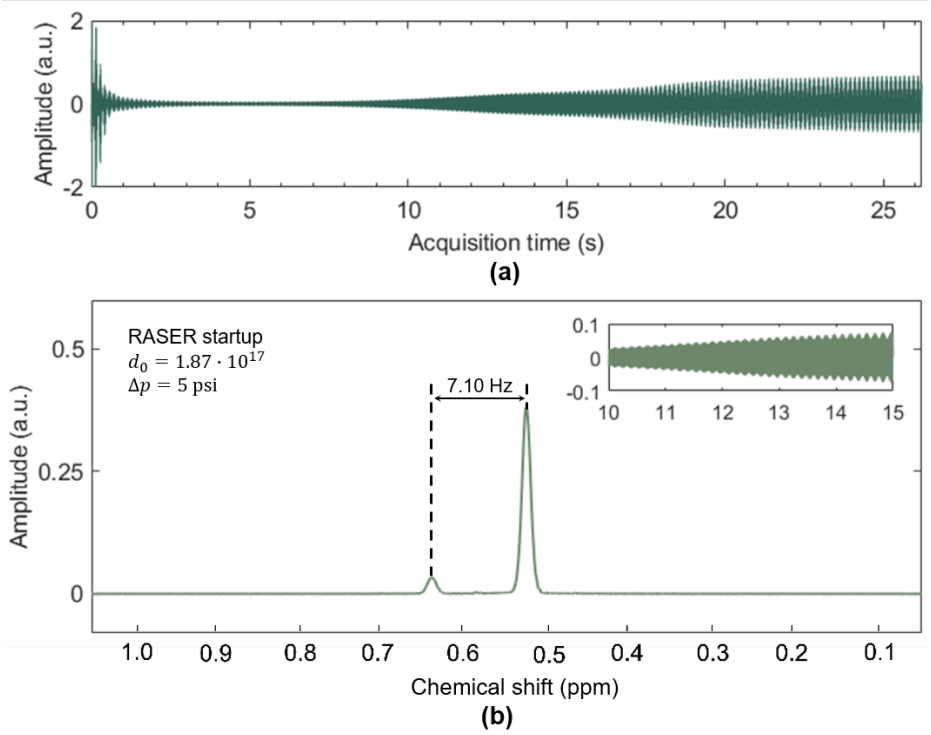

Figure 6.4: **(a)** Continuously pumped RASER signal of EA in the startup regime. (Signal measured with a 90° excitation pulse with acquisition of 131072 points and 200 µs dwell time.) **(b)** FFT of the time sliced RASER start signal. (Adapted from [JY02].)

As discussed above, for the PHIP hyperpolarization of EA, the *para*-H_2 molecule is added to the C=C bond of VA yielding hyperpolarized EA (ALTADENA conditions), which results a spectrum of positively polarized quartet and a negatively polarized triplet (see Figure 6.3). The positively polarized mode is not RASER-active, as population inversion is required for RASER emission.

To identify the two RASER-active modes, the FID section with the sliced time window of $0-2$ s of RASER startup signal in Figure 6.4**a** is analyzed. This FID recorded after the 90° pulse contains signals from both RASER-active modes, as well as from modes that lie below the RASER threshold or are positively polarized, such as the third resonance of the methyl group and the quartet signal from the ethyl group of EA (Figure 6.5**a**).

By analyzing the FFTs of different time windows during the RASER startup regime, it is observed that all non-RASER-active modes decay together with the FID (Figure 6.5**b**). In particular, the intensity of the leftmost component of the methyl triplet remains below the RASER threshold. As a result, only the two peaks on the right side persist and are identified

as RASER-active. This confirms that the EA-pumped RASER operates as a two-mode RASER.

Furthermore, the gradual shift of chemical shifts in the stacked spectra indicates magnetic field drift in the compact NMR magnet.

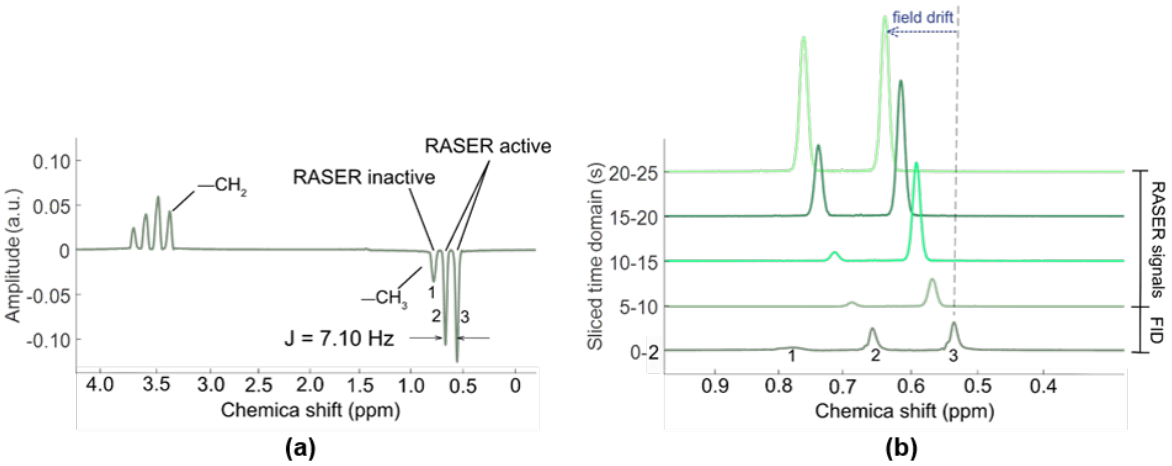

Figure 6.5: Identification of the two RASER-active modes. **(a)** ^{1}H spectrum of the FID with sliced time window of $0-2$ s in RASER startup regime. The ethyl group and methyl group of EA with J-coupling of 7.067 Hz are positively and negatively hyperpolarized respectively. The two negatively polarized lines with high intensity (2 and 3) are RASER active. The most left peak (1) is less intense and RASER inactive. **(b)** Five ^{1}H spectra acquired from different time windows of the continuous RASER signal (displayed in absolute mode). The peak positions shift due to magnetic field drift. (Adapted from [JY02].)

- "Normal NMR"

By increasing the population inversion to $d_0 = 5.22 \cdot 10^{17}$, a RASER with almost equal intensities on both modes is obtained (Figure 6.6**a**). This regime offers a convenient means of accurately measuring the J-coupling, as long as the RASER signal is sustained for a sufficient duration. As shown in the FFT of the 5 s RASER signal in this mode (Figure 6.6**b**), the measured frequency difference of 7.10 ± 0.01 Hz between the two RASER-active peaks is equal to the J-coupling of the methyl group, as previously measured for both thermally polarized and hyperpolarized EA (Figure 6.3).

- Frequency comb

At an even higher population inversion level ($d_0 = 9.98 \cdot 10^{17}$) (Figure 6.7), the spectrum exhibits a frequency comb structure. The two main peaks are separated by 7.18 Hz, and similar spacing is observed in the sidebands, indicating a regular frequency modulation pattern (Figure 6.7**b**). In this case, the measured frequency difference no longer corresponds to the J-coupling constant, as frequency shifts arising from nonlinear spin dynamics dominate the spectral features, which is a typical characteristic of non-linear systems.

- Chaos

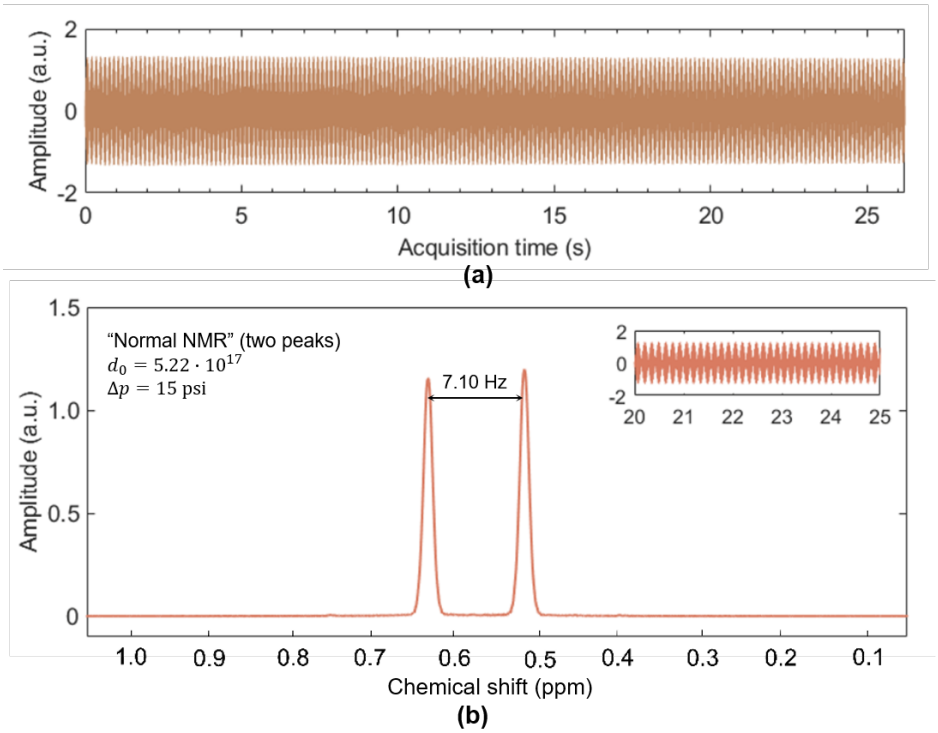

Figure 6.6: **(a)** "Normal NMR" regime. (Signal measured with a 3° excitation pulse with acquisition of 131072 points and 200 µs dwell time.) **(b)** FFT of the time sliced RASER signal with a frequency difference of 7.10 Hz between the two RASER-active peaks. (Adapted from [JY02].)

At a pumping level of $d_0 = 1.09 \cdot 10^{18}$, the RASER signal evolves through distinct dynamical regimes. Between 10-20 s, the signal exhibits a complex mixture of periodic and irregular behavior. This transitional phase is marked by intermittent period-doubling features and the gradual onset of chaotic dynamics, reflecting the system's proximity to a narrow chaotic region in parameter space. From 20 to 25 s, a clear chaotic regime emerges, characterized by irregular beat patterns (Figure 6.8**a**) and a broadband, noise-like spectrum with a continuum of frequencies (Figure 6.8**b**). This spectral signature, resulting from the overlap of multiple bifurcation processes [207], confirms that the system has fully entered a chaotic state.

The chaotic behavior observed in this study is sustained for several seconds, in contrast to previous works where the chaotic regime appeared only transiently (<1 s) due to rapid changes in population inversion within an acquired RASER burst, and thus narrowing the width of the chaotic window [189]. The long-lived chaotic emission observed here is enabled by the strategy of steady-state RASER operation driven by continuous hyperpolarization.

- Period doublings

Upon slightly increasing the population inversion ($d_0 = 1.15 \cdot 10^{18}$) beyond the chaotic regime, the RASER enters a well-defined period-doubling regime. As shown in Figure 6.9**a**, the time-domain signal exhibits a regular beat pattern, and the corresponding spectrum forms an even frequency comb (Figure 6.9**b**). Multiple period-doubling processes are evident, with consecutive peaks spaced by 1.40 Hz and the two dominant peaks separated by 6.99 Hz. This

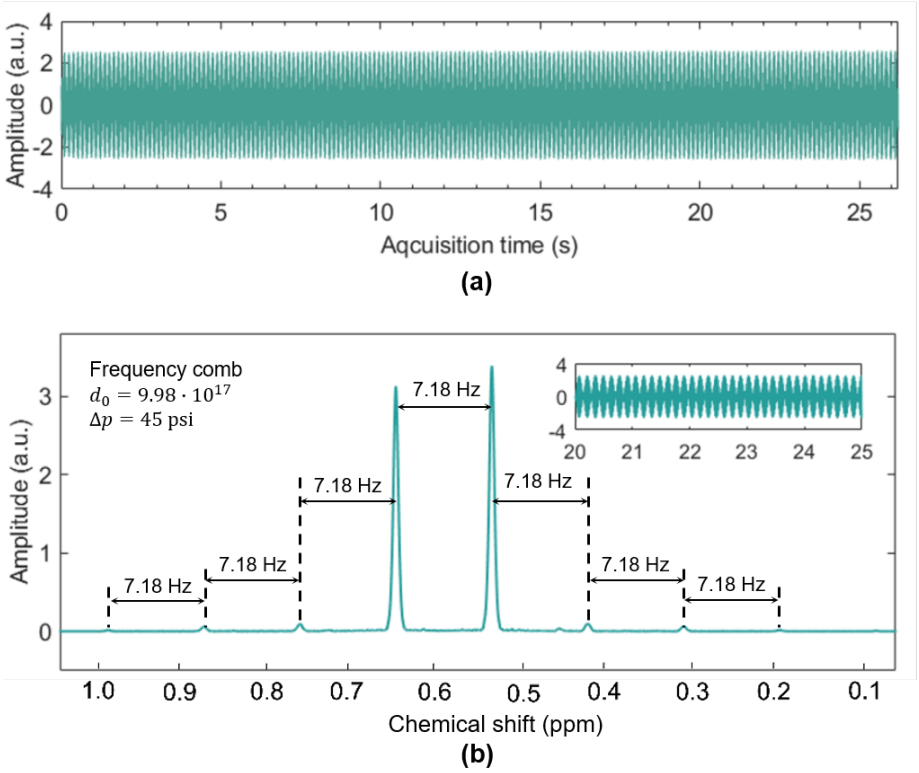

Figure 6.7: **(a)** Frequency comb regime. (Signal acquired with a 3° excitation pulse, 131072 acquisition points, and 200 µsdwell time.) **(b)** FFT of the time sliced RASER signal in frequency comb mode with equidistance between the peaks. (Adapted from [JY02].)

observation reveals the re-emergence of structured nonlinear behavior and indicates that the system remains highly sensitive to small changes in population inversion pumping strength.

Notably, the observation of period doubling behavior both before and after the chaotic window underscores that chaos emerges within a relatively narrow interval of the control parameter, here it is the population inversion in RASER system, where small variations in pumping strength can drive the system through repeated transitions between order and apparent "disorder". Nevertheless, chaos does not merely represent a state of randomness. Rather, it embodies a complex and highly structured dynamical behavior characterized by an infinite hierarchy of motions.

6.4.2 Measurement and calculation the parameters in steady-state RASER

To better understand the pumping conditions underlying the population inversion in the observed RASER regimes, this section presents a quantitative analysis of key parameters in the steady-state RASER system. These include the measurement of the T_1relaxation time, the calculation of polarization levels under both thermal equilibrium and hyperpolarized conditions, the threshold for continuous-flow RASER onset, and the resulting population inversion for each observed regime. The extracted parameters also serve as input for the numerical simulations of the two-mode RASER model discussed in the following section.

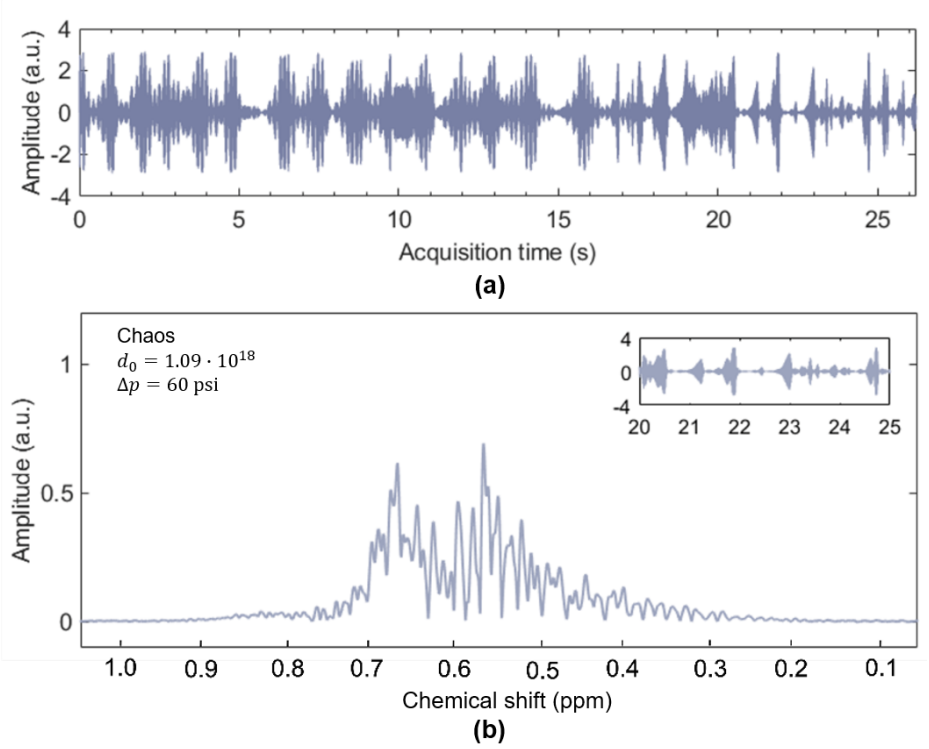

Figure 6.8: **(a)** Chaos regime. (Signal acquired with a 3° excitation pulse with acquisition of 131072 points, and 200 µsdwell time.) **(b)** FFT of the time sliced RASER signal in Chaos mode. (Adapted from [JY02].)

6.4.2.1 Measuring T_1 of the ^{1}H protons in the methyl group of EA to estimate the polarization loss in the sensitive volume

As VA is hydrogenated with *para*-H_2 at the Earth's magnetic field, the resulting spin order in EA exhibits a high singlet character. The hyperpolarized EA is then adiabatically transferred into the 1.45 T, the singlet-triplet basis no longer represents an ideal eigenbasis for the spin system, as the singlet character is substantially reduced. At this field, RASER emission becomes active and is therefore relevant for the simulations. All polarization changes occurring prior to entry into the sensitive volume—including the generation at the Earth's field and relaxation losses during sample transfer—are collectively represented in the simulations as a "pumping" term in the form of d_0. Consequently, thermal T_1 relaxation is considered a reasonable approximation for polarization loss during the experiment and is used as an input parameter for the RASER simulations. The measured T_1 relaxation time of EA is shown in Figure 6.10.

6.4.2.2 Calculating the thermal polarization and the polarization of the HP EA

The thermal polarization P_{thermal} is given as:

$$P_{\text{thermal}} = \tanh\left(\frac{\hbar \cdot \gamma_{\text{H}} \cdot B_0}{2 \cdot k_{\text{B}} \cdot T}\right) \tag{6.5}$$

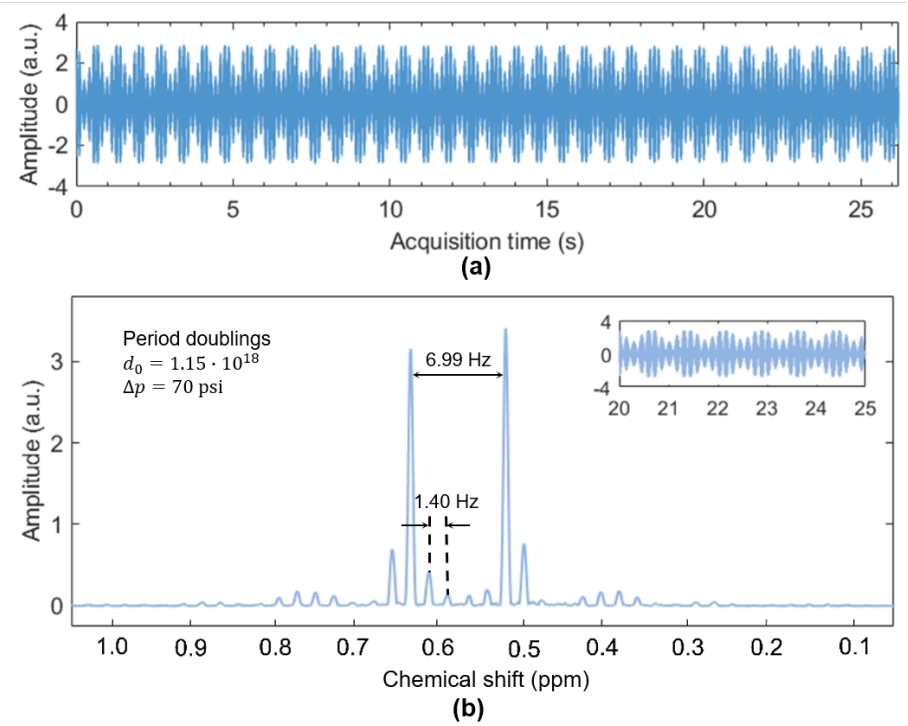

Figure 6.9: (a) Period doublings regime. (Signal measured with a 3° excitation pulse with acquisition of 131072 points and 200 µs dwell time.) **(b)** FFT of the time sliced RASER signal in period doublings mode. (Adapted from [JY02].)

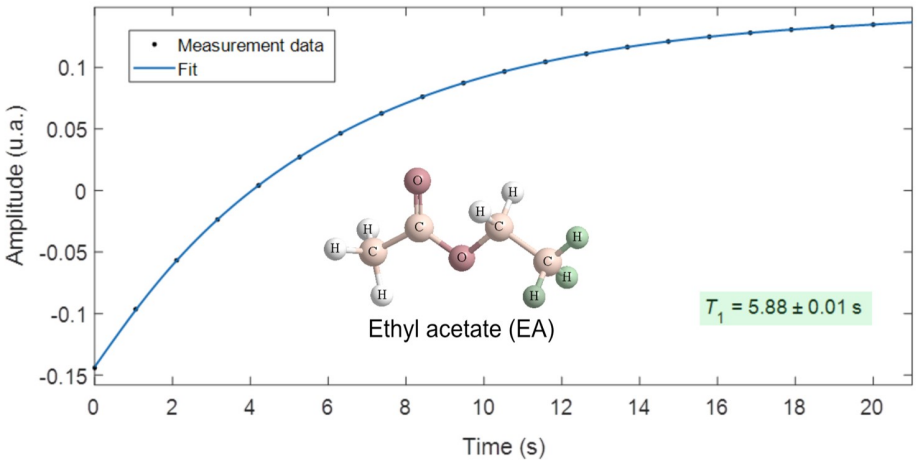

Figure 6.10: T_1 relaxation time of the protons in the methyl group of EA (highlighted in green) measured with the inversion recovery sequence. The sample contained 4 mmol/L [Rh(dppb)(COD)]BF_4 and 400 mmol/L EA in a methanol-d_4 solution and was measured in a standard 5 mm NMR tube on the 1.45 T benchtop NMR. (Adopted from [JY02].)

which gives

$$P_{\text{thermal}} = \tanh\left(\frac{1.054 \cdot 10^{-34} \cdot 2.675 \cdot 10^{8} \cdot 1.45}{2 \cdot 3.38 \cdot 10^{-23} \cdot 293}\right) = 1.98 \cdot 10^{-6} \tag{6.6}$$

at 61.92 MHz (1.45 T) and room temperature (293 K). The polarization P_x under hyperpolarized conditions can be estimated using the following relation:

$$P_x = \epsilon \cdot P_{thermal} = \frac{S_{HP}}{S_{thermal}} \cdot P_{thermal} \tag{6.7}$$

6.4.2.3 Calculation of the continuous-flow RASER threshold

The initiation of RASER action depends on reaching certain threshold conditions. A RASER starts and is sustained, if the population inversion of the RASER active modes is above the RASER threshold. Following [186], the RASER threshold is given by:

$$d_{th} = \frac{\gamma_m \kappa_m}{g_m^2} \tag{6.8}$$

with $\gamma_m = 1/T_2^*$ as the effective transverse relaxation rate of ^{1}H, $\kappa_m = \omega_0/Q$ as the damping rate of the LC circuit with resonance frequency of ω_0 and quality factor of Q, and ${g_m}^2$ as the magnetic coupling constant given in SI units as:

$$g_m^2 = \frac{\mu_0 \hbar {\gamma_H}^2 \omega_H}{4V_s} \tag{6.9}$$

Below are the values of all the constants and parameters:

$k_B = 3.38 \cdot 10^{-23}$ m$^2 \cdot$ kg/(s$^2 \cdot$ K)	- Boltzmann constant;
$T = 293$ K	- room temperature;
$B_0 = 1.4$ T	- static magnetic field strength;
$\omega_H = 3.745 \cdot 10^8$ rad/s	- Larmor frequency of ^{1}H nucleus;
$V_s = 2.5 \cdot 10^{-7}$ m^3	- sensitive volume of the NMR detection coil;
$\mu_0 = 1.257 \cdot 10^{-6}$ T $\cdot$ m/A	- magnetic permeability of vacuum;
$\hbar = 1.054 \cdot 10^{-34}$ m$^2 \cdot$ kg/(s $\cdot$ rad)	- reduced Planck constant;
$\gamma_H = 2.675 \cdot 10^8$ rad/(s $\cdot$ T)	- ^{1}H gyromagnetic ratio;
$T_2^* = 1/(\pi \cdot 3.20$ Hz$) = 0.13$ s	- effective transverse relaxation time;
$Q = 68$	- quality factor of the ^{1}H detection coil.

In addition, the unit for magnetic field Tesla [T] = kg/[A $\cdot$ s^2] in SI units. Thus, the value of the magnetic coupling constant is:

$$\begin{aligned} g_m^2 &= \frac{\mu_0 \hbar {\gamma_H}^2 \omega_H}{4V_s} \\ &= \frac{1.257 \cdot 10^{-6} \cdot 1.054 \cdot 10^{-34} \cdot (2.675 \cdot 10^8)^2 \cdot 3.745 \cdot 10^8}{4 \cdot 2.5 \cdot 10^{-3}} \frac{\text{T} \cdot \text{m}^2 \cdot \text{kg}}{\text{A} \cdot \text{s} \cdot \text{rad}^2 \cdot \text{s}^2 \cdot \text{T}^2} \\ &= 3.55 \cdot 10^{-9} \frac{1}{\text{s}^2} \end{aligned} \tag{6.10}$$

Following Equation (6.8) and Equation (6.9), the RASER threshold can be rewritten as:

$$d_{th} = \frac{4V_s}{\mu_0 \hbar Q \gamma_H^2 T_2^*} \tag{6.11}$$

the RASER threshold during continuous flow is:

$$d_{\mathrm{th}} = \frac{4 \cdot 2.5 \cdot 10^{-7}\ \mathrm{m}^3}{1.257 \cdot 10^{-6}\ \frac{\mathrm{T \cdot m}}{\mathrm{A}} \cdot 1.054 \cdot 10^{-34}\ \frac{\mathrm{m^2 \cdot kg}}{\mathrm{s \cdot rad}} \cdot 68 \cdot (2.675 \cdot 10^{8}\ \frac{\mathrm{rad}}{\mathrm{s \cdot T}})^2 \cdot 0.13\ \mathrm{s}} = 1.19 \cdot 10^{16} \tag{6.12}$$

6.4.2.4 Estimating the pumping of population inversion during continuous flow

Here, a method is introduced to estimate the pumping of population inversion d_0 under continuous flow conditions. The equilibrium amplitude A_{eq} of the transverse spin component and the equilibrium population inversion d_{eq} can be calculated as:

$$A_{\mathrm{eq}} = N_{\mathrm{A}} \cdot c \cdot V_s \cdot P_{\mathrm{thermal}} \cdot \epsilon_{\mathrm{RASER}} \tag{6.13}$$

$$d_{\mathrm{eq}} = N_{\mathrm{A}} \cdot c \cdot V_s \cdot P_{\mathrm{thermal}} \cdot \epsilon_{\mathrm{FID}} \tag{6.14}$$

With N_{A} as the Avogadro constant, c as the RASER active proton concentration in the sample solution, V_s as the sensitive volume of the NMR magnet, and P_{thermal} as the thermal polarization of the NMR magnet. The enhancements $\epsilon_{\mathrm{RASER}}$ and ϵ_{FID} are obtained by FFT of the RASER signals and FID signal calculating the corresponding ^{1}H NMR signal integral ratio of the two RASER active modes on methyl group between the hyperpolarized and at thermally polarized EA.

Since $\dot{d} \approx 0$ and $\dot{A} \approx 0$ in the steady state RASER, only T_1-relaxation and effective T_2-relaxation are considered as loss terms to estimate the pumping of d_0 during continuous flow:

$$d_0 = \sqrt{\left(\frac{d_{\mathrm{eq}}}{e^{1/T_1}}\right)^2 + \left(\frac{A_{\mathrm{eq}}}{e^{-1/T_2{}^*}}\right)^2} \tag{6.15}$$

with e^{-1/T_1} and $e^{-1/T_2{}^*}$ as the T_1- relaxation and effective T_2-relaxation loss rates.

Here, the pumping of population inversion d_0 of the continuous flow RASERs in Figure 6.4-Figure 6.8 is estimated. First, the signal enhancement ϵ is calculated and the corresponding polarization levels and then estimate the pumping of population inversion d_0 as described in the experimental procedures.

6.4.3 Simulation of the two nonlinear-coupled RASER modes

6.4.3.1 Model of two nonlinear-coupled RASER modes

To complement the experimental results, RASER signals were simulated based on the equations from previous works of Appel et al. [186] for N nonlinear-coupled RASER modes. Following these equations, the evolution of each mode μ is described the population inversion

Table 6.1: Calculation of the pumping of population inversion d_0 of the five RASER regimes for Figure 6.4-Figure 6.9 based on Equation (6.5)–(6.15).

	Signal enhancement ϵ	Polarization level P_x (%)	Estimated pumping d_0
FID[1]	1589	0.314	—
RASER start[2]	137	0.027	1.87×10^{17}
"Normal NMR"[3]	953	0.189	5.22×10^{17}
Frequency comb[4]	3440	0.523	9.98×10^{17}
Chaos[5]	3972	0.604	1.09×10^{18}
Period doublings[6]	4514	0.894	1.15×10^{18}

[1] Figure 6.4**a** (0-2 s);
[2] Figure 6.4**a** (10-12 s);
[3] Figure 6.6**a** (20-22 s);
[4] Figure 6.7**a** (20-22 s);
[5] Figure 6.8**a** (20-22 s);
[6] Figure 6.9**a** (20-22 s).

d_μ, the amplitude of the transverse spin component A_μ, and the phase ϕ_μ of each mode:

$$\dot{d}_\mu = \Gamma_\mu(d_{\mu,0} - d_\mu) - \frac{d_\mu}{T_{1,\mu}} - \frac{4{g_\mathrm{m}}^2}{\kappa_\mathrm{m}} \sum_{\tau=1}^{N} A_\tau A_\mu \cos(\phi_\tau - \phi_\mu) \tag{6.16}$$

$$\dot{A}_\mu = -\gamma_\mathrm{m} A_\mu + \frac{{g_\mathrm{m}}^2}{\kappa_\mathrm{m}} d_\mu \sum_{\tau=1}^{N} A_\tau \cos(\phi_\tau - \phi_\mu) \tag{6.17}$$

$$\dot{\phi}_\mu = \omega_\mu + \frac{{g_\mathrm{m}}^2}{\kappa_\mathrm{m}} \frac{d_\mu}{A_\mu} \sum_{\tau=1}^{N} A_\tau \cos(\phi_\tau - \phi_\mu) \tag{6.18}$$

As the simplest model for this case, $N = 2$ modes are used, with a frequency difference of 7.0 Hz, corresponding to the two active RASER modes observed in the experiments (for details on which modes are RASER-active, see Figure 6.5). Distant dipolar fields generated by high spin polarization or magnetic field fluctuations of B_0 are not considered. Using this model, RASER signals are simulated in MATLAB (2021b) by solving the ordinary differential equations with the ODE45 solver. (The MATLAB codes can be found in Appendix B.2.)

For the simulations, two nonlinearly coupled RASER modes with a frequency difference $\Delta\nu = 7.0$ Hz are assumed, matching the two RASER active modes from the experiments. The spectra are compiled into a bifurcation diagram (Figure 6.12**a**), which shows how a system's long-term behavior changes as a control parameter (here is the population inversion d_0) is varied, and is often used to visualize nonlinear chaotic systems such as the logistic map. [211, 212, 213]

6.4.3.2 Generation of a bifurcation diagram of the two-mode RASER system

To generate a bifurcation diagram of the nonlinear-coupled system, several steps are followed. The flow chart is presented in detail in Figure 6.11.

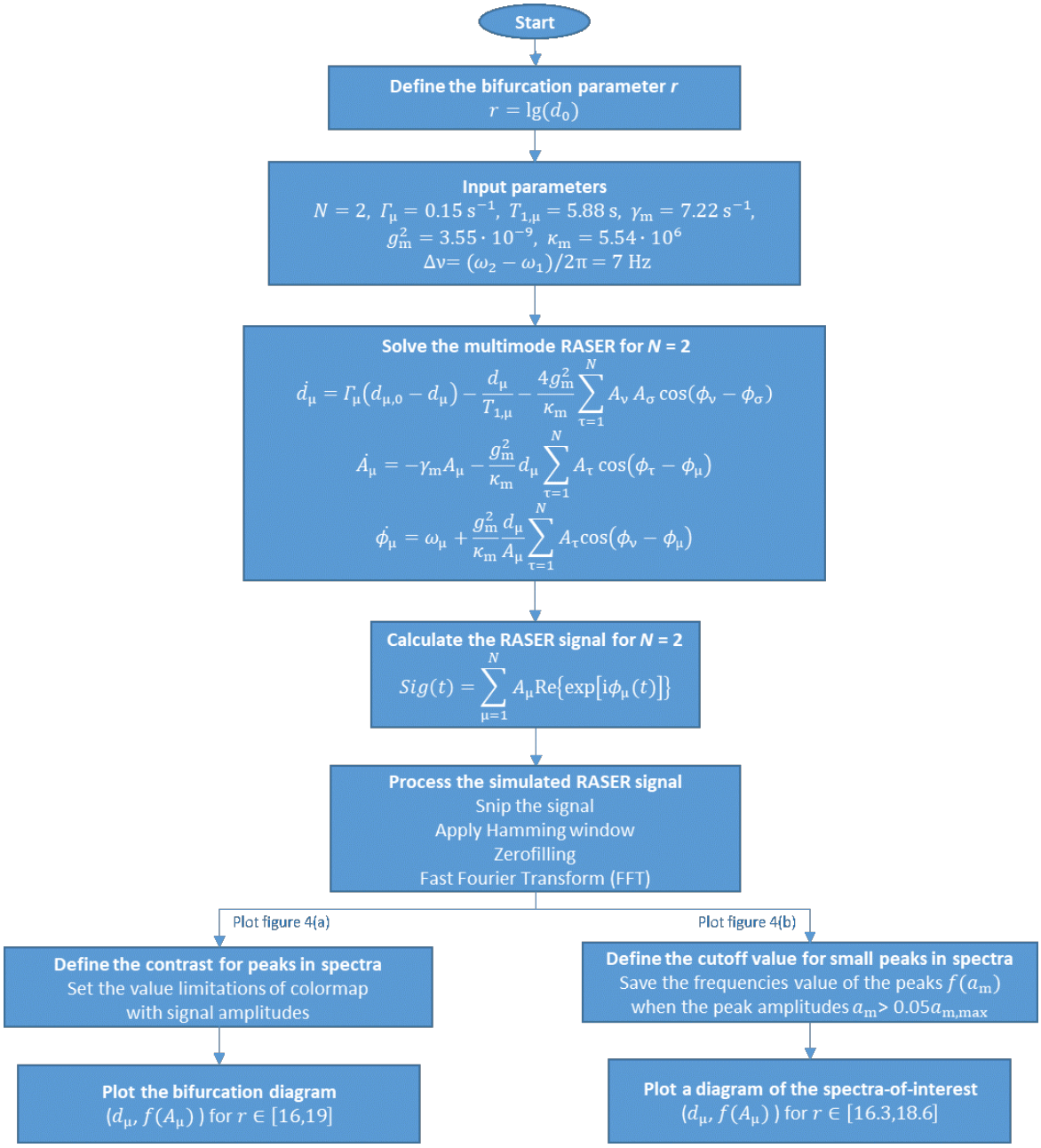

Figure 6.11: Flow chart of the main steps to simulate the bifurcation diagram of two nonlinear-coupled RASER modes (in Figure 6.12). The values for $T_{1,\mu}$, γ_m, and $\Delta\nu$ are chosen to match the experimental conditions in Figure 6.3. (Adopted from [JY02].)

First, RASER signals are simulated at different values d_0. The pumping d_0 is the key parameter that defines the nonlinear system and its logarithm is the analogue to the bifurcation parameter r from bifurcation theory. In the simulation, the input parameters are the pumping rate for the two RASER active modes Γ_μ, the longitudinal relaxation time $T_{1,\mu}$, the

effective transverse relaxation rate γ_m, the magnetic coupling constant g_m^2, the damping rate κ_m of the LC circuit at the NMR detection coil, the frequency difference of the two modes $\Delta\nu$.

Here, the simplest case is considered, where the pumping rates and T_1 relaxation rates are identical for each mode, i.e., $\gamma_1 = \gamma_2$ and $T_{1,1} = T_{1,2}$. In this way, the RASER signal is obtained as

$$\mathrm{Sig}(t) = A_1 \mathrm{Re}\left\{\exp\left[i\phi_1(t)\right]\right\} + A_2 \mathrm{Re}\left\{\exp\left[i\phi_2(t)\right]\right\}. \tag{6.19}$$

The signal is then processed by snipping a slice-of-choice of the signal, applying a Hamming window to suppress Sinc wiggles and zerofilling before and after the signal. After that, the signal is Fourier transformed to obtain a RASER spectrum.

Finally, a contrast method is selected to visualize the dominant frequencies in the bifurcation diagram. This is done either by (a) using a color bar that reflects the peak amplitude (as shown in Figure 6.12**a**), or (b) applying a cutoff threshold to suppress small peaks (as shown in Figure 6.12**b**). For Figure 6.12**b**, a prominence threshold of 0.05 is chosen to select significant peaks. A peak is displayed if its amplitude a_m exceeds 5% of the largest peak amplitude $a_{m,max}$ within the same spectrum, i.e., $a_m > 0.05 a_{m,max}$. (A 3D version of the simulated bifurcation diagram is shown in Appendix B.4.)

6.4.3.3 Mapping the 5 measured RASER signals within simulated bifurcation diagram

The predicted RASER spectra in the bifurcation diagram match with the experimental results. Depending on d_0, they feature the same regimes: two peaks, frequency combs, period doublings, and chaos (Figure 6.12**b**).

The increase of $\Delta\nu$ with increasing d_0 due to frequency shifts, and the reduced $\Delta\nu$ right after the chaotic regime, match the experimental findings. However, global shifts generated for example by distant dipolar fields [191, 214, 215, 216] or external magnetic field fluctuations [194] are not included in the simulation as there are several correction algorithms in post processing. [194, 209] The model is thus kept as simple as possible. Therefore, the model slightly deviates from the experimental results as it neglects other polarized spins in the resonator, and the loss of population inversion by polarized material flowing out of the NMR magnet.

6.5 Conclusion

In summary, a steady-state continuous ALTADENA-PHIP–pumped RASER at 1.45 T was successfully demonstrated. Long-term stability and precise control were achieved using a continuous-flow setup centered on a tube-in-tube gas–liquid reactor. Within the reactor, a highly polarized liquid was generated via hydrogenation of VA with *para*-H_2, serving as the pump source for ^{1}H RASER emission. The tube-in-tube gas-liquid reactor not only mitigates susceptibility artifacts such as bubble-induced instability, but also ensures reliable RASER

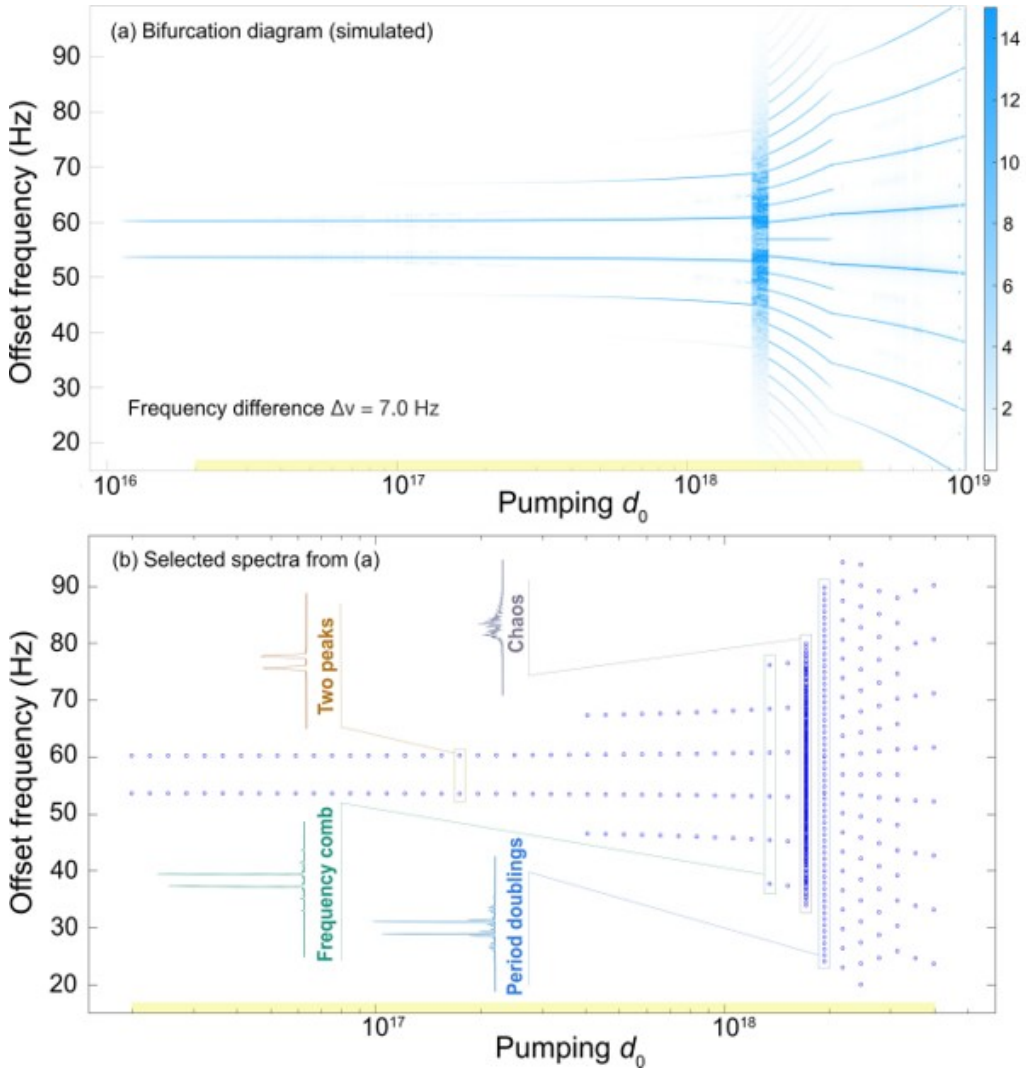

Figure 6.12: Simulated spectra of two continuously pumped RASER modes separated by 7 Hz at different pumping rates d_0. In **(a)**, the signal amplitudes are highlighted in a blue color, while **(b)** depicts the peaks of 45 spectra (only peaks $> 5\%$ of the maximum intensity) in the range of $d_0 \in [2{\cdot}10^{16}, 4{\cdot}10^{18}]$ (highlighted on the pumping axis d_0). With increasing d_0, all RASER regimes appear in the same sequence as for the experiments shown in Figure 6.6-Figure 6.9: two peaks, frequency comb, chaos, and period doublings. (Adopted from [JY02].)

operation over extended durations.

By tuning the polarization level (population inversion), various nonlinear RASER regimes were accessed, as reflected in the corresponding Fourier-transformed spectra. These include two-mode regimes with both equivalent and inequivalent amplitudes, frequency combs, period-doubling sequences, and chaotic behavior. The experimentally observed regimes are in good agreement with simulations based on a two-mode RASER model, enabling regime prediction through mapping the system's behavior onto a logistic bifurcation diagram.

Overall, PHIP in the tube-in-tube platform under continuous-flow conditions offers a robust and tunable experimental framework for RASER applications, including high-precision J-coupling measurements and fundamental investigations of nonlinear spin dynamics.

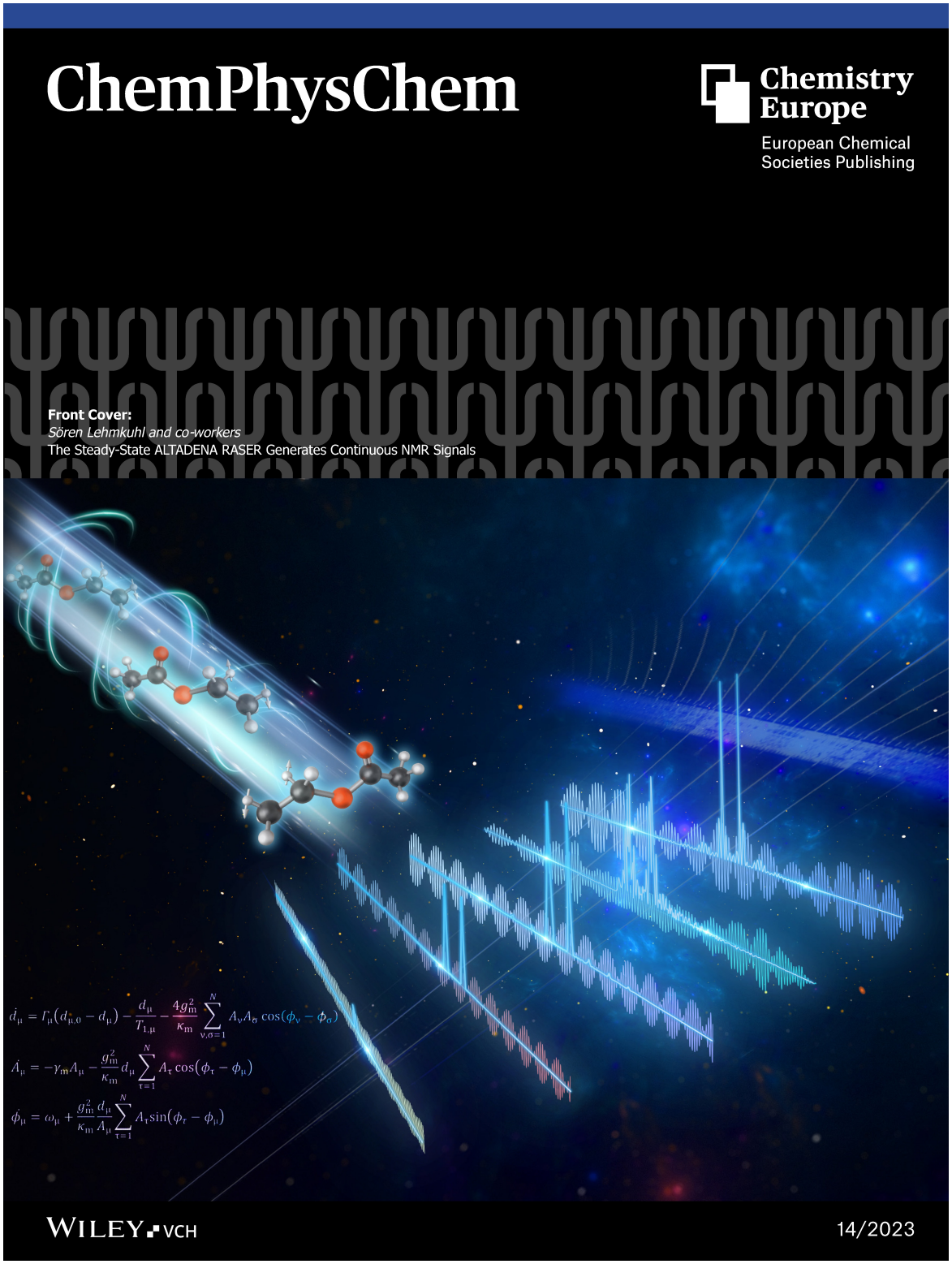

Figure 6.13: This paper has being featured on the cover of the Journal. (Adopted from [JY02].)

Automated SABRE Workstation on a Benchtop NMR

7.1 Overview

Despite the advances demonstrated in Chapters 5 and 6, where continuous-flow gas–liquid reactors were employed to extend SABRE and PHIP methods for accelerating NMR detection and the generation of steady-state RASER emission for precise J-coupling measurement, the implementation of SABRE in routine laboratory practice remains largely manual. Existing routine SABRE workflows often rely on operator-controlled bubbling and sample handling, introducing variability and limiting experimental reproducibility. These constraints present a barrier to the broader adoption of SABRE, particularly in applications requiring standardization, automation, and consistent performance.

To overcome these limitations, this chapter presents the design and implementation of a fully automated SABRE workstation, specifically developed to support routine hyperpolarization experiments on a benchtop NMR platform.

The subsequent sections of this chapter detail the development of the automated system and validate its performance through a series of SABRE experimental protocols. These include assessments of reproducibility across consecutive hyperpolarization cycles, magnetic field optimization for ^{13}C polarization, and time-resolved studies of polarization buildup and decay. In addition, automated SABRE-SHEATH experiments on ^{13}C-pyruvate are performed to demonstrate the platform's capability to support more advanced pulsed protocols. Through these developments, the chapter highlights how automation can streamline SABRE workflows, improve repeatability, and facilitate the routine application of hyperpolarization techniques. The results which are presented within this chapter are published under title "*Development of a fully automated workstation for conducting routine SABRE hyperpolarization*" in the journal ***Scientific Reports*** [JY03].

7.2 Introduction

As it mentioned in Chapter 3.6.2, SABRE can be implemented through three primary methods: shaking, bubbling, and utilizing a gas-liquid reactor. [111] Among these, shaking exhibits the least reproducibility, largely attributable to variations in manual force, making it less suitable for automated processes. [217, 218] The gas-liquid reactors and flow cell setups face challenges due to their large sample volumes and complex fluid management, hindering widespread adoption. [208, 219] Additionally, achieving optimal hyperpolarization requires balancing between contact time and sample transfer time, often leading to compromises in polarization levels. [209, 220] Bubbling is a simple method for delivering *para*-H_2 into the sample solution, and it is compatible with field cycling as well as automation techniques. This makes it a preferred choice for enhancing reproducibility and scalability in SABRE applications. [221, 99, 222]

While some automated setups have demonstrated in specific SABRE application [223, 99, 219] and shown improvements in the reproducibility of SABRE hyperpolarization [224, 221], there is still room for enhancement, particularly in terms of achieving full automation and and broadening functionalities for routine SABRE hyperpolarization. These routine SABRE protocols including activation of the pre-catalyst for SABRE hyperpolarization, field cycling for ^{1}H via SABRE hyperpolarization in milliTesla (mT) range [225, 226] and heteronuclei, such as ^{13}C, ^{15}N via SABRE-SHEATH at microTesla (µT) field [227, 26, 228, 74], and determining polarization buildup and relaxation times across various fields. Additionally, automated setups are ideal for studying the polarization mechanism, such as using field pulse sequences to enhance heteronuclei polarization under SABRE-SHEATH conditions. [229, 230, 231]

To address these challenges and take the opportunities, this study introduces a fully automated lab workstation for conducting routine SABRE and SABRE-SHEATH hyperpolarization at either mT or µT fields with high reproducibility through precise control over experimental conditions. Leveraging an integrated graphical user interface (GUI), even first-time users are able to conveniently operate various SABRE experimental protocols, making the automated workstation a practical tool for studying SABRE hyperpolarization.

7.3 Development of an automated SABRE workstation

The automated SABRE workstation integrates a commercial desktop robotic arm as a core component of the shuttling system for transferring the sample tube (Figure 7.1**a**). The magnetic field for efficient polarization transfer with SABRE is generated by a self-wound solenoid coil positioned either inside or outside of a mu-metal magnetic shield. This component is referred to as the polarization transfer field (PTF) generator. A custom-built controlling system (Figure 7.1**b**) controls the PTF generator, ensuring accurately manipulate both the strength and orientation of the magnetic field required for optimal hyperpolarization conditions. In the subsequent sections, each component of the system will be described in detail to

provide a clear understanding of how they contribute to the overall experimental operation.

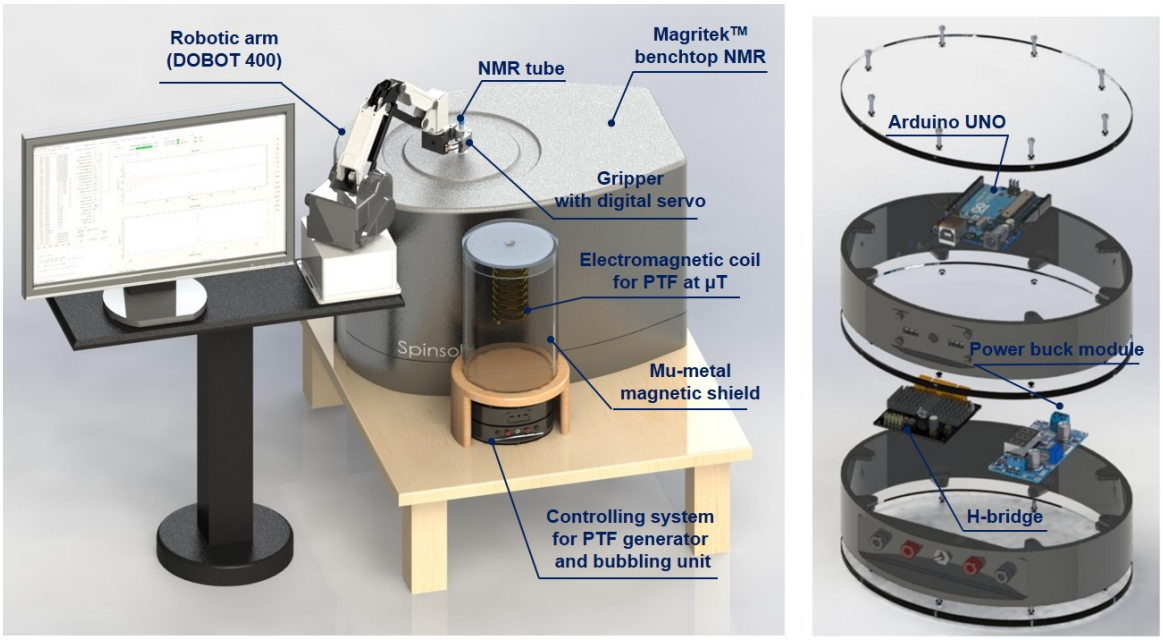

Figure 7.1: (**a**) 3D rendered overview of the automated SABRE workstation for benchtop NMR. The workstation consists of a robotic arm-assisted shuttling system, a self-wound solenoid coil placed in the mu-metal shielding as a µT-field PTF generator and a custom controlling system. (**b**) Explosion view of the controlling system. Several pins on the micro controller (Arduino® UNO R3) are configured to control the bubbling of *para*-H_2 and the gripper on the robotic arm. With the Pulse Width Modulation (PWM) function of Arduino, the H-bridge driver is able to precisely generate the desired magnetic field on the electromagnetic coil. (Adopted from [JY03].)

7.3.1 Robotic arm-assisted shuttling system

The 4-axis desktop robotic arm (MG400, Dobot Robotics, China) featuring a repeatability of ±0.05 mm and a maximum joint speed of 300° per second, enables precise and rapid field cycling of the sample (Figure 7.2**a**). The movement of the robotic arm, including the position coordinates and speed, can be customized through programming in a Python environment. Consequently, the desired position of the sample tube can be programmed by specifying the corresponding spatial coordinates for the gripper (Figure 7.2**b**). The gripper is equipped with a digital servo (LDX-335MG, Hiwonder, China) and features a custom 3D-printed finger designed to match the curvature of the sample holder (Figure 7.2**c**). By programming the gripper to open or close, it is capable of seamlessly picking up and dropping off sample tubes at desired positions. In this work, the average movement speed of the robotic arm was set to 70% of its maximum capacity to balance the transfer speed with safety considerations. Consequently, the transfer time of the hyperpolarized (HP) sample from the PTF to the

detection area of the benchtop NMR was consistently maintained at 3 s across all experiments.

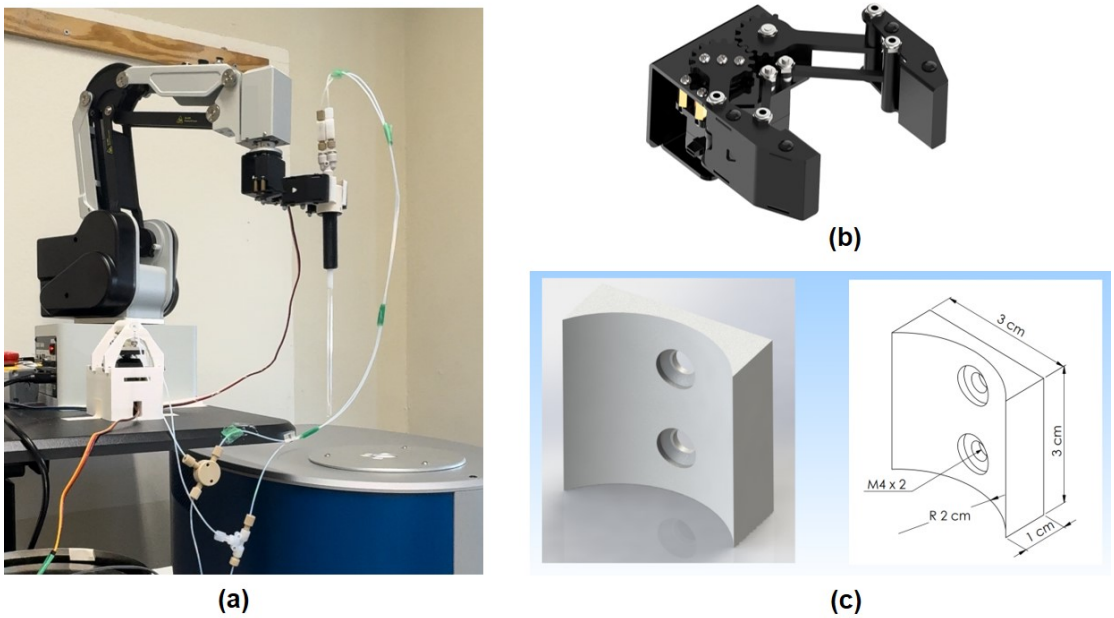

Figure 7.2: **(a)** The robotic arm-assisted shuttling system for fast magnetic fields cycling. (**b**) The anti-block gripper with high torque steering gear. The opening and closing of the gripper were independently controlled by a digital servo, allowing the action of grasping or releasing to be completed within 0.5 s. **(c)** 3D schematic of the finger for the gripper with a curved contour. (Adopted from [JY03].)

7.3.2 Bubbling unit

As mentioned in the introduction, the bubbling method is compatible with field cycling and automated setups. In this work, an automated bubbling unit was developed to efficiently deliver *para*-H_2 into the sample solution (Figure 7.3). The bubbling unit is comprised of a standard 5 mm NMR tube, to which PTFE tubing (ID: 4.35 mm, OD: 6.35 mm) is affixed at the upper portion. The other end of the PTFE tubing is connected to a Y-type fast pneumatic connector, splitting the gas flow into two pathways: one for bubbling and the other for gas release through a back-pressure regulator (BPR) mounted at the downstream. In the bubbling pathway, a capillary tubing (ID: 0.30 mm, OD: 0.60 mm) is inserted into the outer tubing, with its end submerged in the sample solution. A bypass line, created using two T-connectors, bridges the bubbling and releasing pathways to ensure equal pressure in both. A shut-off valve (P-782, IDEX Health&Science, USA) controls the state of the bubbling. When this valve is open, bubbling ceases, and the gas is diverted through the bypass line and subsequently released. Closing the valve blocks the bypass, directing the gas through the capillary tubing where it forms bubbles in the sample solution, before being released through the BPR. This setup was previously introduced in earlier research, where the bubbling process was controlled by manually opening and closing the shut-off valve.[128]

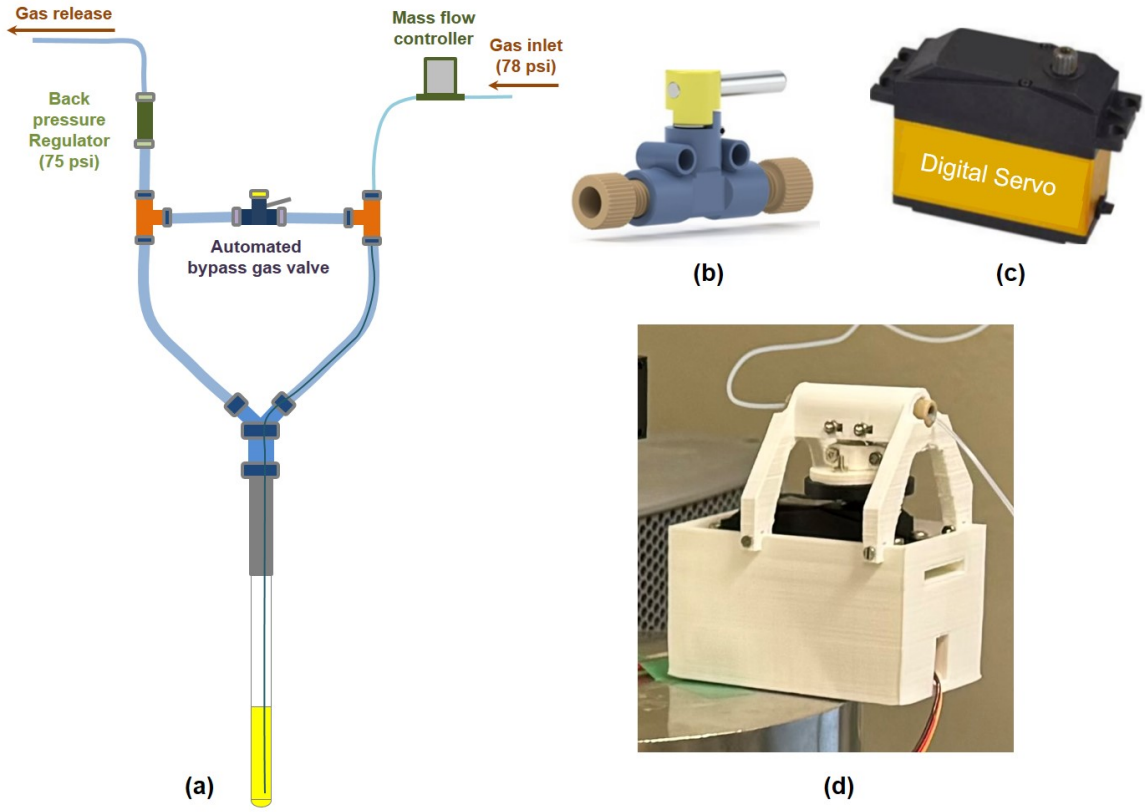

Figure 7.3: **(a)** Schematic drawing of the bubbling unit (not shown in real scale). The automated bypass gas valve includes a shut-off valve **(b)**, a digital servomotor **(c)**, and a scaffold **(d)** for mounting these components together. By controlling the digital servomotor, the automatic bubbling of *para*-H_2 into the sample solution through the capillary tubing is managed. (Adopted from [JY03].)

To automate the bubbling procedure, traditional solenoid valves could be employed as replacements for the manual shut-off valve. However, when controlling hydrogen gas, the solenoid valve must be explosion-proof, which increases the cost and requires more installation space. To enhance experimental safety while maintaining automation, a digital servomotor (HV2060MG, Amewi AMX Racing) is implemented to automatically drive the handle of the shut-off valve (Figure 7.3**c**). A 3D-printed scaffold, as depicted in Figure 7.3**d**, is utilized to assembly of the servomotor and the shut-off valve. The primary benefit of this mechatronic modification to the manual valve is the automated control of the hydrogen gas valve, achieved in a cost-effective and safe manner. Additionally, leveraging the rapid response capability of the digital servomotor, the bubbling process can be switched on and off by the digital servomotor within 0.5 s, ensuring consistent operation of the bubbling process and enhancing the reproducibility of experiments.

7.3.3 PTF generator

SABRE is well known for its dependence on magnetic field strength, thus, selecting an optimal PTF is essential for achieving spontaneous and efficient spin order transfer from *para*-H_2 to

target substrates. In this study, two solenoid coils were constructed, each specifically designed for SABRE hyperpolarization of ^{1}H and heteronuclei, respectively. The first coil is positioned within the stray magnetic field of a benchtop NMR to generate fields in the mT range, suitable for ^{1}H SABRE experiments. The second coil, intended for heteronuclei hyperpolarization via SABRE-SHEATH, is capable of generating PTFs ranging from -13.5 µT to 13.5 µT. This coil is housed within a mu-metal magnetic shield (ZG 206, Magnetic Shield Corporation, USA) to shield the Earth's magnetic field. The core component of the PTF generator is an H-bridge-based driver circuit integrated with a PWM-controlled voltage signal. The H-bridge configuration consists of four switches, which can be transistors or relays, arranged in a manner that allows current to flow through the solenoid in either direction. By programming and toggling these switches in various combinations, it is possible to alter the direction of the magnetic field induced in the coil.

The schematic diagram of the circuit connections of the PTF generator is detailed in Figure 7.4. The process for generating PTFs operates as follows: the micro controller (Arduino® UNO R3) is programmed to emit a square wave signal, which can be modulated using PWM to produce signals with varied duty cycles. Consequently, the H-bridge driver board then outputs the average voltage based on this square wave signal, generating the designated PTF within the electromagnetic coil.

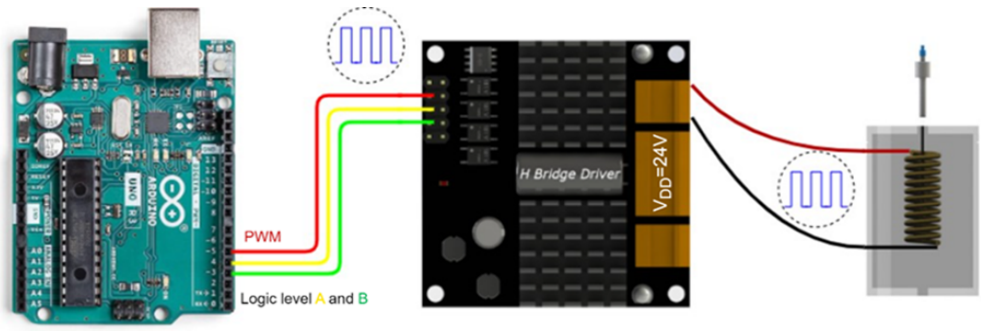

Figure 7.4: Schematic diagram of the circuit connections of the PTF generator. Combination the functions H-bridge and PWM on Arduino, it is capable to precisely control both strength and direction of the magnetic field generated on the solenoid coil. (Adopted from [JY03].)

With the minimum duty cycle change of 1/255, the resolution of the PTF generator achieves a precision of 0.05 milligauss (mG). By programming the corresponding duty cycles into the microcontroller, the PTF was able to be swept precisely and automatically for each SABRE hyperpolarization, facilitating the determination of the optimal PTF for various substrates.

In addition, the PTF generator is capable of producing a field pulse sequence that consists of two alternating magnetic fields with different durations. This functionality facilitates investigation of the polarization transfer mechanisms in SABRE. The following part of this section details how the solenoid coil's delay time is calculated and how the PWM-generated PTF is validated.

In this work, two self-wound solenoid coil A and B are applied for ^{1}H SABRE and ^{13}C SABRE-SHEATH experiments respectively (Figure 7.5). The ^{1}H SABRE experiments were designed to demonstrate high reproducibility and were conducted using a PTF of 6.5 mT. This magnetic field was generated by solenoid coil A powered by direct current (DC).

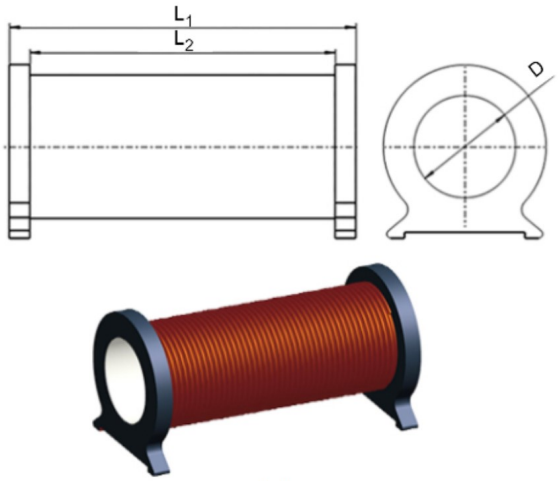

(a)

Parameters	Solenoid coil A	Solenoid coil B
L_1 (cm)	21	21
L_2 (cm)	20	20
D (cm)	4	4
N (Turns)	3500	1300
R_0 (Ω)	50	46.1
PTF range	-10.5 mT- 10.5 mT	-13.5 µT – 13.5 µT

(b)

Figure 7.5: **(a)** Schematic illustration of self-wound solenoid coil. **(b)** Parameters of solenoid coil A and B utilized for generating PTFs in ^{1}H SABRE and ^{13}C SABRE-SHEATH respectively. (Adopted from [JY03].)

To determine the optimal PTF for ^{13}C SABRE-SHEATH experiments, which required a series of magnetic field sweeps of the PTF, a PWM function was employed [232]. This function enabled the generation of a square wave signal through an H-bridge, which was subsequently applied to solenoid coil B. By setting the duty cycle of the PWM and programming the H-bridge circuit, the magnetic fields required for the experiments can be automatically controlled. The calculation and measurement of the time constant τ_{coil} involve assessing the coil's inductance and resistance, which determine how swiftly it can reach its full magnetic field strength upon signal application and decay once the signal ceases.

The effectiveness of this setup hinges on understanding (1) the time constant τ_{coil} of solenoid coil B, which influences how quickly the coil can respond to changes in the PWM signal; (2) the averaging of Hamiltonian of a square wave-shaped magnetic field with fast period T.

In the following content, the calculation and measurement of the time constant of solenoid coil B are depicted, along with an explanation of how the generation of the PTF is controlled by the PWM signal. Furthermore, the hyperpolarization signals from ^{13}C SABRE-SHEATH at the PTF of −0.6 µT, generated by PWM signal and DC power, are presented to validate that there is a negligible difference in the hyperpolarization effects. This holds true whether employing a fast-period, square wave-shaped magnetic field or a static magnetic field, as long as the average field strengths are equivalent.

7.3.3.1 The magnetic flux density inside the solenoid coil

The relationship between the magnitude of the current applied in the solenoid coil and the strength of the generated magnetic field is described as follows:

$$H \cdot L = N \cdot I \tag{7.1}$$

where:

- H is the magnetic field strength measured in Ampere per meter (A/m);
- N is the number of turns in the coil;
- I is the current measured in Ampere (A);
- L is the length of solenoid measured in meters (m).

The magnetic field strength inside the solenoid coil is:

$$B = \mu \cdot H \tag{7.2}$$

where:

- B is the magnetic flux density (T);
- μ is the magnetic permeability of the material (T·m/A).

The solenoid coil is placed in air, the magnetic permeability of which is usually considered close to that of a vacuum. Therefore, the vacuum permeability $\mu_0 \approx 4\pi \times 10^{-7}$ T·m/A is chosen for the next calculations.

By combining Equation (7.1) and Equation (7.2), and incorporating the parameters provided in the Figure 7.5, the relationship between the applied current and the magnetic field generated inside coil B can be derived as follows:

$$B_B = \frac{N_B \cdot \mu_0}{L_B} \cdot I_B \approx 0.00816 I_B \tag{7.3}$$

7.3.3.2 Calculating the inductance of the solenoid coil

During the calculation of the solenoid coil inductance, the selection of the applicable method is crucial for the subsequent analysis of the circuit time constant, especially in scenarios where the magnetic field needs to be switched quickly. The forward and reverse calculations are two common methods, and in the case of manually wound solenoids, it is important to

choose the correct calculation method to minimize errors due to irregularities in the structure. [233, 234, 235]

The forward calculation method directly calculates the inductance value by considering parameters such as the shape, dimensions, number of turns, and permeability of the solenoid coil. In previous work, many researchers applied this method for calculating inductance values of solenoids of different shapes. [233, 236] This method is theoretically accurate, but in the case of manual winding, the irregularity of the solenoid may lead to complex mathematical modeling, making the calculation cumbersome and prone to introducing errors. [236]

The inverse calculation method means that the inductance value can be solved indirectly by measuring some parameters in the circuit, such as the time constant in current decay process. This approach is rooted in the fact that the inertial effects of the inductor result in a non-instantaneous response of the circuit, requiring a finite duration to reach a steady state. This method is more feasible in practical applications because it can overcome irregularities in the shape of the solenoid coil during manual winding. A variety of inverse calculation methods were summarized in previous work. [237, 238]

In the experiments, the method of measuring the time constant in the discharge series RL loop has been chosen, as shown in Figure 7.6. L represents the solenoid coil, R_0 is the resistance of the solenoid coil itself, and R_1 represents the series resistance. The process for measuring inductance involves the following steps. Firstly, the circuit parameters need to be established: The resistance of R_0 is 46.1 Ω and a resistance of 1333 Ω was selected for R_1. Second, energize the circuit and then use an oscilloscope (KEYSIGHT DSOX1240A) to measure the voltage across the resistor R_1. By employing Kirchhoff's laws under the influence of a step voltage (illustrated in Figure 7.6), the relationship between current i and time t in the RL circuit is depicted as follows:

$$i(t) = \frac{V_{high}}{R_0 + R_1}\left(1 - e^{-\frac{R_0+R_1}{L}t}\right) \tag{7.4}$$

This implies that after the step voltage occurs, $i(t)$ undergoes an exponential growth process, gradually reaching a steady-state value. Setting $I_0 = \frac{V_{\text{high}}}{R_0 + R_1}$ and $\tau = \frac{L}{R_0 + R_1}$ yields:

$$i(t) = I_0\left(1 - e^{-\frac{t}{\tau}}\right) \tag{7.5}$$

When $t = \tau$, it gives:

$$i(\tau) = I_0\left(1 - e^{-1}\right) = 0.63I_0 \tag{7.6}$$

where τ represents the time required for the current to increase from 0 to 63% of its steady-state value. In electronics, τ is referred to as the time constant.

From the voltage waveform over time depicted in Figure 7.7, it is discernible that the time constant τ of the circuit with series of the electromagnetic coil B and the resistor R_1 is approximately 10 µs.

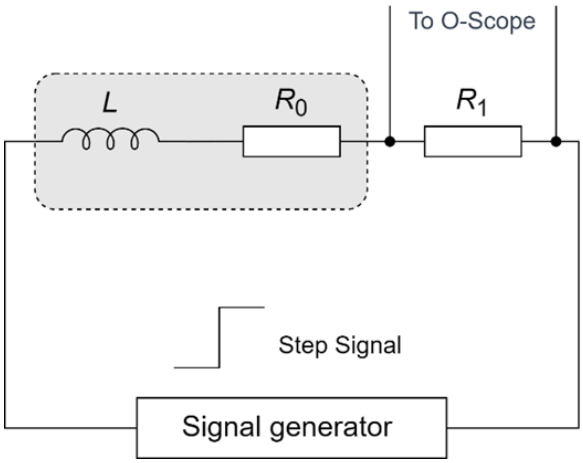

Figure 7.6: A circuit of series RL loop for measuring the inductance of the self-wound solenoid coil. (Adopted from [JY03].)

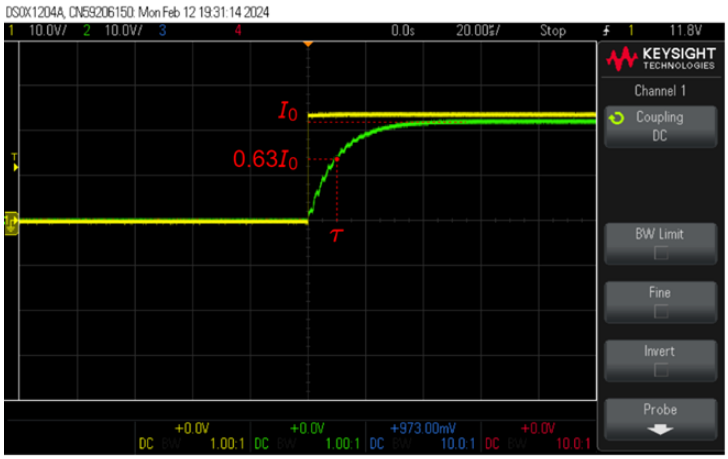

Figure 7.7: Step signal (yellow line) with voltage across the resistor (green line). (Adopted from [JY03].)

By utilizing the relationship $\tau = \dfrac{L}{R_0 + R_1}$, the inductance value L of the coil is calculated as following:

$$L = \tau \cdot (R_0 + R_1) \approx 13.8 \text{ mH} \tag{7.7}$$

It needs to emphasize that due to the use of manually wound coils and associated measurement uncertainties, the purposes of Equation (7.3)-(7.7) are to provide a qualitative understanding and analysis of the system behavior rather than obtain absolute accurate results.

7.3.3.3 Controlling the direction of PTF by H-bridge

In the PTF generator, the manipulation of the magnetic field direction is facilitated by an H-bridge-based drive circuit. Named for its schematic representation that resembles the letter "H", as depicted in Figure 7.8. H-bridge is an electronic circuit that allows for the reversal of the polarity of a voltage applied to a load. [239] The components Q_1, Q_2, Q_3, Q_4 are Metal Oxide Semiconductor Field Effect Transistors (MOSFETs), which serve as electronic

switches. D_1, D_2, D_3, D_4 are diodes designed to protect the electronic switches. When integrated with PWM, precise adjustments of the voltage at both ends of the load are made achievable. The power supply voltage of the controlling system, represented by V_{DD}, is set at 24 V DC.

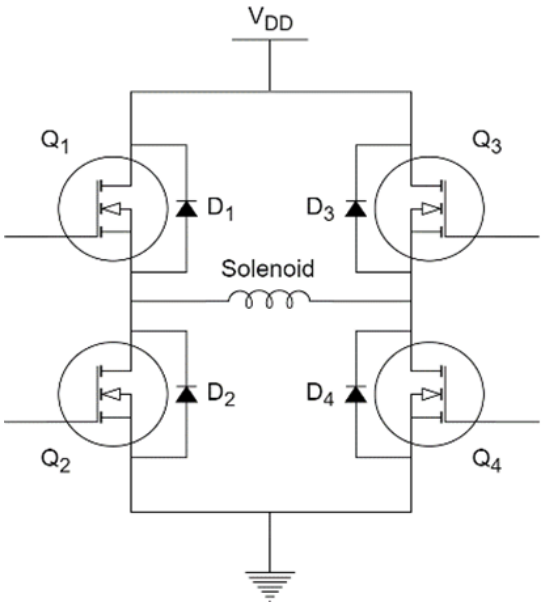

Figure 7.8: The circuit of H-bridge for switching the polarity of the voltage applied to the solenoid. (Adopted from [JY03].)

7.3.3.4 Selecting the appropriate serial resistor to generate µT-field

In ^{13}C SABRE-SHEATH procedures, the required magnetic field range is up to 13 µT. According to Equation (7.3), this necessitates a current range from 0 to 1.59 mA. Given the solenoid coil's resistance R_0 of 46.1 Ω, the required current range translates into a voltage variation from 0 to 0.073 V for the field strength from near-zero to 13 µT. Achieving such voltage control with an accuracy of 0.0056 V per 1 µT present challenges in practice. For the convenience of voltage control within the circuit, a resistor, labeled R_2, is incorporated in series (Figure 7.9).

Another factor that needs to be considered when selecting the resistance in the circuit is the relationship between the resistor value and the time constant, which will be discussed in detail in the next section.

7.3.3.5 Calculating the electromagnetic coil's time constant $\tau_{\mathbf{coil}}$

The time constant in circuits is crucial for characterizing the response capability of the circuit. It quantitatively describes how quickly a circuit can respond to changes in input, fundamentally defining the dynamics of its electrical behavior. The time constant is closely related to the process in which the current changes from its initial variation to a stable state. A small time constant means that the circuit can quickly adapt to changes in signals, achieving the purpose of rapid magnetic field switching. Conversely, a large time constant

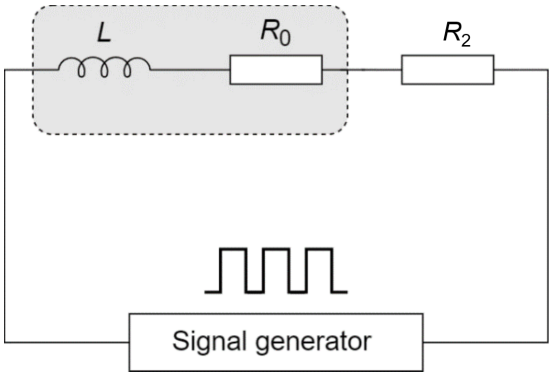

Figure 7.9: The circuit of the solenoid coil in series with the capacitor R_2 for generating µT-field. (Adopted from [JY03].)

means that the circuit cannot adapt quickly to signal changes, requiring a longer time for the magnetic field intensity to stabilize after the switching signal occurs. In the RL circuit, where the solenoid coil is connected in series with resistor R_2, the time constant is defined as follows:

$$\tau_{\text{coil}} = \frac{L}{R} = \frac{L}{R_0 + R_2} \tag{7.8}$$

where L is the inductance of the coil and R is the total resistance in the circuit. In case of fixed value of inductance (L), only the effect of the series resistance value (R_2) on the time constant needs to be considered. Both the phase difference and time constant are important physical parameters with significant implications for the functionality of the PTF generator. Therefore, it is necessary to select the circuit parameters (such as the resistance value and the signal frequency) appropriately to ensure that the phase difference and the time constant are within suitable ranges.

From Equation (7.8), it can be inferred that an increase in the series resistor value leads to a decrease in the time constant. For ^{13}C SABRE-SHEATH at µT-range, an series resistor R_2 with resistance of 8116 Ω was selected to meet the requirements for both the range and fast response of the magnetic field generated by solenoid coil B. Therefore, a time constant of 1.7 µs was determined by utilizing Equation (7.8). Figure 7.10 depicts the waveform obtained by measurements on oscilloscope with $\tau_{\text{coil}} = 1.7$ µs, states the agreement between experimental observations and theoretical predictions.

7.3.3.6 Averaging the Hamiltonian in situation of shaped magnetic field

The Hamiltonian of the spin system at this square wave-shaped magnetic field $B(t)$ is:

$$\hat{\mathcal{H}}(t) = \Delta\gamma_{\text{CH}} B(t) \hat{S}_z + 2\pi \left(J_{\text{HH}} \hat{I}_1 \cdot \hat{I}_2 + J_{\text{CH}} \hat{I}_1 \cdot \hat{S} + J_{\text{CH'}} \hat{I}_2 \cdot \hat{S} \right) \tag{7.9}$$

where $B(t)$ consists of two magnetic fields $B_h(t)$ and $B_l(t)$, the above equation can be rewritten in:

$$\hat{\mathcal{H}}(t) = \Delta\gamma_{\text{CH}} B_{\text{h}}(t) \hat{S}_z + \Delta\gamma_{\text{CH}} B_{\text{l}}(t) \hat{S}_z + 2\pi \left(J_{\text{HH}} \hat{I}_1 \cdot \hat{I}_2 + J_{\text{CH}} \hat{I}_1 \cdot \hat{S} + J_{\text{CH'}} \hat{I}_2 \cdot \hat{S} \right) \tag{7.10}$$

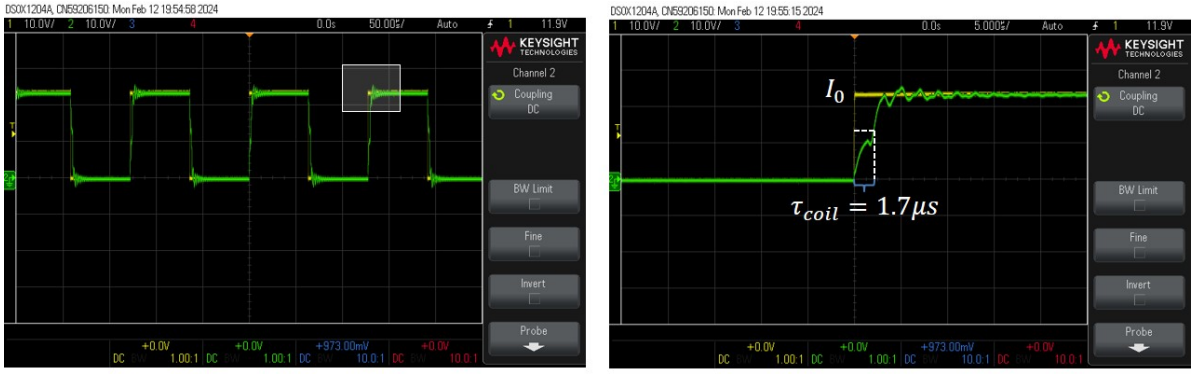

Figure 7.10: **(a)** Square wave signal (yellow line) with voltage across the resistor (green line). **(b)** Local scaling of the signal at the step. (Adopted from [JY03].)

where the magnitude of $B_\mathrm{h} = 13.5$ µT and $B_\mathrm{l} = 0$ are corresponding to the high and low level of the PWM signal. The working times of B_h and B_l in a period are t_1 and t_2 respectively (Figure 7.11). This gives:

$$\hat{\mathcal{H}}(t) = \Delta\gamma_{\mathrm{CH}} B_\mathrm{h}(t_1)\hat{S}_z + 2\pi\left(J_{\mathrm{HH}}\hat{I}_1\cdot\hat{I}_2 + J_{\mathrm{CH}}\hat{I}_1\cdot\hat{S} + J_{\mathrm{CH'}}\hat{I}_2\cdot\hat{S}\right) \tag{7.11}$$

$$= \hat{\mathcal{H}}_1(t) + 2\pi\left(J_{\mathrm{HH}}\hat{I}_1\cdot\hat{I}_2 + J_{\mathrm{CH}}\hat{I}_1\cdot\hat{S} + J_{\mathrm{CH'}}\hat{I}_2\cdot\hat{S}\right) \tag{7.12}$$

When the period of the pulse shaped magnetic field T is faster than any other term in the Hamiltonian at any time, the average Hamiltonian can be applied. [240, 241] The term $\hat{\mathcal{H}}_1(t)$ can be averaged and this gives:

$$\overline{\hat{\mathcal{H}}}_1^{(0)} = \frac{1}{T}\int_0^{t_1}\hat{\mathcal{H}}_1(t)\,dt \tag{7.13}$$

$$= \frac{t_1}{T}\Delta\gamma_{\mathrm{CH}} B_\mathrm{h}\hat{S}_z \tag{7.14}$$

where the ratio t_1/T equals to the duty cycle of the PWM signal applied on the electromagnetic coil. By the definition of the duty cycle of PWM function, the average voltage is:

$$\overline{V} = \frac{t_1}{T}V_\mathrm{h} \tag{7.15}$$

For an electromagnetic coil, the generated magnetic field strength is proportional to the applied voltage ($B \propto V$). The relationship of the average magnetic field $\overline{B}$ and the high magnetic field B_h gives:

$$\overline{B} = \frac{t_1}{T}B_\mathrm{h} \tag{7.16}$$

Therefore, Equation (7.14) can be rewritten in:

$$\overline{\hat{\mathcal{H}}}_1^{(0)} = \Delta\gamma_{\mathrm{CH}}\overline{B}\hat{S}_z \tag{7.17}$$

and the total Hamiltonian is:

$$\hat{\mathcal{H}}(t) = \Delta\gamma_{\mathrm{CH}}\overline{B}\hat{S}_z + 2\pi\left(J_{\mathrm{HH}}\hat{I}_1\cdot\hat{I}_2 + J_{\mathrm{CH}}\hat{I}_1\cdot\hat{S} + J_{\mathrm{CH'}}\hat{I}_2\cdot\hat{S}\right) \tag{7.18}$$

Hence, when the spin system evolves under square-wave shaped magnetic field with period faster than the coherence dynamics of spin evolution, there is negligible difference in hyperpolarization outcomes generated whether at a static magnetic field or at instantaneously changing field, as long as the average magnetic field strength is equivalent to that of the static field.

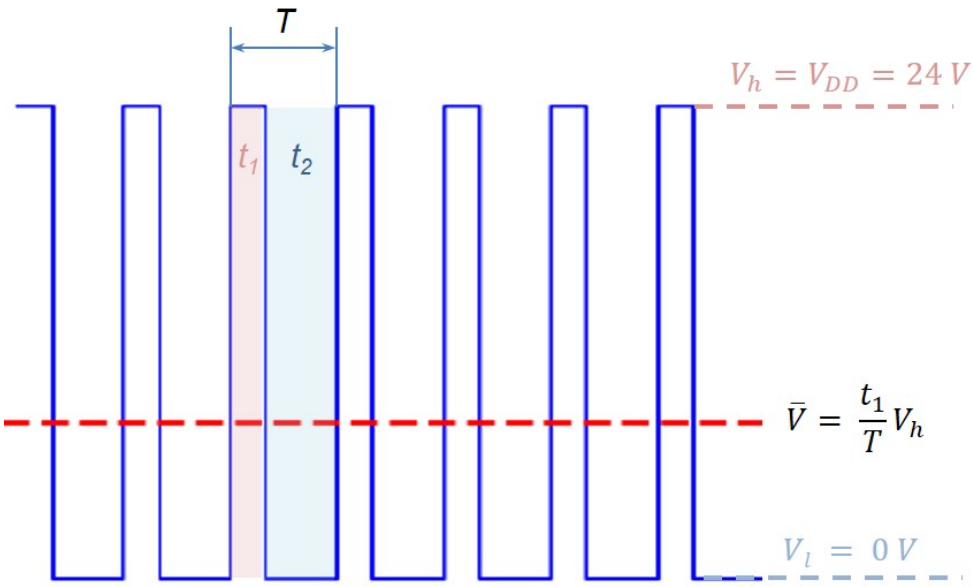

Figure 7.11: Schematic illustration of the average voltage achieved by PWM signal with corresponding duty cycle. Within the period time T, the working durations of high and the low level are t_1 and t_2 respectively. The duty cycle t_1/T is the ratio between the high level duration and the period time. The average voltage over time can be controller by adjusting the duty cycle. (Adopted from [JY03].)

In this work, the PWM signal with the default frequency on Arduino $f = 976.56$ Hz, was employed in the experimental procedures of field sweeping for determining the optimal PTF, buildup time measurement, and T_1 relaxation time measurement for generating desired magnetic field. The time constant of the electromagnetic coil $\tau_{\text{coil}} = 1.7$ µs has been calculated theoretically and measured experimentally. With τ_{coil} is much small than the period time of PWM ($T = 1/f = 1024$ µs), the resulting magnetic field closely follows the square wave pattern dictated by the PWM signal. The period time $T \ll (\Delta\gamma_{\text{CH}} B_{\text{h}})^{-1} = 2324$ µs, the output of the hyperpolarization under a rapidly changing square wave-shaped magnetic field is nearly identical to that observed under a static magnetic field with strength equal to $\overline{B}$. Therefore, by adjusting the duty cycle of the PWM signal from the PTF generator, SABRE hyperpolarization could be controlled at the desired magnetic field.

7.3.3.7 Validation of ^{13}C pyruvate SABRE-SHEATH at the magnetic field generated by PWM

To demonstrate the the average effect of hyperpolarization at square wave-shaped magnetic field with fast period, serial experiments of ^{13}C pyruvate hyperpolarization at its optimal

PTF ($B_{\mathrm{PTF}} = -0.6$ µT) generated by the PWM with period of 1024 µs and by the DC power were conducted. For the DC-generated magnetic field, a 12 V DC power supply was used, and the current was manually adjusted to achieve a static field of −0.6 µT.

For each magnetic generation approach, three times hyperpolarization of the same sample solution were conducted sequentially. The results are shown in Figure 7.12, the spectra with blue and red color are the signal of [1-^{13}C] pyruvate signal hyperpolarized at −0.6 µT generated by PWM function and DC power respectively. By comparison the spectra, the signal intensities of the free and bound pyruvate are nearly identical under both conditions. This demonstrates that the magnetic field generated using the PWM approach at a frequency of 976.56 Hz can effectively be treated as a static magnetic field for the purposes of these experiments.

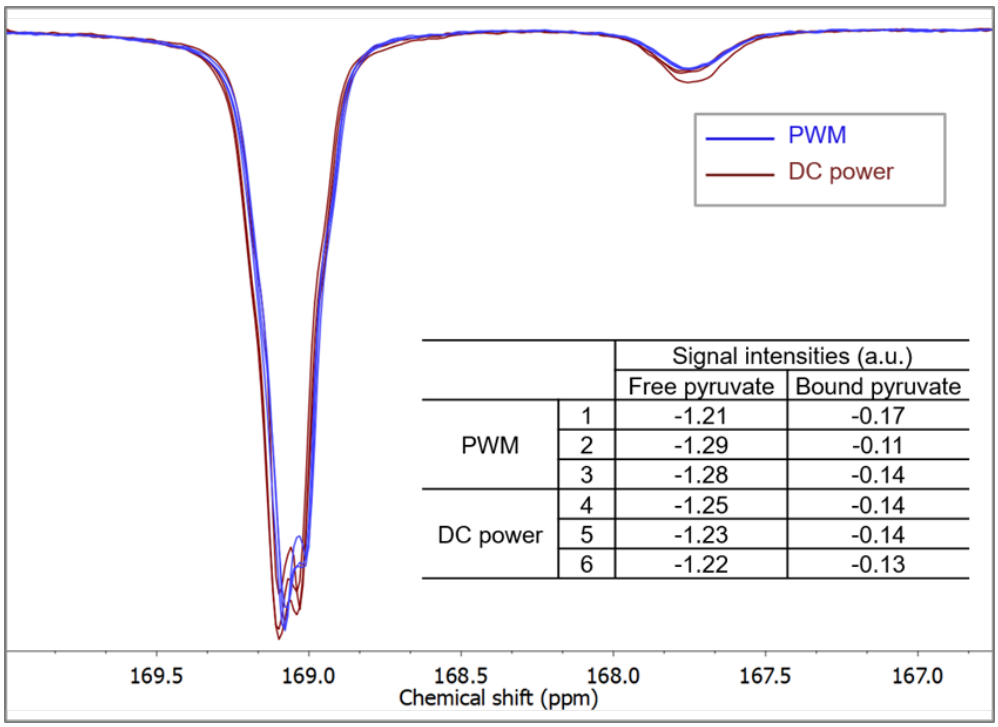

		Signal intensities (a.u.)	
		Free pyruvate	Bound pyruvate
PWM	1	-1.21	-0.17
	2	-1.29	-0.11
	3	-1.28	-0.14
DC power	4	-1.25	-0.14
	5	-1.23	-0.14
	6	-1.22	-0.13

Figure 7.12: Spectra of [1-^{13}C] pyruvate hyperpolarized at −0.6 µT generated by PWM (blue) and by DC power (red). (Adopted from [JY03].)

7.3.4 User-friendly GUI

A GUI is designed based on the experimental procedures of SABRE and SABRE-SHEATH, allows users to easily control various parameters, such as the strength and direction of the PTF, the bubbling time, and configure the field pulse sequence. It typically includes features such as real-time monitoring of system status, automated sequence initiation, and data logging capabilities. The main window of this GUI is depicted in Figure 7.13. The upper left part of the GUI features the general function module, where users can individually operate the bubbling and gripper functions by clicking the corresponding buttons. This design allows for routine tasks such as activating the SABRE pre-catalyst in sample solution or moving the

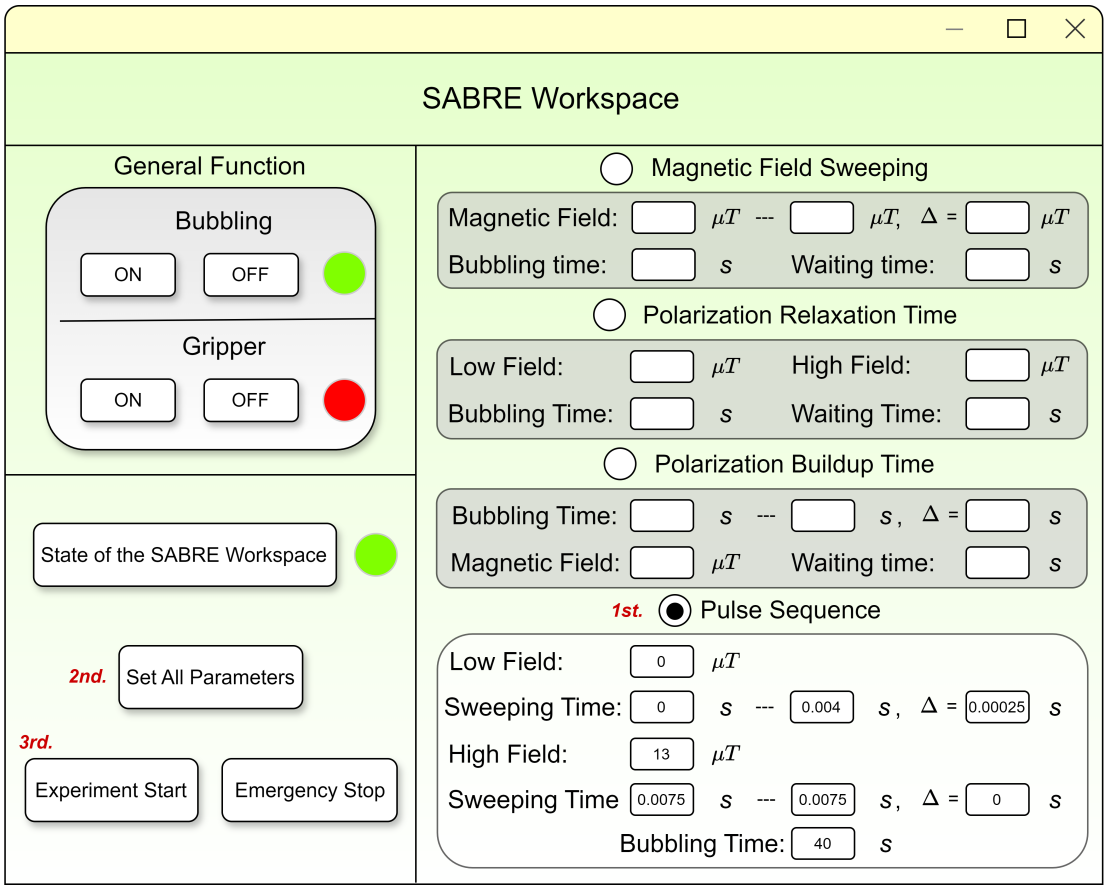

Figure 7.13: The main window of the GUI developed for controlling SABRE and SABRE-SHEATH experiments, showing the layout and functional elements. Upper left: general functions for activation the pre-catalyst by clicking 'Bubbling', and for grasping and releasing the sample tube by clicking 'ON' or 'OFF'. Bottom left: state indicator and issuance of instructions. Right column: four categories of SABRE experimental procedures. (Adopted from [JY03].)

sample tube to a desired position. For instance, the sample tube can be transferred to the benchtop NMR for detection of the thermal equilibrium after activation. The real-time status of the SABRE workstation is visualized by different colors displayed at the bottom of the GUI: blue signifies standby, green indicates operating, and red alerts to a bug. Clicking the Experiment Start' button without selecting any additional procedures or inputting parameters will automatically initiate the SABRE experiments using a set of default parameters. These default settings involve bubbling at the PTF of +0.4 μT for 40 s with a *para*-H_2 gas flow rate of 85 sccm and a pressure of 90 psi. Immediately after bubbling, the sample is transferred to a benchtop NMR for detection. Additionally, all ongoing operations can be immediately halted by clicking the 'Emergency Stop' button for ensuring the safety of both the personnel and the workstation in case of any unexpected situations.

Within the GUI, users can operate four categories of SABRE experimental procedures: magnetic field sweeping, measurements of polarization relaxation time, measurements of polarization buildup time, and pulse sequence. Users can select the desired experiments and

input the necessary parameters displayed in each module to initiate the experiments. The subsequent sections will detail each procedure and present the corresponding experimental results to demonstrate the capabilities of the constructed system.

7.4 Experiments

7.4.1 Chemical sample preparation

- Sample solution for ^{1}H SABRE and ^{13}C SABRE-SHEATH hyperpolarization

For SABRE hyperpolarization of ^{1}H substrates (pyrazine, pyridine, and nicotinamide). Each sample solution contained 3 mmol/L of standard SABRE pre-catalyst [IrCl(COD)(IMes)] and 60 mmol/L of each substrate dissolved in degassed methanol-d_4.

For SABRE-SHEATH and pulsed SABRE-SHEATH of [1-^{13}C] pyruvate, each sample contained 5 mmol/L pre-catalyst [IrCl(COD)(IMes)] (the same catalyst used in ^{1}H SABRE), 25 mmol/L sodium [1-^{13}C] pyruvate, and 40 mmol/L water-free DMSO dissolved in degassed methanol-d_4. All the chemicals were purchased from Sigma Aldrich and used without further purification.

All SABRE sample solutions were prepared under inert gas conditions.

- Enrichment of *para*-H_2

Normal hydrogen gas (ALPHAGAZ^{TM} H_2, 99.999%) flows along the pipeline with an appropriate flow rate (0.5 L/min) controlled by a mass flow controller. A commercial water-cooled helium compressor (Advanced Research System, Model ARS-4HW) offers the cooling source to the cryostat (cold head) at 23 K. After contacting the paramagnetic hydrated iron (III) oxide catalyst ($Fe_2O_3 \cdot H_2O$) in the chamber at the bottom of the cold head, the *para*-H_2 fraction of 98% was generated and collected within an aluminum gas bottle.

- Activation of the pre-catalyst

The prepared sample solution was transferred into a modified 5 mm NMR tube using a 10 cm long needle syringe and tightly capped until connected to the tubing of the bubbling unit. Prior to the experiment, the entire gas line of the bubbling unit was flushed with fresh *para*-H_2 at a flow rate of 30 sccm under ambient pressure for 2 min to ensure the removal of residual air.

After connecting the sample tube to the pneumatic connector of the bubbling unit, the flow rate was set to 85 sccm until the bubbling unit reached a stable over-pressure of 90 psi. Activation of the sample is initiated by clicking the 'ON' button of the bubbling module in the GUI window. Full activation of the SABRE pre-catalyst typically requires 10 min of bubbling time.

7.4.2 Experimental protocols

All the experiments conducted under the room temperature of 25°C. All NMR signals were measured on a Benchtop NMR operating at a ^{1}H frequency of 61.92 MHz (1.45 T, Spinsolve 60 Carbon Ultra, Magritek, Germany). The ^{1}H NMR spectra were obtained with a single pulse excitation experiment, collecting single scan of 32768 points with 200 µs dwell time over a sweep width of 20 ppm using 90° RF pulse with length of 15.8 µs (signal acquisition time 6553.6 ms). The ^{13}C NMR spectra were obtained with a single pulse excitation experiment, collecting single scan of 16384 points with 200 µs dwell time over a sweep width of 240 ppm using 90° pulse length of 81.9 µs (signal acquisition time 3276.8 ms). All the recorded NMR data were processed using MNOVA Software (Mestrelab Research), where the acquired FID were apodized with an exponential filter of 0.3 Hz.

- Regeneration of ^{1}H HP substrates with SABRE at 6.5 mT

^{1}H SABRE hyperpolarization of each sample was performed in three consecutive trials using this automated workstation with the procedure shown in Figure 7.14**a**. The activated sample was bubbled for 20 s with flow rate of 85 sccm at 90 psi at the PTF of 6.5 mT. Immediately after this, the samples were transferred with the robotic arm-assisted shuttling to the benchtop NMR within 3 s to measure the hyperpolarized ^{1}H signal. After each measurement cycle, the sample was returned to the solenoid coil, with the coil powered off for a duration of 60 s. During this period, the signal relaxed back to its thermal equilibrium at the Earth's magnetic field. This process readied the sample for the next batch of hyperpolarization, ensuring that each cycle started from a consistent baseline state.

- Studying field dependency in SABRE-SHEATH of [1-^{13}C] pyruvate

The experimental protocol of 'Magnetic Field Sweeping' on the GUI window was chosen for studying field dependency in SABRE-SHEATH (Figure 7.13). As the procedure illustrated in Figure 7.15**c**, the activated [1-^{13}C] pyruvate sample was hyperpolarized at different magnetic fields by sweeping the generated PTFs in increments of $\Delta B_{\mathrm{PTF}} = 0.1$ µT from -1 µT to 1 µT. In each cycle, the sample solution was bubbled for 40 s with a flow rate of 85 sccm at 90 psi inside the degaussed magnetic shield at the desired PTF. Upon immediate cessation of the *para*-H_2 bubbling, the sample was transferred to the benchtop NMR for ^{13}C detection. After each acquisition, the sample was transferred back into the magnetic shield with the solenoid coil powered off for 60 s. The ^{13}C polarization then relaxed at near-zero field conditions back to its thermal equilibrium.

- Measuring ^{13}C polarization buildup time T_{B} at optimal PTF

The experimental protocol for 'Polarization Buildup Time' was selected on the GUI window (Figure 7.13). As the procedure illustrated in Figure 7.17**a**, the activated [1-^{13}C] pyruvate sample was bubbled for varying durations (from 0 to 75 s in increments of 5 s) at its optimal PTF of -0.6 µT and at 25°C. The sample was transferred to the benchtop NMR for detection immediately after cessation of bubbling. After each acquisition, the sample was transferred back into the magnetic shield with the solenoid coil powered off for 60 s. The ^{13}C polarization

then relaxed at near-zero field conditions back to its thermal equilibrium.

- Measuring ^{13}C polarization relaxation time T_1 at different interesting fields

The experimental protocol for 'Polarization Relaxation Time' was selected on the GUI window (Figure 7.13). As the procedures illustrated in Figure 7.19**a-d**, the sample was initially fully polarized by bubbling *para*-H_2 at -0.6 µT and 25°C for 80 s. Subsequently, the sample tube was immediately exposed to various magnetic fields to observe polarization relaxation. The sample was maintained inside the shield at -0.6 µT, or kept near-zero field (0.026 µT) in situ, or moved outside the magnetic shield to the Earth's field (50 µT), or transferred to a benchtop NMR system at 1.45 T. After varying wait durations at these fields, ^{13}C NMR signals were measured at the benchtop NMR. After each acquisition, the sample was transferred back into the magnetic shield with the solenoid coil powered off for 60 s. The ^{13}C polarization then relaxed at near-zero field conditions back to its thermal equilibrium.

- Pulse sequence of ^{13}C SABRE-SHEATH hyperpolarization

The experimental protocol for 'Pulse Sequence' was selected on the GUI window (Figure 7.13). As the procedure illustrated in Figure 7.21**a**, the sample was bubbled at a flow rate of 85 sccm and 90 psi at the set PTF with field pulse sequence, involving two alternating magnetic fields with corresponding durations τ_L and τ_H for each field. The low and high fields of the pulse sequence were set to near-zero field (0.026 µT) and 13 µT, respectively. Upon immediate cessation of the *para*-H_2 bubbling, the sample was transferred to the benchtop NMR for ^{13}C detection. After each acquisition, the sample was transferred back into the magnetic shield with the solenoid coil powered off for 60 s. The ^{13}C polarization then relaxed at near-zero field conditions back to its thermal equilibrium.

7.5 Results and discussion

7.5.1 Estimating the reproducibility by regeneration of HP substrates with ^{1}H SABRE at 6.5 mT

Multiple ^{1}H SABRE hyperpolarization experiments were conducted on pyridine, pyrazine, and nicotinamide to evaluate the reproducibility of the constructed automated workstation. The enlarged thermal equilibrium spectra (shown in red) and the HP spectra (represented in purple, green, and cyan) are displayed in Figure 7.14**b-d**.

The signal enhancements ϵ of the HP proton species on each substrates with three consecutive SABRE hyperpolarization at a PTF of 6.5 mT shown in Table 7.1. The reproducibility of SABRE hyperpolarization for each substrate was quantified by calculating the relative standard deviation (RSD) of ϵ observed for individual HP species. The results are presented in Table 7.1 with an average relative standard deviation $\bar{\epsilon}$ of 1.03%, indicating an improvement in reproducibility compared to other automated shuttling systems reported by other research groups. For instance, the pneumatic shuttling system operating at high-field condi-

tions documented a standard deviation of 2%, [221] while the shuttling system employing a stepper motor and gear rod reported deviations ranging from 0.2% to 3%. [224]

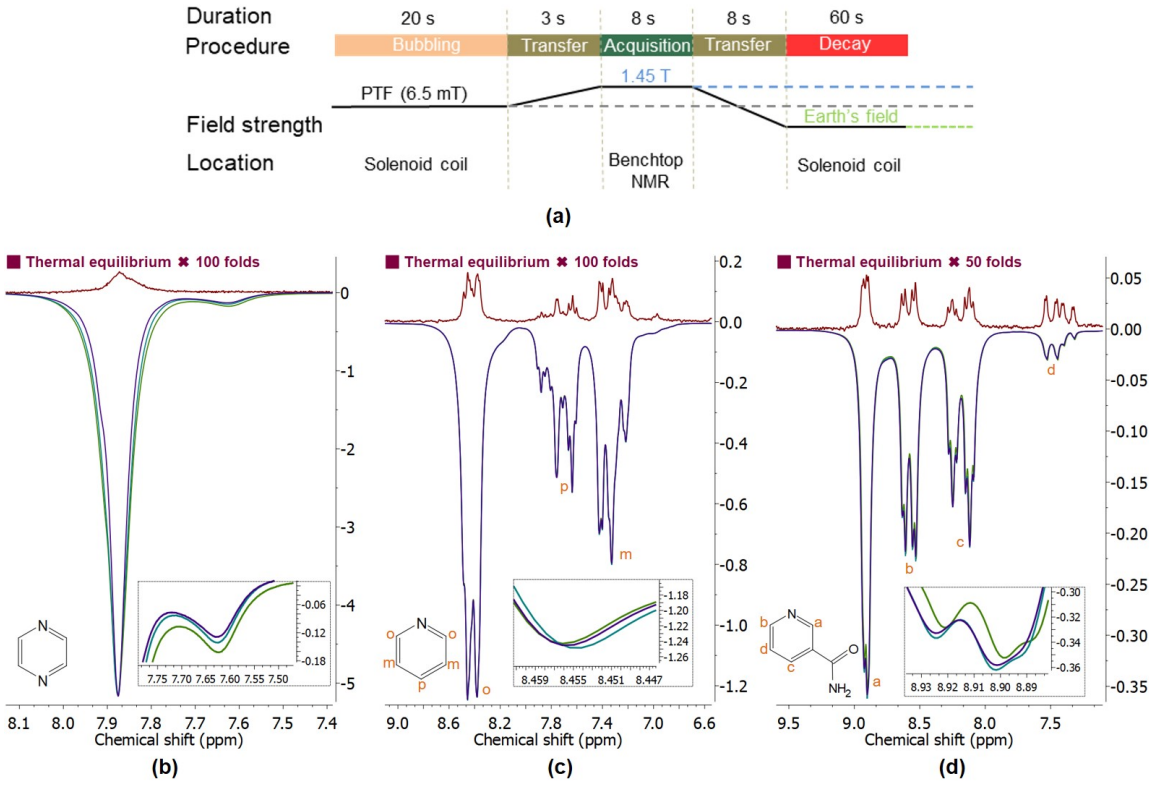

Figure 7.14: ^{1}H SABRE hyperpolarization of pyrazine, pyridine and nicotinamide executed by the automated SABRE workstation. (**a**) Schematic illustration of the experimental protocol for consecutive SABRE hyperpolarization at a PTF of 6.5 mT. (**b-d**) ^{1}H spectra of the thermal references of each sample (red) and the corresponding HP pyrazine, pyridine and nicotinamide generated by repeating the protocols for three times. Insets: zoomed-in views of the HP spectra (in purple, green, and cyan) for each substrate. (Adopted from [JY03].)

7.5.2 Studying field dependency on polarization transfer efficiency of HP [1-^{13}C] pyruvate via SABRE-SHEATH

In this work, the impact of magnetic field strength on the polarization transfer efficiency of [1-^{13}C] pyruvate was studied by systematically varying the magnetic field across a range of values. Previous works on simulations of the spin system at the LAC condition provides a reasonable estimation of the optimal PTF at 0.4 µT for [1-^{13}C] pyruvate. [242, 243] However, the accuracy of the predictions are constrained by the simplification of the actual spin system dynamics, neglecting the influence of external parameters such as binding rates, dissociation rates, and fluctuations in real-time temperature. [103, 109, 244, 229]

To determine the optimal PTF for [1-^{13}C] pyruvate under conditions of this work, the PTFs were set in range from -1 µT to 1 µT. As shown in Figure 7.15**a**, the 21 NMR spectra of HP [1-^{13}C] pyruvate with SABRE-SHEATH at various PTFs demonstrate a significant

	Pyrazine	Pyridine			Nicotinamide			
		ortho	para	meta	a	b	c	d
ϵ_1	-1494.92	-1002.87	-863.95	-622.42	-403.80	-337.25	-304.52	-52.41
ϵ_2	-1528.72	-1007.73	-868.30	-627.85	-418.58	-346.45	-317.17	-51.43
ϵ_3	-1466.27	-1005.73	-867.05	-623.20	-417.55	-345.24	-319.01	-51.56
RSD of ϵ	1.71%	0.20%	0.21%	0.38%	1.63%	1.19%	2.05%	0.84%

Table 7.1: The calculated signal intensity enhancements ϵ of HP pyrazine, pyridine (across three sites: ortho, para, and meta), and nicotinamide (across four sites: a, b, c, and d). The RSDs of the enhancements of each proton species on the three substrates are in the range from 0.20% to 2.05%. (Adopted from [JY03].)

dependence of pyruvate signal intensities on both the strength and direction of the magnetic field. The variations in polarization level across different PTFs present an asymmetrical curve-like pattern (Figure 7.15**b**). Notably, minor differences in the polarization levels at the same magnetic strength but in opposite directions (positive and negative) were observed.

Given that the Earth's magnetic field in the z-direction measured in the laboratory is negative, the reduced signal intensity observed with positive PTFs was speculated due to alterations in the z-direction of the magnetic field when the sample is adiabatically removed from the shield and transferred to the benchtop NMR. The maximum signal intensity of free pyruvate with SABRE-SHEATH at 25°C is observed at −0.6 µT (Figure 7.15**b**).

By taking a sample of [1-^{13}C] vinyl acetate (in a normal 5 mm NMR tube) at thermal equilibrium as a reference (Figure 7.16), the calculated signal enhancement of HP free pyruvate is

$$\epsilon_{^{13}\mathrm{C}} = \frac{S_{\mathrm{HP}}}{S_{\mathrm{Ref}}} \cdot \frac{C_{\mathrm{Ref}}}{C_{\mathrm{HP}}} \cdot \frac{A_{\mathrm{Ref}}}{A_{\mathrm{HP}}} = \frac{13.1605}{0.2696} \cdot \frac{10.13\,\mathrm{mol/L}}{25\,\mathrm{mmol/L}} \cdot 1.053 = 20828 \tag{7.19}$$

The ^{13}C thermal polarization level is

$$P_{\mathrm{thermal}} = \frac{\gamma B_0 \hbar}{2kT} = \frac{67.262\,\mathrm{MHz/T} \cdot 1.45\mathrm{T} \cdot 1.0545718 \times 10^{-34}\,\mathrm{Js}}{2 \cdot 1.380649 \times 10^{-23}\,\mathrm{J/K} \cdot 298\,\mathrm{K}} = 1.25 \times 10^{-4}\% \tag{7.20}$$

Therefore, the polarization level of HP free [1-^{13}C] pyruvate with SABRE-SHEATH at −0.6 µT and 25°C is

$$P_{^{13}\mathrm{C}} = \epsilon_{^{13}\mathrm{C}} \cdot P_{\mathrm{thermal}} = 20808 \cdot 1.25 \times 10^{-4}\% = 2.6\% \tag{7.21}$$

Previous studies have demonstrated that higher polarization levels can be achieved using a temperature cycling method, which involves cooling the sample to 0°C with ice water or air during the bubbling process. [27, 242]. However, cooling introduces practical challenges,

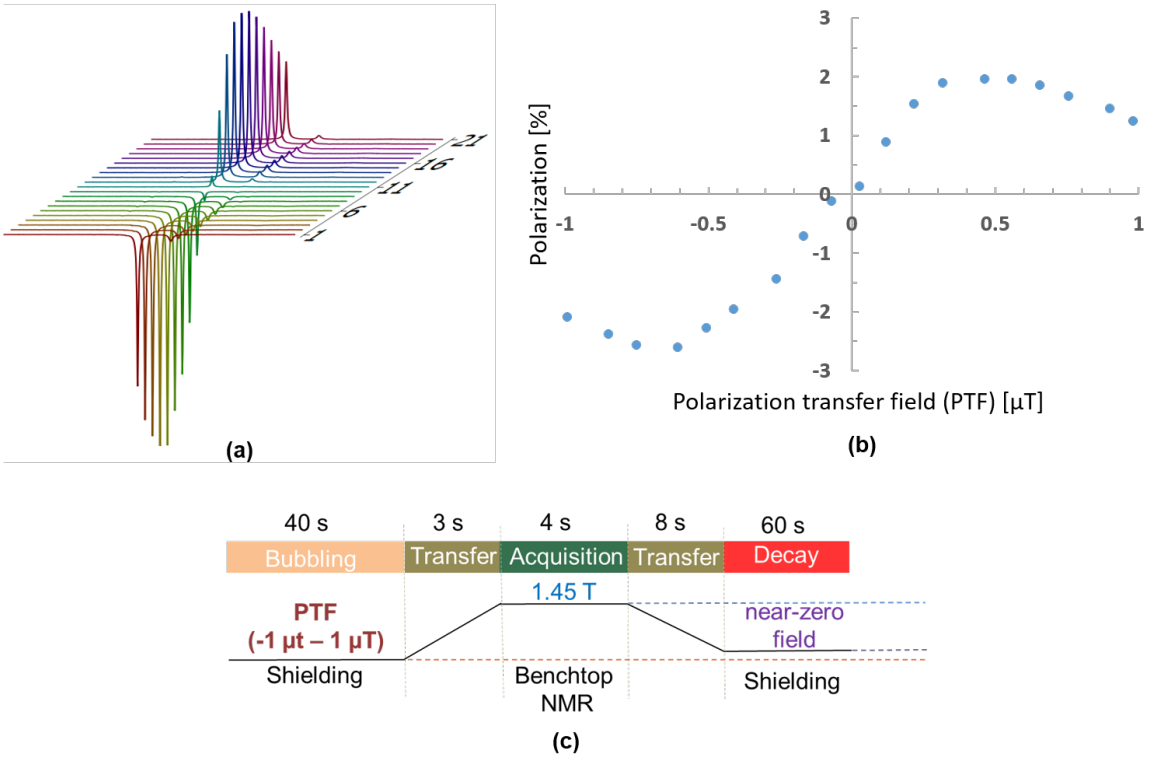

Figure 7.15: Magnetic field dependency on polarization level of [1-^{13}C] pyruvate with SABRE-SHEATH. (**a**) Stacked NMR spectra of HP [1-^{13}C] pyruvate hyperpolarized with SABRE-SHEATH at various PTFs sweeping from −1 μT to 1 μT. (**b**) Polarization levels of the HP free pyruvate at corresponding PTFs. (**c**) Schematic illustration of experimental procedure for studying field dependency. (Adopted from [JY03].)

such as condensation forming on the exterior of the NMR tube, which necessitates manual intervention, such as wiping the tube before insertion into the NMR for detection. This additional step conflicts with the goal of full automation and continuous operation, making such cooling techniques currently incompatible with fully automated systems. Overcoming these limitations would require modifications to the system design, potentially by integrating an automated mechanism to manage or prevent condensation without manual intervention.

7.5.3 Measuring ^{13}C polarization buildup time T_B at optimal PTF

The polarization build-up time in SABRE is influenced by several factors, including the chemical exchange rate within the substrate, the J-coupling network within the spin system, the strength of the PTF, the efficiency of *para*-H_2 delivery to the sample solution, the sample transfer passage and the concentration of the chemicals. Each of these elements plays a role in determining how quickly and effectively polarization can be built up and maintained, affecting the overall polarization level achieved with SABRE.

The polarization buildup time T_B of [1-^{13}C] pyruvate was measured at the optimal PTF of −0.6 μT by varying the bubbling time. The results of the calculated polarization buildup

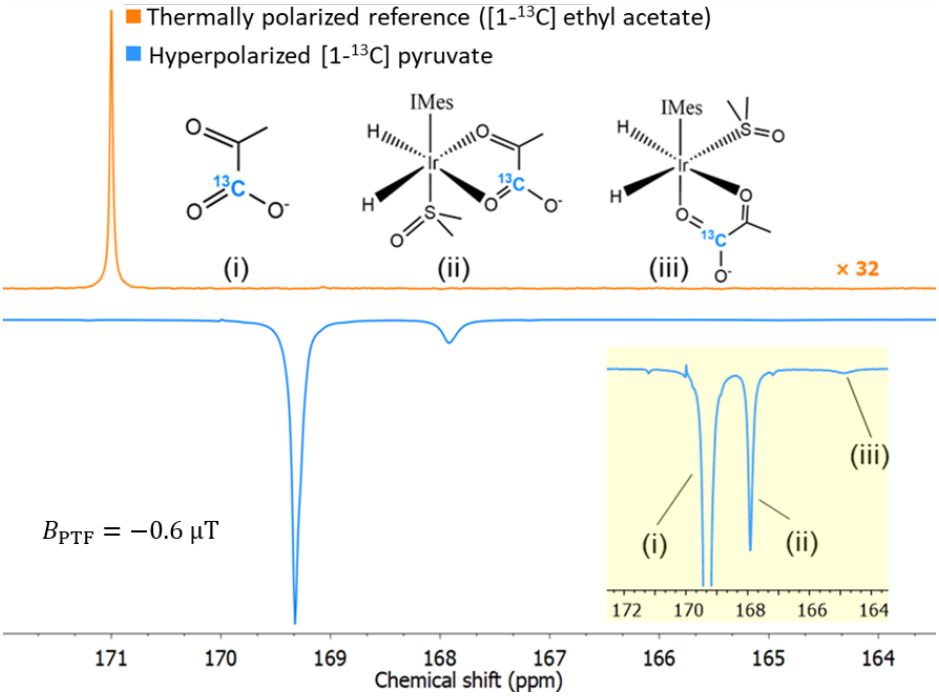

Figure 7.16: NMR spectra of the thermal reference sample of [1-^{13}C] vinyl acetate (orange, signal intensity enlarged with 32 folds) and [1-^{13}C] pyruvate hyperpolarized at −0.6 μT (blue) shows in free (i) and different bound forms (ii and iii). The polarization level of the free [1-^{13}C] pyruvate is 2.6%. (Adopted from [JY03].)

times for both the free and catalyst-bound forms of pyruvate are illustrated in Figure 7.17. The fitting curves were derived using a limited exponential growth equation to model the process of polarization development. The calculated polarization buildup time for the three forms of [1-^{13}C] pyruvate (i, ii and iii) were 38.35 s, 41.57 s and 49.53 s respectively.

The calculated outcome, especially T_B of the two bound form pyruvate (ii and iii), differs from previously reported results of ^{13}C-pyruvate hyperpolarization at low temperatures, where the polarization buildup times for the two forms of catalyst-bound pyruvate are significantly shorter [27]. The primary reason for this discrepancy is that at low temperatures, the exchange of *para*-H_2 is much more efficient than the exchange of pyruvate, which promotes rapid accumulation of polarization on catalyst-bound species [27, 227, 243], leading to shorter polarization time compared to the condition at higher temperature.

7.5.4 Measuring ^{13}C polarization relaxation time T_1 of free pyruvate at different magnetic fields

As a crucial intermediate in numerous biochemical pathways, ^{13}C pyruvate is an ideal marker to study and monitor various metabolic activities within biological systems. [65] A longer polarization relaxation time T_1 of ^{13}C pyruvate allows a more extended monitoring period and observation of more metabolic products. T_1 relaxation time can be determined on an NMR spectrometer using an inversion recovery pulse sequence to measure the NMR signal

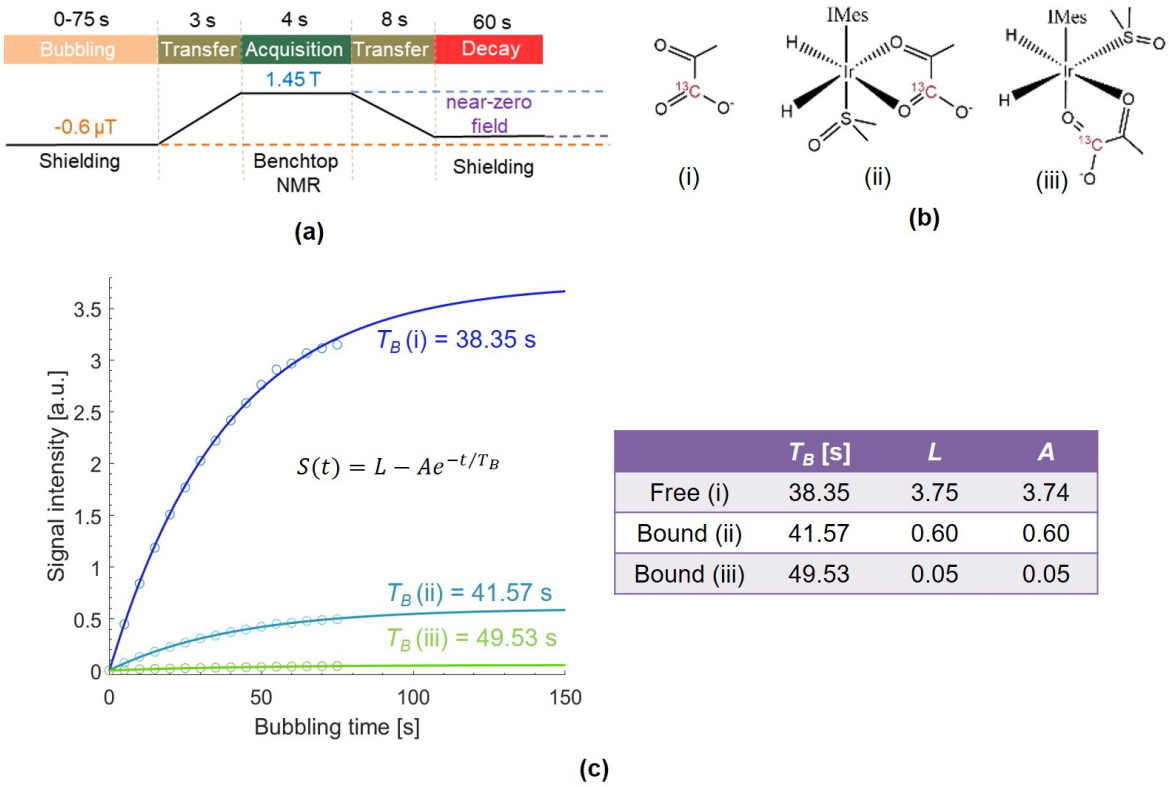

	T_B [s]	L	A
Free (i)	38.35	3.75	3.74
Bound (ii)	41.57	0.60	0.60
Bound (iii)	49.53	0.05	0.05

Figure 7.17: Measuring ^{13}C polarization buildup time T_B of free and bound pyruvate. **(a)** The schematic illustration of the experimental procedure for measuring the polarization buildup time. **(b)** Chemical structures of the free and bound [1-^{13}C] pyruvate. **(c)** Left: the measured polarization levels (circles) of the free pyruvate (i) and bound pyruvate (ii and iii) achieved with different bubbling times of *para*-H_2 and the fitting curves with the model of a limited exponential growth equation $S(t) = L - Ae^{-t/T_B}$. The parameter L is the limitation of the polarization level with infinite bubbling time t and A is initial difference from the limiting value. Right: fitting results of polarization buildup time for the three types of pyruvate. For the pyruvate in forms of i, ii and iii, the corresponding T_B are 38.35 s, 41.57 s and 49.53 s respectively. (Adopted from [JY03].)

over time. However, measuring the hyperpolarization relaxation time of HP substrates is challenging with this method, as they are typically generated at the PTF of low magnetic fields, where the spin–lattice relaxation may occur significantly faster.

In this work, the ^{13}C polarization relaxation time was determined at different magnetic fields using nuclear magnetic resonance dispersion (NMRD) measurements. [245, 246] The HP sample was positioned at specific locations where the polarization was allowed to decay under selected magnetic fields. Four representative magnetic fields were selected for the experiments: a near-zero field, the optimal PTF of −0.6 μT for ^{13}C pyruvate, the Earth's magnetic field of approximately 50 μT, and the high field of 1.45 T from the benchtop NMR magnet. The decay at the first two fields smaller than the Earth's geomagnetic field is facilitated using the PTF generator within the shielding chamber. However, for the fields of 50 μT and 1.45 T, which exceed the capacity of the PTF generator (−13.5 μT to 13.5 μT),

the decay processes are practically conducted at the corresponding locations outside of the shielding chamber.

After decay at the desired magnetic field, the sample was subsequently transferred to the benchtop NMR without delay for the measurement of the residual magnetization. This procedure was iterated multiple times, each with an extended decay duration at the same magnetic field. The measured signal intensities were then utilized to construct a relaxation curve for estimating T_1. The experimental procedures for measuring HP free [1-^{13}C] pyruvate relaxation time T_1 at 1.45 T, 50 µT, −0.6 µT, and near-zero field are illustrated in Figure 7.18**a-d** respectively. The blue block labeled "waiting" in the diagram indicates the intervals during which the HP sample was exposed to the corresponding magnetic fields for relaxation purposes.

The polarization decay curves of free pyruvate under different field conditions (circles) are shown in Figure 7.19. Each data point on the decay curves represents a periodic recording of the HP free pyruvate polarization using a 90° RF pulse at the acquisition field of 1.45 T. A single exponential equation was used to fit the polarization relaxation curves at different fields. The analysis revealed that the polarization decay for free pyruvate varied significantly across different magnetic fields. Specifically, the relaxation times were measured as 96.08 s at 1.45 T, 49.99 s at the Earth's magnetic field, 22.75 s at −0.6 µT, and 4.18 s in a near-zero field environment.

7.5.5 Optimization parameters of pulse sequence for [1-^{13}C] pyruvate hyperpolarization

To showcase the versatility of the constructed workstation, pulsed SABRE-SHEATH experiments were conducted—an innovative technique in the field of SABRE hyperpolarization. This technique involves applying an oscillating pulse sequence to the electromagnetic coil during the bubbling phase, allowing the SABRE-SHEATH hyperpolarization to evolve at two alternating µT-fields, which are deviated from the optimal PTF. Despite these fields creating a weaker J-coupling network, they still facilitate the achievement of a high level of polarization. Preliminary results suggest that this capability stems from the fact that the heteronuclei coupling can be readily interconverted between strong and weak coupling regimes. [243] Therefore, pulsed SABRE-SHEATH allows investigating the complex spin dynamics and optimizing the generated polarization by varying the parameters of the pulse sequence.

The [1-^{13}C] pyruvate SABRE-SHEATH hyperpolarization was optimized by adjusting the parameters of the applied field pulse sequence. In this procedure, the two alternating magnetic fields $B_{\mathrm{Low}} \approx 0$ µT and $B_{\mathrm{High}} = 13$ µT with respective durations τ_{L} and τ_{H} were generated using a square wave consisting of two voltage levels (Figure 7.20**a**). These voltage levels were modulated by PWM with corresponding duty cycles to precisely control the timing and intensity of each magnetic field. The switch time $\tau = 1.7$ µs between high and low levels

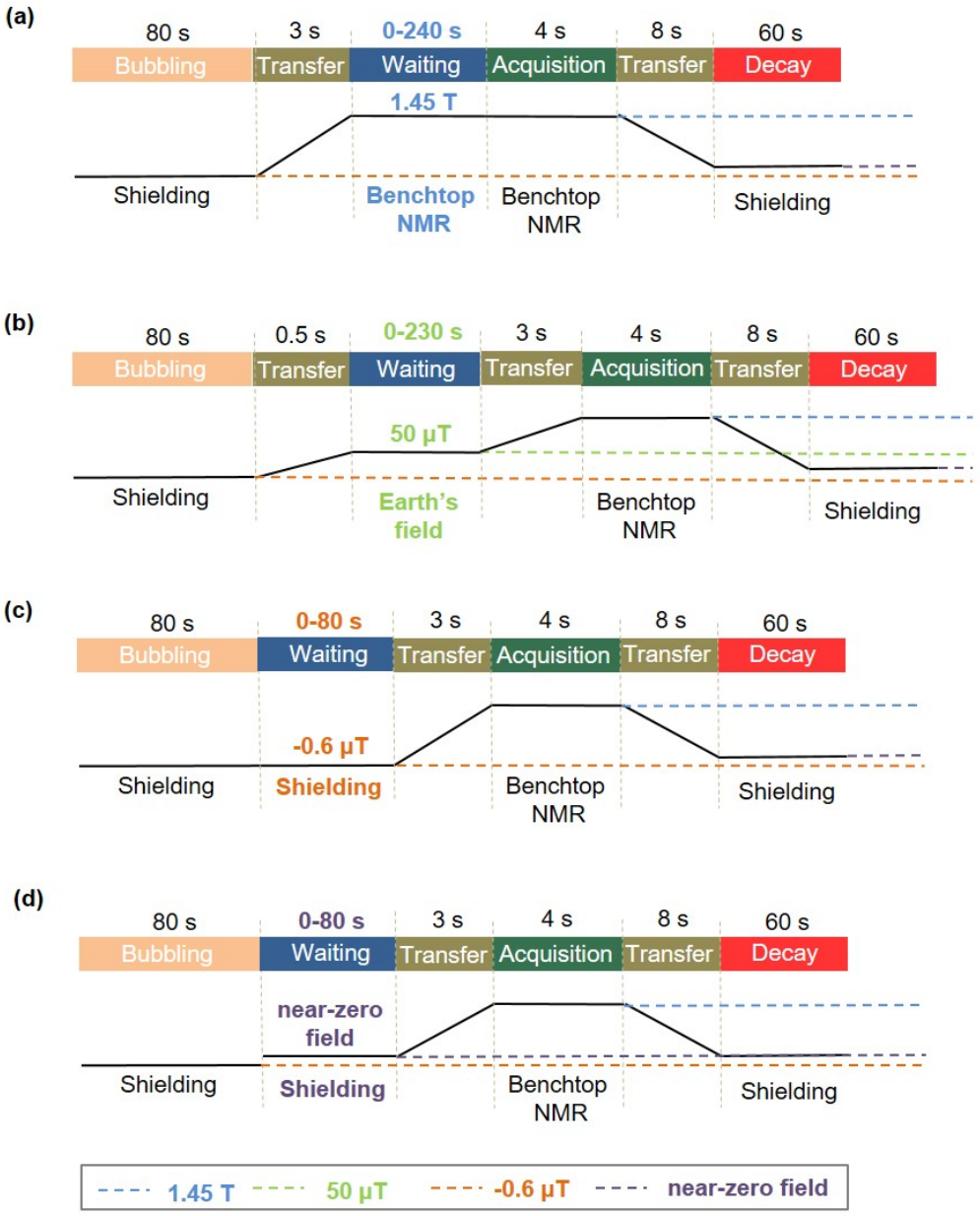

Figure 7.18: Measuring ^{13}C polarization relaxation time of HP free [1-^{13}C] pyruvate at four interesting magnetic fields. **(a-d)** Schematic illustration of experimental procedures for measuring polarization decay time of HP free [1-^{13}C] pyruvate at 1.45 T, the Earth's field (50 μT), −0.6 μT and near-zero field (0.026 μT). (Adopted from [JY03].)

was determined by measuring the time it takes the system to reach approximately 63% of its stable state (Figure 7.20**b**).

To determine the optimum duration time of the low and high fields respectively, four series of pulsed SABRE-SHEATH of [1-^{13}C] pyruvate were performed (Figure 7.21). Initially, the dependence of polarization on the duration of the high-field pulse was investigated while maintaining the duration of the low-field pulse fixed at $\tau_L = 6$ ms. By sweeping the duration of the high-field pulse from 0 to 12 ms in increments of 0.25 ms, the signal intensity of the hyperpolarized free pyruvate was observed to follow a curve resembling a sinusoidal pattern

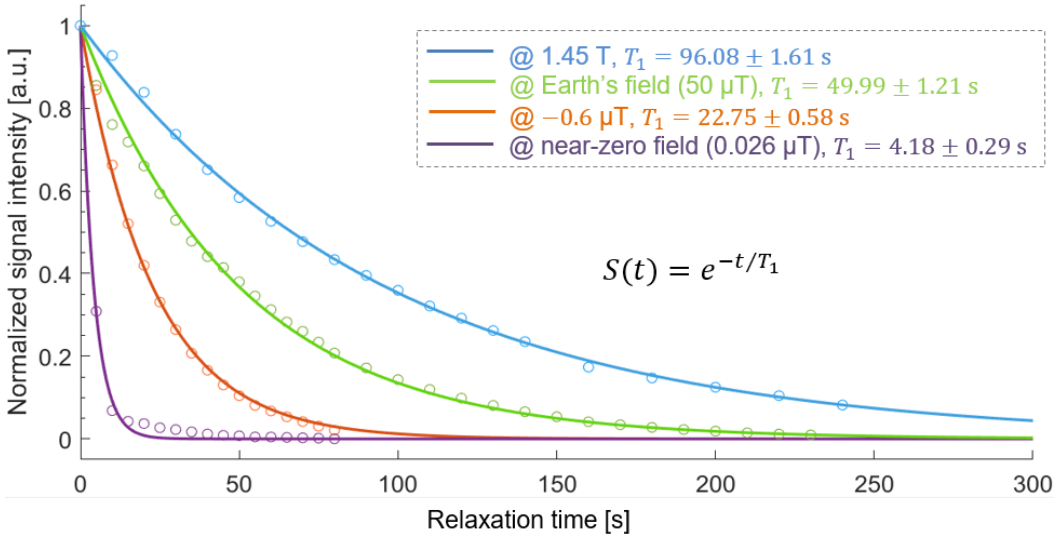

Figure 7.19: Normalized signal intensity (circles) of HP free [1-^{13}C] pyruvate relaxing under the four interesting fields. The polarization relaxation time T_1 was calculated by fitting the normalized signal intensity data to a mono-exponential equation $S(t) = e^{-t/T_1}$. The fitting results of the polarization relaxation time T_1 are 96.08 s at 1.45 T, 49.99 s at the Earth's field, 22.75 s at −0.6 μT, and 4.18 s at near-zero field. (Adopted from [JY03].)

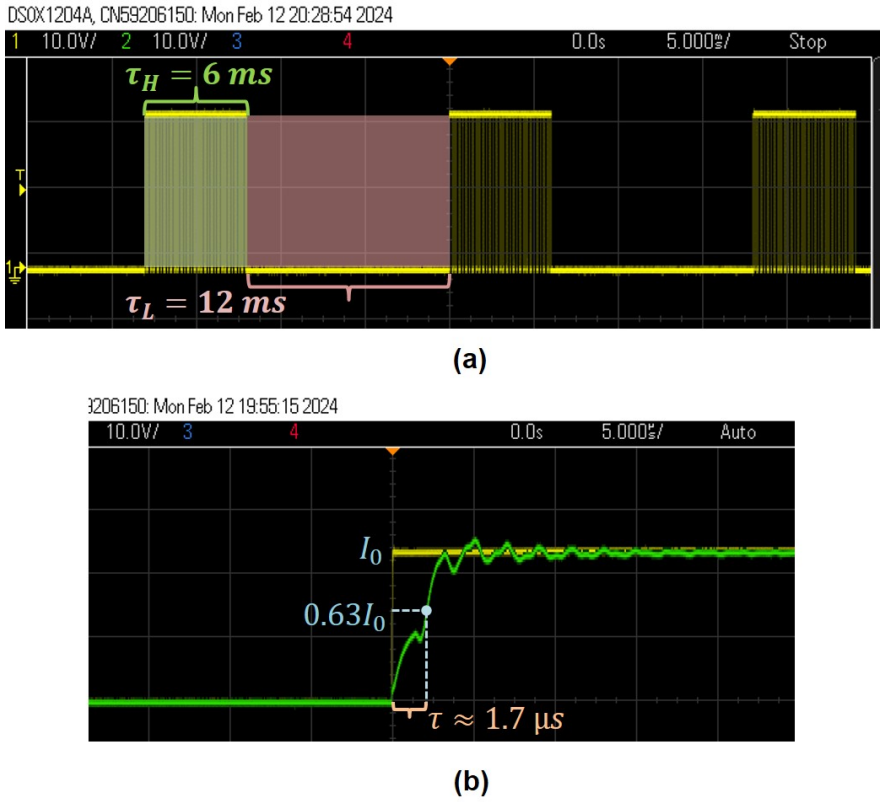

Figure 7.20: **(a)** Example of a square wave signal consisting of two high-and low-levels with duration (τ_H = 6 ms and τ_L = 12 ms) applied to solenoid coil for generating two alternative fields. **(b)** Estimating the switching time τ of the two magnetic fields verified on the oscillator. (Adopted from [JY03].)

(Figure 7.21**b**, blue). As τ_L increases, the extremum of the polarization within the periodic interval gradually decreases.

An additional set of experiments was conducted by sweeping τ_L from 0 to 4 ms with even smaller increments of 0.125 ms to more precisely determine the optimal duration of the high-field pulse. The results indicated that the maximum signal was observed when τ_L was set at 0.25 ms (Figure 7.21**b**, orange). Building on this, the dependence of polarization on the duration of the low-field pulse was iteratively studied. By sweeping τ_L from 0 to 25 ms in increments of 1.25 ms, the maximum polarization was observed when τ_L was set to 7.5 ms (Figure 7.21**c**). This is also demonstrated by the iterative experiments of τ_L sweeping with fixed $\tau_L = 7.5$ ms (Figure 7.21**b**, green). Therefore, the optimal duration times of the high and low fields for pulsed SABRE-SHEATH were $\tau_H = 0.25$ ms and $\tau_L = 7.5$ ms, respectively.

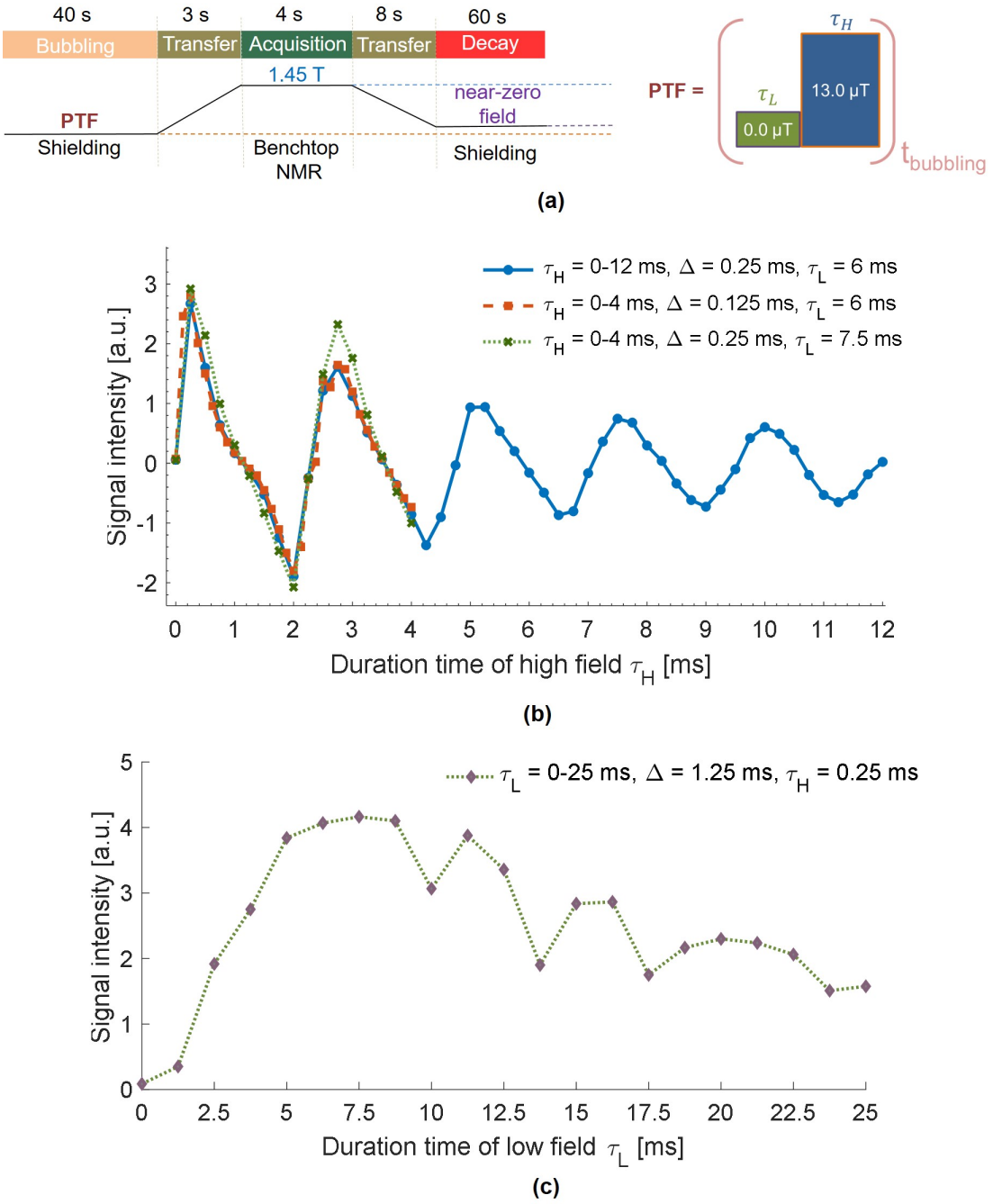

Figure 7.21: Optimizing the polarization level of free pyruvate with respect to durations in pulsed SABRE-SHEATH experiments. (**a**) Schematic illustration of the experimental procedure for pulsed SABRE-SHEATH. The sample solution was bubbled for 40 s at the PTF involving two alternating fields with corresponding durations of τ_L and τ_H. (**b**) Signal intensities of HP free pyruvate hyperpolarized with sweeping the duration time τ_H in the high magnetic field (13 μT). (**c**) Signal intensities of HP free pyruvate hyperpolarized with sweeping the duration time τ_L in the low magnetic field (near-zero field). The maximum signal intensities occur when τ_H = 0.25 ms and τ_L = 7.5 ms of the pulse sequence. Lines connecting each measured point are included to guide the eyes. (Adopted from [JY03].)

7.6 Conclusion

In summary, the constructed SABRE workstation with the robotic arm-assisted shuttling system and the controlling system allows fully automated execution of the SABRE and SABRE-SHEATH hyperpolarization experiments. The tailored GUI simplifies the implementation of various hyperpolarization protocols. These include sample activation, magnetic field sweeping, measurement of buildup and relaxation times under different field conditions, as well as the execution of pulsed SABRE-SHEATH experiments. The flexibility and automation of this setup have enabled multiple applications. These include continuous SABRE hyperpolarization of different substrates with high reproducibility and the precise determination of optimal experimental parameters, such as the PTFs or pulse sequences. The automated SABRE workstation shows promise for optimizing polarization transfer efficiency, investigating the mechanisms of polarization transfer, and high-throughput testing the performance of new SABRE catalysts.

In the future, efforts will be dedicated to developing multi-channel H_2 gas pipeline control systems. This development will facilitate the integration and compatibility of the automated system with a multi-sample carousel, thereby meeting the demands for high-throughput hyperpolarization.

Concluding Remarks

The research presented in this dissertation focuses on advancing hyperpolarization techniques, specifically SABRE and PHIP, through the development of innovative gas–liquid reactor systems and automated experimental platforms to enhance the efficiency and applicability of NMR spectroscopy.

To overcome limitations of conventional *para*-H_2-based hyperpolarization setups, multiple types of gas–liquid reactors were designed, fabricated, and validated through proof-of-concept experiments. Among them, the tube-in-tube reactor demonstrated superior compatibility with both SABRE and PHIP across different NMR spectrometers. Its scalable gas–liquid interfacial area enables efficient polarization transfer, producing high-intensity NMR signals in single-scan acquisitions. This capability significantly reduces acquisition time, especially for low concentration samples.

Building upon these advancements, parallel SABRE hyperpolarization was implemented using a probe equipped with dual NMR detection coils. This configuration enables simultaneous acquisition from two independent channels, effectively accelerates NMR detection and advancing the feasibility of high-throughput NMR workflows.

The tube-in-tube reactor offers additional advantages beyond gas–liquid exchange efficiency, including precise control over flow conditions and full compatibility with continuous-flow operation. Leveraging these attributes, a steady-state RASER was realized via continuous-flow ALTADENA-PHIP. By manipulating gas and liquid pressures, a range of nonlinear RASER regimes—including frequency combs, period-doubling behavior, and chaos—were observed over extended time scales. These results establish the tube-in-tube reactor as a robust platform for exploring nonlinear spin dynamics under well-controlled experimental conditions.

In addition, the stable two-mode RASER regime, operating within the linear response domain, enabled high-precision measurements of scalar J-couplings. To further interpret the experimental observations, numerical simulations based on a two-mode nonlinear model were performed. A three-dimensional bifurcation diagram was developed for the first time, providing a comprehensive visual framework for understanding the transition mechanisms among different RASER regimes. These simulations not only corroborated experimental data

but also offer predictive capabilities for the design of future hyperpolarized spin systems.

Complementing the continuous-flow platforms, a fully automated SABRE workstation was developed based on a robotic arm, tailored for routine hyperpolarization on benchtop NMR spectrometers. This system integrates a precision robotic shuttle for sample handling, a high-efficiency bubbling unit, and a programmable PTF generator capable of delivering precision magnetic fields from zero-field to the micro-Tesla regime via PWM control. All operations are fully automated and accessible through a user-friendly graphical interface, enabling reproducible SABRE hyperpolarization for both proton and heteronuclear targets. This development substantially improves throughput and standardization in routine experiments.

Looking ahead, several promising directions arise from this work:

Further optimization of gas–liquid contactor designs could enhance polarization levels and expand the range of polarizable substrates. The development of falling film gas–liquid reactors with multiple channels presents a promising approach for enhancing mass transfer efficiency through direct gas–liquid contact, while simultaneously enabling the hyperpolarization of multiple sample solutions flowing through separate channels. This reactor design offers potential for scaling up hyperpolarization processes and increasing experimental throughput.

Furthermore, integrating parallel SABRE under continuous-flow conditions with plug-flow operation provides a scalable platform for high-throughput screening. This approach is particularly beneficial for the rapid analysis of low-concentration analytes and holds significant promise for applications in drug discovery and pharmaceutical screening.

Additionally, integration of machine learning algorithms with the automated SABRE workstation could enable real-time optimization of hyperpolarization conditions and adaptive experimental protocols. In the context of RASER-based MRI, the high reproducibility of the automated workstation may support multi-projection acquisition on benchtop instruments, enabling rapid, fully automated, background-signal-free MRI measurements.

Taken together, these contributions advance the field of NMR spectroscopy by improving both sensitivity and throughput, while facilitating the development of scalable and practical hyperpolarization platforms. The multidisciplinary nature of this work—spanning engineering, chemistry, and physics—provides a solid foundation for the continued advancement and broader application of hyperpolarization techniques across scientific research and industrial fields.

Bibliography

[1] Oliver Gutfleisch, Matthew A Willard, Ekkes Brück, Christina H Chen, SG Sankar, and J Ping Liu. Magnetic materials and devices for the 21st century: stronger, lighter, and more energy efficient. *Advanced materials*, 23(7):821–842, 2011.

[2] Kâmil Uğurbil, Gregor Adriany, Peter Andersen, Wei Chen, Michael Garwood, Rolf Gruetter, Pierre-Gil Henry, Seong-Gi Kim, Haiying Lieu, Ivan Tkac, et al. Ultra-high field magnetic resonance imaging and spectroscopy. *Magnetic resonance imaging*, 21(10):1263–1281, 2003.

[3] Helena Kovacs, Detlef Moskau, and Manfred Spraul. Cryogenically cooled probes—a leap in nmr technology. *Progress in Nuclear Magnetic Resonance Spectroscopy*, 46(2-3):131–155, 2005.

[4] Alia Hassan, Caitlin M Quinn, Jochem Struppe, Ivan V Sergeyev, Chunting Zhang, Changmiao Guo, Brent Runge, Theint Theint, Hanh H Dao, Christopher P Jaroniec, et al. Sensitivity boosts by the cpmas cryoprobe for challenging biological assemblies. *Journal of Magnetic Resonance*, 311:106680, 2020.

[5] Moritz Becker, Yen-Tse Cheng, Achim Voigt, Ajmal Chenakkara, Mengjia He, Sören Lehmkuhl, Mazin Jouda, and Jan G Korvink. Artificial intelligence-driven shimming for parallel high field nuclear magnetic resonance. *Scientific Reports*, 13(1):17983, 2023.

[6] J Thomas Vaughan and John R Griffiths. *RF coils for MRI*. John Wiley & Sons, Chichester, 2012.

[7] Piotr Lepucki, Aleksandr I Egunov, Marco Rosenkranz, Renato Huber, Alaleh Mirhajivarzaneh, Dmitry D Karnaushenko, Adam P Dioguardi, Daniil Karnaushenko, Bernd Büchner, Oliver G Schmidt, et al. Self-assembled rolled-up microcoils for nl microfluidics nmr spectroscopy. *Advanced Materials Technologies*, 6(1):2000679, 2021.

[8] Hossein Davoodi, Nurdiana Nordin, Hirokazu Munakata, Jan G Korvink, Neil MacKinnon, and Vlad Badilita. Untuned broadband spiral micro-coils achieve sensitive multinuclear nmr tx/rx from microfluidic samples. *Scientific reports*, 11(1):7798, 2021.

[9] Michael Sattler, M Maurer, J Schleucher, and Christian Griesinger. A simultaneous 15 n, 1 h-and 13 c, 1 h-hsqc with sensitivity enhancement and a heteronuclear gradient echo. *Journal of Biomolecular NMR*, 5:97–102, 1995.

[10] Jonathan RJ Yong, Alexandar L Hansen, Ēriks Kupče, and Tim DW Claridge. Increasing sensitivity and versatility in nmr supersequences with new hsqc-based modules. *Journal of Magnetic Resonance*, 329:107027, 2021.

[11] Hui Xu, Danielle Lustig, and Leah B Casabianca. 13 c saturation-transfer difference (std)-nmr experiments using inept polarization transfer. *Applied Magnetic Resonance*, 51:277–286, 2020.

[12] Richard A. Green, Ralph W. Adams, Simon B. Duckett, Ryan E. Mewis, David C. Williamson, and Gary G.R. Green. The theory and practice of hyperpolarization in magnetic resonance using parahydrogen. *Progress in Nuclear Magnetic Resonance Spectroscopy*, 67:1–48, 2012.

[13] Stefan Glöggler, Johannes Colell, and Stephan Appelt. Para-hydrogen perspectives in hyperpolarized nmr. *Journal of Magnetic Resonance*, 235:130–142, 2013.

[14] Thomas BR Robertson and Ryan E Mewis. Perspective on the hyperpolarisation technique signal amplification by reversible exchange (sabre) in nmr spectroscopy and mr imaging. In *Annual Reports on NMR Spectroscopy*, volume 93, pages 145–212. Elsevier, 2018.

[15] Peter J Rayner and Simon B Duckett. Signal amplification by reversible exchange (sabre): From discovery to diagnosis. *Angewandte Chemie International Edition*, 57(23):6742–6753, 2018.

[16] Henri de Maissin, Philipp R Groß, Obaid Mohiuddin, Moritz Weigt, Luca Nagel, Marvin Herzog, Zirun Wang, Robert Willing, Wilfried Reichardt, Martin Pichotka, et al. In vivo metabolic imaging of [1-13c] pyruvate-d3 hyperpolarized by reversible exchange with parahydrogen. *Angewandte Chemie International Edition*, 62(36):e202306654, 2023.

[17] Diego Gauto, Ons Dakhlaoui, Ildefonso Marin-Montesinos, Sabine Hediger, and Gaël De Paëpe. Targeted dnp for biomolecular solid-state nmr. *Chemical Science*, 12(18):6223–6237, 2021.

[18] Ilia B Moroz and Michal Leskes. Dynamic nuclear polarization solid-state nmr spectroscopy for materials research. *Annual Review of Materials Research*, 52(1):25–55, 2022.

[19] Thomas Biedenbaender, Victoria Aladin, Siavash Saeidpour, and Bjoern Corzilius. Dynamic nuclear polarization for sensitivity enhancement in biomolecular solid-state nmr. *Chemical Reviews*, 122(10):9738–9794, 2022.

[20] Thomas R Gentile, PJ Nacher, B Saam, and TG Walker. Optically polarized he 3. *Reviews of modern physics*, 89(4):045004, 2017.

[21] Laura L Walkup and Jason C Woods. Translational applications of hyperpolarized 3he and 129xe. *NMR in Biomedicine*, 27(12):1429–1438, 2014.

[22] Eleonora Cavallari, Carla Carrera, Silvio Aime, and Francesca Reineri. Studies to enhance the hyperpolarization level in php-sah-produced c13-pyruvate. *Journal of Magnetic Resonance*, 289:12–17, 2018.

[23] Francesca Reineri, Eleonora Cavallari, Carla Carrera, and Silvio Aime. Hydrogenative-phip polarized metabolites for biological studies. *Magnetic Resonance Materials in Physics, Biology and Medicine*, 34:25–47, 2021.

[24] Soumya S Roy, Kate M Appleby, Elizabeth J Fear, and Simon B Duckett. Sabre-relay: a versatile route to hyperpolarization. *The journal of physical chemistry letters*, 9(5):1112–1117, 2018.

[25] Stephan Knecht, Danila A Barskiy, Gerd Buntkowsky, and Konstantin L Ivanov. Theoretical description of hyperpolarization formation in the sabre-relay method. *The Journal of Chemical Physics*, 153(16), 2020.

[26] Milton L Truong, Thomas Theis, Aaron M Coffey, Roman V Shchepin, Kevin W Waddell, Fan Shi, Boyd M Goodson, Warren S Warren, and Eduard Y Chekmenev. 15n hyperpolarization by reversible exchange using sabre-sheath. *The journal of physical chemistry C*, 119(16):8786–8797, 2015.

[27] Patrick TomHon, Mustapha Abdulmojeed, Isaiah Adelabu, Shiraz Nantogma, Mohammad Shah Hafez Kabir, Soren Lehmkuhl, Eduard Y Chekmenev, and Thomas Theis. Temperature cycling enables efficient 13c sabre-sheath hyperpolarization and imaging of [1-13c]-pyruvate. *Journal of the American Chemical Society*, 144(1):282–287, 2021.

[28] Charles P Slichter. *Principles of magnetic resonance*, volume 1. Springer Science & Business Media, Berlin, Heidelberg, 2013.

[29] Richard R Ernst, Geoffrey Bodenhausen, and Alexander Wokaun. *Principles of nuclear magnetic resonance in one and two dimensions*. Oxford university press, 1990.

[30] Frank Holger Försterling. Spin dynamics: basics of nuclear magnetic resonance. *Medical Physics*, 37(1):406–407, 2010.

[31] Malcolm H Levitt. *Spin dynamics: basics of nuclear magnetic resonance*. John Wiley & Sons, Chichester, 2008.

[32] Winfried Kuhn. Nmr microscopy—fundamentals, limits and possible applications. *Angewandte Chemie International Edition in English*, 29(1):1–19, 1990.

[33] Thomas L James. Fundamentals of nmr. *Online Textbook: Department of Pharmaceutical Chemistry, University of California, San Francisco*, pages 1–31, 1998.

[34] Hongzhi Wang, Ming Zhao, Jerome L Ackerman, and Yiqiao Song. Saturation-inversion-recovery: A method for t1 measurement. *Journal of Magnetic Resonance*, 274:137–143, 2017.

[35] Gaby S Pell, Regula S Briellmann, Anthony B Waites, David F Abbott, David P Lewis, and Graeme D Jackson. Optimized clinical t2 relaxometry with a standard

cpmg sequence. *Journal of Magnetic Resonance Imaging: An Official Journal of the International Society for Magnetic Resonance in Medicine*, 23(2):248–252, 2006.

[36] KVR Chary and Girjesh Govil. Basic concepts in nmr spectroscopy. In *NMR in biological systems: from molecules to humans*, pages 1–41. Springer, Dordrecht, 2008.

[37] MJ Lynch, J Masters, JP Pryor, JC Lindon, M Spraul, PJD Foxall, and JK Nicholson. Ultra high field nmr spectroscopic studies on human seminal fluid, seminal vesicle and prostatic secretions. *Journal of pharmaceutical and biomedical analysis*, 12(1):5–19, 1994.

[38] Tsutomu Nakada. Clinical application of high and ultra high-field mri. *Brain and Development*, 29(6):325–335, 2007.

[39] Peter F Flynn, Debra L Mattiello, Howard DW Hill, and A Joshua Wand. Optimal use of cryogenic probe technology in nmr studies of proteins. *Journal of the American Chemical Society*, 122(19):4823–4824, 2000.

[40] Hector C Keun, Olaf Beckonert, Julian L Griffin, Christian Richter, Detlef Moskau, John C Lindon, and Jeremy K Nicholson. Cryogenic probe 13c nmr spectroscopy of urine for metabonomic studies. *Analytical chemistry*, 74(17):4588–4593, 2002.

[41] Luc Darrasse and J-C Ginefri. Perspectives with cryogenic rf probes in biomedical mri. *Biochimie*, 85(9):915–937, 2003.

[42] Daniel Hernandez and Kyoung-Nam Kim. A review on the rf coil designs and trends for ultra high field magnetic resonance imaging. *Investigative Magnetic Resonance Imaging*, 24(3):95–122, 2020.

[43] Andre Dallmann, Bernd Simon, Malgorzata M Duszczyk, Hamed Kooshapur, Arthur Pardi, Wolfgang Bermel, and Michael Sattler. Efficient detection of hydrogen bonds in dynamic regions of rna by sensitivity-optimized nmr pulse sequences. *Angewandte Chemie International Edition*, 52(40):10487–10490, 2013.

[44] Eriks Kupče and Ray Freeman. Compensated adiabatic inversion pulses: broadband inept and hsqc. *Journal of Magnetic Resonance*, 187(2):258–265, 2007.

[45] Teodor Parella, Francisco Sánchez-Ferrando, and Albert Virgili. Improved sensitivity in gradient-based 1d and 2d multiplicity-edited hsqc experiments. *Journal of Magnetic Resonance*, 126(2):274–277, 1997.

[46] Nils Spengler, Peter T While, Markus V Meissner, Ulrike Wallrabe, and Jan G Korvink. Magnetic lenz lenses improve the limit-of-detection in nuclear magnetic resonance. *PLoS One*, 12(8):e0182779, 2017.

[47] Jianyi Liang, Hossein Davoodi, Sagar Wadhwa, Vlad Badilita, and Jan G Korvink. Broadband stripline lenz lens achieves 11× nmr signal enhancement. *Scientific Reports*, 14(1):1645, 2024.

[48] James Eills, Dmitry Budker, Silvia Cavagnero, Eduard Y Chekmenev, Stuart J Elliott, Sami Jannin, Anne Lesage, Joerg Matysik, Thomas Meersmann, Thomas Prisner, et al. Spin hyperpolarization in modern magnetic resonance. *Chemical reviews*, 123(4):1417–1551, 2023.

[49] Jan H Ardenkjaer-Larsen. Introduction to dissolution dnp: Overview, instrumentation, and human applications. *Handbook of High Field Dynamic Nuclear Polarization*, pages 239–259, 2019.

[50] Yoh Matsuki, Toshitaka Idehara, Jun Fukazawa, and Toshimichi Fujiwara. Advanced instrumentation for dnp-enhanced mas nmr for higher magnetic fields and lower temperatures. *Journal of Magnetic Resonance*, 264:107–115, 2016.

[51] Bryce E Ackermann, Byung Joon Lim, Nesreen Elathram, Sirish Narayanan, and Galia T Debelouchina. A comparative study of nitroxide-based biradicals for dynamic nuclear polarization in cellular environments. *ChemBioChem*, 23(24):e202200577, 2022.

[52] Thorsten Maly, Dongtao Cui, Robert G Griffin, and Anne-Frances Miller. 1h dynamic nuclear polarization based on an endogenous radical. *The Journal of Physical Chemistry B*, 116(24):7055–7065, 2012.

[53] Cristina Gabellieri, Steven Reynolds, Arnon Lavie, Geoffrey S Payne, Martin O Leach, and Thomas R Eykyn. Therapeutic target metabolism observed using hyperpolarized 15n choline. *Journal of the American Chemical Society*, 130(14):4598–4599, 2008.

[54] Cornelius von Morze, John A Engelbach, Galen D Reed, Albert P Chen, James D Quirk, Tyler Blazey, Rohit Mahar, Craig R Malloy, Joel R Garbow, and Matthew E Merritt. 15n-carnitine, a novel endogenous hyperpolarized mri probe with long signal lifetime. *Magnetic resonance in medicine*, 85(4):1814–1820, 2021.

[55] Markus Durst, Enrico Chiavazza, Axel Haase, Silvio Aime, Markus Schwaiger, and Rolf F Schulte. α-trideuteromethyl [15n] glutamine: A long-lived hyperpolarized perfusion marker. *Magnetic resonance in medicine*, 76(6):1900–1904, 2016.

[56] Enrico Chiavazza, Alessandra Viale, Magnus Karlsson, and Silvio Aime. 15n-permethylated amino acids as efficient probes for mri-dnp applications. *Contrast media & molecular imaging*, 8(5):417–421, 2013.

[57] Fumitaka Horii, Toshitaka Idehara, Yutaka Fujii, Isamu Ogawa, Akifumi Horii, George Entzminger, and F David Doty. Development of dnp-enhanced high-resolution solid-state nmr system for the characterization of the surface structure of polymer materials. *Journal of Infrared, Millimeter, and Terahertz Waves*, 33:756–765, 2012.

[58] Siddarth Narasimhan, Stephan Scherpe, Alessandra Lucini Paioni, Johan van der Zwan, Gert E Folkers, Huib Ovaa, and Marc Baldus. Dnp-supported solid-state nmr spectroscopy of proteins inside mammalian cells. *Angewandte Chemie International Edition*, 58(37):12969–12973, 2019.

[59] Aany Sofia Lilly Thankamony, Johannes J Wittmann, Monu Kaushik, and Björn Corzilius. Dynamic nuclear polarization for sensitivity enhancement in modern solid-state nmr. *Progress in nuclear magnetic resonance spectroscopy*, 102:120–195, 2017.

[60] Li Zhao, Arthur C Pinon, Lyndon Emsley, and Aaron J Rossini. Dnp-enhanced solid-state nmr spectroscopy of active pharmaceutical ingredients. *Magnetic Resonance in Chemistry*, 56(7):583–609, 2018.

[61] Jan H Ardenkjær-Larsen, Björn Fridlund, Andreas Gram, Georg Hansson, Lennart Hansson, Mathilde H Lerche, Rolf Servin, Mikkel Thaning, and Klaes Golman. Increase in signal-to-noise ratio of> 10,000 times in liquid-state nmr. *Proceedings of the National Academy of Sciences*, 100(18):10158–10163, 2003.

[62] Riccardo Balzan, Laetitia Fernandes, Arnaud Comment, Laetitia Pidial, Bertrand Tavitian, and Paul R Vasos. Dissolution dynamic nuclear polarization instrumentation for real-time enzymatic reaction rate measurements by nmr. *Journal of Visualized Experiments: Jove*, (108):53548, 2016.

[63] Jun Fukazawa, Yuuki Mochizuki, Sakyo Kanai, Natsuko Miura, Makoto Negoro, and Akinori Kagawa. Real-time monitoring of hydrolysis reactions of pyrophosphates with dissolution dynamic nuclear polarization. *The Journal of Physical Chemistry Letters*, 15(28):7288–7294, 2024.

[64] David M Wilson, Kayvan R Keshari, Peder EZ Larson, Albert P Chen, Simon Hu, Mark Van Criekinge, Robert Bok, Sarah J Nelson, Jeffrey M Macdonald, Daniel B Vigneron, et al. Multi-compound polarization by dnp allows simultaneous assessment of multiple enzymatic activities in vivo. *Journal of magnetic resonance*, 205(1):141–147, 2010.

[65] SJ Nelson, D Vigneron, J Kurhanewicz, A Chen, R Bok, and R Hurd. Dnp-hyperpolarized 13 c magnetic resonance metabolic imaging for cancer applications. *Applied magnetic resonance*, 34:533–544, 2008.

[66] N Koyasu, F Hyodo, AE Elhelaly, S Shoda, R Iwasaki, H Tomita, M Takasu, T Mori, Y Noda, H Kato, et al. Early monitoring of redox status based on reduced molecules using in vivo dnp-mri for cancer treatment. *International Journal of Radiation Oncology, Biology, Physics*, 114(3):e528, 2022.

[67] Marie A Schroeder, Kieran Clarke, Stefan Neubauer, and Damian J Tyler. Hyperpolarized magnetic resonance: a novel technique for the in vivo assessment of cardiovascular disease. *Circulation*, 124(14):1580–1594, 2011.

[68] Guilhem J Collier, James A Eaden, Paul JC Hughes, Stephen M Bianchi, Neil J Stewart, Nicholas D Weatherley, Graham Norquay, Rolf F Schulte, and Jim M Wild. Dissolved 129xe lung mri with four-echo 3d radial spectroscopic imaging: quantification of regional gas transfer in idiopathic pulmonary fibrosis. *Magnetic Resonance in Medicine*, 85(5):2622–2633, 2021.

[69] Ho-Fung Chan, Laurie J Smith, Alberto M Biancardi, Jody Bray, Helen Marshall, Paul JC Hughes, Guilhem J Collier, Madhwesha Rao, Graham Norquay, Andrew J Swift, et al. Image phenotyping of preterm-born children using hyperpolarized 129xe lung magnetic resonance imaging and multiple-breath washout. *American Journal of Respiratory and Critical Care Medicine*, 207(1):89–100, 2023.

[70] Lukas Ebner, Jeff Kammerman, Bastiaan Driehuys, Mark L Schiebler, Robert V Cadman, and Sean B Fain. The role of hyperpolarized 129xenon in mr imaging of pulmonary function. *European journal of radiology*, 86:343–352, 2017.

[71] Alexandra Svyatova, Vitaly P Kozinenko, Nikita V Chukanov, Dudari B Burueva, Eduard Y Chekmenev, Yu-Wen Chen, Dennis W Hwang, Kirill V Kovtunov, and Igor V Koptyug. Phip hyperpolarized [1-13c] pyruvate and [1-13c] acetate esters via ph-inept polarization transfer monitored by 13c nmr and mri. *Scientific Reports*, 11(1):5646, 2021.

[72] Kirill V Kovtunov, Ekaterina V Pokochueva, Oleg G Salnikov, Samuel F Cousin, Dennis Kurzbach, Basile Vuichoud, Sami Jannin, Eduard Y Chekmenev, Boyd M Goodson, Danila A Barskiy, et al. Hyperpolarized nmr spectroscopy: d-dnp, phip, and sabre techniques. *Chemistry–An Asian Journal*, 13(15):1857–1871, 2018.

[73] Peter J Rayner, Michael J Burns, Alexandra M Olaru, Philip Norcott, Marianna Fekete, Gary GR Green, Louise AR Highton, Ryan E Mewis, and Simon B Duckett. Delivering strong 1h nuclear hyperpolarization levels and long magnetic lifetimes through signal amplification by reversible exchange. *Proceedings of the National Academy of Sciences*, 114(16):E3188–E3194, 2017.

[74] Thomas Theis, Milton L Truong, Aaron M Coffey, Roman V Shchepin, Kevin W Waddell, Fan Shi, Boyd M Goodson, Warren S Warren, and Eduard Y Chekmenev. Microtesla sabre enables 10% nitrogen-15 nuclear spin polarization. *Journal of the American Chemical Society*, 137(4):1404–1407, 2015.

[75] Danila A Barskiy, Roman V Shchepin, Christian PN Tanner, Johannes FP Colell, Boyd M Goodson, Thomas Theis, Warren S Warren, and Eduard Y Chekmenev. The absence of quadrupolar nuclei facilitates efficient 13c hyperpolarization via reversible exchange with parahydrogen. *ChemPhysChem*, 18(12):1493–1498, 2017.

[76] Danila A Barskiy, Roman V Shchepin, Aaron M Coffey, Thomas Theis, Warren S Warren, Boyd M Goodson, and Eduard Y Chekmenev. Over 20% 15n hyperpolarization

in under one minute for metronidazole, an antibiotic and hypoxia probe. *Journal of the American Chemical Society*, 138(26):8080–8083, 2016.

[77] Jude A Okolie, Biswa R Patra, Alivia Mukherjee, Sonil Nanda, Ajay K Dalai, and Janusz A Kozinski. Futuristic applications of hydrogen in energy, biorefining, aerospace, pharmaceuticals and metallurgy. *International journal of hydrogen energy*, 46(13):8885–8905, 2021.

[78] Atsuyoshi Iida, Nobuyuki Nosaka, Tetsuya Yumoto, Emily Knaup, Hiromichi Naito, Chihiro Nishiyama, Yasuaki Yamakawa, Kohei Tsukahara, Michihisa Terado, Keiji Sato, et al. The clinical application of hydrogen as a medical treatment. *Acta Medica Okayama*, 70(5):331–337, 2016.

[79] Wenguo Liu, Haibin Zuo, Jingsong Wang, Qingguo Xue, Binglang Ren, and Fan Yang. The production and application of hydrogen in steel industry. *International Journal of Hydrogen Energy*, 46(17):10548–10569, 2021.

[80] Ram Ramachandran and Raghu K Menon. An overview of industrial uses of hydrogen. *International journal of hydrogen energy*, 23(7):593–598, 1998.

[81] Arnold Eucken. *Die Molekularwärme des Wasserstoffs bei tiefen Temperaturen.* Verlag der königlichen Akademie der Wissenschaften, Berlin, 1912.

[82] Werner Heisenberg. Mehrkörperprobleme und resonanz in der quantenmechanik. ii. *Original Scientific Papers Wissenschaftliche Originalarbeiten*, pages 551–579, 1985.

[83] Friedrich Hund. Zur deutung der molekelspektren. ii. *Zeitschrift für Physik*, 42(2):93–120, 1927.

[84] Robert S Mulliken. The assignment of quantum numbers for electrons in molecules. i. *Physical Review*, 32(2):186, 1928.

[85] KFu Bonhoeffer and Paul Harteck. Über para-und orthowasserstoff. *Zeitschrift für Physikalische Chemie*, 4(1):113–141, 1929.

[86] Adalbert Farkas, Ladislas Farkas, and P Harteck. Experiments on heavy hydrogen. ii.—the ortho-para conversion. *Proceedings of the Royal Society of London. Series A, Containing Papers of a Mathematical and Physical Character*, 144(852):481–493, 1934.

[87] Ira N Levine, Daryle H Busch, and Harrison Shull. *Quantum chemistry*, volume 6. Pearson Prentice Hall Upper Saddle River, New Jersey, 2009.

[88] George E Schmauch and Alan H Singleton. Technical aspects of ortho-parahydrogen conversion. *Industrial & Engineering Chemistry*, 56(5):20–31, 1964.

[89] Jochen Vogt. *Statistical thermodynamics.* Springer, Cham, 2017.

[90] Guillaume Petitpas, Salvador M Aceves, Manyalibo J Matthews, and James R Smith. Para-h2 to ortho-h2 conversion in a full-scale automotive cryogenic pressurized hydrogen storage up to 345 bar. *International Journal of Hydrogen Energy*, 39(12):6533–6547, 2014.

[91] Jacob W Leachman, Richard T Jacobsen, SG Penoncello, and Eric W Lemmon. Fundamental equations of state for parahydrogen, normal hydrogen, and orthohydrogen. *Journal of Physical and Chemical Reference Data*, 38(3):721–748, 2009.

[92] Guenter Ahlers. Lattice heat capacity of solid hydrogen. *The Journal of Chemical Physics*, 41(1):86–94, 1964.

[93] Jacob W Leachman, Richard T Jacobsen, Eric W Lemmon, Steven G Penoncello, Jacob W Leachman, Richard T Jacobsen, Eric W Lemmon, and Steven G Penoncello. Hydrogen. *Thermodynamic Properties of Cryogenic Fluids*, pages 41–71, 2017.

[94] C Russell Bowers and Daniel P Weitekamp. Transformation of symmetrization order to nuclear-spin magnetization by chemical reaction and nuclear magnetic resonance. *Physical Review Letters*, 57(21):2645, 1986.

[95] C Russell Bowers and Daniel P Weitekamp. Parahydrogen and synthesis allow dramatically enhanced nuclear alignment. *Journal of the American Chemical Society*, 109(18):5541–5542, 1987.

[96] Michael G Pravica and Daniel P Weitekamp. Net nmr alignment by adiabatic transport of parahydrogen addition products to high magnetic field. *Chemical Physics Letters*, 145(4):255–258, 1988.

[97] Ryan E Mewis. Developments and advances concerning the hyperpolarisation technique sabre. *Magnetic Resonance in Chemistry*, 53(10):789–800, 2015.

[98] Ralph W Adams, Juan A Aguilar, Kevin D Atkinson, Michael J Cowley, Paul IP Elliott, Simon B Duckett, Gary GR Green, Iman G Khazal, Joaquín López-Serrano, and David C Williamson. Reversible interactions with para-hydrogen enhance nmr sensitivity by polarization transfer. *Science*, 323(5922):1708–1711, 2009.

[99] Erik T Van Dyke, James Eills, Román Picazo-Frutos, Kirill F Sheberstov, Yinan Hu, Dmitry Budker, and Danila A Barskiy. Relayed hyperpolarization for zero-field nuclear magnetic resonance. *Science advances*, 8(29):eabp9242, 2022.

[100] Peter J Rayner, Ben J Tickner, Wissam Iali, Marianna Fekete, Alastair D Robinson, and Simon B Duckett. Relayed hyperpolarization from para-hydrogen improves the nmr detectability of alcohols. *Chemical Science*, 10(33):7709–7717, 2019.

[101] Roman V Shchepin, Danila A Barskiy, Aaron M Coffey, Thomas Theis, Fan Shi, Warren S Warren, Boyd M Goodson, and Eduard Y Chekmenev. 15n hyperpolarization

of imidazole-15n2 for magnetic resonance ph sensing via sabre-sheath. *ACS sensors*, 1(6):640–644, 2016.

[102] Kevin D Atkinson, Michael J Cowley, Paul IP Elliott, Simon B Duckett, Gary GR Green, Joaquin Lopez-Serrano, and Adrian C Whitwood. Spontaneous transfer of para hydrogen derived spin order to pyridine at low magnetic field. *Journal of the American Chemical Society*, 131(37):13362–13368, 2009.

[103] Andrey N Pravdivtsev, Alexandra V Yurkovskaya, Hans-Martin Vieth, Konstantin L Ivanov, and Robert Kaptein. Level anti-crossings are a key factor for understanding para-hydrogen-induced hyperpolarization in sabre experiments. *ChemPhysChem*, 14(14):3327–3331, 2013.

[104] Bram JA van Weerdenburg, Stefan Glöggler, Nan Eshuis, AHJ Ton Engwerda, Jan MM Smits, René de Gelder, Stephan Appelt, Sybren S Wymenga, Marco Tessari, Martin C Feiters, et al. Ligand effects of nhc–iridium catalysts for signal amplification by reversible exchange (sabre). *Chemical Communications*, 49(67):7388–7390, 2013.

[105] Ralph W Adams, Simon B Duckett, Richard A Green, David C Williamson, and Gary GR Green. A theoretical basis for spontaneous polarization transfer in non-hydrogenative parahydrogen-induced polarization. *The Journal of chemical physics*, 131(19), 2009.

[106] Jacob R Lindale, Shannon L Eriksson, Christian PN Tanner, and Warren S Warren. Infinite-order perturbative treatment for quantum evolution with exchange. *Science advances*, 6(32):eabb6874, 2020.

[107] Jacob R. Lindale, Shannon L. Eriksson, Christian P.N. Tanner, Zijian Zhou, Johannes F.P. Colell, Guannan Zhang, Junu Bae, Eduard Y. Chekmenev, Thomas Theis, and Warren S. Warren. Unveiling coherently driven hyperpolarization dynamics in signal amplification by reversible exchange. *Nature Communications*, 10(1), 2019.

[108] Stephan Knecht and Konstantin L Ivanov. Quantitative quantum mechanical approach to sabre hyperpolarization at high magnetic fields. *The Journal of Chemical Physics*, 150(12), 2019.

[109] Konstantin L Ivanov, Andrey N Pravdivtsev, Alexandra V Yurkovskaya, Hans-Martin Vieth, and Robert Kaptein. The role of level anti-crossings in nuclear spin hyperpolarization. *Progress in nuclear magnetic resonance spectroscopy*, 81:1–36, 2014.

[110] Bogdan A Rodin and Konstantin L Ivanov. Representation of population exchange at level anti-crossings. *Magnetic Resonance*, 1(2):347–365, 2020.

[111] Danila A Barskiy, Aaron M Coffey, Panayiotis Nikolaou, Dmitry M Mikhaylov, Boyd M Goodson, Rosa T Branca, George J Lu, Mikhail G Shapiro, Ville-Veikko Telkki, Vladimir V Zhivonitko, et al. Nmr hyperpolarization techniques of gases. *Chemistry–A European Journal*, 23(4):725–751, 2017.

[112] Andreas B Schmidt, C Russell Bowers, Kai Buckenmaier, Eduard Y Chekmenev, Henri de Maissin, James Eills, Frowin Ellermann, Stefan Gloeggler, Jeremy W Gordon, Stephan Knecht, et al. Instrumentation for hydrogenative parahydrogen-based hyperpolarization techniques. *Analytical chemistry*, 94(1):479–502, 2022.

[113] Grace Russell, Jennifer May, and John T Hancock. An interplay of gases: Oxygen and hydrogen in biological systems. *Oxygen*, 4(1):37–52, 2024.

[114] K Radhakrishnan, PA Ramachandran, PH Brahme, and RV Chaudhari. Solubility of hydrogen in methanol, nitrobenzene, and their mixtures experimental data and correlation. *Journal of Chemical and Engineering Data*, 28(1):1–4, 1983.

[115] Liu, Fumio Takemura, and Akira Yabe. Solubility of hydrogen in liquid methanol and methyl formate at 20 c to 140 c. *Journal of Chemical & Engineering Data*, 41(5):1141–1143, 1996.

[116] Ho A Pray, CE Schweickert, and Bo H Minnich. Solubility of hydrogen, oxygen, nitrogen, and helium in water at elevated temperatures. *Industrial & Engineering Chemistry*, 44(5):1146–1151, 1952.

[117] Erwin Brunner. Solubility of hydrogen in 10 organic solvents at 298.15, 323.15, and 373.15 k. *Journal of chemical and Engineering Data*, 30(3):269–273, 1985.

[118] Wissam Iali, Peter J. Rayner, Adel Alshehri, A. Jonathan Holmes, Amy J. Ruddlesden, and Simon B. Duckett. Direct and indirect hyperpolarisation of amines using: Para hydrogen. *Chemical Science*, 9(15):3677–3684, 2018.

[119] Sören Lehmkuhl, Martin Wiese, Lukas Schubert, Mathias Held, Markus Küppers, Matthias Wessling, and Bernhard Blümich. Continuous hyperpolarization with parahydrogen in a membrane reactor. *Journal of Magnetic Resonance*, 291:8–13, 2018.

[120] Ryan E. Mewis, Kevin D. Atkinson, Michael J. Cowley, Simon B. Duckett, Gary G.R. Green, Richard A. Green, Louise A.R. Highton, David Kilgour, Lyrelle S. Lloyd, Joost A.B. Lohman, and David C. Williamson. Probing signal amplification by reversible exchange using an NMR flow system. *Magnetic Resonance in Chemistry*, 52(7):358–369, 2014.

[121] Vladimir V. Zhivonitko, Ivan V. Skovpin, and Igor V. Koptyug. Strong 31P nuclear spin hyperpolarization produced via reversible chemical interaction with parahydrogen. *Chemical Communications*, 51(13):2506–2509, 2015.

[122] Max E. Gemeinhardt, Miranda N. Limbach, Thomas R. Gebhardt, Clark W. Eriksson, Shannon L. Eriksson, Jacob R. Lindale, Elysia A. Goodson, Warren S. Warren, Eduard Y. Chekmenev, and Boyd M. Goodson. "Direct" 13C Hyperpolarization of 13C-Acetate by MicroTesla NMR Signal Amplification by Reversible Exchange (SABRE). *Angewandte Chemie - International Edition*, 59(1):418–423, 2020.

[123] L. Buljubasich, M. B. Franzoni, H. W. Spiess, and K. Münnemann. Level anti-crossings in ParaHydrogen Induced Polarization experiments with Cs-symmetric molecules. *Journal of Magnetic Resonance*, 219:33–40, 2012.

[124] Ryan E Mewis, Richard A Green, Martin CR Cockett, Michael J Cowley, Simon B Duckett, Gary GR Green, Richard O John, Peter J Rayner, and David C Williamson. Strategies for the hyperpolarization of acetonitrile and related ligands by sabre. *The Journal of Physical Chemistry B*, 119(4):1416–1424, 2015.

[125] Oksana Bondar, Eleonora Cavallari, Carla Carrera, Silvio Aime, and Francesca Reineri. Effect of the hydrogenation solvent in the phip-sah hyperpolarization of [1-13c] pyruvate. *Catalysis Today*, 397:94–102, 2022.

[126] Anton Duchowny, Johannes Denninger, Lars Lohmann, Thomas Theis, Sören Lehmkuhl, and Alina Adams. Sabre hyperpolarization with up to 200 bar parahydrogen in standard and quickly removable solvents. *International Journal of Molecular Sciences*, 24(3):2465, 2023.

[127] Alexey S Kiryutin, Grit Sauer, Sara Hadjiali, Alexandra V Yurkovskaya, Hergen Breitzke, and Gerd Buntkowsky. A highly versatile automatized setup for quantitative measurements of phip enhancements. *Journal of Magnetic Resonance*, 285:26–36, 2017.

[128] Isaiah Adelabu, Md Raduanul H Chowdhury, Shiraz Nantogma, Clementinah Oladun, Firoz Ahmed, Lukas Stilgenbauer, Marianna Sadagurski, Thomas Theis, Boyd M Goodson, and Eduard Y Chekmenev. Efficient sabre-sheath hyperpolarization of potent branched-chain-amino-acid metabolic probe [1-13c] ketoisocaproate. *Metabolites*, 13(2):200, 2023.

[129] Piotr Put, Seyma Alcicek, Oksana Bondar, Łukasz Bodek, Simon Duckett, and Szymon Pustelny. Detection of pyridine derivatives by sabre hyperpolarization at zero field. *Communications Chemistry*, 6(1):131, 2023.

[130] Fraser Hill-Casey, Aminata Sakho, Ahmed Mohammed, Matheus Rossetto, Fadi Ahwal, Simon B Duckett, Richard O John, Peter M Richardson, Robin Virgo, and Meghan E Halse. In situ sabre hyperpolarization with earth's field nmr detection. *Molecules*, 24(22):4126, 2019.

[131] Michael J. Cowley, Ralph W. Adams, Kevin D. Atkinson, Martin C.R. Cockett, Simon B. Duckett, Gary G.R. Green, Joost A.B. Lohman, Rainer Kerssebaum, David Kilgour, and Ryan E. Mewis. Iridium N-heterocyclic carbene complexes as efficient catalysts for magnetization transfer from para -hydrogen. *Journal of the American Chemical Society*, 133(16):6134–6137, 2011.

[132] Peter M Richardson, Andrew J Parrott, Olga Semenova, Alison Nordon, Simon B Duckett, and Meghan E Halse. Sabre hyperpolarization enables high-sensitivity 1 h and 13 c benchtop nmr spectroscopy. *Analyst*, 143(14):3442–3450, 2018.

[133] Elizabeth J Fear, Aneurin J Kennerley, Peter J Rayner, Philip Norcott, Soumya S Roy, and Simon B Duckett. Sabre hyperpolarized anticancer agents for use in 1h mri. *Magnetic Resonance in Medicine*, 88(1):11–27, 2022.

[134] Song-I Han, Sandra Garcia, Thomas J Lowery, E Janette Ruiz, Juliette A Seeley, Lana Chavez, David S King, David E Wemmer, and Alexander Pines. Nmr-based biosensing with optimized delivery of polarized 129xe to solutions. *Analytical chemistry*, 77(13):4008–4012, 2005.

[135] Volker Hessel, Panagiota Angeli, Asterios Gavriilidis, and Holger Löwe. Gas- liquid and gas- liquid- solid microstructured reactors: contacting principles and applications. *Industrial & engineering chemistry research*, 44(25):9750–9769, 2005.

[136] MH Siegel and CW Robinson. Application of airlift gas-liquid-solid reactors in biotechnology. *Chemical Engineering Science*, 47(13-14):3215–3229, 1992.

[137] Martin Brzozowski, Matthew O'Brien, Steven V Ley, and Anastasios Polyzos. Flow chemistry: intelligent processing of gas–liquid transformations using a tube-in-tube reactor. *Accounts of chemical research*, 48(2):349–362, 2015.

[138] Hanna Kierzkowska-Pawlak. Determination of kinetics in gas-liquid reaction systems. an overview. *Ecological Chemistry and Engineering S*, 19(2):175–196, 2012.

[139] Valentin Flores-Payan, Enrique J Herrera-Lopez, Javier Navarro-Laboulais, and Alberto Lopez-Lopez. Parametric sensitivity analysis and ozone mass transfer modeling in a gas–liquid reactor for advanced water treatment. *Journal of industrial and engineering chemistry*, 21:1270–1276, 2015.

[140] VY Dindore, Derk Willem Frederik Brilman, FH Geuzebroek, and GF Versteeg. Membrane–solvent selection for co2 removal using membrane gas–liquid contactors. *Separation and Purification Technology*, 40(2):133–145, 2004.

[141] Stepan D Bazhenov, Alexandr V Bildyukevich, and Alexey V Volkov. Gas-liquid hollow fiber membrane contactors for different applications. *Fibers*, 6(4):76, 2018.

[142] AP Korikov and KK Sirkar. Membrane gas permeance in gas–liquid membrane contactor systems for solutions containing a highly reactive absorbent. *Journal of membrane science*, 246(1):27–37, 2005.

[143] Yilin Xu, Kunli Goh, Rong Wang, and Tae-Hyun Bae. A review on polymer-based membranes for gas-liquid membrane contacting processes: Current challenges and future direction. *Separation and Purification Technology*, 229:115791, 2019.

[144] Meike Roth, Petra Kindervater, Hans Peter Raich, Joachim Bargon, Hans W. Spiess, and Kerstin Münnemann. Continuous 1H and 13C signal enhancement in NMR spectroscopy and MRI using parahydrogen and hollow-fiber membranes. *Angewandte Chemie - International Edition*, 49(45):8358–8362, 2010.

[145] Sören Lehmkuhl, Martin Wiese, Lukas Schubert, Mathias Held, Markus Küppers, Matthias Wessling, and Bernhard Blümich. Continuous hyperpolarization with parahydrogen in a membrane reactor. *Journal of Magnetic Resonance*, 291:8–13, 2018.

[146] James Eills, William Hale, Manvendra Sharma, Matheus Rossetto, Malcolm H. Levitt, and Marcel Utz. High-Resolution Nuclear Magnetic Resonance Spectroscopy with Picomole Sensitivity by Hyperpolarization on a Chip. *Journal of the American Chemical Society*, 141(25):9955–9963, 2019.

[147] Lorenzo Bordonali, Nurdiana Nordin, Erwin Fuhrer, Neil Mackinnon, and Jan G. Korvink. Parahydrogen based NMR hyperpolarisation goes micro: An alveolus for small molecule chemosensing. *Lab on a Chip*, 19(3):503–512, 2019.

[148] Patrick TomHon, Suyong Han, Sören Lehmkuhl, Stephan Appelt, Eduard Y Chekmenev, Milad Abolhasani, and Thomas Theis. A Versatile Compact Parahydrogen Membrane Reactor. *ChemPhysChem*, sep 2021.

[149] Lu Yang and Klavs F Jensen. Mass transport and reactions in the tube-in-tube reactor. *Organic Process Research & Development*, 17(6):927–933, 2013.

[150] Gaowei Wu, Enhong Cao, Simon Kuhn, and Asterios Gavriilidis. A novel approach for measuring gas solubility in liquids using a tube-in-tube membrane contactor. *Chemical Engineering & Technology*, 40(12):2346–2350, 2017.

[151] Haocui Zhang, Guangwen Chen, Jun Yue, and Quan Yuan. Hydrodynamics and mass transfer of gas–liquid flow in a falling film microreactor. *AIChE Journal*, 55(5):1110–1120, 2009.

[152] David Lokhat, Ashveer Krishen Domah, Kuveshan Padayachee, Aman Baboolal, and Deresh Ramjugernath. Gas–liquid mass transfer in a falling film microreactor: Effect of reactor orientation on liquid-side mass transfer coefficient. *Chemical Engineering Science*, 155:38–44, 2016.

[153] Jigar M Jani, Matthias Wessling, and Rob GH Lammertink. A microgrooved membrane based gas–liquid contactor. *Microfluidics and nanofluidics*, 13:499–509, 2012.

[154] Raminder Kaur, M Ramakrishna, and KDP Nigam. Role of dispersed phase in gas-liquid reactions: A review. *Reviews in Chemical Engineering*, 23(3-4):247–300, 2007.

[155] Zheyu Liu, Maojie Chai, Xin Chen, Seyed Hossein Hejazi, and Yiqiang Li. Emulsification in a microfluidic flow-focusing device: Effect of the dispersed phase viscosity. *Fuel*, 283:119229, 2021.

[156] Guan Heng Yeoh, Chi Pok Cheung, and Jiyuan Tu. *Multiphase flow analysis using population balance modeling: bubbles, drops and particles.* Butterworth-Heinemann, 2013.

[157] Ram Wasudeo Sabnis. *Handbook of biological dyes and stains: synthesis and industrial applications*. John Wiley & Sons, Hoboken, New Jersey, 2010.

[158] Pin-Chuan Chen and Lynh Huyen Duong. Novel solvent bonding method for thermoplastic microfluidic chips. *Sensors and Actuators B: Chemical*, 237:556–562, 2016.

[159] Alwin MD Wan, Thomas A Moore, and Edmond WK Young. Solvent bonding for fabrication of pmma and cop microfluidic devices. *Journal of Visualized Experiments: JoVE*, (119):55175, 2017.

[160] K Kneifel, S Nowak, W Albrecht, R Hilke, R Just, and K-V Peinemann. Hollow fiber membrane contactor for air humidity control: Modules and membranes. *Journal of membrane science*, 276(1-2):241–251, 2006.

[161] Stewart Farling, Tobias L Straube, Travis P Vesel, Nick Bottenus, Bruce Klitzman, Ira M Cheifetz, and Marc A Deshusses. Development of a novel intravascular oxygenator catheter: Oxygen mass transfer properties across nonporous hollow fiber membranes. *Biotechnology and bioengineering*, 118(1):345–356, 2021.

[162] Christoph Wolff, Sascha Beutel, and Thomas Scheper. Tubular membrane bioreactors for biotechnological processes. *Applied microbiology and biotechnology*, 97(3):929–937, 2013.

[163] Biogeneral. https://www.biogeneral.com/teflon-af/.

[164] Paul R Resnick and Warren H Buck. Teflon® af: A family of amorphous fluoropolymers with extraordinary properties. In *Fluoropolymers 2: Properties*, pages 25–33. Springer, Boston, MA, 2002.

[165] Brian Murphy and Peter Mcloughlin. Determination of chlorinated hydrocarbon species in aqueous solution using teflon coated atr waveguide/ftir spectroscopy. *International Journal of Environmental & Analytical Chemistry*, 83(7-8):653–662, 2003.

[166] Arindom Datta, In-Yong Eom, Achintya Dhar, Petr Kuban, Rosalynn Manor, Iftikhar Ahmad, Shubhra Gangopadhyay, Tim Dallas, Mark Holtz, Henryk Temkin, et al. Microfabrication and characterization of teflon af-coated liquid core waveguide channels in silicon. *IEEE Sensors Journal*, 3(6):788–795, 2003.

[167] Ka A Triplett, SM Ghiaasiaan, SI Abdel-Khalik, and DL Sadowski. Gas–liquid two-phase flow in microchannels part i: two-phase flow patterns. *International Journal of Multiphase Flow*, 25(3):377–394, 1999.

[168] Toru Sawai, M Kaji, T Kasugai, H Nakashima, and T Mori. Gas–liquid interfacial structure and pressure drop characteristics of churn flow. *Experimental thermal and fluid science*, 28(6):597–606, 2004.

[169] Andrea Cioncolini and John R Thome. Prediction of the entrained liquid fraction in vertical annular gas–liquid two-phase flow. *International Journal of Multiphase Flow*, 36(4):293–302, 2010.

[170] Geoffrey F Hewitt. Churn and wispy annular flow regimes in vertical gas–liquid flows. *Energy & fuels*, 26(7):4067–4077, 2012.

[171] Malcolm H Levitt. *Spin dynamics: basics of nuclear magnetic resonance*. John Wiley & Sons, Chichester, 2013.

[172] Steven M Wright and Lawrence L Wald. Theory and application of array coils in mr spectroscopy. *NMR in Biomedicine: An International Journal Devoted to the Development and Application of Magnetic Resonance In Vivo*, 10(8):394–410, 1997.

[173] Michael A Ohliger and Daniel K Sodickson. An introduction to coil array design for parallel mri. *NMR in Biomedicine: An International Journal Devoted to the Development and Application of Magnetic Resonance In vivo*, 19(3):300–315, 2006.

[174] Ka-Meng Lei, Dongwan Ha, Yi-Qiao Song, Robert M Westervelt, Rui Martins, Pui-In Mak, and Donhee Ham. Portable nmr with parallelism. *Analytical chemistry*, 92(2):2112–2120, 2020.

[175] Ēriks Kupče, Kaustubh R Mote, Andrew Webb, Perunthiruthy K Madhu, and Tim DW Claridge. Multiplexing experiments in nmr and multi-nuclear mri. *Progress in Nuclear Magnetic Resonance Spectroscopy*, 124:1–56, 2021.

[176] Yen-Tse Cheng, Mazin Jouda, and Jan Korvink. Sample-centred shimming enables independent parallel nmr detection. *Scientific Reports*, 12(1):14149, 2022.

[177] Meghan E Halse. Perspectives for hyperpolarisation in compact nmr. *TrAC Trends in Analytical Chemistry*, 83:76–83, 2016.

[178] DM Ginsberg and Melvin J Melchner. Optimum geometry of saddle shaped coils for generating a uniform magnetic field. *Review of Scientific Instruments*, 41(1):122–123, 1970.

[179] Haifeng Zeng, Jiadi Xu, Joseph Gillen, Michael T McMahon, Dmitri Artemov, Jean-Max Tyburn, Joost AB Lohman, Ryan E Mewis, Kevin D Atkinson, Gary GR Green, et al. Optimization of SABRE for polarization of the tuberculosis drugs pyrazinamide and isoniazid. *Journal of magnetic resonance*, 237:73–78, 2013.

[180] Marc A. Shampo, Robert A. Kyle, and David P. Steensma. Nikolay basov—nobel prize for lasers and masers. *Mayo Clinic Proceedings*, 87(1):e3, 2012.

[181] Arthur L Schawlow and Charles H Townes. Infrared and optical masers. *Physical review*, 112(6):1940, 1958.

[182] Theodore H Maiman. Stimulated optical radiation in ruby. *Nature*, 112(1736):493–494, 1960.

[183] Colin E Webb and Julian DC Jones. *Handbook of Laser Technology and Applications: Laser design and laser systems*, volume 2. CRC Press, Boca Raton, FL, 2004.

[184] James Eills, William Hale, Manvendra Sharma, Matheus Rossetto, Malcolm H Levitt, and Marcel Utz. High-resolution nuclear magnetic resonance spectroscopy with picomole sensitivity by hyperpolarization on a chip. *Journal of the American Chemical Society*, 141(25):9955–9963, 2019.

[185] C Breck Hitz, James J Ewing, and Jeff Hecht. *Introduction to laser technology*. John Wiley & Sons, Hoboken, New Jersey, 2012.

[186] Stephan Appelt, A Kentner, S Lehmkuhl, and B Blümich. From laser physics to the para-hydrogen pumped raser. *Progress in nuclear magnetic resonance spectroscopy*, 114:1–32, 2019.

[187] Sergey Korchak, Lukas Kaltschnee, Riza Dervisoglu, Loren Andreas, Christian Griesinger, and Stefan Glöggler. Spontaneous enhancement of magnetic resonance signals using a raser. *Angewandte Chemie*, 133(38):21152–21158, 2021.

[188] Michael A Hope, Snaedis Bjorgvinsdottir, Clare P Grey, and Lyndon Emsley. A magic angle spinning activated 17o dnp raser. *The Journal of Physical Chemistry Letters*, 12(1):345–349, 2020.

[189] Stephan Appelt, Sören Lehmkuhl, Simon Fleischer, Baptiste Joalland, Nuwandi M Ariyasingha, Eduard Y Chekmenev, and Thomas Theis. Sabre and phip pumped raser and the route to chaos. *Journal of Magnetic Resonance*, 322:106815, 2021.

[190] Ute Goerke, Michael Garwood, and Kamil Ugurbil. Functional magnetic resonance imaging using raser. *Neuroimage*, 54(1):350–360, 2011.

[191] N Bloembergen and RV Pound. Radiation damping in magnetic resonance experiments. *Physical Review*, 95(1):8, 1954.

[192] Stanley Bloom. Effects of radiation damping on spin dynamics. *Journal of Applied Physics*, 28(7):800–805, 1957.

[193] Viswanathan V Krishnan and Nagarajan Murali. Radiation damping in modern nmr experiments: Progress and challenges. *Progress in nuclear magnetic resonance spectroscopy*, 68:41–57, 2013.

[194] Martin Suefke, Sören Lehmkuhl, Alexander Liebisch, Bernhard Blümich, and Stephan Appelt. Para-hydrogen raser delivers sub-millihertz resolution in nuclear magnetic resonance. *Nature physics*, 13(6):568–572, 2017.

[195] Oleg G Salnikov, Ivan A Trofimov, Andrey N Pravdivtsev, Kolja Them, Jan-Bernd Hoevener, Eduard Y Chekmenev, and Igor V Koptyug. Through-space multinuclear magnetic resonance signal enhancement induced by parahydrogen and radiofrequency amplification by stimulated emission of radiation. *Analytical chemistry*, 94(43):15010–15017, 2022.

[196] Emmanuelle MM Weber, Dennis Kurzbach, and Daniel Abergel. A dnp-hyperpolarized solid-state water nmr maser: observation and qualitative analysis. *Physical Chemistry Chemical Physics*, 21(38):21278–21286, 2019.

[197] P Bösiger, E Brun, and D Meier. Solid-state nuclear spin-flip maser pumped by dynamic nuclear polarization. *Physical Review Letters*, 38(11):602, 1977.

[198] Quentin Stern, Quentin Reynard-Feytis, Stuart J Elliott, Morgan Ceillier, Olivier Cala, Konstantin Ivanov, and Sami Jannin. Rapid and simple 13c-hyperpolarization by 1h dissolution dynamic nuclear polarization followed by an inline magnetic field inversion. *Journal of the American Chemical Society*, 145(50):27576–27586, 2023.

[199] TE Chupp, RJ Hoare, RL Walsworth, and Bo Wu. Spin-exchange-pumped he 3 and xe 129 zeeman masers. *Physical review letters*, 72(15):2363, 1994.

[200] Thad G Walker and William Happer. Spin-exchange optical pumping of noble-gas nuclei. *Reviews of modern physics*, 69(2):629, 1997.

[201] Arthur C Pinon, Andrea Capozzi, and Jan Henrik Ardenkjær-Larsen. Hyperpolarization via dissolution dynamic nuclear polarization: new technological and methodological advances. *Magnetic Resonance Materials in Physics, Biology and Medicine*, 34:5–23, 2021.

[202] Jonathan R Birchall, Panayiotis Nikolaou, Aaron M Coffey, Bryce E Kidd, Megan Murphy, Michael Molway, Liana B Bales, Boyd M Goodson, Robert K Irwin, Michael J Barlow, et al. Batch-mode clinical-scale optical hyperpolarization of xenon-129 using an aluminum jacket with rapid temperature ramping. *Analytical chemistry*, 92(6):4309–4316, 2020.

[203] Christopher Nelson, Andreas B. Schmidt, Isaiah Adelabu, Shiraz Nantogma, Valerij G. Kiselev, Abubakar Abdurraheem, Henri de Maissin, Sören Lehmkuhl, Stephan Appelt, Thomas Theis, and Eduard Y. Chekmenev. Parahydrogen-induced carbon-13 radiofrequency amplification by stimulated emission of radiation. *Angewandte Chemie International Edition*, 62(5):e202215678, 2023.

[204] Baptiste Joalland, Nuwandi M Ariyasingha, Sören Lehmkuhl, Thomas Theis, Stephan Appelt, and Eduard Y Chekmenev. Parahydrogen-induced radio amplification by stimulated emission of radiation. *Angewandte Chemie*, 132(22):8732–8738, 2020.

[205] Baptiste Joalland, Thomas Theis, Stephan Appelt, and Eduard Y Chekmenev. Background-free proton nmr spectroscopy with radiofrequency amplification by stimulated emission radiation. *Angewandte Chemie International Edition*, 60(50):26298–26302, 2021.

[206] Andrey N Pravdivtsev, Frank D Sönnichsen, and Jan-Bernd Hövener. Continuous radio amplification by stimulated emission of radiation using parahydrogen induced polarization (phip-raser) at 14 tesla. *ChemPhysChem*, 21(7):667–672, 2020.

[207] Sören Lehmkuhl, Simon Fleischer, Lars Lohmann, Matthew S Rosen, Eduard Y Chekmenev, Alina Adams, Thomas Theis, and Stephan Appelt. Raser mri: Magnetic resonance images formed spontaneously exploiting cooperative nonlinear interaction. *Science Advances*, 8(28):eabp8483, 2022.

[208] Lorenzo Bordonali, Nurdiana Nordin, Erwin Fuhrer, Neil MacKinnon, and Jan G Korvink. Parahydrogen based nmr hyperpolarisation goes micro: an alveolus for small molecule chemosensing. *Lab on a Chip*, 19(3):503–512, 2019.

[209] Patrick M TomHon, Suyong Han, Sören Lehmkuhl, Stephan Appelt, Eduard Y Chekmenev, Milad Abolhasani, and Thomas Theis. A versatile compact parahydrogen membrane reactor. *ChemPhysChem*, 22(24):2526–2534, 2021.

[210] William G Hale, Tommy Y Zhao, Diana Choi, Maria-Jose Ferrer, Bochuan Song, Hanqin Zhao, Helena E Hagelin-Weaver, and Clifford R Bowers. Toward continuous-flow hyperpolarisation of metabolites via heterogenous catalysis, side-arm-hydrogenation, and membrane dissolution of parahydrogen. *ChemPhysChem*, 22(9):822–827, 2021.

[211] Mitchell J Feigenbaum. Quantitative universality for a class of nonlinear transformations. *Journal of statistical physics*, 19(1):25–52, 1978.

[212] A Yu Okulov and AN Oraevsky. Space–temporal behavior of a light pulse propagating in a nonlinear nondispersive medium. *JOSA B*, 3(5):741–746, 1986.

[213] Rasika B Naik and Udayprakash Singh. A review on applications of chaotic maps in pseudo-random number generators and encryption. *Annals of Data Science*, 11(1):25–50, 2024.

[214] Nicolaas Bloembergen and PS Pershan. Light waves at the boundary of nonlinear media. *Physical review*, 128(2):606, 1962.

[215] Alain Vlassenbroek, Jean Jeener, and Paul Broekaert. Radiation damping in high resolution liquid nmr: A simulation study. *The Journal of chemical physics*, 103(14):5886–5897, 1995.

[216] Herve Desvaux. Non-linear liquid-state nmr. *Progress in Nuclear Magnetic Resonance Spectroscopy*, 70:50–71, 2013.

[217] Ben J Tickner, Olga Semenova, Wissam Iali, Peter J Rayner, Adrian C Whitwood, and Simon B Duckett. Optimisation of pyruvate hyperpolarisation using sabre by tuning the active magnetisation transfer catalyst. *Catalysis science & technology*, 10(5):1343–1355, 2020.

[218] Alexandra M Olaru, Thomas BR Robertson, Jennifer S Lewis, Alex Antony, Wissam Iali, Ryan E Mewis, and Simon B Duckett. Extending the scope of 19f hyperpolarization through signal amplification by reversible exchange in mri and nmr spectroscopy. *ChemistryOpen*, 7(1):97–105, 2018.

[219] Ryan E Mewis, Kevin D Atkinson, Michael J Cowley, Simon B Duckett, Gary GR Green, Richard A Green, Louise AR Highton, David Kilgour, Lyrelle S Lloyd, Joost AB Lohman, et al. Probing signal amplification by reversible exchange using an nmr flow system. *Magnetic Resonance in Chemistry*, 52(7):358–369, 2014.

[220] Jing Yang, Peng Wang, Jan G Korvink, Jürgen J. Brandner, and Sören Lehmkuhl. The steady-state altadena raser generates continuous nmr signals. *ChemPhysChem*, 24(14):e202300204, 2023.

[221] Patrick TomHon, Evan Akeroyd, Sören Lehmkuhl, Eduard Y Chekmenev, and Thomas Theis. Automated pneumatic shuttle for magnetic field cycling and parahydrogen hyperpolarized multidimensional nmr. *Journal of Magnetic Resonance*, 312:106700, 2020.

[222] Johannes FP Colell, Meike Emondts, Angus WJ Logan, Kun Shen, Junu Bae, Roman V Shchepin, Gerardo X Ortiz Jr, Peter Spannring, Qiu Wang, Steven J Malcolmson, et al. Direct hyperpolarization of nitrogen-15 in aqueous media with parahydrogen in reversible exchange. *Journal of the American Chemical Society*, 139(23):7761–7767, 2017.

[223] Seyma Alcicek, Erik Van Dyke, Jingyan Xu, Szymon Pustelny, and Danila A Barskiy. 13c and 15n benchtop nmr detection of metabolites via relayed hyperpolarization. *Chemistry-Methods*, 3(7):e202200075, 2023.

[224] Frowin Ellermann, Philip Saul, Jan-Bernd Hoevener, and Andrey N Pravdivtsev. Modern manufacturing enables magnetic field cycling experiments and parahydrogen-induced hyperpolarization with a benchtop nmr. *Analytical Chemistry*, 95(15):6244–6252, 2023.

[225] Keilian MacCulloch, Patrick Tomhon, Austin Browning, Evan Akeroyd, Sören Lehmkuhl, Eduard Y Chekmenev, and Thomas Theis. Hyperpolarization of common antifungal agents with sabre. *Magnetic Resonance in Chemistry*, 59(12):1225–1235, 2021.

[226] Thomas BR Robertson, Lysbeth H Antonides, Nicolas Gilbert, Sophie L Benjamin, Stuart K Langley, Lindsey J Munro, Oliver B Sutcliffe, and Ryan E Mewis. Hyperpo-

larization of pyridyl fentalogues by signal amplification by reversible exchange (sabre). *ChemistryOpen*, 8(12):1375–1382, 2019.

[227] Isaiah Adelabu, Patrick TomHon, Mohammad SH Kabir, Shiraz Nantogma, Mustapha Abdulmojeed, Iuliia Mandzhieva, Jessica Ettedgui, Rolf E Swenson, Murali C Krishna, Thomas Theis, et al. Order-unity 13c nuclear polarization of [1-13c] pyruvate in seconds and the interplay of water and sabre enhancement. *ChemPhysChem*, 23(2):e202100839, 2022.

[228] Nikita V Chukanov, Roman V Shchepin, Sameer M Joshi, Mohammad SH Kabir, Oleg G Salnikov, Alexandra Svyatova, Igor V Koptyug, Juri G Gelovani, and Eduard Y Chekmenev. Synthetic approaches for 15n-labeled hyperpolarized heterocyclic molecular imaging agents for 15n nmr signal amplification by reversible exchange in microtesla magnetic fields. *Chemistry–A European Journal*, 27(38):9727–9736, 2021.

[229] Christian PN Tanner, Jacob R Lindale, Shannon L Eriksson, Zijian Zhou, Johannes FP Colell, Thomas Theis, and Warren S Warren. Selective hyperpolarization of heteronuclear singlet states via pulsed microtesla sabre. *The Journal of Chemical Physics*, 151(4), 2019.

[230] Shannon L Eriksson, Jacob R Lindale, Xiaoqing Li, and Warren S Warren. Improving sabre hyperpolarization with highly nonintuitive pulse sequences: Moving beyond avoided crossings to describe dynamics. *Science Advances*, 8(11):eabl3708, 2022.

[231] Xiaoqing Li, Jacob R Lindale, Shannon L Eriksson, and Warren S Warren. Sabre enhancement with oscillating pulse sequences. *Physical Chemistry Chemical Physics*, 24(27):16462–16470, 2022.

[232] Marian K Kazimierczuk. Transfer function of current modulator in pwm converters with current-mode control. *IEEE Transactions on Circuits and Systems I: Fundamental Theory and Applications*, 47(9):1407–1412, 2000.

[233] Andreia Faria, Luís Marques, Carlos Ferreira, Filipe Alves, and Jorge Cabral. A fast and precise tool for multi-layer planar coil self-inductance calculation. *Sensors*, 21(14):4864, 2021.

[234] Christian Peters and Yiannos Manoli. Inductance calculation of planar multi-layer and multi-wire coils: An analytical approach. *Sensors and Actuators A: Physical*, 145:394–404, 2008.

[235] Wenshen Zhou and Shaoying Huang. An accurate model for fast calculating the resonant frequency of an irregular solenoid. *IEEE Transactions on Microwave Theory and Techniques*, 67(7):2663–2673, 2019.

[236] HA Aebischer. Inductance formula for rectangular planar spiral inductors with rectangular conductor cross section. *Advanced electromagnetics*, 9(1):1–18, 2020.

[237] Yas Hosseini Tehrani and Seyed Mojtaba Atarodi. An efficient solution to measure inductance on-the-fly. *Measurement*, 223:113670, 2023.

[238] Se-Yuen Mak. Six ways to measure inductance. *Physics education*, 37(5):439, 2002.

[239] Ameya Wagh, Nilay Sheth, and Jonathon Joshi. Implementation of mosfets in a closed loop h-bridge motor driver using charge pumps. In *2015 Annual IEEE India Conference (INDICON)*, pages 1–5. IEEE, 2015.

[240] Andreas Brinkmann. Introduction to average hamiltonian theory. i. basics. *Concepts in Magnetic Resonance Part A*, 45(6):e21414, 2016.

[241] Jacob R Lindale. *Understanding and Optimizing Dynamics in Hyperpolarized Magnetic Resonance*. PhD thesis, Duke University, Durham, North Carolina, 2021.

[242] Keilian MacCulloch, Austin Browning, David O Guarin Bedoya, Stephen J McBride, Mustapha B Abdulmojeed, Carlos Dedesma, Boyd M Goodson, Matthew S Rosen, Eduard Y Chekmenev, Yi-Fen Yen, et al. Facile hyperpolarization chemistry for molecular imaging and metabolic tracking of [1–13c] pyruvate in vivo. *Journal of magnetic resonance open*, 16:100129, 2023.

[243] Shiraz Nantogma, Shannon L Eriksson, Isaiah Adelabu, Iuliia Mandzhieva, Austin Browning, Patrick TomHon, Warren S Warren, Thomas Theis, Boyd M Goodson, and Eduard Y Chekmenev. Interplay of near-zero-field dephasing, rephasing, and relaxation dynamics and [1-13c] pyruvate polarization transfer efficiency in pulsed sabre-sheath. *The Journal of Physical Chemistry A*, 126(48):9114–9123, 2022.

[244] Danila A Barskiy, Stephan Knecht, Alexandra V Yurkovskaya, and Konstantin L Ivanov. Sabre: Chemical kinetics and spin dynamics of the formation of hyperpolarization. *Progress in Nuclear Magnetic Resonance Spectroscopy*, 114:33–70, 2019.

[245] N Chattergoon, F Martínez-Santiesteban, WB Handler, Jan Henrik Ardenkjær-Larsen, and TJ Scholl. Field dependence of t1 for hyperpolarized [1-13c] pyruvate. *Contrast media & molecular imaging*, 8(1):57–62, 2013.

[246] Andreas B Schmidt, James Eills, Laurynas Dagys, Martin Gierse, Michael Keim, Sebastian Lucas, Michael Bock, Ilai Schwartz, Maxim Zaitsev, Eduard Y Chekmenev, et al. Over 20% carbon-13 polarization of perdeuterated pyruvate using reversible exchange with parahydrogen and spin-lock induced crossing at 50 μt. *The Journal of Physical Chemistry Letters*, 14(23):5305–5309, 2023.

Publications

Journal articles

Published

[JY01] Julia Schulte-Hermann, **Jing Yang**, Andrea C Hurtado Rivera, Jan G Korvink, Neil MacKinnon, and Jürgen J Brandner. Integrating micro process chemistry into an nmr spectrometer. *Chemie Ingenieur Technik*, 96(3):257–278, 2024.

[JY02] **Jing Yang**, Peng Wang, Jan G Korvink, Jürgen J Brandner, and Sören Lehmkuhl. The steady-state altadena raser generates continuous nmr signals. *ChemPhysChem*, 24(14):e202300204, 2023.
(This paper has being featured on the cover of the Journal.)

[JY03] **Jing Yang**, Ruodong Xin, Sören Lehmkuhl, Jan G Korvink, and Jürgen J Brandner. Development of a fully automated workstation for conducting routine sabre hyperpolarization. *Scientific Reports*, 14(1):21022, 2024.

Submitted

[JY04] **Jing Yang***, Yen-Tse Cheng*, Sören Lehmkuhl, Jürgen J Brandner, Mazin Jourda, and Jan G Korvink. Accelerating nmr spectroscopy via parallel sabre in a continuous-flow system. *Review of Scientific Instruments*.
(*These authors contributed equally)

In preparation

[JY05] Julia Schulte-Hermann, **Jing Yang**, Hagen Rießland, Camilla Stolle, Kersten Rabe, Sören Lehmkuhl, Jan G Korvink, Neil MacKinnon. Advancing towards bacteria metabolism monitoring through signal amplification by reversible exchange.

[JY06] Georges Saliba, **Jing Yang**, Jürgen J Brandner, Jan G Korvink. Falling film microreactors for sabre.

[JY07] Sören Lehmkuhl, Simon Fleischer, **Jing Yang**, Eduard Y Chekmenev, Thomas Theis, Stephan Appelt, Jan G Korvink, Mazin Jouda. RASER allows for rapid image acquisition without external radiofrequency excitation.

Conference contributions

[JY08] **Jing Yang**, Peng Wang, Jan G Korvink, Jürgen J Brandner, and Sören Lehmkuhl. Continuous flow phip-raser allows for study of nonlinear phenomena. *The 19th European Magnetic Resonance Congress (EUROMAR 2023)*.
(Poster and flash talk)

[JY09] **Jing Yang**, Peng Wang, Jan G Korvink, Jürgen J Brandner, and Sören Lehmkuhl. The steady-state pihp-raser: Generating a continuous nmr signal. *Quantitative NMR Methods for Reaction and Process Monitoring (NMRPM 2023)*.
(Poster)

[JY10] **Jing Yang**, Ruodong Xin, Sören Lehmkuhl, Jan G Korvink, and Jürgen J Brandner. Automatically hyperpolarizing [1-13c] pyruvate and other substrates through sabre on benchtop nmr. *The Kyoto Winter School (2024), "Towards Holistic Understanding of Life"* .
(Poster and flash talk)

[JY11] **Jing Yang**, Peng Wang, Jan G Korvink, Jürgen J Brandner, and Sören Lehmkuhl. A flow system based on gas-liquid reactor for precise detection of the nmr parameters with nmr hyperpolarization. *The 16th International Conference on Gas–Liquid and Gas–Liquid–Solid Reactor Engineering (GLS-16 2024).*
(Oral presentation)

[JY12] Sören Lehmkuhl, **Jing Yang**, Simon Fleischer, Eduard Y. Chekmenev, Thomas Theis, Stephan Appelt, Mazin Jouda and Jan G. Korvink. The raser approach: exploring self-excitation in nmr and mri. *Experimental Nuclear Magnetic Resonance Conference and the International Society of Magnetic Resonance (ENC-ISMAR 2025).*
(Oral presentation)

Acknowledgements

First and foremost, I would like to express my heartfelt gratitude to my supervisor, Prof. Jan Gerrit Korvink, for his constant guidance and invaluable mentorship throughout my PhD journey. His profound expertise and extensive experience have greatly inspired my academic career, sparking my curiosity and fostering a spirit of exploration in my research endeavors.

Secondly, I would like to express my deep gratitude to my group leader, Prof. Jürgen Brandner, for your encouragement and for providing me with a supportive and open research environment. Throughout my PhD journey, I have always felt incredibly fortunate and grateful to be part of this group.

In the same manner, I would also like to extend my heartfelt thanks to Dr. Sören Lehmkuhl for his patient guidance and for teaching me so much in field of NMR, hyperpolarization and chemistry. Every discussion and exchange with him has been immensely valuable, as he always provided insightful academic advice.

I would like to sincerely thank my examiner, Prof. Jan-Bernd Hövener, for accepting the invitation to join my examination committee. His work and contributions in the field of hyperpolarization have been an invaluable source of inspiration to me.

I would thank Dr. Neil Mackinnon, whose invaluable guidance and support have been instrumental throughout my academic journey.

I would like to thank to my office colleague Julia Schulte-Hermann and Andrea Hurtado for the wonderful times we shared together. Your companionship and mutual support have left me with many beautiful and cherished memories.

I want to thank my dear friend Jianyi Liang, who is also my colleague. We have known each other since our master's studies, always encouraging each other and providing support in both work and life. This friendship is truly invaluable to me.

At the same time, I feel truly fortunate to conduct research in an environment that is both academically stimulating and warm and welcoming. I am deeply grateful to all my colleagues for their support and kindness. Special thanks to Dr. Vlad Badilita, Dr. Mazin Jouda, Dr. Mehrdad Alinaghian, Dr. Sagar Wadhwa, Yen-Tse Cheng, Mengjia He and Simon Fischer.

I would like to acknowledge the invaluable assistance provided by the master's students and HiWis. Peng Wang, Ruodong Xin, Elene Aslanikashvili, Wenxin Long supported me in various aspects of my work, including simulations, programming, manufacturing and conducting experiments.

This PhD research was funded by the German Research Foundation (DFG) under the Grant Agreement No.BR 4175/5-1. I am truly grateful for this contribution. I would also like to thank the Karlsruhe Institute of Technology (KIT) and the Institute of Microstructure Technology (IMT) for their unwavering support throughout my work.

I want to express my heartfelt gratitude to my family for their unwavering support throughout my academic journey. Your love has been my strongest foundation.

I want to thank my boyfriend and my soulmate, Zhaowei Chen. His companionship and encouragement have been an immense source of strength in completing my PhD. He is also about to complete his PhD in the Netherlands, and I sincerely hope he can fulfill his dreams as well. Finally, I want to give a special thanks to my three cats, Mochi, Fermion and Boson. Throughout my PhD journey, they three fluffy cuties have been my constant companions, bringing warmth and joy to my life.

Appendix

A Appendix to Chapter 3

A.1 MATLAB code for calculation the equilibrium percentage of *para*-H_2 at different temperature (Figure 3.2).

```
function calcHydrogenIsomersRatio()
% Constants
hbar = 1.0545718e-34;    % Planck's constant over 2*pi, in J*s
k = 1.380649e-23;        % Boltzmann constant, in J/K
I = 4.5829284120656074e-48;  % Corrected moment of inertia for hydrogen molecule, in kg*m^2

% Specific temperature points and their range for plotting
T = linspace(20, 400, 100);  % Temperature range from 20 K to 400 K
specificTs = [23, 77, 300];  % Specific temperatures to highlight

% Preallocate arrays for percentages
paraPercentages = zeros(size(T));
orthoPercentages = zeros(size(T));

% Calculate para-Hydrogen and ortho-Hydrogen percentages for each temperature
for idx = 1:length(T)
    sumEven = sum(arrayfun(@(J) (2*J + 1) * exp(-(J*(J+1) * hbar^2) / (2*I*k*T(idx))), 0:2:100));
    sumOdd = sum(arrayfun(@(J) (2*J + 1) * exp(-(J*(J+1) * hbar^2) / (2*I*k*T(idx))), 1:2:100));
    total = sumEven + 3 * sumOdd;
    paraPercentages(idx) = 100 * sumEven / total;
    orthoPercentages(idx) = 100 * 3 * sumOdd / total;
end

% Plotting
figure;
plot(T, paraPercentages, 'b-', 'Display Name', 'Para-Hydrogen');  % Plot para-Hydrogen percentage
hold on;
plot(T, orthoPercentages, 'r-', 'DisplayName', 'Ortho-Hydrogen');  % Plot ortho-Hydrogen percentage

% Highlight specific temperatures for para-Hydrogen with dashed lines
specificParaPercentages = interp1(T, paraPercentages, specificTs, 'linear');
for i = 1:length(specificTs)
    xline(specificTs(i), 'k--', 'DisplayName', sprintf('%d K', specificTs(i)));  % Vertical dashed line at specific temperature
    yline(specificParaPercentages(i), 'b--', 'DisplayName', sprintf('Para-H2 at %dK: %.2f%%', specificTs(i), specificParaPercentages(i)));  % Horizontal dashed line at percentage
end

title('Percentage of Hydrogen Isomers vs. Temperature');
xlabel('Temperature (K)');
ylabel('Percentage (%)');
```

```
    legend('show');
    grid on;
end
```

A.2 MATLAB code for generating Figure 3.9

```

% Define the initial parameters
E1_values = linspace(-100, 100, 5000);  % Range of E1 values
E2_values = linspace(100, -100, 5000)  % Energy level of the second state
W = 10;  % Perturbation value, kept constant

% Preallocate arrays for the eigenvalues
E_plus = zeros(size(E1_values));
E_minus = zeros(size(E1_values));

% Compute the eigenvalues for each E1 value using the provided formula
for k = 1:length(E1_values)
    E1 = E1_values(k);
    E2 = E2_values(k);
    % Compute eigenvalues using the provided formula
    delta = E1 - E2;
    E_plus(k) = 0.5 * (E1 + E2) + 0.5 * sqrt(delta^2 + 4*abs(W)^2);
    E_minus(k) = 0.5 * (E1 + E2) - 0.5 * sqrt(delta^2 + 4*abs(W)^2);
end

% Compute E1-E2 values
E_diff = E1_values - E2_values;

% Plot the results
figure;
plot(E_diff / 2, E_plus, 'b-', E_diff / 2, E_minus, 'r-', 'LineWidth', 1.5);
hold on;

% Compute and plot the asymptotes for large |delta| (E1-E2)
asymptote_E_plus = 0.5 * (E1_values + E2_values) + 0.5 * abs(E1_values - E2_values);
asymptote_E_minus = 0.5 * (E1_values + E2_values) - 0.5 * abs(E1_values - E2_values);
plot(E_diff / 2, asymptote_E_plus, 'k--', 'LineWidth', 1); % Asymptote for E_+
plot(E_diff / 2, asymptote_E_minus, 'k--', 'LineWidth', 1); % Asymptote for E_-

xlabel('Energy splitting (\Delta [a.u.])');
xlim([-110,110]);
ylabel('Energy Eigenvalues');
%title('Energy Levels of a Two-Level System with Perturbation');
%legend('E_+', 'E_-', 'Asymptote E_+', 'Asymptote E_-');
grid on;
hold off;
```

A.3 MATLAB code for generating Figure 3.11

```

% Define the initial parameters
E1_values = linspace(-100, 100, 5000);  % Range of E1 values
E2_values = linspace(100, -100, 5000);  % Energy level of the second state
W = 10;  % Perturbation value, kept constant
```

```
6
7  % Compute E1-E2 values
8  E_diff = E1_values - E2_values;
9
10 % Compute mixing angle theta
11 theta = 0.5 * atan2(W, E_diff / 2);  % calculate theta
12
13 % Compute mixing coefficients
14 C_1 = cos(theta);
15 C_2 = sin(theta);
16
17 % Compute the square of the mixing coefficients
18 C_1_squared = C_1 .^ 2;
19 C_2_squared = C_2 .^ 2;
20
21 % Plot the results
22 figure;
23 plot(E_diff/2, C_1_squared, 'b-', 'LineWidth', 1.5);  % figure for |C_1|^2
24 hold on;
25 plot(E_diff/2, C_2_squared, 'r-', 'LineWidth', 1.5);  % figure for |C_2|^2
26 xlabel('Energy splitting (\Delta)');
27 ylabel('Mixing coefficient of LACs (|C_a|^2, |C_b|^2)');
28 %title('Squared Mixing Coefficients as a Function of E_1 - E_2');
29 legend('|C_a|^2', '|C_b|^2)');
30
31 grid on;
32 hold off;
```

A.4 MATLAB code for generating Figure 3.12

```
1  % Constants
2  gamma_H = 2.675e8; % Gyromagnetic ratio of hydrogen (rad T^-1 s^-1)
3  gamma_C = 6.728e7; % Gyromagnetic ratio of carbon-13 (rad T^-1 s^-1)
4  J_CH = 10; % Coupling constant in Hz, converted to rad s^-1 later
5  J_CH = 2 * pi * J_CH; % Convert to rad s^-1
6
7  % Pauli matrices
8  I = [1/2 0; 0 1/2];
9  Sx = [0 1; 1 0];
10 Sy = [0 -1i; 1i 0];
11 Sz = [1 0; 0 -1];
12
13 % Define spin matrices for both spins
14 I_Hx = kron(Sx, I); I_Hy = kron(Sy, I); I_Hz = kron(Sz, I);
15 Sx = kron(I, Sx); Sy = kron(I, Sy); Sz = kron(I, Sz);
16
17 % External magnetic field values (in microTesla)
18 B_fields = linspace(-1e-6, 1e-6, 200); % From -10 \muT to 10 \muT
19
20 % Preallocate energy levels and diagonal elements array
21 energy_levels = zeros(length(B_fields), 4); % 4 energy levels for a two-spin system
22 diagonal_elements = zeros(length(B_fields), 4); % 4 diagonal elements for each B
       field
23 eig_2x2_levels = zeros(length(B_fields), 2); % Eigenvalues of the 2x2 matrix for each
        B field
24
25 for i = 1:length(B_fields)
```

```
    B_field = B_fields(i);

    % Hamiltonian construction
    H_zeeman_H = -gamma_H * B_field * I_Hz;
    H_zeeman_C = -gamma_C * B_field * Sz;
    H_coupling = J_CH * (I_Hx * Sx + I_Hy * Sy + I_Hz * Sz);

    H_total = H_zeeman_H + H_zeeman_C + H_coupling;

    % Calculate eigenvalues (energy levels)
    energy_levels(i, :) = eig(H_total);

    % Extract diagonal elements
    diagonal_elements(i, :) = diag(H_total);

    % Extract 2x2 submatrix from the middle two rows and columns of H_total
    H_2x2 = H_total(2:3, 2:3);

    % Calculate eigenvalues of the 2x2 submatrix
    eig_2x2_levels(i, :) = eig(H_2x2);
end

% Plot the energy levels as a function of the magnetic field
figure('Position', [100, 100, 300, 150]);
hold on;

% Plot diagonal elements H_11 and H_44
plot(B_fields * 1e6, diagonal_elements(:, 1) / (2 * pi), 'r-', 'LineWidth', 1.5); % Plot H_11

% Plot eigenvalues of the 2x2 submatrix
plot(B_fields * 1e6, eig_2x2_levels(:, 1) / (2 * pi), 'b-', 'LineWidth', 1.5); % Plot first eigenvalue of 2x2 submatrix
plot(B_fields * 1e6, eig_2x2_levels(:, 2) / (2 * pi), 'g-', 'LineWidth', 1.5); % Plot second eigenvalue of 2x2 submatrix
plot(B_fields * 1e6, diagonal_elements(:, 4) / (2 * pi), 'm-', 'LineWidth', 1.5); % Plot H_44
hold off;
% Labels and Title
xlabel('Magnetic Field (\muT)', 'FontSize', 22);
ylabel('Energy (Hz)', 'FontSize', 22);
%title('Energy Levels vs Magnetic Field');
set(gca, 'FontSize', 22);
pbaspect([4 2 1]);
grid off;

figure('Position', [100, 100, 300, 150]);
hold on;
% Plot all diagonal elements H_11 and H_44

plot(B_fields * 1e6, diagonal_elements(:, 1) / (2 * pi), 'r--', 'LineWidth', 1.5); % Plot H_11
plot(B_fields * 1e6, diagonal_elements(:, 2) / (2 * pi), 'b--', 'LineWidth', 1.5); % Plot H_22
plot(B_fields * 1e6, diagonal_elements(:, 3) / (2 * pi), 'g--', 'LineWidth', 1.5); % Plot H_33
plot(B_fields * 1e6, diagonal_elements(:, 4) / (2 * pi), 'm--', 'LineWidth', 1.5); % Plot H_44
hold off;
```

```
77
78  % Labels and Title
79 xlabel('Magnetic Field (\muT)', 'FontSize', 22);
80 ylabel('Energy without perturbation terms (Hz)', 'FontSize', 22);
81 %title('Energy Levels vs Magnetic Field');
82 set(gca, 'FontSize', 22);
83 grid off;
```

A.5 MATLAB code for generating the Hamiltonian with singlet-triplet basis in three-spin system (Equation 3.67)

```
1  % Symbol tool
2  syms gamma_H gamma_C B_field J_HH J_CH_01 J_CH_02 real
3
4  % Definetion of the symbol of H
5  H = [ -gamma_H*B_field-gamma_C*B_field/2+J_HH/4+J_CH_01/4+J_CH_02/4, 0, 0, 0, 0, 0,
       0, 0;
6            0, -gamma_H*B_field+gamma_C*B_field/2+J_HH/4-J_CH_01/4-J_CH_02/4, J_CH_02
                /2, 0, J_CH_01/2, 0, 0, 0;
7            0, J_CH_02/2, -gamma_C*B_field/2-J_HH/4+J_CH_01/4-J_CH_02/4, 0, J_HH/2, 0,
                0, 0;
8            0, 0, 0, gamma_C*B_field/2-J_HH/4-J_CH_01/4+J_CH_02/4, 0, J_HH/2, J_CH_01
                /2, 0;
9            0, J_CH_01/2, J_HH/2, 0, -gamma_C*B_field/2-J_HH/4-J_CH_01/4+J_CH_02/4, 0,
                0, 0;
10           0, 0, 0, J_HH/2, 0, gamma_C*B_field/2-J_HH/4+J_CH_01/4-J_CH_02/4, J_CH_02
                /2, 0;
11           0, 0, 0, J_CH_01/2, 0, J_CH_02/2, gamma_H*B_field-gamma_C*B_field/2+J_HH/4-
                J_CH_01/4-J_CH_02/4, 0;
12           0, 0, 0, 0, 0, 0, 0, gamma_H*B_field+gamma_C*B_field/2+J_HH/4+J_CH_01/4+
                J_CH_02/4];
13
14 % Definition of unit matrix z
15 z = [
16     [1, 0, 0, 0, 0, 0, 0, 0];
17     [0, 1, 0, 0, 0, 0, 0, 0];
18     [0, 0, 1, 0, 0, 0, 0, 0];
19     [0, 0, 0, 1, 0, 0, 0, 0];
20     [0, 0, 0, 0, 1, 0, 0, 0];
21     [0, 0, 0, 0, 0, 1, 0, 0];
22     [0, 0, 0, 0, 0, 0, 1, 0];
23     [0, 0, 0, 0, 0, 0, 0, 1]
24 ];
25
26 % Definition of S0, Tp, Tm, T0 and alpha, beta
27 S0 = [0, -1, 1, 0];
28 Tp = [1, 0, 0, 0];
29 Tm = [0, 0, 0, 1];
30 T0 = [0, 1, 1, 0];
31 alpha = [1, 0];
32 beta = [0, 1];
33
34 % Calculation of Kronecker of the singlet-triplet and the Zeeman basis and save it in
       the tramsformation matrix (tr)
35 tr = [
36     kron(S0, alpha);
```

```
    kron(Tp, beta);
    kron(T0, alpha);
    kron(S0, beta);
    kron(Tm, alpha);
    kron(T0, beta);
    kron(Tm, beta);
    kron(Tp, alpha)
];

% Normalization of each row
for i = 1:size(tr, 1)
    tr(i, :) = tr(i, :) / norm(tr(i, :));
end
% transform in symbol matrix
tr = sym(tr);

% calculation of the transformation matrix
Transform = z * tr;

% calculation of H_trans
H_trans = Transform * H * Transform';

% Display the matrix H_trans
disp('Transformed Hamiltonian:')
disp(simplify(H_trans))
```

A.6 MATLAB code for generating Figure 3.14

```
%%%without perturbation
%%Caculation of the row of the H_transform and the diagonal elments of the
%%H_transform (ii). The real B values are consistent with the crosssection
%%of the H_transform (ii).
clear all;
% Definition of constants
gamma_H = 42.57e6; % Gyromagnetic ration of proton
gamma_C = 10.7e6; % Gyromagnetic ration of carbon
J_HH = -10.6; % J-coupling constant of I_a and I_b
J_CH_01 = -0.97; % J-coupling constant of I_a and S
J_CH_02 = -0.06; % J-coupling constant of I_b and S
B_min = -1e-6; % Minimum magnetic field (in Tesla)
B_max = 1e-6; % Maximum magnetic field (in Tesla)
B_points = 1000; % Number of points for magnetic field

% Magnetic Field Range
B = linspace(B_max, B_min, B_points); % Magnetic field values

min_value_001 = inf;
min_value_002 = inf;
B1_001 = NaN; %
B1_002 = NaN; %

z = eye(8);

S0 = [0, -1, 1, 0];
Tp = [1, 0, 0, 0];
Tm = [0, 0, 0, 1];
T0 = [0, 1, 1, 0];
```

```
alpha = [1, 0];
beta = [0, 1];

tr = [
    kron(S0, alpha);
    kron(Tp, beta);
    kron(T0, alpha);
    kron(S0, beta);
    kron(Tm, alpha);
    kron(T0, beta);
    kron(Tm, beta);
    kron(Tp, alpha)
];

for i = 1:size(tr, 1)
    tr(i, :) = tr(i, :) / norm(tr(i, :));
end

Transform = z * tr;

energy_levels = zeros(B_points, 8);

for i = 1:B_points
    B_field = B(i);

    % Hamiltonian Matrix (8x8) for the two-spin system
    H = [ -gamma_H* B_field-gamma_C* B_field/2+J_HH/4+J_CH_01/4+J_CH_02/4, 0, 0, 0,
        0, 0, 0, 0;
          0, -gamma_H* B_field+gamma_C* B_field/2+J_HH/4-J_CH_01/4-J_CH_02/4, J_CH_02
              /2, 0, J_CH_01/2, 0, 0, 0;
          0, J_CH_02/2, -gamma_C* B_field/2-J_HH/4+J_CH_01/4-J_CH_02/4, 0, J_HH/2, 0,
               0, 0;
          0, 0, 0, gamma_C* B_field/2-J_HH/4-J_CH_01/4+J_CH_02/4, 0, J_HH/2, J_CH_01
              /2, 0;
          0, J_CH_01/2, J_HH/2, 0, -gamma_C* B_field/2-J_HH/4-J_CH_01/4+J_CH_02/4, 0,
               0, 0;
          0, 0, 0, J_HH/2, 0, gamma_C* B_field/2-J_HH/4+J_CH_01/4-J_CH_02/4, J_CH_02
              /2, 0;
          0, 0, 0, J_CH_01/2, 0, J_CH_02/2, gamma_H* B_field-gamma_C* B_field/2+J_HH
              /4-J_CH_01/4-J_CH_02/4, 0;
          0, 0, 0, 0, 0, 0, 0, gamma_H* B_field+gamma_C* B_field/2+J_HH/4+J_CH_01/4+
              J_CH_02/4];

    H_transformed = Transform * H * Transform';

    energy_levels(i, :) = sum(H_transformed, 2)';
    ii_energy_levels(i, :) = diag(H_transformed)';
end

figure;
hold on;
for j = 1:3
    plot(B * 1e6, energy_levels(:, j), '--', 'LineWidth', 1.5);
end
xlabel('Magnetic Field (\muT)','FontSize', 16);
ylabel('Energy of each basis state','FontSize', 16);
set(gca, 'FontSize', 16);
pbaspect([2 3 1]);
%xlim([0, 0.6e-6]);
```

```
%title('Sum of Row Values as a Function of Magnetic Field');
legend('S_0\alpha', 'T_+\beta', 'T_0\alpha');
grid off;
hold off;

figure;
hold on;
for j = 1:3
    plot(B * 1e6, ii_energy_levels(:, j), '--', 'LineWidth', 1.5);
end
xlabel('Magnetic Field (\muT)','FontSize', 16);
ylabel('Energy without purterbation terms (Hz)','FontSize', 16);
set(gca, 'FontSize', 16);
pbaspect([2 3 1]);
%title('Diagonal Elements H(ii) as a Function of Magnetic Field');
legend('S_0\alpha', 'T_+\beta', 'T_0\alpha');
grid off;
hold off;

figure;
hold on;
for j = 4:6
    plot(B * 1e6, energy_levels(:, j), '--', 'LineWidth', 1.5);
end
xlabel('Magnetic Field (\muT)','FontSize', 16);
ylabel('Energy of each basis state','FontSize', 16);
set(gca, 'FontSize', 16);
pbaspect([2 3 1]);
%xlim([0, 0.6e-6]);
%title('Sum of Row Values as a Function of Magnetic Field');
legend('S_0\beta', 'T_-\alpha', 'T_0\beta');
grid off;
hold off;

figure;
hold on;
plot(B * 1e6, ii_energy_levels(:, 4), '--', 'LineWidth', 1.5,'Color', '#FF00FF');
plot(B * 1e6, ii_energy_levels(:, 5), '--', 'LineWidth', 1.5, 'Color', '#006400');
plot(B * 1e6, ii_energy_levels(:, 6), '--', 'LineWidth', 1.5, 'Color', '#BDB76B');

xlabel('Magnetic Field (\muT)','FontSize', 16);
ylabel('Energy without purterbation terms (Hz)','FontSize', 16);
set(gca, 'FontSize', 16);
pbaspect([2 3 1]);
%title('Diagonal Elements H(ii) as a Function of Magnetic Field');
legend('S_0\beta', 'T_-\alpha', 'T_0\beta');
grid off;
hold off;

figure;
hold on;
plot(B * 1e6, ii_energy_levels(:, 1), '--', 'LineWidth', 1.5, 'Color', [0, 0.4470,
    0.7410]);
plot (B * 1e6, ii_energy_levels(:, 2), '--', 'LineWidth', 1.5, 'Color', [0.8500,
    0.3250, 0.0980]);
plot(B * 1e6, ii_energy_levels(:, 3), '--', 'LineWidth', 1.5,  'LineWidth', 2, 'Color
    ', [0.9290, 0.6940, 0.1250]); %
plot(B * 1e6, ii_energy_levels(:, 4), '--', 'LineWidth', 1.5,'Color', '#FF00FF');
plot(B * 1e6, ii_energy_levels(:, 5), '--', 'LineWidth', 1.5, 'Color', '#006400');
```

```
137 plot(B * 1e6, ii_energy_levels(:, 6), '--', 'LineWidth', 1.5, 'Color', '#BDB76B');
138 plot (B * 1e6, ii_energy_levels(:, 7), '--', 'LineWidth', 1.5, 'Color', [0.4500,
        0.3250, 0.0980]);
139 plot(B * 1e6, ii_energy_levels(:, 8), '--', 'LineWidth', 1.5,  'LineWidth', 1.5, '
        Color', [0.1290, 0.6940, 0.1250]);
140
141 xlabel('Magnetic Field (\muT)','FontSize', 16);
142 ylabel('Energy without purterbation terms (Hz)','FontSize', 16);
143 %xlim([0, 1]);
144 set(gca, 'FontSize', 16);
145 % pbaspect([2 3 1]);
146 %title('Diagonal Elements H(ii) as a Function of Magnetic Field');
147 % legend('S_0\alpha', 'T_+\beta', 'T_0\alpha', 'S_0\beta', 'T_-\alpha', 'T_0\beta');
148 legend('S_0\alpha', 'T_+\beta', 'T_0\alpha', 'S_0\beta', 'T_-\alpha', 'T_0\beta', 'T_
        -\beta','T_+\alpha');
149 grid off;
150 hold off;
```

A.7 MATLAB code for generating Figure 3.15

```
1
2  clear all
3  % Definition of constants
4  gamma_H = 42.57e6;
5  gamma_C = 10.7e6;
6  J_HH = -10.6;
7  J_CH_01 = -0.97;
8  J_CH_02 = -0.06;
9  B_min = -1e-6; % Minimum magnetic field (in Tesla)
10 B_max = 1e-6; % Maximum magnetic field (in Tesla)
11 B_points = 1000; % Number of points for magnetic field
12
13 % Magnetic Field Range
14 B = linspace(B_max, B_min, B_points); % Magnetic field values
15
16 min_value_001 = inf;
17 min_value_002 = inf;
18 B1_001 = NaN;
19 B1_002 = NaN;
20
21 z = eye(8);
22 S0 = [0, -1, 1, 0];
23 Tp = [1, 0, 0, 0];
24 Tm = [0, 0, 0, 1];
25 T0 = [0, 1, 1, 0];
26 alpha = [1, 0];
27 beta = [0, 1];
28
29 tr = [
30     kron(S0, alpha);
31     kron(Tp, beta);
32     kron(T0, alpha);
33     kron(S0, beta);
34     kron(Tm, alpha);
35     kron(T0, beta);
36     kron(Tm, beta);
37     kron(Tp, alpha)
```

```
];

for i = 1:size(tr, 1)
    tr(i, :) = tr(i, :) / norm(tr(i, :));
end

Transform = z * tr;

transformed_energy_levels_01 = zeros(B_points, 2);
transformed_energy_levels_02 = zeros(B_points, 2);
transformed_energy_levels_03 = zeros(B_points, 2);
transformed_energy_levels_04 = zeros(B_points, 2);

for i = 1:B_points
    B_field = B(i);

    % Hamiltonian Matrix (8x8) for the two-spin system
    H = [ -gamma_H* B_field-gamma_C* B_field/2+J_HH/4+J_CH_01/4+J_CH_02/4, 0, 0, 0,
        0, 0, 0, 0;
          0, -gamma_H* B_field+gamma_C* B_field/2+J_HH/4-J_CH_01/4-J_CH_02/4, J_CH_02
              /2, 0, J_CH_01/2, 0, 0, 0;
          0, J_CH_02/2, -gamma_C* B_field/2-J_HH/4+J_CH_01/4-J_CH_02/4, 0, J_HH/2, 0,
               0, 0;
          0, 0, 0, gamma_C* B_field/2-J_HH/4-J_CH_01/4+J_CH_02/4, 0, J_HH/2, J_CH_01
              /2, 0;
          0, J_CH_01/2, J_HH/2, 0, -gamma_C* B_field/2-J_HH/4-J_CH_01/4+J_CH_02/4, 0,
               0, 0;
          0, 0, 0, J_HH/2, 0, gamma_C* B_field/2-J_HH/4+J_CH_01/4-J_CH_02/4, J_CH_02
              /2, 0;
          0, 0, 0, J_CH_01/2, 0, J_CH_02/2, gamma_H* B_field-gamma_C* B_field/2+J_HH
              /4-J_CH_01/4-J_CH_02/4, 0;
          0, 0, 0, 0, 0, 0, 0, gamma_H* B_field+gamma_C* B_field/2+J_HH/4+J_CH_01/4+
              J_CH_02/4];

    H_transformed = Transform * H * Transform';
    lac_01 = H_transformed(1:2, 1:2);
    lac_02 = H_transformed(2:3, 2:3);
    lac_03 = H_transformed(4:5, 4:5);
    lac_04 = H_transformed(5:6, 5:6);

    ii_energy_levels(i, :) = diag(H_transformed)';

    eig_lac_01 = eig(lac_01);
    eig_lac_02 = eig(lac_02);
    eig_lac_03 = eig(lac_03);
    eig_lac_04 = eig(lac_04);

    transformed_energy_levels_01(i, :) = eig_lac_01;
    transformed_energy_levels_02(i, :) = eig_lac_02;
    transformed_energy_levels_03(i, :) = eig_lac_03;
    transformed_energy_levels_04(i, :) = eig_lac_04;

    diff_value_001 = abs(eig_lac_01(1) - eig_lac_02(2));
    diff_value_002 = abs(eig_lac_03(1) - eig_lac_04(2));

    if diff_value_001 < min_value_001
        min_value_001 = diff_value_001;
        B1_001 = B_field;
    end
```

```
89
90      if diff_value_002 < min_value_002
91          min_value_002 = diff_value_002;
92          B1_002 = B_field;
93      end
94  end
95
96  [~, i1] = min(abs(B - B1_001));
97  [~, i2] = min(abs(B - B1_002));
98
99  eig_values_001 = nan(1, B_points);
100 eig_values_002 = nan(1, B_points);
101
102 eig_values_001(1:i1) = transformed_energy_levels_02(1:i1, 2);
103 eig_values_001(i1:end) = transformed_energy_levels_01(i1:end, 1);
104
105 eig_values_002(1:i2) = transformed_energy_levels_03(1:i2, 1);
106 eig_values_002(i2:end) = transformed_energy_levels_04(i2:end, 2);
107
108 figure; %%LAC_01 02
109 hold on;
110 plot(B * 1e6, transformed_energy_levels_01(:, 2), 'LineWidth', 2); % S_0\alpha
111 plot(B * 1e6, transformed_energy_levels_01(:, 1), 'LineWidth', 2); % S_0\alpha
112 % plot(B * 1e6, eig_values_001, 'LineWidth', 2); % T_+\beta
113 plot(B * 1e6, transformed_energy_levels_02(:, 2), 'LineWidth', 2); % T_0\alpha
114 plot(B * 1e6, transformed_energy_levels_02(:, 1), 'LineWidth', 2); % T_0\alpha
115 hold off;
116 set(gca, 'FontSize', 16)
117 xlabel('Magnetic field strength (\muT)','FontSize', 16);
118 ylabel('Energy (Hz)','FontSize', 16);
119 pbaspect([2 3 1]);
120 grid off;
121 % legend('S_0\alpha', 'T_+\beta', 'T_+\beta', 'T_0\alpha')
122
123 figure;%%LAC_03 04
124 hold on;
125 plot(B * 1e6, transformed_energy_levels_03(:, 2), 'LineStyle', '-', 'LineWidth', 2, '
      Color', '#FF00FF'); % S_0\beta
126 % plot(B * 1e6, transformed_energy_levels_03(:, 2), 'LineStyle', '-', 'LineWidth', 2,
      'Color', '#006400'); % S_0\beta
127 plot(B * 1e6, eig_values_002, 'LineStyle', '-', 'LineWidth', 2, 'Color', '#006400');
      % T_-\alpha
128 % plot(B * 1e6, transformed_energy_levels_04(:, 1), 'LineStyle', '-', 'LineWidth', 2,
      'Color', '#006400'); % S_0\beta
129 plot(B * 1e6, transformed_energy_levels_04(:, 1), 'LineStyle', '-', 'LineWidth', 2,'
      Color', '#BDB76B'); % T_0\beta
130 hold off;
131 set(gca, 'FontSize', 16)
132 xlabel('Magnetic field strength (\muT)','FontSize', 16);
133 ylabel('Energy (Hz)','FontSize', 16);
134 pbaspect([2 3 1]);
135
136 grid off;
137 % legend('S_0\beta', 'T_-\alpha', 'T_-\alpha', 'T_0\beta');
138 % legend('S_0\alpha', 'T_+\beta', 'T_0\alpha', 'S_0\beta', 'T_-\alpha', 'T_0\beta');
139 %
140 figure; %% all LACs
141 hold on;
142 plot(B * 1e6, transformed_energy_levels_01(:, 2), 'LineWidth', 2); % S_0\alpha
```

```
143 plot(B * 1e6, eig_values_001, 'LineWidth', 2); % T_+\beta
144 plot(B * 1e6, transformed_energy_levels_02(:, 1), 'LineWidth', 2); % T_0\alpha
145 plot(B * 1e6, transformed_energy_levels_03(:, 2), 'LineStyle', '-', 'LineWidth', 2, '
    Color', '#FF00FF'); % S_0\beta
146 plot(B * 1e6, eig_values_002, 'LineStyle', '-', 'LineWidth', 2, 'Color', '#006400');
    % T_-\alpha
147 plot(B * 1e6, transformed_energy_levels_04(:, 1), 'LineStyle', '-', 'LineWidth', 2,'
    Color', '#BDB76B'); % T_0\beta
148 plot(B * 1e6, ii_energy_levels(:, 7), '--', 'LineWidth', 1.5, 'Color', [0.4500,
    0.3250, 0.0980]);
149 plot(B * 1e6, ii_energy_levels(:, 8), '--', 'LineWidth', 1.5,  'LineWidth', 2, 'Color
    ', [0.1290, 0.6940, 0.1250]);
150
151 hold off;
152 set(gca, 'FontSize', 16)
153 xlabel('Magnetic field strength (\muT)','FontSize', 16);
154 ylabel('Energy (Hz)','FontSize', 16);
155 grid off;
156 legend('S_0\alpha', 'T_+\beta', 'T_0\alpha','S_0\beta', 'T_-\alpha', 'T_0\beta', 'T_
    -\beta','T_+\alpha')
157 %
158 %
159 %
160 %%%%%%%%% State of population in LAC 01 and 02
161
162 d_transformed_energy_levels_011 = diff(transformed_energy_levels_01(:, 1)) ./ diff(B
    * 1e6);
163 d_transformed_energy_levels_012 = diff(transformed_energy_levels_01(:, 2)) ./ diff(B
    * 1e6);
164 d_transformed_energy_levels_021 = diff(transformed_energy_levels_02(:, 1)) ./ diff(B
    * 1e6);
165 d_transformed_energy_levels_022 = diff(transformed_energy_levels_02(:, 2)) ./ diff(B
    * 1e6);
166
167 %%%%%%%%% State of population in LAC 03 and 04
168
169 d_transformed_energy_levels_031 = diff(transformed_energy_levels_03(:, 1)) ./ diff(B
    * 1e6);
170 d_transformed_energy_levels_032 = diff(transformed_energy_levels_03(:, 2)) ./ diff(B
    * 1e6);
171 d_transformed_energy_levels_041 = diff(transformed_energy_levels_04(:, 1)) ./ diff(B
    * 1e6);
172 d_transformed_energy_levels_042 = diff(transformed_energy_levels_04(:, 2)) ./ diff(B
    * 1e6);
173
174 figure; %%%state of population for LACs 01 and 02 in onr figure
175 hold on;
176 plot(B(1:end-1) * 1e6, d_transformed_energy_levels_011,  'LineWidth', 2, 'Color', [0,
     0.4470, 0.7410]);
177 plot(B(1:end-1) * 1e6, d_transformed_energy_levels_012,  'LineWidth', 2, 'Color',
    [0.8500, 0.3250, 0.0980]);
178 plot(B(1:end-1) * 1e6, d_transformed_energy_levels_021,  'LineWidth', 2, 'Color',
    [0.8500, 0.3250, 0.0980]);
179 plot(B(1:end-1) * 1e6, d_transformed_energy_levels_022,  'LineWidth', 2, 'Color',
    [0.9290, 0.6940, 0.1250]);
180 hold off;
181
182 figure; %%%state of population for LACs 03 and 04 in onr figure
183 hold on;
```

```
184 plot(B(1:end-1) * 1e6, d_transformed_energy_levels_031, 'LineWidth', 2, 'Color', '#
        FF00FF');
185 plot(B(1:end-1) * 1e6, d_transformed_energy_levels_032, 'LineWidth', 2, 'Color', '
        #006400');
186 plot(B(1:end-1) * 1e6, d_transformed_energy_levels_041, 'LineWidth', 2, 'Color', '
        #006400');
187 plot(B(1:end-1) * 1e6, d_transformed_energy_levels_042, 'LineWidth', 2, 'Color', '#
        BDB76B');
188 hold off;
189
190 %%%
191 E22 = nan(1, length(d_transformed_energy_levels_012));
192 E22(1:i1) = d_transformed_energy_levels_022(1: i1, 1);
193 E22(i1+1:end) = d_transformed_energy_levels_011(i1+1:end,1);
194
195 E33 = nan(1, length(d_transformed_energy_levels_032));
196 E33(1:i2) = d_transformed_energy_levels_031(1: i2, 1);
197 E33(i2+1:end) = d_transformed_energy_levels_042(i2+1:end,1);
198
199 figure; %%%state of population for LACs 03 and 04 in onr figure
200 hold on;
201 plot(B(1:end-1) * 1e6, d_transformed_energy_levels_032, 'LineWidth', 2, 'Color', '#
        FF00FF');
202 plot (B(1:end-1) * 1e6, E33, 'LineWidth', 2, 'Color', '#006400');
203 plot(B(1:end-1) * 1e6, d_transformed_energy_levels_041, 'LineWidth', 2, 'Color', '#
        BDB76B'); ha
204 hold off;
205
206 set(gca, 'FontSize', 16)
207 xlabel('Magnetic field strength (\muT)','FontSize', 16);
208 ylabel('State of population)','FontSize', 16); %dE/dB unit in [Hz/\muT]
209 grid on;
210
211 figure; %%%state of population for LACs 01 and 02 in onr figure
212 hold on;
213 plot(B(1:end-1) * 1e6, d_transformed_energy_levels_012, 'LineWidth', 2, 'Color', [0,
        0.4470, 0.7410]);
214 plot (B(1:end-1) * 1e6, E22, 'LineWidth', 2, 'Color', [0.8500, 0.3250, 0.0980]);
215 plot(B(1:end-1) * 1e6, d_transformed_energy_levels_021, 'LineWidth', 2, 'Color',
        [0.9290, 0.6940, 0.1250]);
216 % plot(B(1:end-1) * 1e6, d_transformed_energy_levels_032, 'LineWidth', 2, 'Color',
        '#FF00FF');
217 % plot (B(1:end-1) * 1e6, E33, 'LineWidth', 2, 'Color', '#006400');
218 % plot(B(1:end-1) * 1e6, d_transformed_energy_levels_041, 'LineWidth', 2, 'Color',
        '#BDB76B');
219 hold off;
220
221 pbaspect([4 3 1]);
222 set(gca, 'FontSize', 16)
223 xlabel('Magnetic field strength (\muT)','FontSize', 16);
224 ylabel('State of population','FontSize', 16); %dE/dB unit in [Hz/\muT]
225
226 grid on;
227
228 figure; %%%state of population for all four LACs in onr figure
229 hold on;
230 plot(B(1:end-1) * 1e6, d_transformed_energy_levels_012, 'LineWidth', 2, 'Color', [0,
        0.4470, 0.7410]);
231 plot (B(1:end-1) * 1e6, E22, 'LineWidth', 2, 'Color', [0.8500, 0.3250, 0.0980]);
```

```
232 plot(B(1:end-1) * 1e6, d_transformed_energy_levels_021,  'LineWidth', 2, 'Color',
        [0.9290, 0.6940, 0.1250]);
233 plot(B(1:end-1) * 1e6, d_transformed_energy_levels_032,  'LineWidth', 2, 'Color', '#
        FF00FF');
234 plot (B(1:end-1) * 1e6, E33, 'LineWidth', 2, 'Color', '#006400');
235 plot(B(1:end-1) * 1e6, d_transformed_energy_levels_041,  'LineWidth', 2, 'Color', '#
        BDB76B');
236 hold off;
237
238 pbaspect([4 3 1]);
239 set(gca, 'FontSize', 16)
240 xlabel('Magnetic field strength (\muT)','FontSize', 16);
241 ylabel('Partial dirivative of energy','FontSize', 16); %dE/dB unit in [Hz/\muT]
242 grid on;
```

B Appendix for Chapter 6

B.1 An integrated representation of the measured five RASER regimes

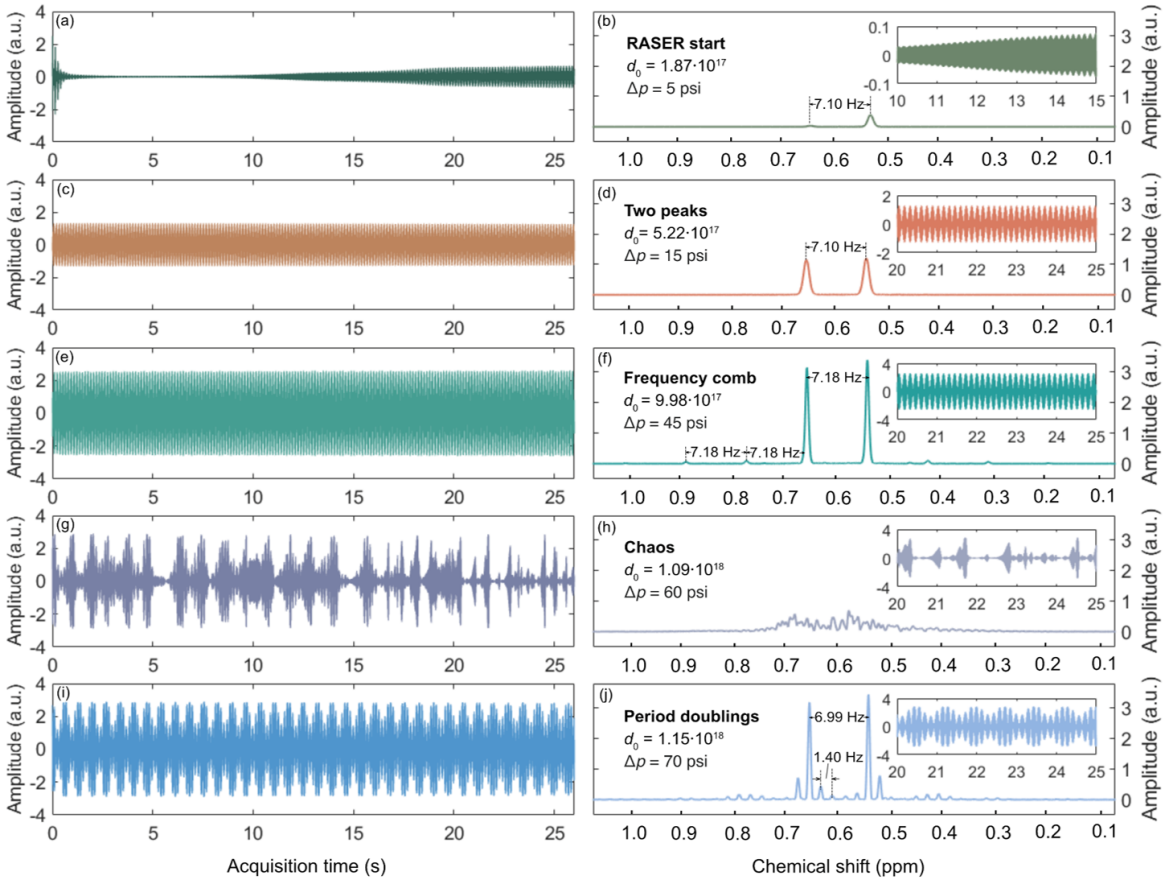

Figure B1: Continuously pumped RASERs of hyperpolarized EA. Left column: ^{1}H RASER signals stemming from the two RASER active modes introduced in Figure 6.3. Right column: Corresponding Fourier transformed spectra of selected time slices (shown in the insets). The spectra show different RASER regimes depending on the pumping d_0: **(b)** starting RASER, **(d)** the "normal NMR" mode with two peaks, **(f)** frequency comb, **(h)** chaos, and **(j)** period doublings. The flow rate was set to 4 mL/min in all experiments as a compromise between residence time in the reactor and transport time to the magnet. (Adopted from [JY02].)

B.2 ODE system for simulation of the two-mode RASER system

```
%% mainfunc
function dydt = ODEsystem(~,y,GAMMA_m,gamma_m,k_m,T_1_inv,g_m2,w_m,d_0,N,d_0_same)
dydt = zeros(3*N,1);
T1=@sumterm1; %sumterm in d_m
T2=@sumterm2; %sumterm in A_m
T3=@sumterm3; %sumterm in phi_m

for u = 1:N %3N Gleichungen zeugen
    if d_0_same==1
        dydt(3*u-2) = GAMMA_m*(d_0-y(3*u-2))- y(3*u-2)*T_1_inv - T1(u);
```

```
    else
        dydt(3*u-2) = GAMMA_m*(d_0-y(3*u-2))- y(3*u-2)*T_1_inv - T1(u);
    end
    dydt(3*u-1) = -gamma_m*y(3*u-1) + T2(u);
    dydt(3*u) =  w_m(u) + T3(u);

end

    function T1 = sumterm1(~)
        T1=zeros();
        for m = 1 :3: 3*N % A_v, v = 1,2,3...
            for n =1 :3 :3*N % A_sigma,sigma = 1,2,3...
                T1 = T1 + 4*g_m2/k_m*y(m+1)*y(n+1)*cos(y(m+2)-y(n+2));
            end
        end
    end
    function T2 = sumterm2(u)
        T2=zeros();
        for m = 1:3:3*N % tao = 1,2,3...
            T2 = T2 + g_m2/k_m*y(3*u-2)*y(m+1)*cos(y(m+2)-y(3*u));
        end
    end
    function T3 = sumterm3(u)
        T3=zeros();
        for m = 1:3:3*N % tao = 1,2,3...
            T3 = T3 + g_m2/k_m*y(3*u-2)/y(3*u-1)*y(m+1)*sin(y(m+2)-y(3*u));
        end
    end
end
```

B.3 MATLAB code for generating Figure 6.12

```
%% read from input.xlsx

Name=  {'jing'}; % always from 1 in the beginning

N=readmatrix([cell2mat(Name),'(input).xlsx'],"Sheet","Sheet1",'Range','A2:A2');
GAMMA_m=readmatrix([cell2mat(Name),'(input).xlsx'],"Sheet","Sheet1",'Range','B2:B2');
% GAMMA_m=GAMMA_m(2:end);
gamma_m=readmatrix([cell2mat(Name),'(input).xlsx'],"Sheet","Sheet1",'range','C2:C2');
k_m=readmatrix([cell2mat(Name),'(input).xlsx'],"Sheet","Sheet1",'range','D2:D2');
T_1_inv=1./(readmatrix([cell2mat(Name),'(input).xlsx'],"Sheet","Sheet1",'range','E2:
    E2'));
g_m2=readmatrix([cell2mat(Name),'(input).xlsx'],"Sheet","Sheet1",'range','F2:F2');
Fs=readmatrix([cell2mat(Name),'(input).xlsx'],"Sheet","Sheet1",'range','G2:G2');
T_max=readmatrix([cell2mat(Name),'(input).xlsx'],"Sheet","Sheet1",'range','H2:H2');
y0_matrix_read=readmatrix([cell2mat(Name),'(input).xlsx'],"Sheet","Sheet2",'range','
    A1');
delta_nu=readmatrix([cell2mat(Name),'(input).xlsx'],"Sheet","Sheet1",'range','J2:J2')
    ;
d_0start=readmatrix([cell2mat(Name),'(input).xlsx'],"Sheet","Sheet1",'range','I2:I2')
    ;
y0_matrix=y0_matrix_read(:,1:N);
y0 = reshape(y0_matrix,1,[]); % reshape matrix to vector
d_th=log10(    d_0start);
d_0=zeros(numel(d_th),50);

```

```
for j =1:numel(d_th)
    d_0(j,:)=logspace(d_th(j),19,50);
end
Delta=N*delta_nu; %0.1 0.1375 0.175 0.2 0.25 0.3
Nu_0=readmatrix([cell2mat(Name),'(input).xlsx'],"Sheet","Sheet1",'range','K2:K2');

%% result compute
str = cell(1,numel(d_th));
color=rand(numel(d_th),3); % color definition

m = 1 ;  %8:numel(d_th)
delta_nu=Delta./N;  %interval compute
w_m=zeros(N,1);
for n =1:N
    w_m(n)=2*pi*(Nu_0-0.5*(Delta(m)-delta_nu(m)*(2*n-1)));
end

str{m}=['Frequency \nu_{2}-\nu_{1}=' mat2str(delta_nu(m)) 'Hz'];
tspan = (0:1/Fs:T_max);
f_max= nan(15000,numel(d_0(1,:)));
spectrum_max=nan(15000,numel(d_0(1,:)));

lenalpha=numel(tspan);
f_end=100; %find the max alpha in 0- 100 Hz
 d_0_reduced=zeros(1,length(d_0));
d_0=zeros(1,length(d_0))

for i=1:numel(d_0(1,:))

    Sumalpha=zeros();

    if d_0(i)<=10^17
        Min_Prominance=0.05;
    elseif (10^17<d_0(i))&&(d_0(i)<10^18)
        Min_Prominance=0.05;
    elseif d_0(i)>10^18
        Min_Prominance=0.01;
    end

    for section=1:numel(GAMMA_m)

        [t,y] = ode45(@(t,y) ODEsystem(t,y,GAMMA_m(section),gamma_m,k_m,T_1_inv,g_m2,
            w_m,d_0(m,i),N),tspan,y0);

        for n1=2:3:3*N
            Sumalpha =real(y(:,n1).*exp(1i.*y(:,n1+1)))+Sumalpha;
        end
    end

    snippet=Sumalpha(ceil((lenalpha-1)/4):end); % filter Anfangsauslenkungen
    [f,spectrum]=FFT_Hemming0(snippet,Fs);
    spectrum=abs(spectrum);

    f_1=f(1:ceil(2*f_end/Fs*numel(spectrum)));
    spectrum_1(:,i) = spectrum(1:ceil(2*f_end/Fs*numel(spectrum))).';
    [TF,P]= islocalmax(spectrum_1(:,i),'MinProminence',Min_Prominance*max(spectrum));
         %find the max alpha in 0- 100 Hz; threshold 0.1 Maximum of spectrum
    f_max(:,i)=[f_1(TF),nan(1,15000-length(f_1(TF)))];
    spectrum_max(:,i)=[spectrum_1(TF,i);nan(15000-length(spectrum_1(TF,i)),1)];
```

```
79      t_reduce=40; % d_0_reduce t
80      d_0_reduced(i)=GAMMA_m(1)*(d_0(i)-y(Fs*t_reduce,1))- y(Fs*t_reduce,1)*T_1_inv;
81  end
82  %% logistical map
83
84  fig = figure(1);
85  fig.WindowState = 'maximized';
86  semilogx(d_0(m,:),f_max,'o','MarkerSize',4,Color='b',MarkerEdgeColor='auto',
        MarkerFaceColor='auto' );
87  xlabel('Pumping d_{0}','FontSize',12);
88  ylabel('Frequency (Hz)','FontSize',12);
89  legend(str{m},'Location','northwest','FontSize',12);
90  grid on
91  saveas(gcf,[[num2str((Delta(m)/N))] '(1)Hz.jpg'],'jpg')
92  save('output(y).mat','d_0','f_1','spectrum_1')
```

B.4 Simulated bifurcation diagram with 500 spectra

According the flowchart shown in Figure 6.11, 500 spectra are simulated in the range of $d_0 \in [2 \cdot 10^{16}, 4 \cdot 10^{18}]$ to plot the bifurcation diagram (Figure B2**a**). The blue colorbar shows the amplitudes of the peaks in the spectra. In Figure B2**b**, the peak amplitude is visualize in a 3D plot.

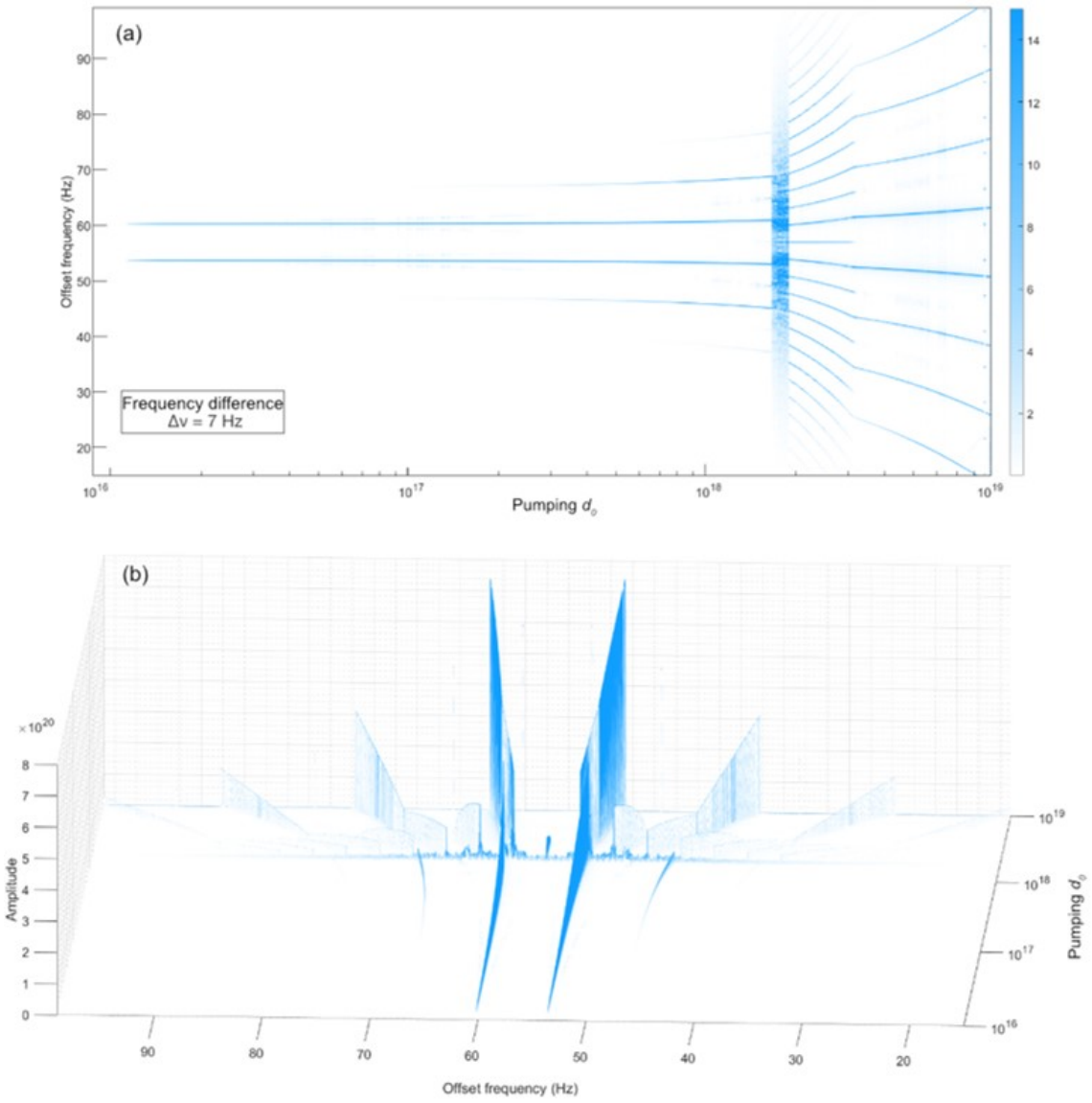

Figure B2: Two visualizations of a simulated bifurcation diagram of two nonlinear-coupled RASER modes following the flow chart showing in Figure 6.11. The image is based on 500 spectra in the range of $d_0 \in [10^{16}, 10^{19}]$ with the peak amplitudes visualized by **(a)** the color bar at right (as in Figure 6.12**a**) and **(b)** in a 3D mesh surface plot. (Adopted from [JY02].)

List of Figures

List of Tables